WATER WAVE INTERACTION WITH DIFFERENT STRUCTURES AND OBSTACLES DUE TO VARIOUS TYPES OF BOTTOM TOPOGRAPHY IN A HOMOGENEOUS FLUID AND A TWO-LAYER FLUID

by

Ayan Chanda

DEPARTMENT OF MATHEMATICS
INDIAN INSTITUTE OF TECHNOLOGY
GUWAHATI
GUWAHATI-781039, INDIA
July, 2021

WATER WAVE INTERACTION WITH DIFFERENT STRUCTURES AND OBSTACLES DUE TO VARIOUS TYPES OF BOTTOM TOPOGRAPHY IN A HOMOGENEOUS FLUID AND A TWO-LAYER FLUID

A Thesis Submitted in Partial Fulfillment
of the Requirements for the Degree of
Doctor of Philosophy

by

Ayan Chanda
(Roll No. - 166123002)

DEPARTMENT OF MATHEMATICS
INDIAN INSTITUTE OF TECHNOLOGY GUWAHATI
GUWAHATI-781039, INDIA
July, 2021

Dedicated To My Parents

Shri Ashish Kr. Chanda
&
Smt. Aparna Chanda

Declaration

I do hereby declare that this thesis entitled **Water wave interaction with different structures and obstacles due to various types of bottom topography in a homogeneous fluid and a two-layer fluid** is a presentation of my original research work done under the supervision of **Dr. Swaroop Nandan Bora**, Professor, Department of Mathematics, Indian Institute of Technology Guwahati for the award of the degree of Doctor of Philosophy and this work has not been submitted elsewhere for a degree.

July, 2021

Ayan Chanda
Roll No. 166123002
Department of Mathematics
Indian Institute of Technology Guwahati

Certificate

It is to certify that the work contained in this thesis entitled **Water wave interaction with different structures and obstacles due to various types of bottom topography in a homogeneous fluid and a two-layer fluid** has been carried out by **Ayan Chanda**, a student in the Department of Mathematics, Indian Institute of Technology Guwahati under my supervision for the award of the degree of Doctor of Philosophy and this work has not been submitted elsewhere for a degree.

July, 2021

Dr. Swaroop Nandan Bora
Professor
Department of Mathematics
Indian Institute of Technology Guwahati

Acknowledgements

There are a number of people without whose cooperation and goodwill this thesis would not have been completed, and whom I would like to acknowledge here.

First and foremost, I am very grateful to my supervisor Prof. Swaroop Nandan Bora for his generous guidance throughout these years. I would also like to express my deep appreciation for his caring attitude, patience, understanding and support. He helped me to overcome many obstacles that emerged while working on several problems throughout my passage of time as a research scholar. In a good way, he always used to push for better results and helped me in every possible way. His continuous encouragement and advice made it possible for me to work on this thesis. I must also acknowledge his confidence in me and the amount of freedom I was given in carrying out my research. I could not have imagined having a better advisor and mentor like him for my Ph.D study.

Besides my supervisor, I would like to express my gratitude to my doctoral committee members Prof. Durga Charan Dalal, Prof. Natesan Srinivasan and Prof. Rajen Kumar Sinha for their continuous encouragement and insightful comments over the years to improve my research work. I must not fail to sincerely appreciate and acknowledge the financial support received from the Ministry of Education (earlier Ministry of Human Resource Development), Government of India. I sincerely acknowledge Indian Institute of Technology Guwahati for providing a very congenial academic environment and all kinds of support. I am also grateful to all the staff members of the Department of Mathematics for their assistance in various ways during my research period.

I would also like to thank all the faculty members and all HODs, during my Ph.D, of the Department of Mathematics. I am very grateful to Dr. Bhupen Deka for his worthy guidance during my M.Sc. project.

I would like to thank my friends Abhijit, Shamik, Shyam, Ankita, Shantiram, Somnath, Rakesh, Subhadeep, Nilay, Mrityunjoy, Koushik and many others for all their encouragement and support during this period. It is my great pleasure to thank my college friends Mithun, Jayanta Sarkar, Jayanta Roy, Amitesh and Subhamoy for their wonderful friendship since my college days. My special appreciation goes to my childhood friends Rony, Koustav, Gourab, Anirban and Aritra with whom I have shared some of the best moments of my life. I am also thankful to my seniors Dr. Santu Das and Dr. Sunanda Saha for their several helpful advice.

I owe my deepest gratitude to Debamita for being so supportive and encouraging throughout. Thanks to her for being always by my side at every step of this journey and beyond.

Finally I would like to extend my deepest gratitude to my parents for everything they have done for me from the very first day of my life. I am grateful for their unconditional love which surrounds me and gives me the strength at every moment of my life. I also take the opportunity to thank all other family members for their blessings, love, concern and moral support.

Last but not the least, I would like to thank God for giving me the strength, ability, and opportunity to undertake this research study and to complete it, especially during a tough period due to COVID-19.

July, 2021 **Ayan Chanda**

ABSTRACT

This thesis attempts to contribute to the understanding of the mechanism behind the interaction of water waves with an elastic bottom topography, an ice-sheet and some porous structures, the importance of which has been increasing with continuing attempts made to promote the economic and commercial benefits of coastal and polar regions in a sustainable and environment-friendly manner. The research in the thesis focuses on various aspects of water wave scattering in the area of coastal and polar engineering, and aims to shed some light on both the nature and applications from the angle of hydrodynamics.

This thesis studies (i) water wave scattering by a small undulation on an elastic sea-bed in a two-layer fluid of finite depth, which is bounded by either a rigid flat structure or a very thin ice-sheet; (ii) interaction of water waves by dual submerged porous barriers in a homogeneous fluid subject to different upper and lower surface boundary conditions. To solve the elastic sea-bed or ice-covered problems, the flexural boundary is considered as a thin elastic plate and is based on the Euler-Bernoulli beam equation. The surface tension at the interface of the layers is completely ignored and each fluid layer is considered to be immiscible. Furthermore, the assumptions of linear and time harmonic motions are followed.

The first issue is to investigate the scattering of a train of small amplitude harmonic water waves by a small bottom undulation on an elastic sea-bed, for a two-layer fluid flow, for both normal and oblique incidences. Furthermore, it is assumed that the fluid is of finite depth and the upper fluid is (i) free to the atmosphere; or (ii) covered by a rigid lid; or (iii) covered by a thin ice-sheet. In this study, mixed boundary value problems are set up for the purpose of determining a velocity potential in each layer where the governing equation happens to be modified Helmholtz equation in two-dimensions for oblique incidence and Laplace's equation in three-dimensions for normal incidence within the fluid. The governing equation is followed by boundary conditions near the upper rigid boundary or the ice-cover surface or the free surface, at the interface between the two fluids and at the elastic bottom boundary. As the fluid domain extends to infinity,

far-field conditions or infinity conditions arise to ensure the uniqueness of the problem. Applying a simple perturbation technique with a very small parameter δ, which quantifies the smallness of the bottom undulation of the elastic sea-bed, directly to the boundary value problems, the original problems are reduced to two simpler boundary value problems for the first-order correction of the potentials. The mathematical tools utilized in this part of the thesis in obtaining the solution of the boundary value problem are Fourier transform technique and application of residue theorem. From the solutions of the velocity potentials, the reflection and transmission coefficients are evaluated approximately up to the first-order of δ in terms of integrals consisting of the shape function which represents the bottom undulation. In order to validate the theoretical results, different types of shape functions are thought of as appropriate to represent such a bottom deformation so as to evaluate the integrals explicitly for the reflection and transmission coefficients. With regard to these shape functions, the particular case of a patch of sinusoidal ripples (with the same wavenumber or two different wavenumbers) is considered which represents the irregular bottom topography and is similar to some common naturally available obstacles formed at the sea-bed on account of sedimentation and ripple growth of sands. It has been established that a sea-bed with a sinusoidal undulation possesses the capacity to bounce back the energy from the incident wave. This occurrence has a substantial role in connection with coastal protection and also with the likely growth of ripples for an erodible bed. Due to elasticity, a sufficient part of the wave energy gets dissipated by the sea-bed. To create a tranquility zone, it is required to reduce the wave reflection such that the incident wave attenuates in the vicinity of the bottom undulation. For this type of ripple patch, in the case of a sea-bed covered by a free surface, it is observed that when the oblique wave is incident on the interface, energy transfer takes place to the free surface. However, for free surface oblique incident waves, no such energy transfer to the interface takes place because of the parameter ranges. Moreover, in the case of a channel bed assumed bounded above by a rigid boundary, it is observed that Bragg resonance takes place for such problems when the wavenumber of the sea-bed takes a value approximately twice the interface wavenumber. For the case of an elastic sea-bed covered by an ice-sheet, wave energy conversion from one wave mode to the other is exhibited through graphical representations corresponding to various physical parameters of the system. Problems corresponding to water wave scattering by different types of unevenness on the elastic sea-bed of a two-layer fluid are useful in the construction of an effective reflector of the incident wave energy for protecting coastal areas from the rough sea in the polar regions and in many other activities in coastal and ocean engineering.

In the later part of the thesis, oblique water wave scattering by a pair of submerged vertical porous barriers of different heights and having different porous-effect parameters in an infinite channel of finite depth is considered subject to different conditions: (i) the sea-bed is porous; or (ii) the sea-bed is elastic; or (iii) the sea-bed is impermeable and the upper surface is covered by a thin ice-sheet; or (iv) the sea-bed is porous and the upper surface is covered by a thin ice-sheet. Boundary value problems consisting of the governing equation, boundary conditions and matching conditions in terms of the porous effect parameters and elastic parameters are derived. The whole fluid domain is divided into three regions and boundary value problems are formulated in each of these regions. The matching conditions across the porous barriers are derived and with the help of least square method, a matrix system is constructed. The reflection and transmission coefficients as well as the energy loss are computed by solving the matrix system and the effects of various structural parameters are studied graphically. Lower reflection and higher transmission are acquired by affecting an increase in the inertial effect of the porous barriers. However, for fixed properties of the porous barriers, the transmission coefficient is not affected when the positions of the porous barriers are interchanged.

NOMENCLATURE

g	acceleration due to gravity
T	time period
θ	angle of incidence
ω	$= \frac{2\pi}{T}$: angular frequency of the incoming water waves
K	$= \omega^2/g$
ρ_h	density of the homogeneous fluid
ρ_1	lower fluid density
ρ_2	upper fluid density
ρ	$= \rho_2/\rho_1$: density ratio
h_0	thickness of the ice-sheet
E	Young's modulus of the ice-sheet
ν	Poisson's ratio of the ice-sheet
Q	$= Eh_0^3/[12(1-\nu^2)]$, the flexural rigidity of the ice-sheet
θ	angle of incidence of the wave train
f	linearized friction factor (a real number)
S	inertial coefficient
R_p	$= f - \mathrm{i}S$: dimensionless impedance of the porous structure
G	porosity parameter of the sea-bed
$\mathcal{G}_1$	non-dimensional porous-effect parameter of the first porous barrier
$\mathcal{G}_2$	non-dimensional porous-effect parameter of the second porous barrier
L	distance between the vertical barriers

LIST OF FIGURES

LIST OF TABLES

CONTENTS

CHAPTER 1

INTRODUCTION

1.1 Preamble

Fluid dynamics is a very important part of the recent interdisciplinary activities concerning engineering and science, especially in applied mathematics, which deals with the motion of fluid (both liquid and gas) or that of bodies in contact with fluids. Aerodynamics, a part of fluid dynamics, is concerned with the motion of gas while the motion of liquid (mainly water) is studied in hydrodynamics. Fluid dynamics has a wide range of applications, including calculating forces and moments on aircraft in aviation industry, measuring the mass flow rate of petroleum through pipelines, predicting weather patterns, modelling fission weapon detonation and understanding the property of interstellar objects like Nebulae in cosmology. The solution to a fluid dynamics problem is acquired by calculating various properties of the fluid, such as flow velocity, pressure, density, and temperature, as functions of space and time.

The most fundamental equations that arise in fluid mechanics are the conservation laws such as conservation of mass, momentum and energy. Continuum assumption is one of the fundamental concepts in order to define the fluid properties like density, volume, temperature, pressure etc. Under the continuum assumption, a fluid can be treated as a continuous matter instead of being made up with particles so that we can define the fluid properties at infinitesimally small points, and they vary continuously from one point to the next within the fluid.

Fluid flow may be classified into different categories according to its various properties. If the fluid properties do not change with respect to time, then the fluid flow is called a steady flow; otherwise, it is called an unsteady one. A uniform fluid flow is the one in which the velocity is the same at a given instant at every point in the fluid. Fluid flows for which this does not hold are said to be nonuniform. If the density of a fluid changes significantly with changes in pressure and temperature, then the fluid flow is called a compressible fluid flow; and if the change in density is negligible, it is called an incompressible fluid flow. However, the rate of volumetric strain of a fluid element is given by the rate of change of volume per unit original volume, which becomes the divergence of the velocity vector. In other words, flows in which there is no volumetric strain are known as incompressible flows ([89]). It is important to note that Mach number (the ratio of the speed of the flow to the speed of sound) of the fluid flow is used in order to identify compressible and incompressible flows, particularly in aerodynamics. Viscosity is one important property of fluid, which is a measure of its resistance to gradual deformation at a given rate. A fluid flow is called inviscid or non-viscous if the viscosity is negligible, otherwise it is called viscous. The mathematical relation between the shear stress and shear rate of a fluid subjected to a mechanical stress is defined by Newton's law of viscosity. The ratio of shear stress to shear rate is a constant, for a given temperature and pressure, and is defined as the viscosity or coefficient of viscosity. A fluid which satisfies a very close linear relation between stress and strain is known as a Newtonian fluid (for example, water, air etc.) and the one which does not follow any linear relation between stress and strain is known as a non-Newtonian fluid (for example, ketchup, custard, toothpaste, blood, and shampoo). Turbulent flow is a fluid motion distinguished by chaotic changes in pressure and flow velocity. Basically, recirculation, swirl in the flow and randomness in the fluid make a flow turbulent. If turbulence is not presented in the flow, then the fluid flow is known as a laminar flow. Based on the velocity (Mach number (M)) of the flow, fluid flow is also known as subsonic ($M < 0.8$), transonic ($0.8 < M < 1.2$), supersonic ($1.2 < M < 5$) and hypersonic ($5 < M < 10$).

A flow field with a velocity vector $\mathbf{v}$ is said to be irrotational if curl $\mathbf{v} = 0$; otherwise, it is rotational. The condition of irrotationality guarantees the existence of a scalar function Φ, called the velocity potential. If the flow is both irrotational and incompressible, then the equation of continuity becomes Laplace's equation with respect to the velocity potential.

It seems no exaggeration to say that wave motion is the most fundamental characteristic of all physical phenomena. Fluid motion is specified in the form of waves, a form of oscillation which propagates through space and time, transferring energy from one point to another, usually without permanent displacement of the particles of the medium. There are two different types of waves, especially, mechanical wave (water wave, sound wave etc.) which requires a medium, and electromagnetic wave (radio wave, infrared radiation, visible light, ultraviolet radiation, X-ray etc.) which does not require a medium to traverse. Furthermore, corresponding to the direction of propagation, waves are also classified into two different categories as longitudinal wave (water wave) in which particles of the medium vibrates parallel to the direction of the wave and transverse wave (sound wave) which vibrates perpendicular to the direction of the wave or its path of propagation.

Wave propagation and its applications are crucial from the point of view of their credible implementation in many areas of physical interest, including the fields of water waves, acoustics and electromagnetic waves. A wave is a dynamic disturbance in such a way that when it propagates through a medium, energy is transmitted to distant points without any displacement of the particles of the medium. The energy from the sun is transmitted by waves through the ether. When some musical instrument is played upon in a room, sound waves spread throughout the room. In real life, a simple example of water waves is the one when we throw a stone into a pond and observe sinusoidal ripples around the point of impact and spreading in all directions. Several other instances are – when wind blows over water region (lake, ocean etc.) and creates ripples on the water surface; the relative motion of a ship in an ocean; flow over a bottom undulation under the water region. These types of waves have small amplitudes of oscillation. But there also exist some other types of waves in which the amplitude of the wave is not that much small but is significantly visible, like tidal waves, rogue waves and tsunami waves.

Generally, water waves may be classified into two types based on their wavelengths. When the wavelength is assumed to be larger than the depth of water, the analogous study is called shallow water wave theory. The waves belonging to this category are tidal waves, tsunami waves and long waves in shallow water. Furthermore, there are waves whose wavelength is assumed to be much smaller than the depth of water so that the effect of the disturbance diminishes gradually as one goes away downwards from the free surface, and they are called deep water waves (or short waves). One example of such waves is rogue wave. If d is the depth of water and λ is the wavelength of the wave, for $d/\lambda < 1/20$, the wave is known as a shallow water wave or a long wave, and for $d/\lambda > 1/2$, the wave is known as a deep water wave. There also exist waves which are neither shallow water waves nor deep water waves, and they are known as intermediate depth water waves (when $1/20 < d/\lambda < 1/2$). Moreover, if it is assumed that the amplitude of the wave is smaller compared to the wavelength, then the theory is called linearized water wave theory. This theory has been derived on the basis of the assumption that the velocity components of water particles along with their derivatives and the free surface elevation are small, i.e., the motion is assumed to be very small. In reality, ocean waves or surface waves are often nonlinear, but it is found that consideration of linearized theory is sufficient in handling most of the problems related to marine and offshore engineering, simultaneously keeping most of the features intact. In the present thesis, all the physical problems are formulated and solved on the basis of linearized theory of water waves.

A broad interest has been reported of investigation of different kinds of water waves problems by various researchers for several applications. The practical importance of water waves is evident in areas such as hydro-acoustics, submerged navigation, hydro-biology, hydro-optics and ocean research. Particularly in ocean research, proper knowledge of water waves is required for predicting the behaviour of floating structures (immersed totally or partially) such as ships, submarines and tension-leg platforms, and for describing flows over various bottom topographies. Furthermore, the consideration of investigating the wave patterns of ships and other vessels in motion is associated to the calculation of the wave-making resistance and the other hydrodynamic characteristics that are used in marine design. Another area of application is the mathematical modeling of unsteady waves resulting from phenomena such as underwater earthquakes, blasts, etc. Further, attenuation of water waves by suitable breakwaters has immense importance in coastal and offshore engineering.

An ocean rarely contains a fluid of constant density – it always seems to comprise of more than one fluid layer (like fresh water layer, salty water layer, muddy layer etc). Density stratification is an important feature of geophysical flows such as those occurring in the oceans and the atmosphere. Stratification can have significant effects on the mixing process and the dynamics of fluid flows. In lakes and oceans, stratification occurs due to density variations resulting from changes in temperature, salinity or concentration of any other solute, or as a combination of some of these, and it is disrupted by different natural processes including breaking waves, wind action, Coriolis forces and tides, resulting in flows of interest in oceanography. Such sharp density gradients can be generated in the ocean due to gravitational settling of sediments carried by fluids or by solar heating of the upper layer or in an estuary or a fjord into which fresh river water flows over oceanic water which is more saline and consequently heavier. This is being idealized by considering a two-layer system with a fluid of lighter density lying over a fluid of heavier density. Unlike the case of a homogeneous fluid, the two-layer fluid system, having a free surface and an interface, gives rise to fast modes (surface waves) as well as slow modes (internal waves). It should be noted that these kind of problems arise while modelling an underwater pipe bridge across one of the Norwegian fjords which consists of a layer of fresh water on the top of a deep layer of salt water.

In the areas of applied mathematics and mathematical physics, many physical problems can be constructed as mixed boundary value problems governed by elliptic partial differential equations. In order to formulate the physical problem mathematically, water is considered to be confined in a region bounded by a free surface (in contact with the atmosphere) or a rigid surface or an elastic surface (ice-sheet) or any other medium. However, the incorporation of virtual boundaries is made up for the sake of simplification. If an object is considered to be submerged or emerged in water, then the surface of the object in contact with water is treated as the boundary. For scattering or radiation problems, time harmonic waves are taken into consideration, and based on the physics of the problem, the governing partial differential equation happens to be either Laplace's equation or modified Helmholtz equation in three or two dimensions. Some other aspects are that the domain is unbounded, the behaviour of the velocity potential is not known completely at large distances and the boundary conditions of Dirichlet type (no derivative involved) or Neumann type (only derivative involved) or Robin type (mixture of derivative and non-derivative) in certain physical problems etc.

We would like to address briefly on the development of water wave theory in general from the very beginning. A detailed review on the origins of water wave theory is given in Craik [22]. Depending on the outcome of his findings, we are going to point out some of the very important early works. Sir Isaac Newton was the first to attempt a theory of water waves. In *Book II*, *Prop. XLV* of *Principia* (1687), Newton proposed a questionable analogy of oscillation in a U-tube, correctly deducing that the frequency of deep water waves must be proportional to the inverse of the square root of the wavelength (which he termed as the breadth of the wave). Newton's arguments were supported by many authors, among them the Dutch Wilhelm-Jacobs' Gravesande and the French Charles Bossut. Much later, after Leonhard Euler's derivation of the equations of hydrodynamics during 1757-1761, Pierre-Simon Laplace took up the challenge in 1776 to achieve the complete form of wave motion correctly but he failed. In 1781 and 1786, Joseph-Louis Lagrange derived the linearized governing equations for small amplitude waves, and obtained the solution for the limiting case of long plane waves in shallow water. But he wrongly claimed that his shallow water results should remain a good approximation for deep water waves because most of the motion was confined near the surface. A remarkable paper by Franz Joseph von Gerstner (in 1802) gave the first exact nonlinear solution for waves of finite amplitude on deep water. But the Gerstner wave solution was disregarded due to the consideration of wave motion which was not irrotational. Its independent rediscovery by W.J. Macquorn Rankine in 1863 revived the interest in it. In 1818, Simeon D. Poisson gave a brief and correct derivation of the frequency of linear sinusoidal standing waves in finite depth whereas Augustin-Louis Cauchy's work (he was awarded a prize in 1816 for this work which eventually got published in 1827) was valid for infinite depth water only. The Cauchy-Poisson analysis is now acknowledged as an important milestone in the mathematical theory of initial value problems. At the same time, Ernst Heinrich Weber and Wilhelm Eduard Weber published a book "Wellenlehre auf Experimente Gegründet" in 1825 which described the laboratory experiments on plane periodic wave trains in a channel, together with comments and extracts from the theoretical works available at that time. After a few years, in 1837, John Scott Russell provided a remarkable report on wave characteristics in seas, rivers and canals. His experiments are now well known for the discovery of nonlinear solitary waves. He had distinguished four types of waves: waves of translation, including his newly found solitary waves, tides, and bores; oscillatory waves, or periodic wave trains; capillary waves; and corpuscular waves, which are compressive sound waves propagating through water. In the following year, George Green gave an exemplary analysis of the effects of slow variations on the motion of waves in a variable canal of small depth and width, though restricted to the long linear shallow water wave. In 1840, Philip Kelland investigated long waves of small amplitude in canals with nonrectangular cross sections (mainly triangular cross section), and correctly derived the wave speed. The representation of a solitary wave by discontinuous expressions was taken up by Samuel Earnshaw in 1847. He pointed out the conspicuous lack of success in obtaining general solutions to the equations of hydrodynamics, and he emphasized the need to limit theoretical studies to restricted classes of motions, based on hypotheses suggested by experiments. A nonlinear theory attempted by him failed which George Gabriel Stokes developed later. In 1876, Lord Rayleigh derived the correct approximate solution, retaining both dispersion and nonlinearity, and he further observed that Earnshaw's solution was not irrotational. George Biddell Airy's main focus of interest was tidal phenomenon but he also wrote a substantial section on the "Theory of Waves in Canal" and "Account of Experiments on Waves", both in 1841. He gave the now-standard linear theory for plane waves. Airy then focussed on small amplitude waves in canals with slowly varying depth and cross-section. Airy's results for long waves agreed with the earlier works done by Green and Kelland. In 1895, Horace Lamb gave an accessible account of the Cauchy-Poisson analysis in his book *Hydrodynamics* but it was restricted to two-dimensional disturbances.

A long-standing but persistent problem in the area of water wave theory is the determination of the effect of the bed topography and the obstacle(s) on a given wave field. For instance, when coastal engineers tackled some practical problems, then their aim was to predict the amplitude of waves in harbours where both man-made breakwaters and the shape of the ocean-bed affected wave behaviour. This sort of problems involving scattering, diffraction and refraction of waves are mathematically formidable for linearized water wave theory, irrespective of whether taking into consideration of relatively simple bed and/or obstacle geometries. When a train of incident surface (or internal) waves travelling from a large distance is incident on an obstacle submerged or partially immersed in water, a portion of it is reflected by the obstacle, which is known as the reflected wave while another portion is transmitted over or below it, which is known as the transmitted wave. The reflected waves and the transmitted waves are called outgoing waves as they go away from the obstacle after striking. This is known as wave scattering, and in this process, damping of waves occurs which reduces the amplitude of the waves. Scattering process is characterized by two physical quantities: reflection coefficient and transmission coefficient, which play a fundamental role in the mathematical study of water wave scattering problems since they provide a measure for the amount of reflected and transmitted waves. The reflection coefficient K_r and transmission coefficient K_t are, respectively, given by

$$\begin{aligned} K_r &= \frac{\text{Amplitude of the reflected wave}}{\text{Amplitude of the incident wave}}, \\ K_t &= \frac{\text{Amplitude of the transmitted wave}}{\text{Amplitude of the incident wave}}. \end{aligned}$$

This piece of information is extremely beneficial in order to construct offshore structures or in the problem of generation of surface (or internal) waves by any obstacle introduced in the wave-maker problem. But due to several complexity, many researchers sometimes lay emphasis on the determination of these quantities directly instead of going into details of the solution.

Scattering as discussed here is due to the wave interaction with a stationary object or geometry. However, there are some other aspects of water wave propagation, such as radiation and trapping. In the radiation problem, the incident waves are removed and the structure is forced to oscillate at a prescribed frequency. A floating structure undergoes six degrees of freedom: the translational motions in the x-, y- and z- directions referred to as surge, sway and heave, respectively, and the rotational motions about x-, y- and z-axes referred to as pitch, roll and yaw, respectively (Fig. 1.1). On the other hand, a trapped mode is a solution of the corresponding homogeneous boundary value problem and represents a free oscillation with finite energy of the fluid surrounding the fixed structure. These modes persist in some localized region including the free surface while decaying rapidly to zero as the free surface extends to infinity.

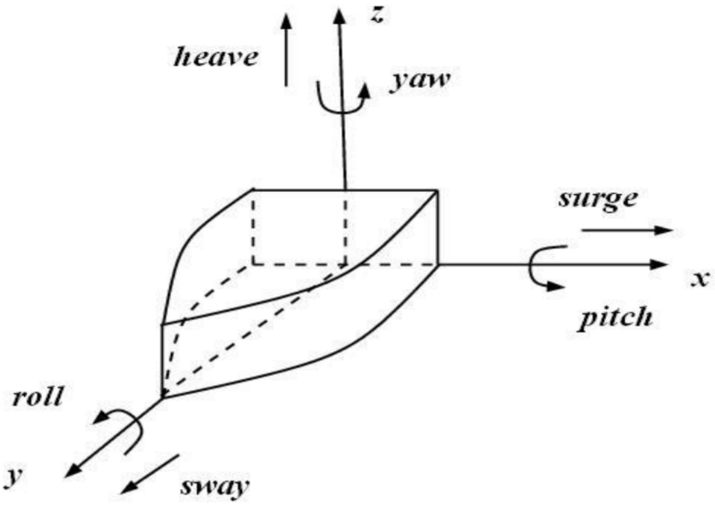

Figure 1.1: Motions of a floating body [77]

Another important phenomenon is wave interference in which two waves superpose to form a resultant wave of greater, lower, or the same amplitude. The interference of waves causes the medium to take on a shape that results from the net effect of the two individual waves upon the particles of the medium. The principle of superposition of waves states that when two or more propagating waves of the same type are incident on the same point, the resultant amplitude at that point is equal to the vector sum of the amplitudes of the individual waves. If a crest of a wave meets a crest of another wave of the same frequency at the same point, then the amplitude is the sum of the individual amplitudes

– this is called constructive interference. If a crest of one wave meets a trough of another wave, then the amplitude is equal to the difference in the individual amplitudes – this is known as destructive interference. Constructive interference occurs when the phase difference between the waves is an even multiple of π, whereas destructive interference occurs when the difference is an odd multiple of π.

Study of propagation of water waves in a homogeneous or a two-layer fluid and the interaction of waves with a floating or submerged obstacle are crucial from the point of view of their credible implementation in coastal and marine engineering. In the last two decades, there has been a substantial interest to address this kind of issues by various researchers. The matter of reflection of oblique waves by small bed fluctuations has experienced an increasing attention since it has an enormous impact in the enhancement of functioning of structures such as shore-parallel bars or pipes, etc. The other class of problems which studies the problem of wave scattering by submerged porous barriers under different situation is important for their possible applications in ocean engineering. High amplitude waves like tidal waves, rogue waves and tsunami waves are such kind of waves where a huge amount of energy is carried through waves which may create destruction in coastal areas, structures in ocean (petroleum extraction machinery) and floating objects (ships, submarines). Due to this, the study of the development of various breakwaters has commanded sufficient attraction in the intensification of various human activities in maritime environment. Majority of the coastal structures are mainly used as breakwaters to protect the offshore areas from hazards of the rough sea and make those structures of porous material to dissipate wave energy. This type of problems is also very useful for designing ships, submarines, offshore structures, etc. The work presented in this thesis is solely concerned with the effect of bed topography with elastic or porous nature and that of porous structures on the water wave scattering.

In the following section, we present a brief description of the basic equations in linearized water wave theory for the case of finite ocean depth.

1.2 Basic equations in linearized water wave theory

We consider the fluid to be homogeneous, incompressible and inviscid, and the motion irrotational. For the treatment of wave motion as discussed here, a Cartesian coordinate system (x, y, z) is adopted with the y-axis directed vertically downwards. The bottom surface is considered as $y = h(x, z)$, where $h(x, z)$ is the local fluid depth and the fluid domain is unbounded in both x and z directions, i.e., $-\infty < x < \infty$; $-\infty < z < \infty$.

The equations for conservation of mass (the equation of continuity) and momentum (Euler's equation of motion) for inviscid incompressible fluid with velocity $\mathbf{u}$ are given by

$$\nabla \cdot \mathbf{u} \;=\; 0, \tag{1.1}$$

$$\frac{\partial \mathbf{u}}{\partial t} + (\mathbf{u} \cdot \nabla)\mathbf{u} = \mathbf{g} - \frac{\nabla p}{\rho_h}, \tag{1.2}$$

where ρ_h is the uniform fluid density, $\mathbf{g}$ is the acceleration due to gravity and p is the pressure in the fluid relative to the atmospheric pressure. We also make the simplifying assumptions that the flow is irrotational and hence the velocity field $\mathbf{u}$ can be written as the gradient of a scalar velocity potential $\Phi(x, y, z, t)$, i.e., $\mathbf{u} = \pm\nabla\Phi$, where t represents time dependence of the fluid motion. Here we consider, throughout this thesis, $\mathbf{u} = \nabla\Phi$. Principle of conservation of mass requires that the divergence of the velocity is zero so that Φ satisfies **Laplace's equation**

$$\nabla^2\Phi = 0, \quad \text{in the fluid region.} \tag{1.3}$$

Utilizing the identity

$$\mathbf{u} \times (\nabla \times \mathbf{u}) = \frac{1}{2}\nabla(\mathbf{u} \cdot \mathbf{u}) - \mathbf{u} \cdot \nabla\mathbf{u}, \tag{1.4}$$

we can write the convective acceleration as

$$\mathbf{u} \cdot \nabla\mathbf{u} = \frac{1}{2}\nabla(\nabla\Phi \cdot \nabla\Phi), \tag{1.5}$$

with $\nabla \times \mathbf{u} = 0$ since the flow is irrotational. If gravity acts in the positive y-direction, we can write

$$\mathbf{g} = \nabla(gy). \tag{1.6}$$

The momentum equation, therefore, becomes

$$\nabla\left[\frac{\partial\Phi}{\partial t} + \frac{1}{2}\nabla\Phi \cdot \nabla\Phi + \frac{p}{\rho_h} - gy\right] = 0, \tag{1.7}$$

which after integration can be written as

$$\frac{\partial\Phi}{\partial t} + \frac{1}{2}\nabla\Phi \cdot \nabla\Phi + \frac{p}{\rho_h} - gy = C(t), \tag{1.8}$$

for some function $C(t)$. However, we can take $C(t) = 0$ by using the simple transformation

$$\Phi = \Phi + \int_0^t C(s)ds,$$

which does not affect the velocity field. For this type of flow, we obtain **Bernoulli's equation**

$$\frac{\partial\Phi}{\partial t} + \frac{1}{2}\nabla\Phi \cdot \nabla\Phi + \frac{p}{\rho_h} - gy = 0. \tag{1.9}$$

We now turn our attention to the surface of the fluid. Since the atmospheric pressure is constant at the free surface and it balances the pressure of the fluid, it may be taken as zero. Then Bernoulli's equation (1.9) reduces to the following **dynamic free surface boundary condition**:

$$\frac{\partial \Phi}{\partial t} + \frac{1}{2}\nabla\Phi\cdot\nabla\Phi - g\eta = 0 \quad \text{on} \quad y = \eta(x, z, t), \tag{1.10}$$

where $y = \eta(x, z, t)$ defines the instantaneously varying free surface elevation and $y = 0$ is the mean free surface.

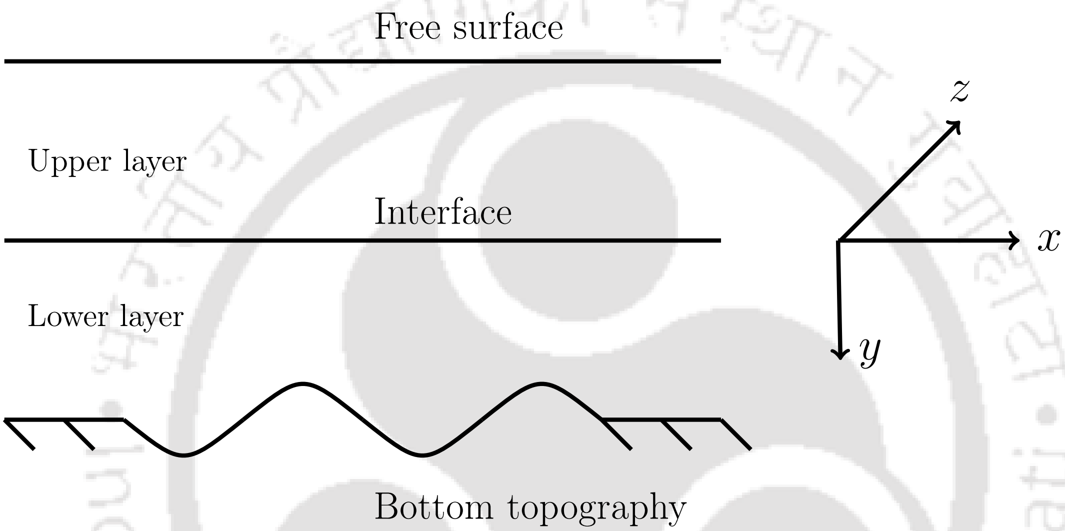

Figure 1.2: Schematic diagram depicting the geometry

We note that the fluid particles cannot cross the air-water interface and hence it is obtained by equating the vertical speed of the free surface itself to that of a fluid particle at the free surface, which gives the **kinematic boundary condition at the free surface**:

$$\frac{\partial \Phi}{\partial y} = \frac{\partial \eta}{\partial t} + \frac{\partial \eta}{\partial x}\frac{\partial \Phi}{\partial x} + \frac{\partial \eta}{\partial z}\frac{\partial \Phi}{\partial z}, \quad \text{at} \quad y = \eta(x, z, t). \tag{1.11}$$

For sufficiently small motions relative to the wavelength, the above nonlinear free surface conditions (1.10) and (1.11) may be linearized about the undisturbed state. The linearized theory requires the amplitude of the fluid motion to be much smaller compared to the wavelength throughout the fluid domain including the vicinity of any structure, and hence the amplitude of any structural motion must also be small relative to other length scales. It is consistent with the linearization to apply the free surface boundary conditions on $y = 0$, in which case the dynamic condition (1.10) becomes

$$\frac{\partial \Phi}{\partial t} - g\eta = 0 \quad \text{on} \quad y = 0, \tag{1.12}$$

and the kinematic condition (1.11) becomes

$$\frac{\partial \Phi}{\partial y} = \frac{\partial \eta}{\partial t} \quad \text{on} \quad y = 0. \tag{1.13}$$

These two conditions may be combined by differentiation of (1.12) with respect to t and substitution for $\frac{\partial \eta}{\partial t}$ in (1.13) to get the linearized free surface condition

$$\frac{\partial^2 \Phi}{\partial t^2} - g\frac{\partial \Phi}{\partial y} = 0 \quad \text{on} \quad y = 0. \tag{1.14}$$

When there is an impermeable sea-bed with the local fluid depth $h(x, z)$, then there will be no flow normal to the bed and hence

$$\frac{\partial \Phi}{\partial \mathbf{n}} = 0 \quad \text{on} \quad y = h(x, z), \tag{1.15}$$

where $\mathbf{n}$ is an outward unit normal to the bed.

All the results, here and in the subsequent chapters, are based on the linearized water wave theory and relate to time-harmonic motion with a specified frequency. For time-harmonic motions of radian frequency ω, time may be removed from the problem by writing

$$\Phi(x, y, z, t) = \text{Re}\ \{\phi(x, y, z)e^{-\mathrm{i}\omega t}\}, \tag{1.16}$$

where ϕ is a complex-valued potential and Re denotes the real part. From Eq. (1.3), it follows that ϕ satisfies Laplace's equation

$$\nabla^2 \phi = 0 \tag{1.17}$$

throughout the fluid domain. In terms of ϕ, the linearized free surface condition (1.14) becomes

$$\frac{\partial \phi}{\partial y} + K\phi = 0 \quad \text{on} \quad y = 0, \tag{1.18}$$

where $K = \frac{\omega^2}{g}$ and the bed condition (1.15) becomes

$$\frac{\partial \phi}{\partial \mathbf{n}} = 0 \quad \text{on} \quad y = h(x, z). \tag{1.19}$$

The above information is all about homogeneous fluid problems. For the case of two-layer fluid problems, we consider the motion under gravity in an incompressible and inviscid fluid of densities ρ_1 and ρ_2 ($< \rho_1$) for the lower and the upper fluids, respectively, separated by a common interface. Here the fluids are considered to be immiscible. A right-handed

Cartesian coordinate system is considered in which the y-axis points vertically downward into the lower layer fluid region and $y = 0$ is the position of the surface of separation between the two fluids at rest. The motion in each fluid is assumed to start from rest so that it is irrotational and can be described by the velocity potentials $\Phi_1(x, y, z, t)$ and $\Phi_2(x, y, z, t)$ in the lower and the upper layer fluids, respectively. Then, the equation of continuity becomes

$$\nabla^2\Phi_1 = 0, \quad \text{in the lower fluid region,} \tag{1.20}$$

$$\nabla^2\Phi_2 = 0, \quad \text{in the upper fluid region.} \tag{1.21}$$

Let $y = \chi(x, z, t)$ denote the depression of the interface. The linearized kinematic condition at the interface produces

$$\frac{\partial\Phi_1}{\partial y} = \frac{\partial\Phi_2}{\partial y} = \frac{\partial\chi}{\partial t} \quad \text{on} \quad y = 0, \tag{1.22}$$

where it is assumed that χ and its partial derivatives are small. The condition (1.22) also gives the condition of continuity of the normal component of the velocity across the common interface. If p_1 and p_2 are the pressure at a point in the lower layer fluid and upper layer fluid, respectively, the linearized Bernoulli's equation in the lower layer is

$$\frac{\partial\Phi_1}{\partial t} = gy - \frac{p_1}{\rho_1} \quad \text{in} \quad y \geq \chi. \tag{1.23}$$

Similarly, the linearized Bernoulli equation in the upper layer is

$$\frac{\partial\Phi_2}{\partial t} = gy - \frac{p_2}{\rho_2} \quad \text{in} \quad y \leq \chi. \tag{1.24}$$

The condition of continuity of pressure at the interface $y = \chi$ then produces

$$\frac{\partial\Phi_1}{\partial t} - g\chi = \rho\left(\frac{\partial\Phi_2}{\partial t} - g\chi\right) \quad \text{on} \quad y = \chi, \tag{1.25}$$

where the ratio ρ_2/ρ_1 of the densities of the two fluids is denoted by ρ so that $0 < \rho < 1$. Expanding $\frac{\partial\Phi_1}{\partial t}(x, y, z, t)$ and $\frac{\partial\Phi_2}{\partial t}(x, y, z, t)$ by Taylor's series about $y = 0$ and neglecting the terms of second and higher order of smallness, the above condition becomes

$$\frac{\partial\Phi_1}{\partial t} - g\chi = \rho\left(\frac{\partial\Phi_2}{\partial t} - g\chi\right) \quad \text{on} \quad y = 0. \tag{1.26}$$

Elimination of χ between (1.22) and (1.26) gives one of the linearized conditions at the interface as

$$\frac{\partial^2 \Phi_1}{\partial t^2} - g\frac{\partial \Phi_1}{\partial y} = \rho\left(\frac{\partial^2 \Phi_2}{\partial t^2} - g\frac{\partial \Phi_2}{\partial y}\right) \quad \text{on} \quad y = 0, \tag{1.27}$$

while another linearized condition at the interface, called continuity of normal velocity, can be obtained as

$$\frac{\partial \Phi_1}{\partial y} = \frac{\partial \Phi_2}{\partial y} \quad \text{on} \quad y = 0. \tag{1.28}$$

1.3 General theory for flow across thin porous structure

Before we proceed to the theory of flow inside a porous medium (or material), it is important to emphasize the significance of a porous medium. A porous medium or a porous material is a material consisting of pores through which fluid (be it gas or liquid such as water) can pass. The skeleton portion of the medium is mainly solid (but foam is considered to be porous though). A porous medium may be an aggregate of a large number of particles like sand, gravels or a solid containing many capillaries such as porous rock. Many natural substances such as rocks and soil (aquifers, petroleum reservoirs), zeolites, biological tissues (bones, wood, cork), and man-made materials such as cements and ceramics can be considered as porous media. Many of the important properties of such substances can be rationalized only by considering them to be porous media.

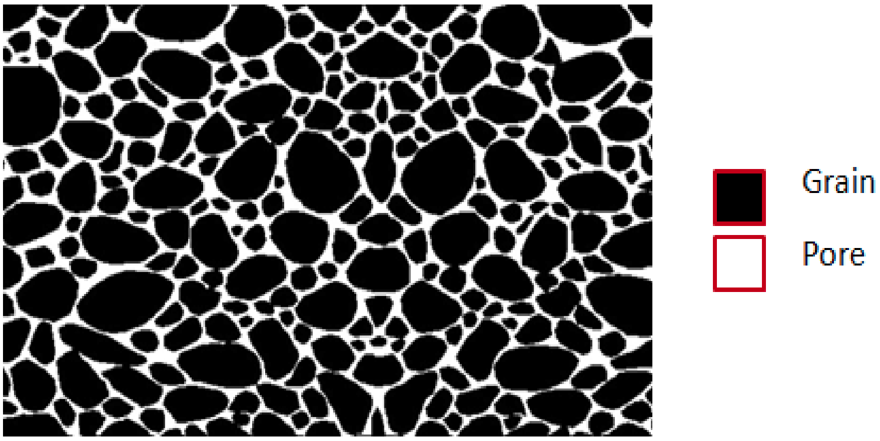

Figure 1.3: Microscopic cross section image of a porous medium [1]

A saturated porous medium is the one in which all void space is filled with fluid. But there are some porous materials like soil near the ground surface in which the void is partially filled with liquid and the remaining part is occupied by air. Flow through this type of porous material is termed unsaturated.

When the fluid percolates through a porous material, the actual path of an individual fluid particle cannot be followed analytically due to the complexity of microscopic flow in the pores. In order to overcome the complexity, the gross effect of the phenomenon represented by a microscopic law applied to the fluid mass, such as the space averaged change with respect to the space and time in the macroscopic quantities, is required to be considered. The characterizing property of a porous material is its *porosity*. It is a non-dimensional quantity which measures the void space in the material; and is the fraction of the volume of void over the total volume of the material. It is common to describe porous media based on the porosity γ_p which is defined as

$$\gamma_p = \frac{\text{Volume associated with voids}}{\text{Total volume}}. \tag{1.29}$$

Generally, porous structures can be categorized into three types depending upon the pore size, namely, microporous (smaller than 2 nanometers), mesoporous (between 2 and 50 nanometers) and macroporous (larger than 50 nanometers). Metallic foams are good examples of porous materials with higher porosity (ranging from 0.6 to 0.95). The construction of these types of materials can be carried out through a number of means, the main one being the "lost-foam casting". Porous structures, with high porosity but with considerable stability, in order to be used as breakwaters in ocean and coastal engineering, can be constructed from low melting metals and alloys such as copper, aluminium, lead, tin, zinc, etc. The porous structure under consideration in the last four chapters of this thesis is taken as such type of a structure. Figure 1.3 represents a rough visual representation of a porous structure at microscopic level.

Small amplitude wave motion in three dimensions is considered within an undeformable porous medium. It is assumed that the porous structure is homogeneous and isotropic (uniform properties of the material in all directions). The fluid motion follows the continuity equation and the equation of motion in terms of the seepage fluid velocity $U(x, y, z, t) = \mathbf{u}(x, y, z)e^{-\mathrm{i}\omega t}$ and dynamic pressure $P(x, y, z, t) = p(x, y, z)e^{-\mathrm{i}\omega t}$, which are given by

$$\nabla \cdot \mathbf{u} = 0, \tag{1.30}$$

$$\frac{\nabla p}{\rho_h} + \omega R_p \mathbf{u} = 0, \tag{1.31}$$

where ω is the angular wave frequency and $R_p = f - \mathrm{i}S$ is the dimensionless impedance of the porous medium.

Let us consider a thin porous barrier of width b placed vertically at $x = 0$ where the x- and y-axes are defined along transverse and longitudinal directions, respectively, of the porous barrier (Fig. 1.4). If L_0 is the length scale along the y-direction, it is assumed

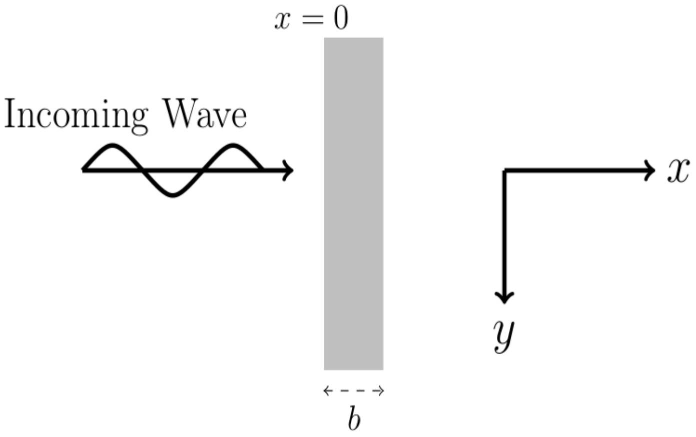

Figure 1.4: Schematic diagram for flow near porous boundary

that

$$\frac{b}{L_0} \ll 1. \tag{1.32}$$

Now using the small thickness assumption (1.32) of the barrier and the continuity of mass flux and pressure along the boundary $x = 0^{\pm}$, the following porous boundary condition can be used (Yu [100]):

$$\mathbf{u}|_{x=0^+} = \mathbf{u}|_{x=0^-} = \frac{k_0 G}{\rho_h \omega}\left(p|_{x=0^-} - p|_{x=0^+}\right) \quad \text{at} \quad x = 0^{\pm}, \tag{1.33}$$

where k_0 is the incident wavenumber and G is the dimensionless complex porous-effect parameter defined by

$$G = \frac{\gamma}{k_0 b R_p} = G_r + \mathrm{i}G_i, \tag{1.34}$$

where G_r denotes the real part and G_i denotes the imaginary part. It should be noted that $G = 0$ when either $\gamma = 0$ or $R_p \to \infty$ (i.e., both the real and imaginary parts of R_p tend to ∞) or when the barrier is considered to be solid. With an increase in either G_r or G_i, the wall starts to behave like a permeable structure. In practice, G always possesses positive real and imaginary parts except when the resistance effect against the flow dominates the inertial effect of the fluid inside the porous material, in which case G becomes real. Similarly, when the inertial effect dominates the resistance effect, G becomes purely imaginary.

When the velocity component is replaced by the gradient of its potential, i.e.,

$$\mathbf{u}|_{x=0^+} = \left.\frac{\partial \phi}{\partial x}\right|_{x=0^+} \quad \text{and} \quad \mathbf{u}|_{x=0^-} = \left.\frac{\partial \phi}{\partial x}\right|_{x=0^-}, \tag{1.35}$$

and with the consideration of linearized Bernoulli's equation

$$p|_{x=0^+} = \mathrm{i}\rho_h\omega\phi|_{x=0^+} \quad \text{and} \quad p|_{x=0^-} = \mathrm{i}\rho_h\omega\phi|_{x=0^-}, \tag{1.36}$$

Eq. (1.33) can be converted into the following equation:

$$\left.\frac{\partial\phi}{\partial x}\right|_{x=0^-} = \left.\frac{\partial\phi}{\partial x}\right|_{x=0^+} = \mathrm{i}k_0 G\Big(\phi|_{x=0^-} - \phi|_{x=0^+}\Big). \tag{1.37}$$

1.4 Role of various types of upper and lower boundary in wave propagation

1.4.1 Very large floating structures

One of the biggest challenges for mankind is the scarcity of land space for various developmental activities. As about 70 percent of the earth surface is covered by ocean, i.e., the land takes up only about 30 percent of the earth's total surface area, there is a need to utilize the ocean space for various human activities by developing large platforms which can float on the sea surface like a giant structure. In the twentieth century, humanity ran into a new problem – lack of land. Now, in the beginning of the third millennium, this problem has become serious, with the fast growth of the world's population and corresponding expansion of industrial development and urban agglomeration. Countries such as Japan, China, Korea, the Netherlands, and Belgium have a very high population density. Many other countries in Europe and Asia are approaching the same problem.

VLFS or very large floating structures (or, as some literature refer to them, very large floating platforms, VLFP for short) can be constructed to create floating airports, bridges, breakwaters, piers and docks, storage facilities (for instance for oil), wind and solar powerplants, for military purposes, to create industrial space, emergency bases, entertainment facilities, recreation parks, mobile offshore structures and even for habitation. Actually, the last could become a reality sooner than one may expect: already different concepts have been proposed for building floating cities or huge living complexes in oceans.

Very large floating structures may be classified under two broad categories [96], namely the pontoon-type and the semi-submersible type as shown in Fig. 1.5. The former type is a simple flat box structure and features high stability, low manufacturing cost and easy maintenance and repair. In open sea, where the wave heights are relatively large, it is necessary to use the semi-submersible type VLFS to minimize the effects of waves while maintaining a constant buoyant force. VLFSs of the semi-submersible type are used for oil or gas exploration in sea and other purposes. They are fixed in place by column tubes, piles, or other bracing systems.

Figure 1.5: Pontoon-type VLFS and semi-submersible-type VLFS [96]

In contrast, the pontoon-type VLFS just floats (lies) on the sea surface. The pontoon-type VLFS is very flexible compared to other kinds of offshore structures, so that the elastic deformations are more important than their rigid body motions. Thus, hydroelastic analysis takes center stage in the analysis of the pontoon-type VLFSs. However, this pontoon-type of floating structure is suitable only for use in calm waters associated with naturally sheltered coastal formations. To further reduce the height of waves that impact these pontoon-type VLFS, breakwaters are usually constructed nearby. In open seas, where the wave heights are relatively large, it is necessary to use the semi-submersible type of VLFS to minimize the effects of waves while maintaining a constant buoyant force.

During the last three decades, there has been a significant interest in the study of hydroelastic analysis of very large floating structures. A similar class of problems arises in the study of wave-ice interaction problems in which the floating ice sheet is modelled as a thin elastic plate.

1.4.2 Sea ice

Wave propagation under sea ice cover (or ice-sheet) is a fundamental issue of contemporary marine science and engineering. Its significance may be explained from two perspectives: one from the wave modeling and the other from the ice modeling. Global wave climate has both environmental and engineering implications. It contributes to, and is in turn influenced by, all mass, momentum, and energy exchange between air and sea. Ship motion, deep sea and offshore operations need accurate information of the wave condition.

According to its proximity to land or sea, ice-covered sea region may be roughly classified into landfast ice, also called fast ice, the shear zone, and the marginal ice zone (MIZ), as shown in Fig. 1.6 (taken from [99]). This classification depends on the distance from the coast. Farthest from the coast, the MIZ is adjacent to open water. In this zone, sea ice has a significant dynamic behaviour influenced by ocean waves. Fast ice is frozen to the coast, often grounded by icebergs or ice ridges. In shear zone and the MIZ, ice may drift. In the densely packed shear zone, drifting causes divergence/convergence and shear. These large scale deformations create leads and ridges. In the marginal ice zone, the ice thickness is relatively lower and hence divergence/convergence and shear do not change the surface morphology as signifcantly as in the shear zone. A detailed description of the three different sea ice zones, as proposed by Wadhams [94], is briefly discussed below.

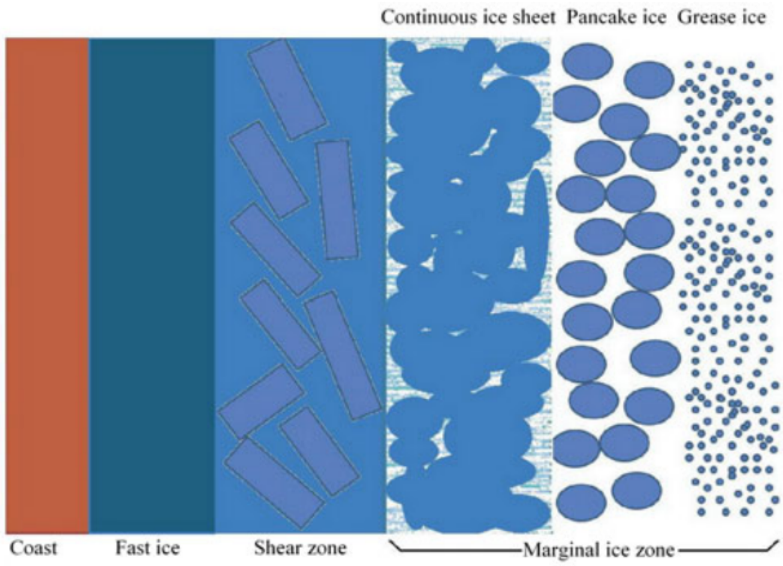

Figure 1.6: Sketch on the spatial distribution of sea ice [94]

Fast ice: This is the ice which grows seaward from a coast and which stays in place throughout the winter, while breaking up, drifting away or melting in spring. Fast ice is stabilized by the presence of grounded pressure ridges in its outermost part. Only long waves may travel into this region. All high frequency waves are generally attenuated before they arrive at the coast.

The shear zone: This type of ice forms when drifting pack ice moves against a coastal boundary which can be either fast ice or the land itself. The shearing and convergence of the pack's motion generates a band of highly deformed ice which has a higher density of ridging than the ice further out in the ocean. Waves that propagate into this region can be severely scattered due to the ridges.

The marginal ice zone (MIZ): The MIZ is that part of the ice cover which is close enough to the open ocean boundary to be affected by its presence. The ice in the MIZ has much greater freedom of movement than the ice in the other two regions, and a number of ice-ocean-atmosphere interaction phenomena occur. It is known that in the MIZ, waves may fracture ice floes to change the floe size distribution due to the high wave energy. They may enhance frazil ice production by increasing heat transfer. They may regulate the pancake ice size, as well as causing floe rafting. Therefore, to model the ice-covered ocean dynamics in the marginal ice zone, a wave ice interaction model is required to be provided.

There are three classical wave propagation models in the MIZ: mass loading model, thin elastic plate model and viscous layer model. For a continuous ice sheet, the thin elastic plate model is probably a good model. Mass loading model can describe the disconnected pancake ice region, as long as the interaction among pancake floes is negligible since these floes are very small relative to the significant wavelength. The viscous layer model is probably a good model for the grease ice region, because the dominant effect from grease ice is viscous damping. All three models are useful under specific ice conditions.

Attenuation of amplitude of water waves propagating in sea ice occurs mainly due to two reasons: (i) a conservative scattering by the ice floes which results in the relocation of the energy in all directions; and (ii) a true dissipation due to the friction (viscosity), the inelastic collisions and the breakup of ice floes, which actually results in the relocation of the energy to the other parts of the associated system, i.e., atmosphere/ice/water. Both processes need to be accommodated in any model of earth system or ice/ocean or wave forecasting parametrization. Dissipation is important in the planetary system models in which energy conversion takes place. Remarkable perversion of the penetrating ocean wave spectrum takes place due to the ice-floes getting reflected and transmitted, and them extracting energy from those waves with the aid of either an elastic flexure or an inter-floe collision. Similarly, water wave propagation in an ocean containing a floating ice-sheet has received importance while developing effective reflectors of the incident wave energy which can be installed in order to protect coastal areas from dangerous waves, mainly near and in the polar regions. Such problems involving wave-ice interaction usually arises naturally in some parts of both Arctic and Antarctic regions. As a result, extensive interest has been evoked in the scientific community for dealing with ice-wave interaction problems stemming from the current significant scientific and research activities in the Antarctic region. Thus, there is a strong feeling among researchers that a possible and feasible next step forward is to try the initiation of modeling of scattering of oblique flexural gravity waves in the polar region. Consequently, there is a strong likelihood in providing impetus to researchers in getting a clear and proper understanding of the physical conditions arising naturally in areas such as oceanography, coastal engineering, offshore engineering, Arctic engineering and some other disciplines connected to ocean engineering.

1.4.3 Wave propagation over dissipative sea-beds

It has been noticed that water waves which propagate over a non-rigid bed are attenuated as a result of energy dissipation within the bed. When waves are attenuated in coastal waters, the mechanism of energy dissipation generally involves some form of bottom interaction. Most theories of wave attenuation, such as that due to bottom friction or to percolation in a permeable bed, are based on the assumption that the sea-bed is rigid in its response to water waves. There is an increasing evidence, however, that, as waves propagate over the sea-bed, small deflections can be induced in the sea-bed itself. Bjerrum [11] mentioned about waves in North Sea causing sea-bed deflections of up to 5 cm. Associated with such deflections, there is inevitably some dissipation of wave energy due to the internal friction within the sea-bed. This mechanism may be a contributing factor in an explanation of wave attenuation over continental shelves and in coastal waters.

Mud or cohesive sediment is a mixture of clay particles, silt, (fine) sand, organic material, sometimes gas, and water. This sediment mixture has cohesive properties because of low permeability and electrochemical attraction of clay particles and organic material. Effect of muddy sea-bed is important in many real world applications:

1. Mud deposits adversely affect the navigation.
2. Unfortunately, today many mud deposits are contaminated, endangering the ecosystem and increasing the costs of dredging operations progressively.
3. Mud is also one of the controlling factors for ecological development in the water system and shapes the physical and biological lanscape. Life, feeding, breeding and growth of biological organism is highly dependent on the oxygenation of water.
4. sediment transport: erosion of beaches and accretions,
5. undermining of coastal structures,
6. silt up of navigation channels and ports.

It is well known to engineering practice that a soil under some load does not assume an instantaneous deflection under that load but settles gradually at a variable rate. Such settlement is very apparent in clays and sands saturated with water. The settlement is caused by a gradual adaptation of the soil to the load variation. This process is known as soil consolidation. Sandy beaches consist of unconsolidated sediment and are permeable. In the coastal environment, changes of pressure associated with both the mean and the oscillatory water wave flows induce a groundwater flow of sea water within the porous medium. The mean flow plays a significant role concerning water table formation. Furthermore, this component percolates through the permeable bottom and influences the wave forces on structures supported by or extending into the bottom. On the other hand, the oscillatory component of the wave field contributes to damping of the waves over a porous beach. Knowledge of both the above components is important concerning the interaction of various physical processes, biodiversity and productivity of sandy beaches, sediment transport and coastal structure stability.

The problem of the wave and sea-bed interaction has been widely studied by coastal engineers in recent years. It is well known that gravity water waves propagating over the ocean generate significant dynamic pressure on the sea-bed. These pressure fluctuations further induce effective stresses and pore pressure within the soil matrix. Once the pore pressure becomes excessive with accompanying reduction in effective stresses, a sedimentary bed may become unstable, leading to sea-bed instability such as liquefaction and shear failure, resulting in the offshore installations (such as pipelines, soil storage tanks, piers, breakwaters etc.) being damaged by the wave-induced sea-bed instability, rather than from construction causes.

In conventional ocean engineering, most wave theories are based on the assumption of waves propagating over a rigid sea-bed. This implies that those theories use the wave pressures obtained from the solution with the consideration of a rigid sea-bed and those are used as the input forces in the whole wave-sea-bed interaction. This means that the vertical velocity vanishes at the sea-bed. Thus, the effects of sea-bed response on the wave characteristics cannot be examined. However, the wave characteristics, which are important in ocean engineering, are affected by the characteristics of sedimentary beds in ocean environments. In other words, the wave characteristics (such as the damping of water wave, wavelength and wave pressure) can also get modified by the sea-bed response if the sea-bed is a dissipative medium (porous or elastic medium). Therefore, it is necessary to couple the wave field and dissipative flow to provide a better estimation of wave characteristics.

In this thesis, mainly two types of dissipative beds, namely, (1) porous sea-bed, and (2) elastic sea-bed, are considered. Here the sea-bed (porous or elastic) is considered just as a boundary, and the motion beyond it is not considered. Also, the elastic sea-bed can be modeled as a thin elastic plate (following Euler-Bernoulli beam equation), which is similar to the problem of wave interaction with very large floating structures.

1.5 Derivation of the elastic plate condition

In this thesis, the upper surface or the lower surface (sea-bed) is considered as an elastic boundary for some problems. This type of boundary is modelled as a thin elastic plate of uniform surface density $\epsilon\rho_h$ having Young's modulus E and Poisson's ratio ν; ϵ a constant having the dimension of length measured by $\epsilon = (\rho_0/\rho_h)h_0$, with ρ_0 and ρ_h, respectively, as the densities of elastic plate and the fluid and h_0 as the very small thickness of elastic plate. Let us choose $y = 0$ as the position of the thin elastic plate at rest. Here it may be for the case of an ice-sheet as the upper surface.

In this case, the linearized Bernoulli's equation takes the form

$$\frac{\partial \Phi}{\partial t} = gy - \frac{p}{\rho_h}. \tag{1.38}$$

Let $y = \zeta(x, z, t)$ denote the depression of the elastic plate surface. Newton's equation of motion for a small element of the elastic plate surface produces

$$\epsilon \rho_h \frac{\partial^2 \zeta}{\partial t^2} = \epsilon \rho_h g + P_A - p - Q \nabla^4_{x,z} \zeta \quad \text{on} \quad y = \zeta(x, z, t), \tag{1.39}$$

where P_A is the atmospheric pressure and $Q = Eh_0^3/[12(1 - \nu^2)]$ is the flexural rigidity of the elastic plate and $\nabla^4_{x,z}$ the two-dimensional biharmonic operator. Using (1.38) in (1.39) and after linearization, we get

$$\epsilon \rho_h \frac{\partial^2 \zeta}{\partial t^2} = \epsilon \rho_h g + P_A - \rho_h \left(g\zeta - \frac{\partial \Phi}{\partial t} \right) - Q \nabla^4_{x,z} \zeta \quad \text{on} \quad y = 0. \tag{1.40}$$

The kinematic condition is

$$\frac{\partial \Phi}{\partial y} = \frac{\partial \zeta}{\partial t} \quad \text{on} \quad y = 0. \tag{1.41}$$

Eliminating ζ between (1.40) and (1.41), we get

$$(\Phi - \epsilon \Phi_y)_{tt} = (D \nabla^4_{x,z} + 1) g \Phi_y \quad \text{on} \quad y = 0, \tag{1.42}$$

where $D = Q/(\rho_h g)$. In terms of ϕ, the elastic plate condition (1.42) becomes

$$(D \nabla^4_{x,z} + 1 - \epsilon K) \frac{\partial \phi}{\partial y} + K \phi = 0 \quad \text{on} \quad y = 0. \tag{1.43}$$

In a similar manner, the above derivation will work for an elastic sea-bed, instead of the ice-sheet, under the similar conditions.

1.6 Brief description of previous works and motivation

Study of propagation of water waves in a homogenous or a two-layer fluid and the interaction of waves with a floating or submerged obstacle are crucial from the point of view of their credible implementation in coastal and marine engineering. In the last two decades, a broad interest has been reported of investigation of this kind of issues by various researchers. The matter of reflection of oblique waves by a small bed fluctuation has experienced an increasing attention since it has an enormous impact in the enhancement of functioning of shore-parallel bars or pipes. When a train of water waves strikes an obstacle located at the bottom of an ocean, some portion of the wave is reflected by it, and some portion is transmitted over it. Interestingly, it is not difficult to find a class of commonly occurring bottom-standing hindrance, for example, sand swells, which exhibits smallness in some sense which allows a perturbation technique to be exploited to compute the first-order corrections to both reflection and transmission coefficients.

Some significant works on the phenomenon of scattering by bed topography with small undulation for a homogeneous fluid flow have been accomplished in the last few decades. Miles [69] examined water waves propagating over a small bottom undulation located on an impermeable sea-bed. He analyzed the reflection and transmission of first-order through some integrals by utilizing a perturbation method for a train of oblique incident wave proliferating in a homogeneous fluid. Davies [27] dealt with a sinusoidal bottom undulation of small amplitude at the sea-bed and employed Fourier transform method to manage the water wave scattering problem for normal incidence. An experimental proof was provided by Heathershaw [41] to support the theoretical results of reflection of wave energy due to the resonant interactions which took place between the surface water waves and the undulating bed topography. Davies [27] and Davies and Heathershaw [28] highlighted the Bragg resonance phenomenon (it occurred when the wavenumber of the bottom undulation was double of that of the incident surface wave) when the bottom contained periodic undulations. Such type of resonant wave interactions has a paramount role in the development of nearshore surface waves. However, the perturbation theory gets disrupted near the Bragg resonance condition. To get rid of this disadvantage, Mei [68] established the wave evolution and reflection theory for offshore sandbars parallel to a coast. Guazzeli et al. [37] experimentally verified that Bragg resonance interactions of higher order occurred between linear gravity waves and a sinusoidal bed with double the wavenumber. Porter and Porter [76] discussed the nature of water wave propagation over periodic beds for a two-dimensional problem by employing linear water wave theory. Craig et al. [20] presented a systematic derivation and analysis of the equations of motion of water waves on the free surface of a channel of fluid over a variable bottom. Guyenne and Nicholls [39] presented a numerical method for simulation of nonlinear waves over a variable impermeable sea-bed. The higher-order spectral method included contributions up to an arbitrary order with respect to the perturbation parameter for the uneven sea-bed. Fourier transform method was appropriately utilized for this work.

Coming to similar works in two-layer fluids, Stokes [91] investigated waves propagating in a two-layer fluid not containing any structures. Lamb [53] demonstrated that time-harmonic gravity waves, for a given frequency, propagate due to two different modes at the free surface and the interface in a two-layer fluid. Kassem [46] investigated linear wave propagation in a two-layer fluid where one of the layers contained various types of basic singularities. He acquired, for constant depth of each layer, the velocity potentials which described line sources. Sturova [92] examined radiation of water waves by a moving horizontal cylinder placed in the lower layer of a two-layer fluid of constant depth, with a rigid lid replacing the free surface. Sturova [93] also examined the radiation and diffraction of the internal wave for a fixed submerged body in a stratified fluid flowing through a channel. Using the method of multipole expansions, Linton and Cadby [56] examined the scattering of oblique waves by horizontal cylinders in a two-layer fluid having a free surface with the upper layer being of finite depth and the lower layer being of infinite depth. By utilizing linear theory of water waves, Chamberlain and Porter [12] investigated wave scattering in a two-layer fluid corresponding to a mean depth which varied in three-dimensions. Maiti and Mandal [59] employed Green's function technique to investigate the reflection of oblique surface waves over a small deformation of bed for a two-layer fluid which contained a free surface. Mohapatra and Bora [71] examined scattering of oblique waves by a small undulating sea-bed for a two-layer fluid flow when the free surface was approximated by a rigid lid. Panda and Martha [74] investigated oblique wave scattering by a small undulation on the porous bottom in a two-layer fluid by utilizing perturbation technique in association with Fourier transform technique. Craig et al. [21], in a very important work, considered the nonlinear interaction of internal waves and surface waves in a three-dimensional two-layer fluid. By using Hamiltonian perturbation theory, it was established that long internal waves could be modeled by the KP II (Kadomtsev-Petviashvili II) equation which generated a resonant interaction with modulated surface waves at resonant wavenumbers. Existence of two linear wave modes in the form of free-surface and interfacial modes was clearly observed.

In the last few years, an increasing interest has been reported of investigation by various researchers on ocean wave interaction with very large floating structures (VLFS) in order to utilize the ocean space. This concern has arisen because of urban planning in a good number of countries which has been growing continually due to increase in population resulting in shortage of land, and also in countries having coastlines of long stretch. Such countries use the process of land reclamation from the ocean for the purpose of preventing overcrowding in the available land. Therefore, authorities, planners, engineers and researchers recommend utilization of VLFS for human dwelling, setting up of industrial area and storage space responding to the above stated demands. It is known that a VLFS is easy to design, control and remove, and has been beneficial due to the fact that it can be artificially produced which makes it an easily floating space on water body and simultaneously has a minimal adverse environmental effect on the marine ecosystem. The behaviour of a VLFS is supposed to be elastic because of the significance of the localized deflection/vibration of such a long structure due to the occurrence of continuous excitation of small amplitude waves despite of the fact that the thickness of such structures is much smaller than their length. Information on various recent enhancement on VLFS is available in the works of Wang and Tay [95], Lamas-Pardo et al. [52] and the references cited therein. Interaction of surface gravity waves with such flexible floating structures gives rise to the flexural gravity waves. As a consequence, the investigation of water wave interaction with VLFS plays a significant role in both Arctic engineering and marine technology. During the last two decades, various mathematical and numerical techniques have been presented to reduce the wave-induced structural responses on VLFS.

There has been a credible interest in the investigation of ice-wave interaction problems due to an increase in scientific activities in polar regions and utilization in marine engineering. One of the reasons is to understand the mechanism and the effects of wave proliferation through the earthquake regions. Interaction of water waves with a floating thin ice plate with infinite or finite length, modeled as a thin elastic plate, creates interesting mathematical problems to marine researchers drawing attention of various types of practical problems in order to obtain their useful solutions. Ocean surface waves penetrate up to hundreds of kilometres into the ice-covered ocean (Kohout et al. [48]). The region occupied by the waves is known as the marginal ice zone (MIZ). Waves have a profound impact on the ice cover in the MIZ. Surface waves are expected to be a dominant process controlling the total extent of the MIZ as well as the size distribution of sea ice (Williams et al. [97], Williams et al. [98]). Fox and Squire [32, 34] analyzed water wave proliferation into a floating ice-sheet from the open ocean and they produced an accurate linearized model for studying reflection and transmission at the edges of the ice-sheet. An extensive study on scattering of water waves due to the presence of floating ice-sheets of non-uniform thickness is found in the analysis and description by Bennetts [8] and Bennetts et al. [9]. Subsequently, a detailed study on the important link between sea-ice interaction and VLFS hydro-elasticity was carried out by Squire [90]. Further, Watanabe et al. [96] and Chen et al. [14] presented some significant developments in matters related to water wave interaction with flexible floating structures in a homogeneous fluid of uniform water depth. Bhattacharjee et al. [10] and Karmakar et al. [45] studied scattering of flexural gravity waves by a varying sea bottom. Using perturbation technique, Maiti and Mandal [60] investigated the scattering of surface waves by an undulating sea-bed in an ice-covered ocean. Mohapatra and Bora [72] examined wave propagation in a two-layer fluid over a small distortion at the bottom of a sea by considering the upper layer to be bounded above by a thin ice-sheet. They computed the first-order corrections to the velocity potential, reflection and transmission coefficients by utilizing the techniques of perturbation and Fourier transform. Further, Chen et al. [13] considered a two-dimensional continuum model for linear gravity waves propagating across an ice-covered sea. By assuming the floating sea ice as a homogeneous isotropic poro-elastic material and the underlying ocean as a weakly compressible fluid, they analyzed wave dispersion and attenuation in details. Cho and Kim [16] studied the interaction of oblique monochromatic incident waves with a submerged horizontal flexible membrane by the application of the multi-domain boundary element method and the eigenfunction expansion method. In both instances, the analytical and numerical results found excellent agreement with the experimental data. Hassan et al. [40], by using the matched eigenfunction method for the two-dimensional and three-dimensional problems, studied the interaction between surface gravity waves and finite (and also semi-infinite) lengths of submerged elastic plates. In this method, a boundary value problem was formulated with the Laplace's equation as the governing equation with the potential satisfying certain higher order boundary conditions on the boundary of the submerged structure (discussed in Fox and Squire [32]). Recently, Behera and Sahoo [5], by utilizing eigenfunction expansion method, discussed the hydroelastic behaviour of interaction of surface gravity wave with a submerged horizontal flexible permeable thin plate.

A number of investigations has been accomplished with regard to a porous sea-bed by various researchers. Contrary to the case of propagation of waves over an impermeable bed, dissipation mechanisms linked to the porous medium contribute significantly to the damping of the waves when water wave propagates over a porous sea-bed, and thus, transformation of wave characteristics is observed. Sollitt and Cross [88] were the pioneers in introducing an effective model which accounted for a wave-induced flow in a porous medium and till date, it has found its place as a very robust model. Belibassakis [7], by developing an enhanced coupled-mode system, modeled wave-induced pressure and groundwater flow in coastal regions of variable bathymetry for the layer beneath the porous sea-bed. Corvaro et. al [18] studied the wave damping induced by a porous sea-bed and they noticed a significant change in the wave characteristics when waves propagated over a porous medium. Using the theory of Sollitt and Cross [88], and mild slope assumption, Rojanakamthorn et al. [78, 79] developed a mathematical model for breaking and non-breaking waves propagating over a general finite permeable sea-bed. Gu and Wang [35] examined the interaction of water wave with a permeable sea-bed consisting of a granular material taking into consideration inertial and non-linear resistances theoretically as well as experimentally. Mase and Takeba [67] discussed the time-dependent and time-independent water wave problems for the situation where the sea-bed was taken as a permeable rippled bed. They found that reflected and transmitted energy became smaller for this instance than for the case of impermeable rigid rippled bed because of energy dissipation taking place in the porous medium. Zhu [103] investigated the water wave proliferation inside a porous medium on a ripple sea-bed in a homogeneous fluid by utilizing Galerkin eigenfunction expansion technique. Silva et al. [86] examined the proliferation of water waves over a homogeneous, isotropic submerged permeable bed and evaluated the coefficients. In order to investigate the influence of several wave and soil parameters, Li and Jeng [55] calculated the wave-induced pore pressure and essential stresses in a permeable sea-bed near a breakwater head. Employing perturbation and Fourier transform techniques, Martha et al. [66] examined the oblique wave scattering by a small distortion on a sea-bed with the incorporation of reasonable porosity of the bed. Behera et al. [4] took up the scattering problem of oblique waves by an elastic plate floating for both the cases of homogeneous and immiscible two-layer fluids with the consideration of a porous sea-bed.

In the works mentioned above, the sea-bed under consideration has either an infinite depth or a finite depth with the bed being a flat impermeable one or a permeable one. But the flexibility that a sea-bed exhibits is also one of the extremely significant features which has not been taken into account in these previous studies. The wave-structure interaction problems over flexible beds have been studied by a handful of researchers. One important stimulus of studying water wave scattering/traping problems due to the presence of an elastic bottom arises because of their applicability in the construction of underwater pipe bridges, wave power devices, very large floating structures like floating oil storage bases, mobile offshore base for utilization of ocean space for various activities such as military operations, etc. In some previous studies, it was established that the wave characteristics are significantly affected in the presence of an elastic sea-bed. It has been found that while considering water waves passing over a deformable bottom, the constant depth water bounded below by a perfectly elastic soil of infinite depth has a shear which represents a soft marine sediment. In this context, Mallard and Dalrymple [63] pointed out a significant change in the wave characteristics due to the elasticity of the bottom while carrying out investigation on the wave propagation over a deformable bottom which has an immense impact on the water wave kinematics and dynamics in addition to demonstrating the elastic behaviour of the soil. The results of their work, which clearly examine the soil displacement and stresses, act as a basis for estimating the effects of a deformable bottom on pipelines, cables and pile-supported structures connected to the bottom. Dawson [29] extended the work in [63] by including the effect of soil inertia and thereby analyzed the wave motion. He established that soil inertia formed an indispensable part of such problems and that ignoring it might lead to serious errors. Due to the varied nature of bottom soil characteristics, significant decay in wave amplitude is often observed when wave propagates over continental shelves as well as in the coastal waters. Eyov et al. [31] presented a mathematical solution for a two-dimensional linear problem of acoustic gravity waves in a compressible ocean with an elastic bottom in order to compare the physical properties of progressive waves over a rigid ground and slowly-varying bathymetry. Their work enriched the knowledge on acoustic-gravity waves in a way that could assist, among others, the early detection of tsunami. These works amply justify that the study of elastic sea-bed is important in tackling various problems since significant change in waves is observed due to elasticity.

Going further into some other applications, Chiba et al. [15] examined the hydroelastic vibration of a frictionless liquid in a cylindrical tank with a free surface and a flexible membrane bed. The free vibration characteristics of the fluid-structure interaction and its comprehensive understanding play a very vital role in various engineering topics such as resonance-free condition in the propellant in space vehicles, resisting and avoiding earthquakes by large-capacity oil containers in the petrochemical industry. Further, some other structures such as very large floating oil storage tanks, ships and submarines will be in a position to avoid or can be subjected to reduced localized vibrations. Several aspects of wave oscillation in flexible tanks can be found in the book by Ibrahim [42]. Under the assumptions of small amplitude water wave and structural response, Mohapatra and

Sahoo [73] took up the problem of surface gravity wave propagation over an elastic sea-bed in a homogeneous fluid. They examined the wave features for both deep and shallow water waves. Saha and Bora [81] investigated the effect of an elastic bottom on trapped modes supported by a submerged structure placed in one of the layers of a two-layer fluid in finite depth. Mohapatra [70] considered a hydroelastic model to inspect the wave radiation by an immersed oscillating sphere over an infinitely extended flexible base surface in a homogeneous fluid, by utilizing the multipoles expansion approach. Sarangi and Mohapatra [83] investigated the effects of an elastic deformable sea-bed on water wave diffraction in a homogeneous fluid with the help of Green's function.

There is a phenomenal interest to explore the wave propagation in an ocean with a free surface, where the lower surface is taken as a flexible base surface. Investigation of the matter of water wave propagation in a two-layer fluid over an irregular shape for such kind of a sea-bed has not been carried out till now. This is our main motivation for considering the water wave proliferation over a small undulation on a flexible sea-bed as a substitute for unbending and absorbent bed of the sea. In this context, it is pertinent to mention that the study of effects of elastic sea-bed is mainly motivated by applications as can be seen from all the above works, particularly those in [29, 31, 63]. These works establish that the characteristics of soil play a very crucial role in obtaining a solution which takes into account the elastic effect of the bottom. This shows why problems of scattering of waves over a deformable bottom, inclusive of elasticity, has essential implications.

The study of the development of various breakwaters has commanded sufficient attraction due to the huge impact they have in the intensification of various human activities in maritime environment. Furthermore, with global trading in upward trend, large expansion in harbour traffic has resulted in deteriorating prevailing wave conditions in and around various ports and harbors all around the globe. Moreover, unusual rise in sea level has reached an alarming proportion and subsequently, an additional pressure on the existing coastal infrastructures has arisen. Therefore, the investigation of water wave interaction with coastal structures has immensely helped in providing important information in terms of various physical processes linked to coastal protection as well as attenuation of wave heights in important confined water bodies such as bays/ports/harbours. Majority of the coastal structures, mainly used as breakwaters to protect shore and/or to create a tranquility zone by affecting reduction of wave impact near such locations, are usually vertical and rigid. These structures normally collapse under extreme wave conditions like tsunami and storm surges. In order to reduce waveloads on such structures, it is considered that perforated/wave absorbing structures of various configurations can be utilized as suitable alternatives rather than the conventional fixed rigid structures which are used to provide protection from wave attack at required locations but may be temporary only. In order to minimize the wave loading on the marine structures, various porous breakwaters have been utilized owing to their capability of damping the wave amplitude. It is a well known fact that surface wave interaction with any submerged structure always causes a phase shift of the waves resulting in a destructive interference of the incident and reflected waves. However, the permeability of the specific submerged structure helps to dissipate the wave energy.

In ocean and coastal engineering, water wave interaction with floating or submerged structures is considered to be a very important aspect. It seems pertinent to discuss the significance of vertical submerged barriers in shielding coastal regions from erosion as well as several other activities taking place along the coastline. Investigation of several aspects of water wave interaction with rigid vertical barriers has been presented by Dalrymple and Martin [23], Porter and Evans [75] and others. Dalrymple and Martin [23] considered a long array of offshore breakwaters and analyzed various hydrodynamic phenomena arising out of their interaction with water waves. Porter and Evans [75] used the Galerkin approximation to examine the complementary solution for the problem of water wave scattering by vertical barriers in finite depth and they further went ahead to solve the sloshing problem in a rectangular tank containing a fluid and a vertical barrier. Significant development of modeling of water wave scattering by porous barrier(s) has taken place in this direction over the last few decades. Chwang [17] used Darcy's law to establish his porous wave-maker theory while investigating waves passing through a porous structure. Yu [100] studied a diffraction problem for the fluid motion through a breakwater in the form of thin permeable structures and he demonstrated that, in the event of neglecting inertial effect of the porous structure, the performance of a permeable breakwater came out to be an underestimate. Sahoo et al. [82] showed that porous breakwaters effectively reduced the hydrodynamic pressure on both sides of submerged barriers which established that neglecting the effect of porosity of the breakwaters would lead to a flawed solution. They examined the surface wave scattering by porous vertical barriers of various configurations. The main boundary value problem was converted into dual/triple series relations by using the eigenfunction expansion method, and then the complete solution was obtained by using the least-square approximation method. Li et al. [54] applied multi-term Galerkin method in investigating the scattering of water waves by vertical thin porous barriers. An analytical solution of water wave scattering by a totally submerged or a surface-piercing vertical porous barrier was presented by Manam and Sivanesan [65]. Many researchers such as Koley et al. [49], Koley and Sahoo [50], Kaligatla et al. [43, 51] investigated the scattering and trapping aspects of water waves in the presence of vertical flexible porous barriers. Liu and Li [58] considered a dual curtain-wall wave-breaker comprising of a sea-ward porous barrier and a shore-ward impermeable wall, and evaluated its hydrodynamic performance. Das and Bora [26] analyzed surface gravity wave scattering by a dual submerged porous barrier, where the sea-bed was considered as an impermeable one. Recently, the investigation of water wave scattering by dual submerged barriers with variable porosity has been studied in [38, 85].

In the works mentioned above, water wave interaction with either a VLFS or a submerged regular structure was discussed. But the investigation of water wave interaction with a submerged structure beneath a VLFS or a floating ice-sheet has not been considered in these previous studies. This type of wave-structure interaction problems has been studied by some researchers only. Maiti and Mandal [61] considered flexural gravity waves due to a semi-infinite elastic plate and discussed its scattering by an inclined submerged vertical rigid barrier through the application of the hyper singular integral equation method. Manam and Kaligatla [64] solved the problem of flexural gravity wave scattering by a submerged rigid vertical barrier for deep water. In a recent study, Behera et al. [6] studied oblique flexural gravity wave interaction with a submerged porous plate by considering linear water wave theory and small-amplitude response of the structure. In particular, some classical methods, for bottom-mounted structure or floating-type breakwaters, are used for achieving wave force attenuation impacting the VLFS. Recently, Singla et al. [87] investigated the mitigation of structural responses of a VLFS in the presence of a vertical porous barrier.

In recent times, a significant interest has been observed in the analysis of ice-wave interaction as a result of rapidly increasing scientific activities taking place in the polar regions. On the other hand, perforated/wave absorbing structures of various configurations have been used in the coastal countries to protect coastal infrastructures/facilities from unpredictable and harsh wave actions. Some other naturally formed porous media include the likes of muddy or sandy ocean bed in which water can penetrate the sea-bed, and underwater vegetation field which resists the wave motion and dissipate incoming wave energy.

Realizing the importance of wave scattering by elastic beds as shown by the works mentioned above, we are immensely motivated to study the propagation of water waves in a homogeneous fluid and a two-layer fluid with the upper surface having different geometries and the lower surface having a dissipative (mainly, elastic and porous) bottom. Consequently, a probable next step is to initiate an extensive analytical and mathematical modeling to throw light on issues like water wave scattering over a dissipative sea-bed and water wave interaction with different types of structures. This, as a result, may very likely lead researchers to a precise and proper understanding of the conditions that arise in oceanography, ocean engineering and allied areas. With this motivation, we come up with formulation and solutions of certain ocean engineering problems pertaining to such investigations.

1.7 Outline of the thesis

This thesis is arranged in nine chapters with the present chapter dealing with the basic ideas and relevant equations in the linearized theory of water waves, previous important works and our motivation to carry out the present investigation. Chapters 2–8 present the seven problems taken up while Chapter 9 summarizes the findings and gives idea to take up new problems in this area of research. In this thesis, we investigate two types of problems: (i) the water wave scattering by a small undulation on an elastic sea-bed in a two-layer fluid of finite depth, which is bounded by a free surface or a rigid flat structure or a very thin ice-sheet; (ii) the interaction of water waves by a pair of submerged porous barriers in a homogeneous fluid subject to different upper surface and bottom boundary conditions. The main mathematical tools utilized in this thesis are (a) Fourier transform technique and application of residue theorem, (b) the eigenfunction expansion method, and (c) the least square method.

Chapter 2 deals with the problem of the scattering of water waves by a small undulation on an elastic sea-bed for the oblique incidence case, where the upper layer has a free surface. Utilizing the perturbation technique which involves the small parameter δ, the governing boundary value problem is reduced to a simpler boundary value problem for the first-order correction of the potentials. Fourier transform technique is applied to the simpler boundary value problems from which the first order corrections to the velocity potentials are determined. Then, the corresponding reflection and transmission coefficients are determined by the application of residue theorem. One particular undulating bottom topography is taken up as an example in order to evaluate explicitly the integrals for the reflection and transmission coefficients. It is noticed that when the oblique wave is incident on the interface, energy transfer takes place to the free surface, but for the free surface oblique incident waves, no such energy transfer to the interface takes place because of the parameter ranges. Also, it can be inferred that large reflection of the incident waves can be induced by an elastic bottom undulation due to the existence of Bragg resonance.

A study on oblique water wave scattering by a small undulation on an elastic sea-bed, where the upper surface is bounded above by a rigid lid, is carried out in **Chapter 3**. By using the same perturbation technique used in Chapter 2, the corresponding boundary value problem is reduced first to a simpler boundary value problem for the first-order correction of the potentials. The solutions are obtained by using the same procedure as applied in Chapter 2. After obtaining these solutions, the quantities of physical interest, namely, the reflection and transmission coefficients, are evaluated up to the first-order of δ in terms of integrals involving the shape function representing the bottom undulation of the channel-bed. It is observed that when the ratio of the wavenumber of the undulating bed and the wavenumber of the incident wave approaches two, the theory predicts the existence of resonance between the undulating elastic sea-bed and the interface of the layers. In **Chapter 4**, we investigate the propagation of normal incident waves over a small undulation located on an elastic sea-bed in a fluid flow for a two-layer fluid in which a floating ice-sheet covers the upper fluid. Adopting the same mathematical procedure used in Chapters 2 and 3, the reflection and transmission coefficients are computed by carrying out an appropriate integration for the integrals containing a shape function depicting the sea-bed undulation. It shows that the flexural wave moment is significantly affected as compared to the interfacial wave influence. It is noted that an appreciable variation in the elastic specification of the ice-sheet and the elastic sea-bed has a considerable influence for wave scattering by the undulating elastic sea-bed.

Chapter 5 deals with the water wave scattering by two fully submerged thin vertical porous barriers of different heights placed at a finite distance from each other above a porous sea-bed. An infinite channel of finite depth is divided into three regions in each of which different velocity potentials are considered and the corresponding boundary value problems are formulated. The complete analytical solution in each of the regions is acquired by employing eigenfunction expansion and least square method. With the help of the matching boundary conditions along the common vertical boundaries of any two adjacent regions, the reflection and transmission coefficients as well as the energy loss are obtained numerically by applying a matrix method. Then those are examined corresponding to various values of parameters such as porous-effect parameter, the submergence depth of barriers from the free surface, the angle of incidence and the porosity of the sea-bed. It is seen that the occurrence of minima in wave reflection is due to an increase in the inertial effect of the porous barriers which dissipate a significant portion of the wave energy, and a reasonable change in the porosity of the sea-bed has a significant impact when the propagating wave encounters the submerged structure. In **Chapter 6**, the same investigation is carried out in which the porous sea-bed is replaced by an elastic sea-bed. The effect of various values of elastic parameters on wave scattering is investigated along with the other investigations carried out in Chapter 5. Significant variation in the elastic specification of the sea-bed commands considerable influence when the propagating wave impinges upon the submerged vertical porous barriers. The vertical porous barriers are found to dissipate a significant portion of the wave energy when an increase in the inertial effect of the porous plates is affected. Furthermore, wave transmission undergoes reasonable reduction due to the energy dissipation by the elastic sea-bed.

Chapter 7 is devoted to a problem related to the scattering of ocean waves by a pair of submerged porous barriers where the upper surface is bounded by a floating ice-sheet. Here the sea-bed is considered as an impermeable one. The same mathematical procedure, namely, eigenfunction expansion and least square method as applied in Chapters 5 and 6, is used to get the analytical solution. Besides the reflection and transmission coefficients, the energy loss and the hydrodynamic forces acting on the barriers are also computed and those are examined corresponding to the various structural parameters. The effects of the floating ice-sheet on the flexural waves are examined by obtaining various results on the hydrodynamic wave characteristics. In the presence of the floating ice-sheet, a sufficient amount of energy loss takes place as a consequence of the interference of the incident and reflected waves while another part of the wave energy gets dissipated when it passes through the porous barriers. It is noticed that a moderate plate elasticity is considered helpful for use in coastal engineering for wave attenuation. In **Chapter 8**, we extend the work carried out in Chapter 7 by considering a porous sea-bed instead of an impermeable sea-bed. Along with other investigations, we also look into the effect of the variations of porosity parameter of the sea-bed on flexural gravity wave scattering. The porosity of the sea-bed is responsible for a reasonable amount of the wave energy getting dissipated. Occurrence of maximum energy loss or energy dissipation is observed for the case of submerged porous barriers of greater height with moderate porosity placed closer to the porous sea-bed.

Finally, **Chapter 9** consists of a brief summary of the results obtained in this thesis, mainly emphasizing the important observations. It also provides information for the scope of future investigations.

CHAPTER 2

SCATTERING OF LINEAR OBLIQUE WATER WAVES OVER AN ELASTIC BOTTOM UNDULATION IN A TWO-LAYER FLUID

2.1 Introduction

The objective of this chapter is to investigate oblique water wave scattering over a small undulation located on an elastic sea-bed in a two-layer fluid, with the upper layer exposed to the atmosphere. Following Euler-Bernoulli beam equation, the elastic sea-bed is approximated as a thin elastic plate. The scattering takes place due to a train of progressive waves propagating from the negative infinity which is incident on the undulating sea-bed. Considering an irrotational motion in an incompressible and inviscid fluid, and applying perturbation technique, the first-order corrections to the velocity potentials is evaluated by an appropriate application of Fourier transform and, subsequently, the corresponding reflection and transmission coefficients are computed through integrals containing a shape function which depicts the bottom undulation. To validate the theoretical results, a patch of sinusoidal swell is thought of as appropriate to represent such a bottom deformation. The important energy balance equations involving the reflection and transmission coefficients is found to be satisfied almost accurately which are shown through two tables.

2.2 Formulation of the scattering problem

Propagation of water waves of comparatively small amplitude under the action of gravity in an inviscid, incompressible two-layer fluid with an irrotational motion over an undulating elastic sea-bed is considered. Effect of surface tension at the interface of the two fluids, of which the upper layer has a free surface and the lower layer has a small undulation at the elastic bottom, is neglected since its contribution is known to be very insignificant. It may be noted that in all the works in this thesis, surface tension is not taken into account since its contribution is found to be inconsequential. Considering Euler-Bernoulli beam equation, the elastic sea-bed is approximated as a thin elastic plate. When it is said that the elastic plate is thin, it is meant that the thickness of the plate is much smaller compared to the horizontal length of the plate. The sea-bed can be idealized as a thin, linear elastic plate of uniform mass density and thickness. Linearity here is justified because, due to the consideration of small curvature, the elastic bed bends to the passing waves. Further, the consideration of elasticity of the bed is justified since the oscillatory nature of the problem does not allow an elastic process to act in any significant way. Also, because of the infinite length of the elastic sea-bed, the rotary inertia and the shear deformation terms are neglected. Due to all above considerations, the elastic sea-bed can be modeled as a thin elastic plate which follows Euler-Bernoulli beam equation as in [3], which is considered similar as in the problem of wave interaction with very large floating structures (discussed in [14]). The validity of a thin plate theory has been demonstrated by Fox and Squire [33].

A right-handed Cartesian co-ordinate system is considered in which the y-axis points vertically downwards (in order to conveniently represent the undulating sea-bed by a positive quantity); $y = -h_f$ and $y = 0$, respectively, represent the undisturbed free surface and undisturbed interface, as shown in Fig. 2.1. It is further considered that the sea-bed has a small undulation in the form $y = h_b + \delta b(x)$, where $b(x)$ depicts the shape of bottom undulation and is a differentiable function with compact support (that is $b(x) \to 0$ as $|x| \to \infty$), $\delta \ll 1$ is a non-dimensional number signifying the smallness of the bottom undulation and h_b is the uniform finite depth of the lower layer fluid on either side of the undulation. Assuming linear water wave theory and taking all these assumptions into account, the time harmonic velocity potentials in the lower layer fluid of density ρ_1 and in the upper layer fluid of density $\rho_2 (< \rho_1)$ can, respectively, be expressed as $\Phi(x, y, z, t) = \mathrm{Re}\{\phi(x, y) \exp(\mathrm{i}\gamma z) \exp(-\mathrm{i}\omega t)\}$ and $\Psi(x, y, z, t) = \mathrm{Re}\{\psi(x, y) \exp(\mathrm{i}\gamma z) \exp(-\mathrm{i}\omega t)\}$ for the oblique waves, where $\mathrm{Re}\{\cdot\}$ denotes the real part, i is the imaginary quantity $= \sqrt{-1}$, γ is the component of the wavenumber u in the z-direction and ω is the angular wave frequency of the incoming waves.

The boundary value problems involving these potentials ψ and ϕ are governed by the modified Helmholtz equation as follows:

$$(\nabla^2_{x,y} - \gamma^2)\psi = 0 \quad \text{in the upper fluid,} \tag{2.1}$$

$$(\nabla^2_{x,y} - \gamma^2)\phi = 0 \quad \text{in the lower fluid,} \tag{2.2}$$

where the two-dimensional Laplacian operator $\nabla^2_{x,y}$ is given by $\nabla^2_{x,y} = \frac{\partial^2}{\partial x^2} + \frac{\partial^2}{\partial y^2}$.

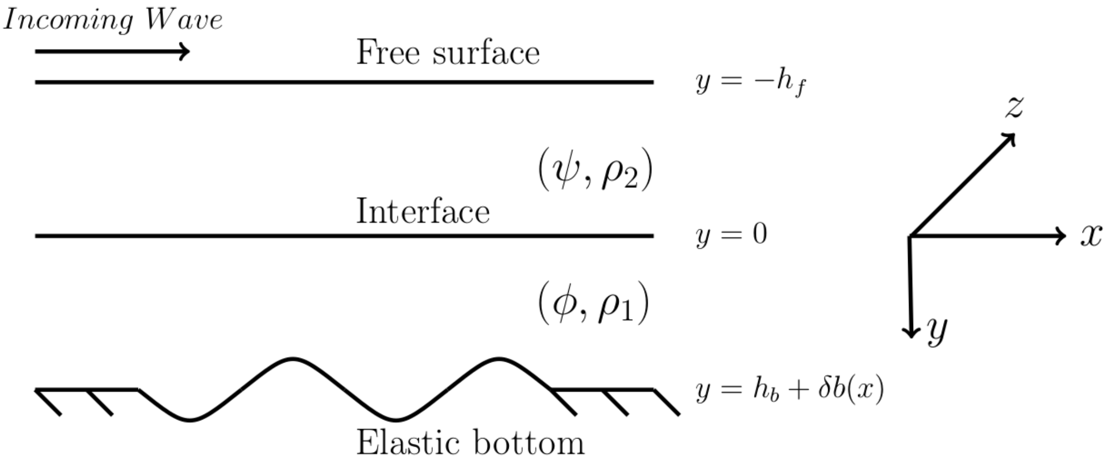

Figure 2.1: Domain definition sketch

The linearized mean free surface boundary condition is given by

$$\frac{\partial\psi}{\partial y}+K\psi=0 \quad \text{on} \quad y=-h_f, \tag{2.3}$$

where $K=\omega^2/g$ with g as the usual gravitational constant. Equation (2.3) is the combined linearized dynamic and kinematic boundary condition at the free surface.

Let the ratio ρ_2/ρ_1 of the densities of the two fluids be denoted by ρ. The linearized boundary condition at the mean interface $y=0$ can be written as

$$\frac{\partial\phi}{\partial y} = \frac{\partial\psi}{\partial y}, \tag{2.4}$$

$$K\phi+\frac{\partial\phi}{\partial y} = \rho\Big(K\psi+\frac{\partial\psi}{\partial y}\Big). \tag{2.5}$$

Boundary conditions (2.4) and (2.5), respectively, represent the continuity of the normal velocity and pressure across the two layers. The very important linearized boundary condition at the elastic bottom is given by (in a similar manner as in Sarangi and Mohapatra [83])

$$K\phi+\Big\{D\Big(\frac{\partial^2}{\partial x^2}-\gamma^2\Big)^2+1-\epsilon K\Big\}\frac{\partial\phi}{\partial n}=0 \quad \text{on} \quad y=h_b+\delta b(x), \tag{2.6}$$

where $D=(Q/\rho_1 g)$, $Q=Eh_0^3/[12(1-\nu^2)]$ is the flexural rigidity of the elastic bed; E is the Young's modulus, ν is the Poisson's ratio; $\epsilon=(\rho_0/\rho_1)h_0$; ρ_0 is the density of the elastic sea-bed, h_0 is the very small thickness of the elastic sea-bed and $\dfrac{\partial}{\partial n}$ is the derivative in the direction of the normal to the bottom surface at a point (x,y). The Euler-Bernoulli equation for a thin ice-cover, which was approximated as a thin elastic plate, is derived in details in the Appendix of Saha and Bora [80] for an impermeable flat sea-bed. In a similar manner, the same approximation applies on the elastic sea-bed as considered in the present problem. The presence of either an ice-sheet or an elastic sea-bed gives rise to flexural gravity waves. Mohapatra and Sahoo [73] considered surface gravity wave interaction with an elastic sea-bed which was modeled as a thin elastic plate.

By utilizing the knowledge of linear water wave theory in a two-layer fluid, the representation of a train of progressive waves along the positive x-direction is given by

$$\psi(x,y) = \exp(\pm \mathrm{i}x\sqrt{u^2-\gamma^2})[u\cosh u(y+h_f) - K\sinh u(y+h_f)] \quad \text{in} \quad -h_f \le y \le 0, \tag{2.7}$$

$$\phi(x,y) = \exp(\pm \mathrm{i}x\sqrt{u^2-\gamma^2}) f(u,y) \quad \text{in} \quad 0 \le y \le h_b, \tag{2.8}$$

where

$$f(u,y) = \frac{(K\cosh uh_f - u\sinh uh_f)[(Du^4+1-\epsilon K)u\cosh u(y-h_b) - K\sinh u(y-h_b)]}{K\cosh uh_b + (Du^4+1-\epsilon K)u\sinh uh_b}. \tag{2.9}$$

Note that wavenumber u satisfies the dispersion relation

$$\triangle(u) \equiv 0, \tag{2.10}$$

where

$$\begin{aligned}\triangle(u) &= K^3\sinh uh_b\cosh uh_f + K^2(Du^4+1-\epsilon K)u\cosh uh_f\cosh uh_b + \rho K^3\\ &\times\cosh uh_b\sinh uh_f + \rho K^2u(Du^4+1-\epsilon K)\sinh uh_f\sinh uh_b - Ku^2(Du^4+1-\epsilon K)\\ &\times\cosh uh_f\sinh uh_b - K^2u\cosh uh_f\cosh uh_b - Ku^2(Du^4+1-\epsilon K)\cosh uh_b\sinh uh_f\\ &-K^2u\sinh uh_b\sinh uh_f + u^3(Du^4+1-\epsilon K)\sinh uh_b\sinh uh_f + Ku^2\sinh uh_f\\ &\times\cosh uh_b - \rho u^2K\sinh uh_f\cosh uh_b - \rho(Du^4+1-\epsilon K)u^3\sinh uh_f\sinh uh_b.\end{aligned} \tag{2.11}$$

It is obvious that $u = 0$ is a root of Eq. (2.10). A detailed discussion on the role of zero root can be found in Appendix A. The same applies to the problems in Chapters 3 and 4 too. In dispersion relation (2.10), there are two positive real roots, say m and M, restricted by $0 < m < M$, which correspond to the propagating modes, two pairs of complex conjugate roots corresponding to the non-propagating modes, and an infinite number of purely imaginary roots corresponding to the evanescent modes. It is further to be noted that the negative values of all of these are also roots which are nothing but wavenumbers of the waves traveling in the negative direction. It is apparent that since there exist exactly two positive roots m and M of (2.10), as seen in [81], there are two modes of waves which propagate at the interface (say, interfacial mode) and at the free surface (say, free surface mode), respectively, along the positive x-direction. Both wavenumbers attain increasing values corresponding to increasing values of the elastic parameter of the sea-bed. The potency of the evanescent mode of waves understandably faces exponential decay with an increase in the distance from the interface at which they are formed. Because of the presence of such evanescent modes of waves in the fluid, it so happens that a portion of the incident interfacial wave gets trapped which leads to the formation of a standing wave over the bottom irregularities when the incident wave undergoes scattering by the bottom undulation. This phenomenon is commonly recognized as *Anderson localization*. Detailed description in connection with Anderson localization is available in the works of Guazzelli et al. [36], Devillard et al. [30], and An and Ye [102]. However, it is found that these waves do not bring any change to the asymptotic behaviour of the resultant reflected and transmitted waves.

Progressive waves corresponding to mode m (interfacial mode) can be expressed in the following forms:

$$\psi(x,y) = \exp\left(\pm \mathrm{i}x\sqrt{m^2-\gamma^2}\right)[m\cosh m(y+h_f) - K\sinh m(y+h_f)] \text{ in } -h_f \le y \le 0, \tag{2.12}$$

$$\phi(x,y) = \exp\left(\pm \mathrm{i}x\sqrt{m^2-\gamma^2}\right)f(m,y) \quad \text{in} \quad 0 \le y \le h_b, \tag{2.13}$$

where the inequality $\gamma < m$ must be satisfied in order that these progressive waves exist. In a similar way, progressive waves corresponding to mode M (free-surface mode) have the following forms:

$$\psi(x,y) = \exp\left(\pm \mathrm{i}x\sqrt{M^2-\gamma^2}\right)[M\cosh M(y+h_f) - K\sinh M(y+h_f)] \text{ in } -h_f \le y \le 0, \tag{2.14}$$

$$\phi(x,y) = \exp\left(\pm \mathrm{i}x\sqrt{M^2-\gamma^2}\right)f(M,y) \quad \text{in} \quad 0 \le y \le h_b. \tag{2.15}$$

Here also, the inequality $\gamma < M$ must be satisfied so that these progressive waves exist.

It may be noted that the formulation here, along with most of the parameters used above, is similar to the one that can be found in Mohapatra and Bora [72].

We consider a plane wave of mode m incident at an angle θ, $0 \le \theta < \pi/2$, to the positive x-axis as follows:

$$\psi_0(x,y) = \exp\left(\mathrm{i}mx\cos\theta\right)[m\cosh m(y+h_f) - K\sinh m(y+h_f)] \quad \text{in } -h_f \le y \le 0, \tag{2.16}$$

$$\phi_0(x,y) = \exp\left(\mathrm{i}mx\cos\theta\right)f(m,y) \quad \text{in} \quad 0 \le y \le h_b. \tag{2.17}$$

In this case, the following holds:

$$\gamma = m\sin\theta. \tag{2.18}$$

Due to the fact that $M > m$, we must have $\sqrt{M^2-\gamma^2}$ as real and consequently, the scattered wave due to the free surface mode M exists corresponding to any value of m. Equivalently, this happens corresponding to all values of K (we get different m and M for different values of K) and for all incident angles θ.

The angle θ_f of the scattered waves due to wavenumber M has the following form:

$$\tan\theta_f = \frac{m\sin\theta}{\sqrt{M^2-m^2\sin^2\theta}}.$$

Since $\sqrt{M^2-m^2\sin^2\theta} > m\cos\theta$, it must be true that we must have $\tan\theta_f < \tan\theta$ which in turn gives $|\theta_f| < \theta$. Therefore, if an oblique wave train of mode m propagating from the positive x-direction is incident at an angle θ, $0 \le \theta < \pi/2$, on the deformation at the elastic bottom of a two-layer fluid region, then the occurrence of reflected and transmitted waves for both interfacial and free-surface modes takes place for any such angle of incidence θ. With the knowledge that the wave train undergoes partial reflection by and partial transmission over the bottom undulation, the asymptotic behaviours of potentials ψ and ϕ, respectively, take the following forms:

$$\psi(x,y) \sim \begin{cases} [m\cosh m(y+h_f) - K\sinh m(y+h_f)](\exp(\mathrm{i}mx\cos\theta) + r^{(m)}\exp(-\mathrm{i}mx\cos\theta)) \\ +R^{(m)}[M\cosh M(y+h_f) - K\sinh M(y+h_f)]\exp(-\mathrm{i}x\sqrt{M^2-m^2\sin^2\theta}), \\ \qquad\qquad\qquad\qquad\qquad\qquad\qquad \text{as } x\to-\infty, \\ \\ t^{(m)}[m\cosh m(y+h_f) - K\sinh m(y+h_f)]\exp(\mathrm{i}mx\cos\theta) + \\ T^{(m)}[M\cosh M(y+h_f) - K\sinh M(y+h_f)]\exp(\mathrm{i}x\sqrt{M^2-m^2\sin^2\theta}), \\ \qquad\qquad\qquad\qquad\qquad\qquad\qquad \text{as } x\to\infty, \end{cases} \tag{2.19}$$

$$\phi(x,y) \sim \begin{cases} f(m,y)(\exp(\mathrm{i}mx\cos\theta) + r^{(m)}\exp(-\mathrm{i}mx\cos\theta)) + \\ R^{(m)}f(M,y)\exp(-\mathrm{i}x\sqrt{M^2-m^2\sin^2\theta}), \qquad \text{as } x\to-\infty, \\ \\ t^{(m)}f(m,y)\exp(\mathrm{i}mx\cos\theta) + T^{(m)}f(M,y)\exp(\mathrm{i}x\sqrt{M^2-m^2\sin^2\theta}), \text{as } x\to\infty. \end{cases} \tag{2.20}$$

The undetermined coefficients $r^{(m)}$ and $R^{(m)}$ appearing in Eqs. (2.19) and (2.20) are the reflection coefficients related to the reflected wave modes m and M, respectively, due to an obliquely incident wave of wavenumber m. In a similar manner, $t^{(m)}$ and $T^{(m)}$ are the transmission coefficients related to the transmitted wave modes m and M, respectively, due to an obliquely incident wave of mode m. Our endeavour is to evaluate these four coefficients.

The boundary condition (2.6) satisfied at the uneven bottom $y = h_b + \delta b(x)$ is now approximated (by ignoring the terms with higher powers of δ) in a similar manner as in Sarangi and Mohapatra [83] as

$$K\Big[\phi + \delta b(x)\frac{\partial \phi}{\partial y}\Big] + \Big\{D\Big(\frac{\partial^2}{\partial x^2} - \gamma^2\Big)^2 + 1 - \epsilon K\Big\}\Big[\frac{\partial \phi}{\partial y} - \delta\Big(\frac{\partial}{\partial x}\Big\{b(x)\frac{\partial \phi}{\partial x}\Big\} - \gamma^2 b(x)\phi(x,y)\Big)\Big] + O(\delta^2) = 0 \quad \text{on} \quad y = h_b. \tag{2.21}$$

A wave of mode M incident at an angle θ to the positive x-axis has the following form:

$$\psi_0(x,y) = \exp(\mathrm{i}Mx\cos\theta)[M\cosh M(y+h_f) - K\sinh M(y+h_f)] \text{ in } -h_f \le y \le 0, \tag{2.22}$$

$$\phi_0(x,y) = \exp(\mathrm{i}Mx\cos\theta)f(M,y) \quad \text{in} \quad 0 \le y \le h_b, \tag{2.23}$$

where $f(\cdot\ ,\cdot)$ is given by Eq. (2.9).

For this case, we have

$$\gamma = M\sin\theta \quad \text{and} \quad \sqrt{m^2-\gamma^2} = \sqrt{m^2 - M^2\sin^2\theta}. \tag{2.24}$$

For a given angle θ, there is a possibility of existence of a value of m, i.e., a value of K, for which we can have $m = M\sin\theta$ resulting in $\sqrt{m^2-\gamma^2} = 0$. This specific value of K is termed as the cut-off frequency of the waves as defined by Linton and Cadby [56] and is denoted by K_c. For $K > K_c$, that is, for the case $m > M\sin\theta$ (for a fixed θ), $\sqrt{m^2-\gamma^2}$ always takes real values which establishes that the reflected and transmitted waves of mode m exist and that they propagate in the fluid. On the other hand, for $K < K_c$, that is, for $m < M\sin\theta$ (for a fixed θ), $\sqrt{m^2-\gamma^2}$ is purely imaginary which corresponds to an evanescent mode, and hence it can be concluded that there do not exist reflected and transmitted waves of mode m. Because of this, one does not come across propagating waves due to wavenumber m. Accordingly, the existence of cut-off frequency tells that waves with any frequency having values lower than the cut-off frequency attain attenuation instead of propagation.

In Fig. 2.2, the values of Kh_b, the non-dimensionalized cut-off frequency, are plotted against the incident wave angle $\theta = \sin^{-1}(\frac{m}{M})$, for depth values $h_b/h_f = 2, 5, 10, 45$ and density ratio $\rho = 0.5$. Before going further ahead, it is felt essential to put forward some justification about the chosen value of the density ratio ρ. It is known that, for a two-layer fluid consisting usually of fresh water and salt water, the value of ρ would ideally be around

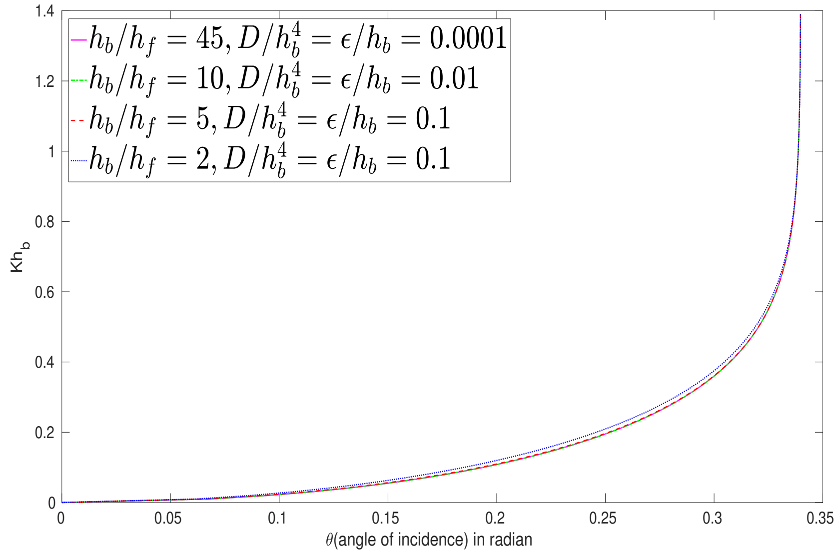

Figure 2.2: Cut-off frequency Kh_b due to an incident wave of wave number M

0.97. The same qualitative features are observed for such a density ratio, but the effects of the interface are much smaller and cannot be appreciated. In this context, the density ratio ρ is chosen to be 0.5 in order to observe the features clearly. The same was followed by some other researchers including Linton and McIver [57] and Linton and Cadby [56], for the scattering problem in a two-layer fluid with the density ratio chosen as 0.5 for the same reason. The value $\rho = 0.5$ will be considered for all relevant works in this thesis, whenever required. It is observed that for $\theta \approx 0.339718$ (in radian) $\approx \pi/9.24$, $Kh_b \to \infty$. Such an angle is known as the critical angle, usually denoted by θ_c. Figure 2.2 also shows that, for a wave of mode M incident at an angle θ to the x-axis and propagating in the positive x-direction resulting in the point (θ, Kh_b) lying on the left side of the curve, the existence of reflected and transmitted waves of mode m is guaranteed. On the other hand, if this point lies on the right side of this curve, then no reflected and transmitted waves of mode m exist. It may be noted that the curve for Kh_b corresponding to $h_b/h_f = 45$ is almost similar to the curve presented in Figure 1 of Linton and Cadby [56] where the lower layer was of infinite depth. In the presence of the elastic bottom, we notice that corresponding to certain values of incident angle θ less than this θ_c, the existence of one or two or three cut-off frequencies is ensured. Corresponding to those frequencies, which are either greater than the cut-off frequency or which lie between two appropriate cut-off frequencies, energy transfer takes place from the waves with higher wavenumber to the waves with lower wavenumber in the scattering procedure.

Thus an oblique wave of mode M, which is incident on the bottom undulation of the elastic bed of the two-layer fluid and makes an angle θ with the positive x-axis where $\theta < \sin^{-1}(\frac{m}{M})$, the far-field behaviours of potential functions ψ and ϕ, respectively, have the following forms:

$$\psi(x,y) \sim \begin{cases} [M\cosh M(y+h_f) - K\sinh M(y+h_f)](\exp(\mathrm{i}Mx\cos\theta)+ \\ R^{(M)}\exp(-\mathrm{i}Mx\cos\theta)) + r^{(M)}[m\cosh m(y+h_f) - K\sinh m(y+h_f)] \\ \exp(-\mathrm{i}x\sqrt{m^2 - M^2\sin^2\theta}), \qquad \text{as } x \to -\infty, \\ \\ T^{(M)}[M\cosh M(y+h_f) - K\sinh M(y+h_f)]\exp(\mathrm{i}Mx\cos\theta)+ \\ t^{(M)}[m\cosh m(y+h_f) - K\sinh m(y+h_f)]\exp(\mathrm{i}x\sqrt{m^2 - M^2\sin^2\theta}), \\ \qquad \text{as } x \to \infty, \end{cases} \tag{2.25}$$

$$\phi(x,y) \sim \begin{cases} f(M,y)(\exp(\mathrm{i}Mx\cos\theta) + R^{(M)}\exp(-\mathrm{i}Mx\cos\theta)) \\ +r^{(M)}f(m,y)\exp(-\mathrm{i}x\sqrt{m^2 - M^2\sin^2\theta}), \qquad \text{as } x \to -\infty, \\ \\ T^{(M)}f(M,y)\exp(\mathrm{i}Mx\cos\theta) + t^{(M)}f(m,y)\exp(\mathrm{i}x\sqrt{m^2 - M^2\sin^2\theta}), \\ \qquad \text{as } x \to \infty. \end{cases} \tag{2.26}$$

In (2.25) and (2.26), the unknown coefficients $r^{(M)}$ and $R^{(M)}$ are the reflection coefficients related to the reflected wave modes m and M, respectively, due to an obliquely incident wave of wavenumber M. In a similar manner, $t^{(M)}$ and $T^{(M)}$ are the transmission coefficients related to the transmitted wave modes m and M, respectively, due to an obliquely incident wave of mode M. We are required to evaluate these four coefficients.

The coefficients $r^{(M)}$ and $t^{(M)}$ exist only when the angle of incidence θ satisfies $\theta < \sin^{-1}(\frac{m}{M})$. Consequently, when the incident wave has the mode M, then it satisfies the corresponding modified Helmholtz equation with $\gamma = M\sin\theta$, $0 < \theta < \sin^{-1}(\frac{m}{M})$, the free surface condition, the interface condition and the bottom condition (2.21). In addition, both potentials also satisfy the far-field behaviours given by (2.25) and (2.26) containing the unknown coefficients. The procedure to evaluate these coefficients (as well as $r^{(m)}$, $R^{(m)}$, $t^{(m)}$ and $T^{(m)}$ for the interfacial mode) for any arbitrary bed shape is not a very straightforward task. However, employing perturbation technique for calculating these coefficients up to first-order with the assumption of small bottom deformation gives some direction. Then we move forward to calculate the relevant first-order potential function and the associated reflection and transmission coefficients related to the respective mode of waves, in the next section.

2.3 Solution for the potentials and coefficients

2.3.1 Perturbation method

We consider an oblique wave train of mode m incident at an angle θ, $0 \leq \theta < \pi/2$, on the bottom undulation of the elastic sea-bed under consideration. If there exists no bottom distortion, it is obvious that this wave train propagates with no disturbance. Subsequently, this results in only the transmission of waves taking place along the positive x-direction. This consideration and the boundary condition (2.21) in an appropriate form allow us to write the velocity potentials ψ and ϕ, the reflection coefficients $r^{(m)}$and $R^{(m)}$ and the transmission coefficients $t^{(m)}$ and $T^{(m)}$ (introduced for interfacial wave mode in the previous section), appropriately in perturbation series in terms of the small perturbation parameter δ as

$$\psi = \psi_0 + \delta\psi_1 + O(\delta^2), \tag{2.27}$$

$$\phi = \phi_0 + \delta\phi_1 + O(\delta^2), \tag{2.28}$$

$$r^{(m)} = \delta r_1^{(m)} + O(\delta^2), \tag{2.29}$$

$$R^{(m)} = \delta R_1^{(m)} + O(\delta^2), \tag{2.30}$$

$$t^{(m)} = 1 + \delta t_1^{(m)} + O(\delta^2), \tag{2.31}$$

$$T^{(m)} = \delta T_1^{(m)} + O(\delta^2), \tag{2.32}$$

where ψ_0 and ϕ_0 are, respectively, given by (2.16) and (2.17).

However, it is observed that this type of perturbation expansion given by (2.27)-(2.32) is not valid at Bragg resonance for which the reflection coefficient takes higher values than the undulation parameter δ, as mentioned by Mei [68]. It is well known that Bragg resonance occurs for water wave problems when the wavenumber of the bottom undulation takes a value approximately double of that of the interface wavenumber. However, in order to avoid this difficulty, Mei [68] produced a theory involving wave evolution and reflection at and near Bragg resonance condition for structures such as shore-parallel sinusoidal bars. The perturbation expansions as given by (2.27)-(2.32) are assumed to be valid throughout the present work due to Bragg resonance not being considered in the present work.

We now substitute the expansions given by the relations (2.27)-(2.32) into (2.1)-(2.5), (2.19)-(2.21) with $\gamma = m\sin\theta$. By carrying out comparison of the first-order terms of the perturbation parameter δ from both sides of the equations, the coupled BVP of first-order velocity potentials ψ_1 and ϕ_1 is obtained as follows:

$$(\nabla^2_{x,y} - \gamma^2)\psi_1 = 0 \quad \text{in} \quad -h_f \leq y \leq 0, \tag{2.33}$$

$$(\nabla^2_{x,y} - \gamma^2)\phi_1 = 0 \quad \text{in} \quad 0 \leq y \leq h_b, \tag{2.34}$$

$$\begin{aligned}
\frac{\partial \psi_1}{\partial y} + K\psi_1 &= 0 \quad \text{on} \quad y = -h_f, &(2.35)\\
\frac{\partial \phi_1}{\partial y} &= \frac{\partial \psi_1}{\partial y} \quad \text{on} \quad y = 0, &(2.36)\\
\rho\Big(K\psi_1 + \frac{\partial \psi_1}{\partial y}\Big) &= K\phi_1 + \frac{\partial \phi_1}{\partial x} \quad \text{on} \quad y = 0, &(2.37)\\
K\phi_1 + \Big\{D\Big(\frac{\partial^2}{\partial x^2} - \gamma^2\Big)^2 + 1 - \epsilon K\Big\}\frac{\partial \phi_1}{\partial y} &= q(x) \quad \text{on} \quad y = h_b, &(2.38)
\end{aligned}$$

$$\begin{aligned}
\text{where } q(x) = f(m,y)\Big[D\Big(\frac{\partial^2}{\partial x^2} - \gamma^2\Big)^2 + 1 - \epsilon K\Big]\Big\{\mathrm{i}m\cos\theta\frac{\partial}{\partial x}\Big(b(x)\exp{(\mathrm{i}mx\cos\theta)}\Big)\\
-m^2\sin^2\theta\; b(x)\exp{(\mathrm{i}mx\cos\theta)}\Big\} - Kb(x)\frac{df(m,y)}{dy}\exp{(\mathrm{i}mx\cos\theta)},
\end{aligned} \tag{2.39}$$

which is to be evaluated on $y = h_b$.

Further, the asymptotic behaviours of ψ_1 and ϕ_1 have the following forms:

$$\psi_1(x,y) \sim \begin{cases} r_1^{(m)}[m\cosh m(y+h_f) - K\sinh m(y+h_f)]\exp{(-\mathrm{i}mx\cos\theta)} + \\ R_1^{(m)}[M\cosh M(y+h_f) - K\sinh M(y+h_f)]\exp{(-\mathrm{i}x\sqrt{M^2 - m^2\sin^2\theta})}, \\ \hfill \text{as } x \to -\infty, \\ t_1^{(m)}[m\cosh m(y+h_f) - K\sinh m(y+h_f)]\exp{(\mathrm{i}mx\cos\theta)} + \\ T_1^{(m)}[M\cosh M(y+h_f) - K\sinh M(y+h_f)]\exp{(\mathrm{i}x\sqrt{M^2 - m^2\sin^2\theta})}, \\ \hfill \text{as } x \to \infty, \end{cases} \tag{2.40}$$

$$\phi_1(x,y) \sim \begin{cases} r_1^{(m)} f(m,y)\exp{(-\mathrm{i}mx\cos\theta)} + R_1^{(m)} f(M,y)\exp{(-\mathrm{i}x\sqrt{M^2 - m^2\sin^2\theta})}, \\ \hfill \text{as } x \to -\infty, \\ t_1^{(m)} f(m,y)\exp{(\mathrm{i}mx\cos\theta)} + T_1^{(m)} f(M,y)\exp{(\mathrm{i}x\sqrt{M^2 - m^2\sin^2\theta})}, \\ \hfill \text{as } x \to \infty. \end{cases} \tag{2.41}$$

2.3.2 Boundary value problems in ψ_1 and ϕ_1

The BVP for the first-order potentials ψ_1 and ϕ_1, as described by Eqs. (2.33)-(2.39), along with (2.40)-(2.41), is now decomposed into two independent BVPs for ψ_1 and ϕ_1 as follows:

BVP-I for ψ_1 is

$$\begin{aligned}(\nabla^2_{x,y}-\gamma^2)\psi_1 &= 0 \quad \text{in} \quad -h_f \le y \le 0, && (2.42)\\ \frac{\partial \psi_1}{\partial y}+K\psi_1 &= 0 \quad \text{on} \quad y=-h_f, && (2.43)\\ \frac{\partial \psi_1}{\partial y} &= \zeta(x) \quad \text{on} \quad y=0, && (2.44)\end{aligned}$$

with $\zeta(x)$ known on $y=0$ and ψ_1 having the far-field behaviour

$$\psi_1(x,y) \sim \begin{cases} r_1^{(m)}[m\cosh m(y+h_f)-K\sinh m(y+h_f)]\exp(-\mathrm{i}mx\cos\theta)+ \\ R_1^{(m)}[M\cosh M(y+h_f)-K\sinh M(y+h_f)]\exp(-\mathrm{i}x\sqrt{M^2-m^2\sin^2\theta}), \\ \qquad\qquad\qquad\qquad \text{as } x\to-\infty, \\ t_1^{(m)}[m\cosh m(y+h_f)-K\sinh m(y+h_f)]\exp(\mathrm{i}mx\cos\theta)+ \\ T_1^{(m)}[M\cosh M(y+h_f)-K\sinh M(y+h_f)]\exp(\mathrm{i}x\sqrt{M^2-m^2\sin^2\theta}), \\ \qquad\qquad\qquad\qquad \text{as } x\to\infty. \end{cases} \tag{2.45}$$

BVP-II for ϕ_1 is

$$\begin{aligned}(\nabla^2_{x,y}-\gamma^2)\phi_1 &= 0 \quad \text{in} \quad 0\le y\le h_b, && (2.46)\\ \frac{\partial \phi_1}{\partial y} &= \zeta(x) \quad \text{on} \quad y=0, && (2.47)\\ K\phi_1+\Big\{D\Big(\frac{\partial^2}{\partial x^2}-\gamma^2\Big)^2+1-\epsilon K\Big\}\frac{\partial \phi_1}{\partial y} &= q(x) \quad \text{on} \quad y=h_b, && (2.48)\end{aligned}$$

with the asymptotic behaviour

$$\phi_1(x,y) \sim \begin{cases} r_1^{(m)}f(m,y)\exp(-\mathrm{i}mx\cos\theta)+R_1^{(m)}f(M,y)\exp(-\mathrm{i}x\sqrt{M^2-m^2\sin^2\theta}), \\ \qquad\qquad\qquad\qquad \text{as } x\to-\infty, \\ t_1^{(m)}f(m,y)\exp(\mathrm{i}mx\cos\theta)+T_1^{(m)}f(M,y)\exp(\mathrm{i}x\sqrt{M^2-m^2\sin^2\theta}), \\ \qquad\qquad\qquad\qquad \text{as } x\to\infty. \end{cases} \tag{2.49}$$

By using Eqs. (2.44) and (2.47), Eq. (2.37) can be expressed in the following form:

$$K(\phi_1-\rho\psi_1)=(\rho-1)\zeta(x) \quad \text{on} \quad y=0. \tag{2.50}$$

2.3.3 Fourier transform technique

In order to solve the above BVPs, we define the Fourier transform of $\psi_1(x,y)$ and $\phi_1(x,y)$ with respect to x with the assumption that those Fourier transforms exist and denote them by $\overline{\psi_1}$ and $\overline{\phi_1}$, respectively, as follows:

$$\begin{aligned} \overline{\psi}_1(\beta, y) &= \int_{-\infty}^{\infty} \psi_1(x, y) e^{-\mathrm{i}\beta x} \mathrm{d}x, && (2.51) \\ \text{and} \quad \overline{\phi}_1(\beta, y) &= \int_{-\infty}^{\infty} \phi_1(x, y) e^{-\mathrm{i}\beta x} \mathrm{d}x. && (2.52) \end{aligned}$$

Now with the application of Fourier transform to Eqs. (2.42)-(2.44), we have the following boundary value problem for $\overline{\psi}_1$:

$$\begin{aligned} \overline{\psi}_{1yy} - \hat{\beta}^2 \overline{\psi}_1 &= 0 \quad \text{in} \quad -h_f \le y \le 0, && (2.53) \\ \overline{\psi}_{1y} + K \overline{\psi}_1 &= 0 \quad \text{on} \quad y = -h_f, && (2.54) \\ \overline{\psi}_{1y} &= \bar{\zeta}(\beta) \quad \text{on} \quad y = 0, && (2.55) \end{aligned}$$

where $\hat{\beta}^2 = \beta^2 + \gamma^2$, and $\bar{\zeta}(\beta)$ denotes the Fourier transform of $\zeta(x)$. The solution for the above problem is obtained as

$$\overline{\psi}_1(\hat{\beta}, y) = \frac{[\hat{\beta} \cosh \hat{\beta}(y + h_f) - K \sinh \hat{\beta}(y + h_f)]}{-K \cosh \hat{\beta} h_f + \hat{\beta} \sinh \hat{\beta} h_f} \frac{\bar{\zeta}(\beta)}{\hat{\beta}}. \quad (2.56)$$

Similarly, application of Fourier transform to Eqs. (2.46)-(2.48) gives rise to the following BVP for $\overline{\phi}_1$:

$$\begin{aligned} \overline{\phi}_{1yy} - \hat{\beta}^2 \overline{\phi}_1 &= 0 \quad \text{in} \quad 0 \le y \le h_b, && (2.57) \\ \overline{\phi}_{1y} &= \bar{\zeta}(\beta) \quad \text{on} \quad y = 0, && (2.58) \\ K \overline{\phi}_1 + (D\hat{\beta}^4 + 1 - \epsilon K) \overline{\phi}_{1y} &= \bar{q}(\beta) \quad \text{on} \quad y = h_b, && (2.59) \end{aligned}$$

where $\bar{q}(\beta)$ denotes the Fourier transform of the function $q(x)$ given by

$$\bar{q}(\beta) = S(m, \beta) \int_{-\infty}^{\infty} e^{\mathrm{i}(m \cos\theta - \beta)x} b(x) \mathrm{d}x, \quad (2.60)$$

with

$$\begin{aligned} S(m, \beta) &= f(m, h_b) \Big[D \Big\{ m \cos\theta (m \cos\theta - \beta)^5 - m^2 (4 \cos^2\theta + 1)(m \cos\theta - \beta)^4 \\ &+ 2m^3 \cos\theta (3 + 2\cos^2\theta)(m \cos\theta - \beta)^3 - 2m^4 (4\cos^2\theta + 1)(m \cos\theta - \beta)^2 \\ &+ 5m^5 \cos\theta (m \cos\theta - \beta) - m^6 \Big\} + (1 - \epsilon K)(m^2 \cos^2\theta - \beta m \cos\theta - m^2) \Big] \\ &+ \frac{mK^2 (K \cosh m h_f - m \sinh m h_f)}{K \cosh m h_b + (D m^4 + 1 - \epsilon K) m \sinh m h_b}. \quad (2.61) \end{aligned}$$

The problem given by (2.57)-(2.59) is solved to get the following solution:

$$\overline{\phi}_1(\hat{\beta},y)=\frac{\hat{\beta}\bar{q}(\beta)\cosh\hat{\beta}y+\bar{\zeta}(\beta)[K\sinh\hat{\beta}(y-h_b)-(D\hat{\beta}^4+1-\epsilon K)\hat{\beta}\cosh\hat{\beta}(y-h_b)]}{\hat{\beta}[K\cosh\hat{\beta}h_b+(D\hat{\beta}^4+1-\epsilon K)\hat{\beta}\sinh\hat{\beta}h_b]}. \tag{2.62}$$

For calculating the value of $\bar{\zeta}(\beta)$, application of Fourier transform to Eq. (2.50) gives

$$K(\overline{\phi}_1-\rho\overline{\psi}_1)=(\rho-1)\bar{\zeta}(\beta)\quad\text{on}\quad y=0. \tag{2.63}$$

By substituting Eqs. (2.56) and (2.62) in Eq. (2.63), the value of $\bar{\zeta}(\beta)$ is obtained as

$$\bar{\zeta}(\beta)=\frac{K\hat{\beta}[\hat{\beta}\sinh\hat{\beta}h_f-K\cosh\hat{\beta}h_f]\bar{q}(\beta)}{\triangle(\hat{\beta})}, \tag{2.64}$$

where the form of $\triangle(\hat{\beta})$ is given by (2.11). From Eq. (2.10), it is noticed that $\triangle(\hat{\beta})$ gives only two non-zero positive roots m and M on the real axis of β. Substituting the value of $\bar{\zeta}(\beta)$ in Eqs. (2.56) and (2.62) and affecting inverse Fourier transform, the expressions for $\psi_1(x,y)$ and $\phi_1(x,y)$ can be written, respectively, as

$$\psi_1(x,y)=\frac{K}{2\pi}\int_{-\infty}^{\infty}\frac{[\hat{\beta}\cosh\hat{\beta}(y+h_f)-K\sinh\hat{\beta}(y+h_f)]}{\triangle(\hat{\beta})}\bar{q}(\beta)e^{\mathrm{i}\beta x}\mathrm{d}\beta, \tag{2.65}$$

$$\phi_1(x,y)=\frac{1}{2\pi}\int_{-\infty}^{\infty}\frac{[\cosh\hat{\beta}y+\frac{K(\hat{\beta}\sinh\hat{\beta}h_f-K\cosh\hat{\beta}h_f)}{\triangle(\hat{\beta})}G(\hat{\beta},y)]}{[K\cosh\hat{\beta}h_b+(D\hat{\beta}^4+1-\epsilon K)\hat{\beta}\sinh\hat{\beta}h_b]}\bar{q}(\beta)e^{\mathrm{i}\beta x}\mathrm{d}\beta, \tag{2.66}$$

$$\text{where}\quad G(\hat{\beta},y)=K\sinh\hat{\beta}(y-h_b)-(D\hat{\beta}^4+1-\epsilon K)\hat{\beta}\cosh\hat{\beta}(y-h_b).$$

Since $\triangle(\hat{\beta})$ has two non-zero positive zeros at $\hat{\beta}=m$ and $\hat{\beta}=M$, corresponding to $\beta_1=\sqrt{m^2-\gamma^2}$ and $\beta_2=\sqrt{M^2-\gamma^2}$, respectively, on the positive real axis of β, the above integrals have poles at β_1 and β_2. Therefore, there is a need for the path in each integral in (2.65) and (2.66) to be indented below the poles at β_1 and β_2.

2.4 Determination of reflection and transmission coefficients

The first-order coefficients $r_1^{(m)}$, $t_1^{(m)}$and $R_1^{(m)}$, $T_1^{(m)}$ with respect to the interfacial and free surface modes, respectively, due to the obliquely incident wave of mode m, can be explicitly evaluated by letting $x\to\pm\infty$ in Eqs. (2.65) or (2.66) and then carrying out comparison of the expressions with those in Eqs. (2.45) or (2.49).

To acquire the first-order reflection coefficients, we let $x \to -\infty$ in either (2.65) or (2.66). As $x \to -\infty$, the behaviour of $\psi_1(x, y)$ or $\phi_1(x, y)$ can be found by rotating the path of the integral, which involves the term $\bar{q}(-\beta)$, into a contour in the first quadrant in order that we can incorporate the residue terms at the poles β_1 and β_2. The path of the integral containing the term $\bar{q}(\beta)$ in Eqs. (2.65) or (2.66) is rotated into a contour in the fourth quadrant so that this integral makes no contribution as $x \to -\infty$. Subsequently, comparing the resultant integral with Eqs. (2.45) or (2.49), we get the final expression for $r_1^{(m)}$ and $R_1^{(m)}$, respectively, as

$$\begin{aligned} r_1^{(m)} &= \frac{\mathrm{i}K\bar{q}(-m\cos\theta)}{\cos\theta\triangle'(m)} \\ &= \frac{\mathrm{i}KS(m, -m\cos\theta)}{\cos\theta\triangle'(m)} \int_{-\infty}^{\infty} e^{2\mathrm{i}mx\cos\theta} b(x)\mathrm{d}x, \qquad (2.67) \\ R_1^{(m)} &= \frac{\mathrm{i}KM\bar{q}(-\sqrt{M^2 - m^2\sin^2\theta})}{\sqrt{M^2 - m^2\sin^2\theta}\triangle'(M)} \\ &= \frac{\mathrm{i}KMS(m, -\sqrt{M^2 - m^2\sin^2\theta})}{\triangle'(M)} \int_{-\infty}^{\infty} e^{\mathrm{i}x(m\cos\theta + \sqrt{M^2 - m^2\sin^2\theta})} b(x)\mathrm{d}x, \qquad (2.68) \end{aligned}$$

where S is given by Eq. (2.61) and $\triangle'$ denotes the derivative operator of $\triangle$.

In a similar way, the evaluation of first-order transmission coefficients can be achieved by letting $x \to \infty$ in either (2.65) or (2.66). As $x \to \infty$, the behaviour of $\psi_1(x, y)$ or $\phi_1(x, y)$ can be obtained in the same manner as was done for the case $x \to -\infty$. Since the integral involving the term $\bar{q}(-\beta)$ makes no contribution as $x \to \infty$ (as explained earlier), comparison of the resultant integral with Eqs. (2.45) or (2.49) gives the final expressions for $t_1^{(m)}$ and $T_1^{(m)}$, respectively, as follows:

$$\begin{aligned} t_1^{(m)} &= \frac{\mathrm{i}K\bar{q}(m\cos\theta)}{\cos\theta\triangle'(m)} \\ &= \frac{\mathrm{i}KS(m, m\cos\theta)}{\cos\theta\triangle'(m)} \int_{-\infty}^{\infty} b(x)\mathrm{d}x, \qquad (2.69) \\ T_1^{(m)} &= \frac{\mathrm{i}KM\bar{q}(\sqrt{M^2 - m^2\sin^2\theta})}{\sqrt{M^2 - m^2\sin^2\theta}\triangle'(M)} \\ &= \frac{\mathrm{i}KMS(m, \sqrt{M^2 - m^2\sin^2\theta})}{\triangle'(M)} \int_{-\infty}^{\infty} e^{\mathrm{i}x(m\cos\theta - \sqrt{M^2 - m^2\sin^2\theta})} b(x)\mathrm{d}x. \qquad (2.70) \end{aligned}$$

Now assuming that a train of oblique incident waves of mode M propagates over the undulating bottom topography, the related first-order reflection and transmission coefficients $r_1^{(M)}$, $R_1^{(M)}$, $t_1^{(M)}$ and $T_1^{(M)}$ can be evaluated by following the same procedure as adopted previously for the case of mode m. After calculation and simplification, these coefficients can be found as follows:

$$r_1^{(M)} = \frac{\mathrm{i}KmS(M,-\sqrt{m^2-M^2\sin^2\theta})}{\triangle'(m)}\int_{-\infty}^{\infty} e^{\mathrm{i}x(M\cos\theta+\sqrt{m^2-M^2\sin^2\theta})}b(x)\mathrm{d}x, \tag{2.71}$$

$$R_1^{(M)} = \frac{\mathrm{i}KS(M,-M\cos\theta)}{\cos\theta\triangle'(M)}\int_{-\infty}^{\infty} e^{2\mathrm{i}Mx\cos\theta}b(x)\mathrm{d}x, \tag{2.72}$$

$$t_1^{(M)} = \frac{\mathrm{i}KmS(M,\sqrt{m^2-M^2\sin^2\theta})}{\sqrt{m^2-M^2\sin^2\theta}\triangle'(m)}\int_{-\infty}^{\infty} e^{\mathrm{i}x(M\cos\theta-\sqrt{m^2-M^2\sin^2\theta})}b(x)\mathrm{d}x, \tag{2.73}$$

$$T_1^{(M)} = \frac{\mathrm{i}KS(M,M\cos\theta)}{\cos\theta\triangle'(M)}\int_{-\infty}^{\infty} b(x)\mathrm{d}x. \tag{2.74}$$

All these coefficients are in integral form containing the shape function $b(x)$, and can be calculated for a given shape function of the bottom undulation of the elastic sea-bed. Next we go ahead to investigate the reflection and transmission by considering a particular form of the bottom undulation in the form of a sinusoidal ripple bed.

2.5 Special form of an undulating bottom profile

Now we deal with a specific shape function $b(x)$ which represents the irregular bottom topography which is similar to some common naturally available obstacles formed at the sea-bed on account of sedimentation and ripple growth of sands. Davies [27] established that a sea-bed with sinusoidal undulation possesses the capacity to bounce back the energy from the incident wave. This occurrence has a substantial role in connection with coastal protection and also with the likely growth of ripples for an erodible bed. To create a tranquillity zone, it is required to reduce the wave reflection such that the incident wave attenuates in the vicinity of the bottom undulation. Due to elasticity, wave energy gets dissipated by the sea-bed. Due to the physical significance of such bed topographies having sinusoidal ripples, enormous importance is accorded to such topographies and therefore, the following appropriate example is considered in order to substantiate the results obtained in the earlier sections.

The following shape function $b(x)$, consisting of a patch of sinusoidal ripples at the bottom with amplitude a, is taken up on an otherwise flat bottom (Mohapatra and Bora [72]):

$$b(x) = \begin{cases} a\sin lx, & -\frac{n\pi}{l} \le x \le \frac{n\pi}{l}, \\ 0, & \text{otherwise}, \end{cases} \tag{2.75}$$

where l denotes the ripple wavenumber in $-\frac{n\pi}{l} \le x \le \frac{n\pi}{l}$ and $n \in \mathbb{N}$. This patch of ripples has n number of ripples.

Assume that a train of progressive waves with wavenumber m (interfacial mode) strikes the bottom undulation obliquely. The reflection and transmission coefficients $r_1^{(m)}$, $R_1^{(m)}$,

$t_1^{(m)}$ and $T_1^{(m)}$, correct up to the first-order, due to the obliquely incident wave of mode m, are now acquired by putting $b(x)$ from Eq. (2.75) into Eqs. (2.67)-(2.70). For this shape function, $t_1^{(m)}$ vanishes identically. The other required coefficients are obtained as

$$r_1^{(m)} = (-1)^n \frac{2aKlS(m,-m\cos\theta)}{\cos\theta\triangle'(m)} \frac{\sin(\frac{2mn\pi\cos\theta}{l})}{l^2-4m^2\cos^2\theta}, \tag{2.76}$$

$$R_1^{(m)} = (-1)^n \frac{2aKMlS(m,-\sqrt{M^2-m^2\sin^2\theta})}{\cos\theta\triangle'(M)} \frac{\sin\left(\frac{n\pi(m\cos\theta+\sqrt{M^2-m^2\sin^2\theta})}{l}\right)}{l^2-(m\cos\theta+\sqrt{M^2-m^2\sin^2\theta})^2}, \tag{2.77}$$

$$T_1^{(m)} = (-1)^n \frac{2aKMlS(m,\sqrt{M^2-m^2\sin^2\theta})}{\cos\theta\triangle'(M)} \frac{\sin\left(\frac{n\pi(m\cos\theta-\sqrt{M^2-m^2\sin^2\theta})}{l}\right)}{l^2-(m\cos\theta-\sqrt{M^2-m^2\sin^2\theta})^2}. \tag{2.78}$$

Because $M > m\sin\theta$, it is evident that the reflected and transmitted waves occur corresponding to both modes m and M for all angles of incidence.

Next, the train of progressive waves with wavenumber M (free surface mode) obliquely incident on the bottom undulation is taken up. In this case, the first-order reflection and transmission coefficients $r_1^{(M)}$, $R_1^{(M)}$, $t_1^{(M)}$ and $T_1^{(M)}$ due to the obliquely incident wave of mode M are acquired by the substitution of $b(x)$ from Eq. (2.75) into Eqs. (2.71)-(2.74). For this specific shape function $b(x)$, $T_1^{(M)}$ vanishes identically. The remaining coefficients are evaluated as

$$r_1^{(M)} = (-1)^n \frac{2aKmlS(M,-\sqrt{m^2-M^2\sin^2\theta})}{\cos\theta\triangle'(m)} \frac{\sin\left(\frac{n\pi(M\cos\theta+\sqrt{m^2-M^2\sin^2\theta})}{l}\right)}{l^2-(M\cos\theta+\sqrt{m^2-M^2\sin^2\theta})^2}, \tag{2.79}$$

$$R_1^{(M)} = (-1)^n \frac{2aKlS(M,-M\cos\theta)}{\cos\theta\triangle'(M)} \frac{\sin(\frac{2Mn\pi\cos\theta}{l})}{l^2-4M^2\cos^2\theta}, \tag{2.80}$$

$$t_1^{(M)} = (-1)^n \frac{2aKmlS(M,\sqrt{m^2-M^2\sin^2\theta})}{\cos\theta\triangle'(m)} \frac{\sin\left(\frac{n\pi(M\cos\theta-\sqrt{m^2-M^2\sin^2\theta})}{l}\right)}{l^2-(M\cos\theta-\sqrt{m^2-M^2\sin^2\theta})^2}. \tag{2.81}$$

It is noticed from Eqs. (2.76)-(2.81) that, for a given number of ripples n, these first-order coefficients exhibit oscillation. Additionally, it is observed from (2.76) that if the incident wavenumber m and the ripple wavenumber l satisfy $l = 2m\cos\theta$, the theory breaks down and subsequently, the production of a large amount of reflected wave energy by the sea-bed is predicted around this singularity. It implies resonant interaction taking place between the incident wave and the sinusoidal ripples. Further, when $l = m\cos\theta + \sqrt{M^2-m^2\sin^2\theta}$

and $l = m\cos\theta - \sqrt{M^2 - m^2\sin^2\theta}$, respectively, in (2.77) and (2.78), the occurrence of resonant interaction can be predicted between the incident wave and the ripple bed. Likewise, the occurrence of resonance due of an incident wave of mode M can be examined. When resonance takes place, it can also be noticed that the largest peak value of each coefficient varies linearly with n. Furthermore, the reflection and transmission coefficients also depend on the elastic parameters D and ϵ.

Evaluation of the coefficients given by (2.76)-(2.81) is carried out in the next section in order to study how various parameters affect the wave energy due to reflection and transmission.

2.6 Results and discussion

A MATLAB program is devised to examine the effects of various parameters such as the angle of incidence, the number of ripples of the undulating bottom, the elastic parameters etc. on the hydrodynamic coefficients given by (2.76)-(2.81) for the patch of sinusoidal ripples on an elastic sea-bed given by Eq. (2.75). The primary objective of the present work is to find the pattern of distribution of incident wave energy between the transmitted and reflected waves. Here we present the graphical representation and the related explanation for first-order reflection and transmission coefficients evaluated corresponding to various values of different dimensionless parameters.

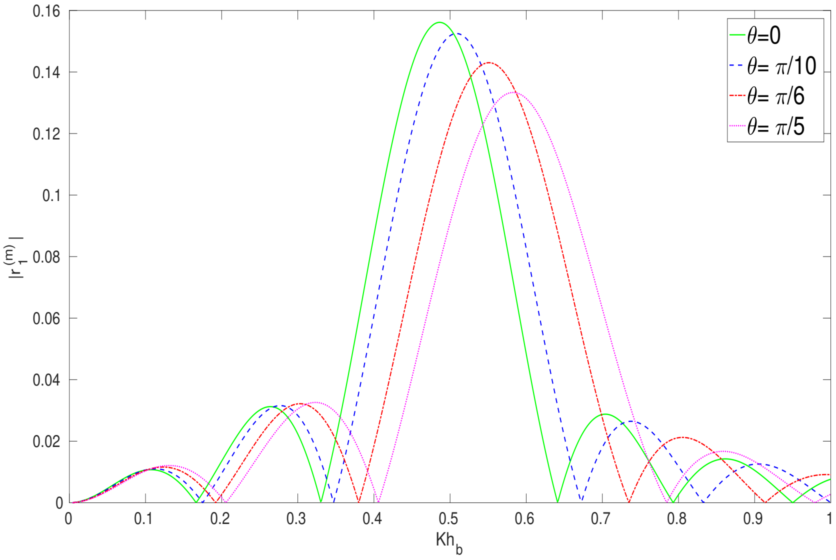

Figure 2.3: Reflection coefficient $|r_1^{(m)}|$ plotted against Kh_b for various angle of incidence θ corresponding to a propagating wave of mode m with $n = 3$, $h_b/h_f = 2$, $a/h_b = 0.1$, $lh_b = 1$, $\rho = 0.5$, $D/h_b^4 = 1$, $\epsilon/h_b = 0.001$

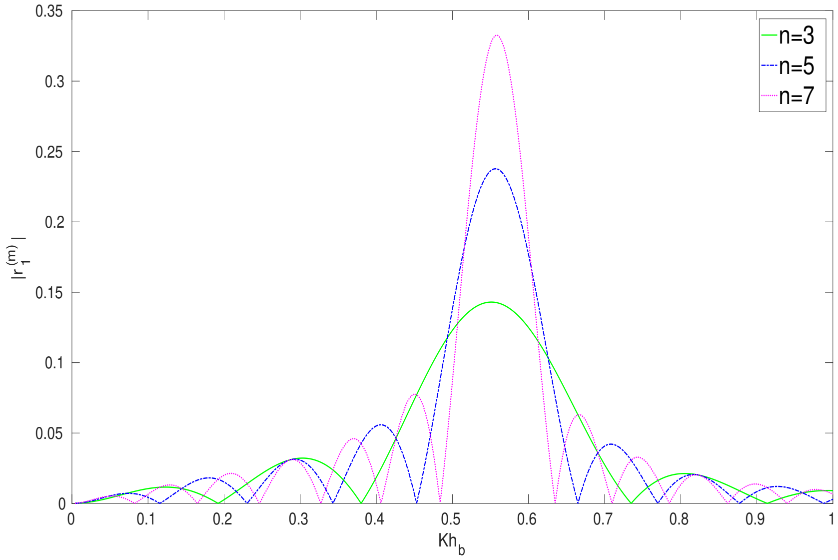

Figure 2.4: Reflection coefficient $|r_1^{(m)}|$ plotted against Kh_b for different number of ripples corresponding to a propagating wave of mode m with $\theta = \pi/6$, $D/h_b^4 = 1$, $\epsilon/h_b = 0.001$, $h_b/h_f = 2$, $\rho = 0.5$, $a/h_b = 0.1$, $lh_b = 1$

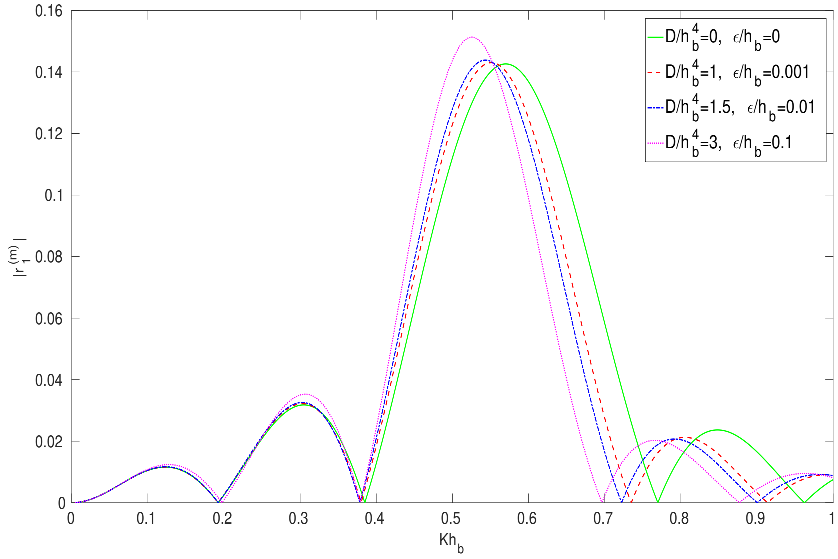

Figure 2.5: Reflection coefficient $|r_1^{(m)}|$ plotted against Kh_b for different elastic parameter values corresponding to a propagating wave of mode m with $\theta = \pi/6, n = 3$, $h_b/h_f = 2$, $\rho = 0.5$, $a/h_b = 0.1$, $lh_b = 1$

In Figs. 2.3-2.11, the first-order reflection and transmission coefficients are presented for an obliquely incident wave with wavenumber m (interfacial mode) making an angle θ with the bottom undulation. For these figures, the following dimensionless values are considered: the depth ratio $h_b/h_f = 2$, the amplitude of the sinusoidal ripples $a/h_b = 0.1$,

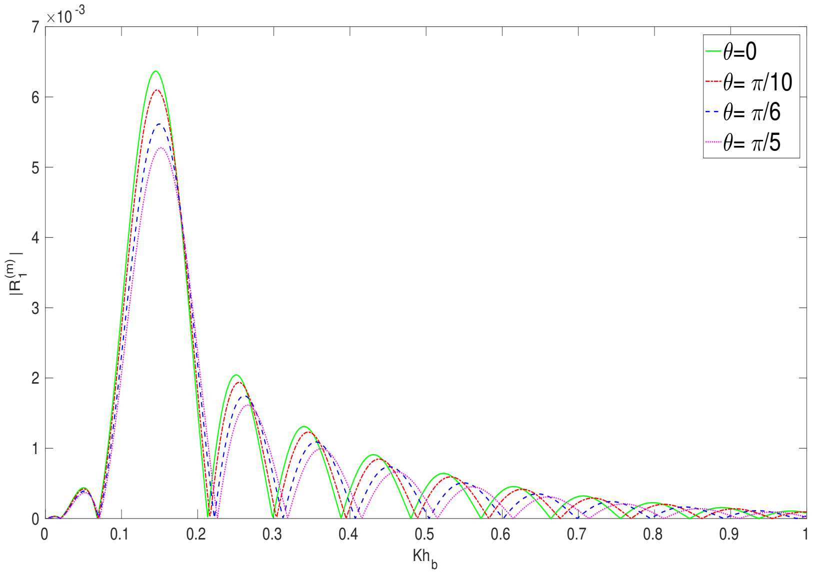

Figure 2.6: Reflection coefficient $|R_1^{(m)}|$ plotted against Kh_b for various angle of incidence θ corresponding to a propagating wave of mode m with $n = 3$, $h_b/h_f = 2$, $a/h_b = 0.1$, $lh_b = 1$, $\rho = 0.5$, $D/h_b^4 = 1$, $\epsilon/h_b = 0.001$

the ripple wavenumber $lh_b = 1$, the density ratio $\rho = 0.5$, and the elastic parameters (except for Figs. 2.5, 2.8, 2.11) $D/h_b^4 = 1$, $\epsilon/h_b = 0.001$. Figures 2.3, 2.6 and 2.9 show curves corresponding to four different angles of incidence, namely, $\theta = 0$, $\pi/10$, $\pi/6$ and $\pi/5$, while the sum of the ripples in the bottom undulation is taken as $n = 3$. Figure 2.3 establishes that the peak values of the reflection coefficient $|r_1^{(m)}|$ for waves with wavenumber m for an obliquely incident wave of wavenumber m decrease as the angle of incidence θ increases. For the normal incidence case ($\theta = 0$), $r_1^{(m)}$ attains the maximum value at 0.15613655, which corresponds to $mh_b \cos\theta = 0.497221$ (when $Kh_b = 0.486$), i.e., for the situation when the ripple wavenumber lh_b of the bed takes a value approximately twice the value of the interface wavenumber $mh_b \cos\theta$ along the x-axis. When $lh_b = 2mh_b \cos\theta$, the peak value is seen to be very high. A similar result is noticed when the angle of incidence θ takes non-zero values. Therefore, it can be inferred that large reflection of the incident waves can be induced by an elastic bottom undulation.

We can further conclude that a resonant interaction occurs between the incident wave and the ripple bed. Figures 2.6 and 2.9, respectively, present the first-order reflection and transmission coefficients of wavenumber M for an obliquely incident wave of wavenumber m which shows that with an increase in the value of θ, both $|R_1^{(m)}|$ and $|T_1^{(m)}|$ decrease. The maximum values of $|R_1^{(m)}|$ and $|T_1^{(m)}|$ are, respectively, found to be 0.006368 and 0.0120003 for the normal incidence. The reflected energy is found to be smaller in comparison with the transmitted energy for both cases of normal and oblique incidences. The non-zero values of both $|R_1^{(m)}|$ and $|T_1^{(m)}|$ tell that exchange of energy from one mode to other mode

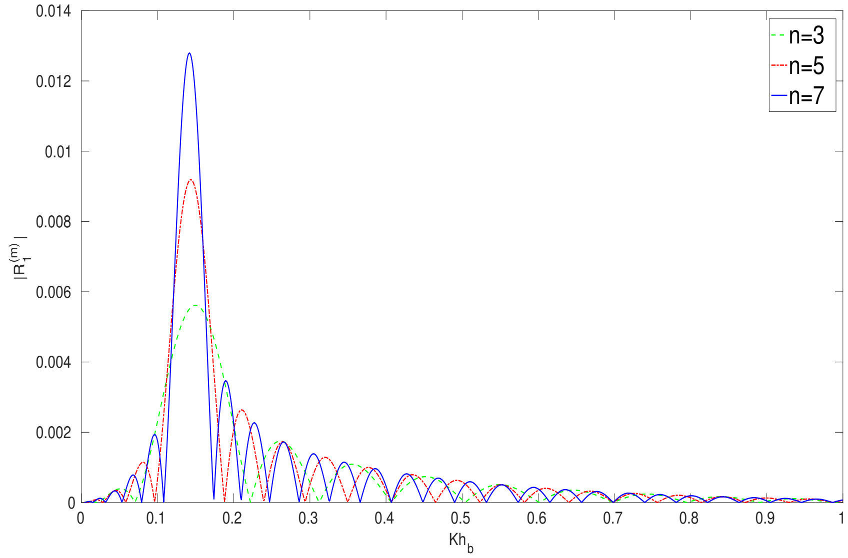

Figure 2.7: Reflection coefficient $|R_1^{(m)}|$ plotted against Kh_b for different number of ripples corresponding to a propagating wave of mode m with $\theta = \pi/6$, $D/h_b^4 = 1$, $\epsilon/h_b = 0.001$, $h_b/h_f = 2$, $\rho = 0.5$, $a/h_b = 0.1$, $lh_b = 1$

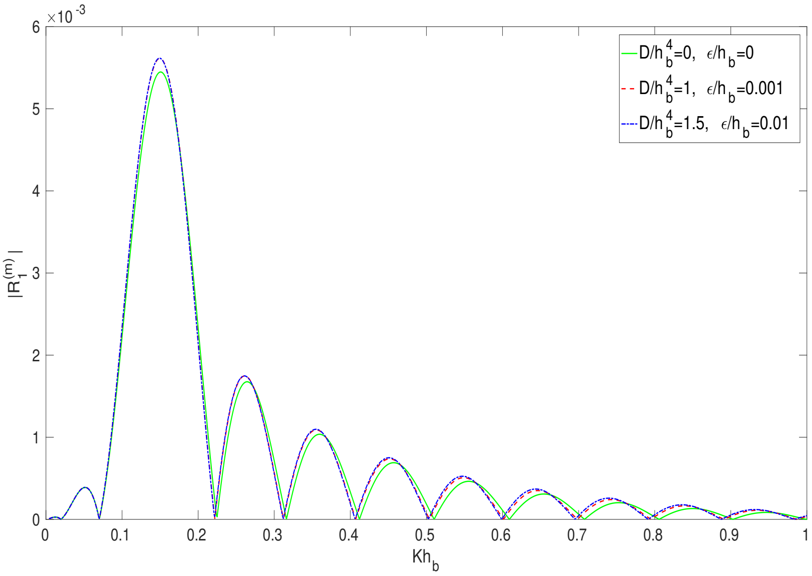

Figure 2.8: Reflection coefficient $|R_1^{(m)}|$ plotted against Kh_b for different elastic parameter values corresponding to a propagating wave of mode m with $\theta = \pi/6, n = 3$, $h_b/h_f = 2$, $\rho = 0.5$, $a/h_b = 0.1$, $lh_b = 1$

is feasible.

The curves presented in Fig. 2.5 for $|r_1^{(m)}|$ correspond to four different sets of values of the elastic parameters ($D/h_b^4 = 0$, $\epsilon/h_b = 0$), ($D/h_b^4 = 1$, $\epsilon/h_b = 0.001$), ($D/h_b^4 = 1.5$, $\epsilon/h_b = 0.01$) and ($D/h_b^4 = 0.01$, $\epsilon/h_b = 0.1$), and those in Figs. 2.8 and 2.11 for

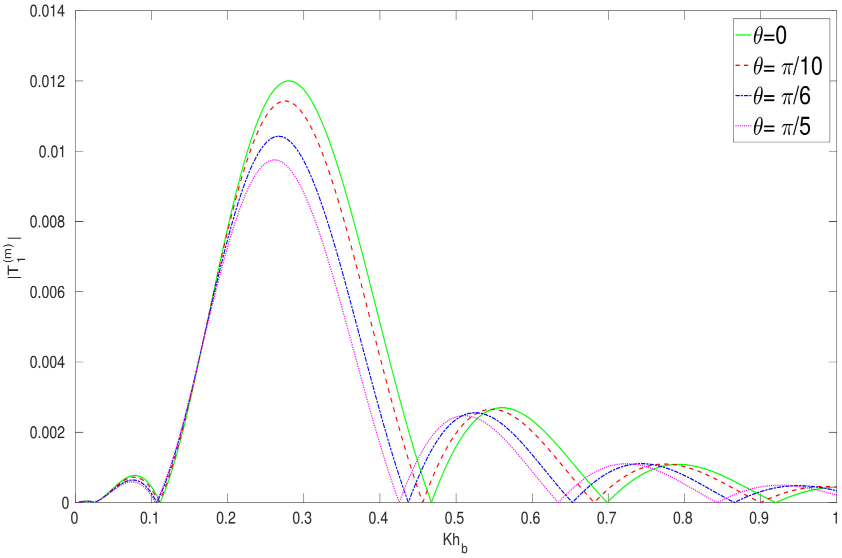

Figure 2.9: Transmission coefficient $|T_1^{(m)}|$ plotted against Kh_b for various angle of incidence θ corresponding to a propagating wave of mode m with $n = 3$, $h_b/h_f = 2$, $a/h_b = 0.1$, $lh_b = 1$, $\rho = 0.5$, $D/h_b^4 = 1$, $\epsilon/h_b = 0.001$

$|R_1^{(m)}|$ and $|T_1^{(m)}|$, respectively, correspond to three different sets of values of the elastic parameters $(D/h_b^4 = 0,\ \epsilon/h_b = 0)$, $(D/h_b^4 = 1,\ \epsilon/h_b = 0.001)$ and $(D/h_b^4 = 1.5,\ \epsilon/h_b = 0.01)$ with $n = 3$ and $\theta = \pi/6$, respectively. Figure 2.5 shows that, with an increase in the value of the elastic parameters of the sea-bed, the reflection coefficient $|r_1^{(m)}|$ increases. It is noticed from Figs. 2.8 and 2.11 that an increase in the value of elastic parameters D/h_b^4, ϵ/h_b results in increasing values of reflection coefficient $|R_1^{(m)}|$ and the transmission coefficient $|T_1^{(m)}|$. But the non-zero values of both $|R_1^{(m)}|$ and $|T_1^{(m)}|$ with wavenumber M for various elastic parameters establish that energy conversion from one wavenumber to the other is going to happen. Figures 2.5 and 2.8 show that the reflection coefficient due to the reflected wave of wavenumber M is much less than that of the reflected wave with wavenumber m. Another observation is that, with an increase in the values of the elastic parameters, the rate of change of the coefficients is higher for both the modes. It implies that when the incident wave encounters the undulating elastic bottom, the energy involved with reflection and transmission is quite sensitive to the change in the values of the elastic parameter.

In Figs. 2.4, 2.7 and 2.10, the fixed angle of incidence is taken as $\theta = \pi/6$, the values of the elastic parameters are considered as $D/h_b^4 = 1$, $\epsilon/h_b = 0.001$ and the curves are plotted for different number of bed ripples. It clearly establishes an increase in the peak values of the reflection coefficient $|r_1^{(m)}|$ of waves of wavenumber m for an incident wave of wavenumber m striking the undulation obliquely, as shown in Fig. 2.4, corresponding to an increase in the number of ripples. It is evident from Figs. 2.7 and 2.10 that there is

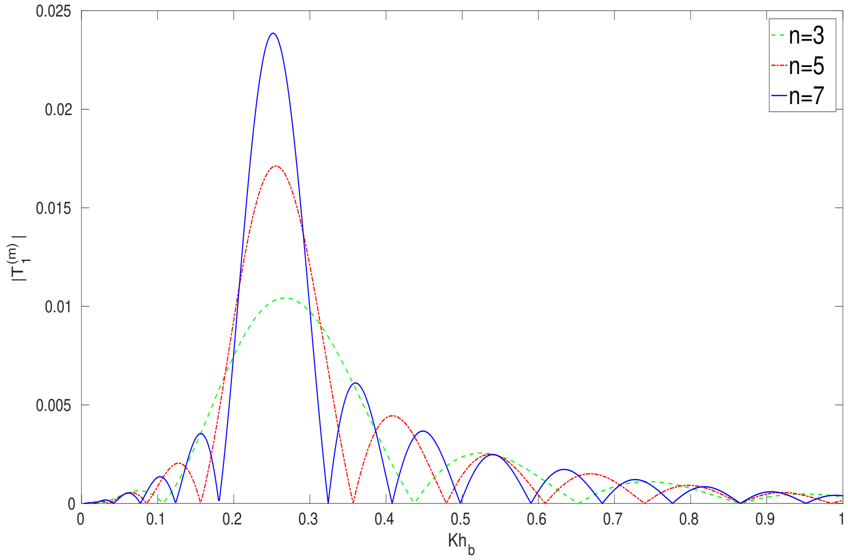

Figure 2.10: Transmission coefficient $|T_1^{(m)}|$ plotted against Kh_b for different number of ripples corresponding to a propagating wave of mode m with $\theta = \pi/6$, $D/h_b^4 = 1$, $\epsilon/h_b = 0.001$, $h_b/h_f = 2$, $\rho = 0.5$, $a/h_b = 0.1$, $lh_b = 1$

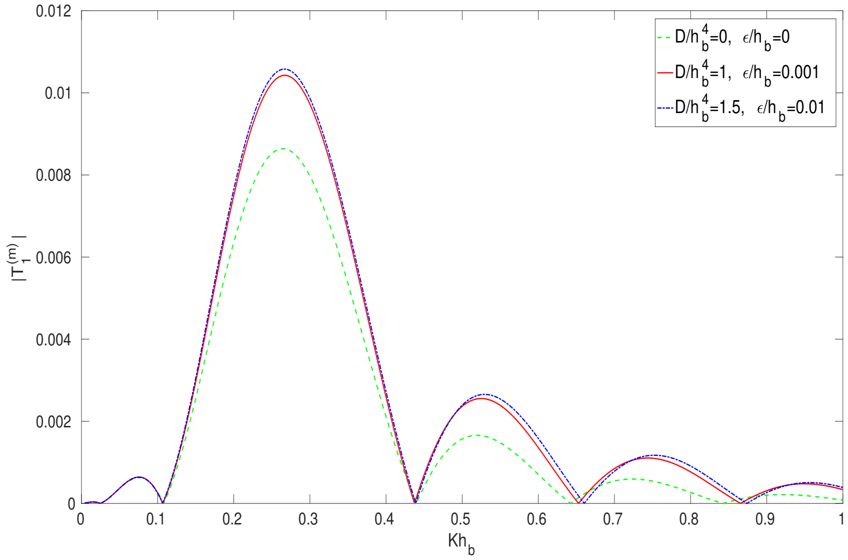

Figure 2.11: Transmission coefficient $|T_1^{(m)}|$ plotted against Kh_b for different elastic parameter values corresponding to a propagating wave of mode m with $\theta = \pi/6, n = 3$, $h_b/h_f = 2$, $\rho = 0.5$, $a/h_b = 0.1$, $lh_b = 1$

an increase in the peak values of the reflection and transmission coefficients of the waves of wavenumber M, for an obliquely incident wave of wavenumber m, corresponding to an increase in the number of ripples. It can be seen that when the number of bed ripples increases, then the reflection and transmission coefficients become unbounded for some specific values of Kh_b. The curve plotted for $n = 7$ shows that the maximum value of $|r_1^{(m)}|$ is attained at 0.332546 which corresponds to $mh_b \cos\theta = 0.498156$ (when $Kh_b = 0.558$), that is, for the situation when the ripple wavenumber lh_b of the bottom undulation takes a value approximately twice of that of the interface wavenumber $mh_b \cos\theta$. Similar observations can be recorded for the coefficients $|R_1^{(m)}|$ and $|T_1^{(m)}|$. This phenomenon, as mentioned earlier also, is called Bragg resonance. With an increase in the number of ripples, the reflection coefficient $|R_1^{(m)}|$ and transmission coefficient $|T_1^{(m)}|$, with respect to Kh_b, exhibit a significant oscillatory behaviour with an increasing number of zeros. This oscillatory behaviour takes place because the incident wave interacts with the undulating elastic bottom, free-surface and the interface multiple times.

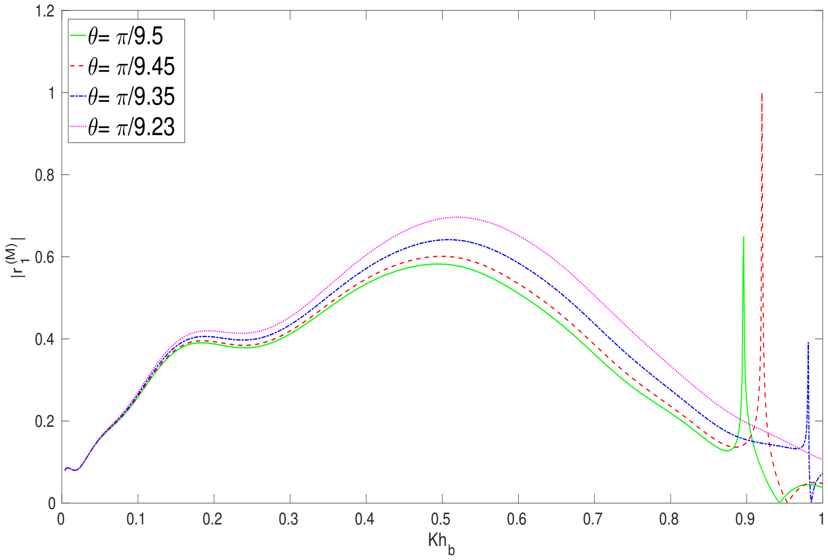

Figure 2.12: Reflection coefficient $|r_1^{(M)}|$ plotted against Kh_b for various angle of incidence θ corresponding to a propagating wave of mode M with $n = 3$, $\rho = 0.5$, $h_b/h_f = 2$, $a/h_b = 0.1$, $lh_b = 1$, $D/h_b^4 = 1$, $\epsilon/h_b = 0.001$

The study of an oblique incident wave of wavenumber M (free surface mode) presents an intriguing case since it establishes the existence of cut-off frequencies below which it is not possible for energy conversion to take place from one wavenumber to the other. Correspondingly, Figs. 2.12-2.20 present the coefficients $|r_1^{(M)}|$, $|R_1^{(M)}|$ and $|t_1^{(M)}|$ plotted against Kh_b with $\rho = 0.5$, $h_b/h_f = 2$, $a/h_b = 0.1$, $lh_b = 1$ and the values of the elastic parameters as $D/h_b^4 = 1$, $\epsilon/h_b = 0.001$ (except for Figs. 2.14, 2.17, 2.20). Different curves in Figs. 2.12 and 2.18 show $|r_1^{(M)}|$ and $|t_1^{(M)}|$ plotted against Kh_b for different values of $\theta = \pi/9.5$, $\pi/9.45$, $\pi/9.35$ and $\pi/9.23$ with $n = 3$. When $\theta = \pi/9.23$, which is just marginally greater than the critical angle $\theta_c \approx 0.339718$ (in radian) $\approx \pi/9.24$, it is found that there is no propagation of wave of wavenumber m in the fluid. In Figs. 2.12 and 2.18, the cut-off frequencies considered are $K_c h_b \approx 0.896, 0.92$ and 0.981, corresponding

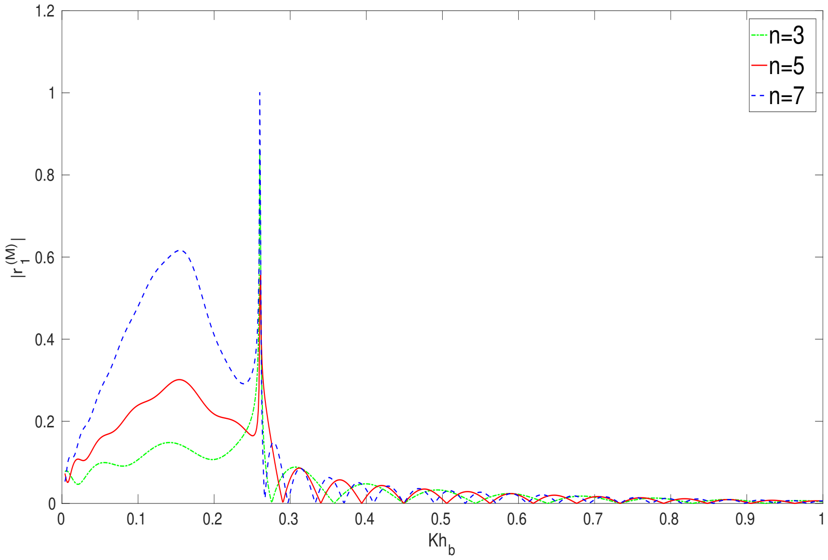

Figure 2.13: Reflection coefficient $|r_1^{(M)}|$ plotted against Kh_b for different number of ripples corresponding to a propagating wave of mode M with $D/h_b^4 = 1$, $\epsilon/h_b = 0.001$, $\theta = \pi/15$, $\rho = 0.5,\ h_b/h_f = 2,\ a/h_b = 0.1,\ lh_b = 1$

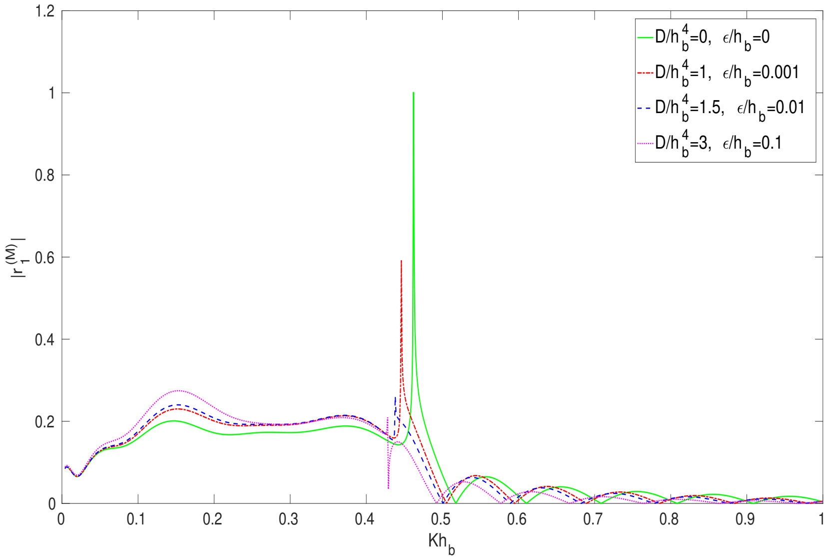

Figure 2.14: Reflection coefficient $|r_1^{(M)}|$ plotted against Kh_b for different elastic parameter values corresponding to a propagating wave of mode M with $\theta = \pi/12,\ n = 3,\ \rho = 0.5,\ h_b/h_f = 2,\ a/h_b = 0.1,\ lh_b = 1$

to the incident angles $\theta = \pi/9.5,\ \pi/9.45$, and $\pi/9.35$, respectively. For these angles and for all frequency values greater than the cut-off frequency, energy conversion takes place from one mode to the other. For each curve that corresponds to $\theta = \pi/9.5,\ \pi/9.45$, and $\pi/9.35$, there is only one spike because of the presence of only one cut-off frequency.

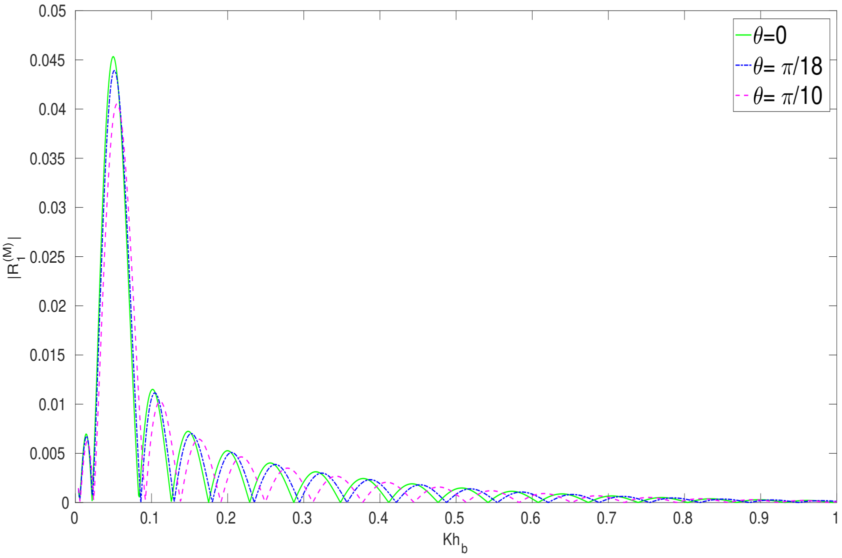

Figure 2.15: Reflection coefficient $|R_1^{(M)}|$ plotted against Kh_b for various angle of incidence θ corresponding to a propagating wave of mode M with $n = 3$, $\rho = 0.5$, $h_b/h_f = 2$, $a/h_b = 0.1$, $lh_b = 1$, $D/h_b^4 = 1$, $\epsilon/h_b = 0.001$

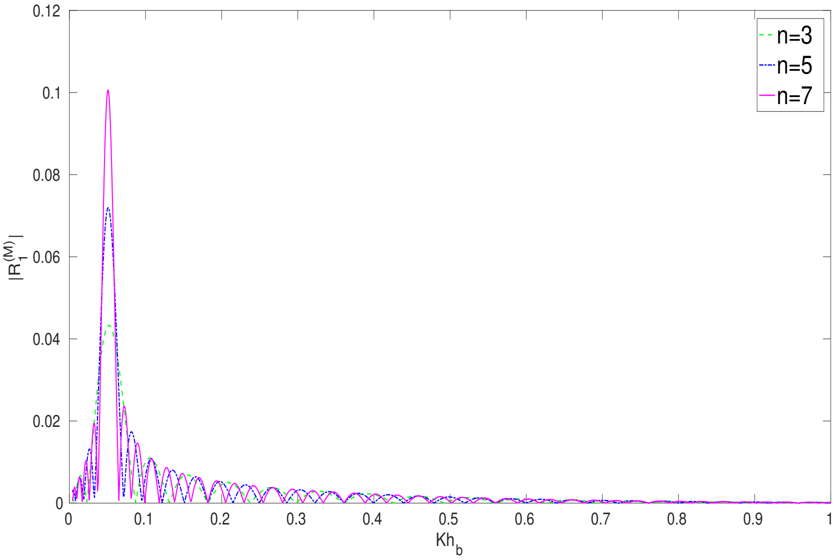

Figure 2.16: Reflection coefficient $|R_1^{(M)}|$ plotted against Kh_b for different number of ripples corresponding to a propagating wave of mode M with $D/h_b^4 = 1$, $\epsilon/h_b = 0.001$, $\theta = \pi/15$, $\rho = 0.5$, $h_b/h_f = 2$, $a/h_b = 0.1$, $lh_b = 1$

With θ taking the value $\theta = \pi/9.23$, which is slightly greater than the critical angle for the given values of Kh_b, no spike in the curve is observed. These two figures establish that, corresponding to a particular frequency just below the cut-off frequency, there occur maximum reflection and maximum transmission of the incident wave of wavenumber M.

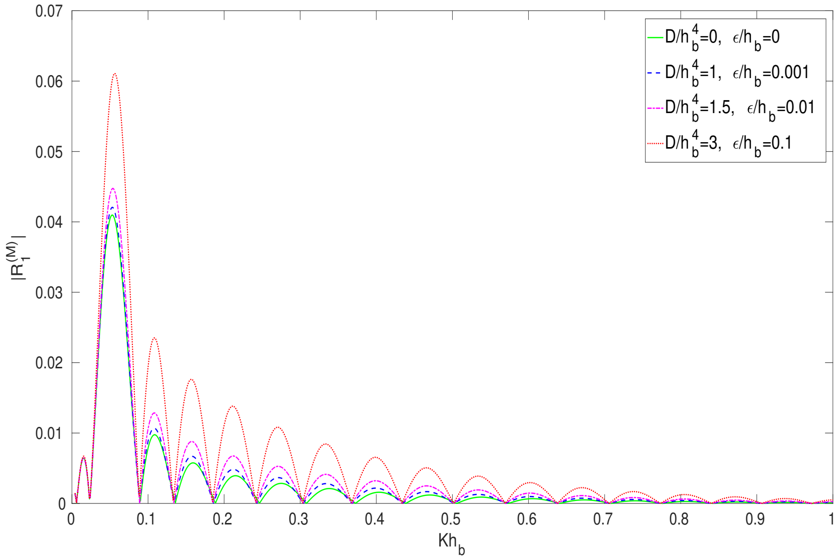

Figure 2.17: Reflection coefficient $|R_1^{(M)}|$ plotted against Kh_b for different elastic parameter values corresponding to a propagating wave of mode M with $\theta = \pi/12$, $n = 3$, $\rho = 0.5$, $h_b/h_f = 2$, $a/h_b = 0.1$, $lh_b = 1$

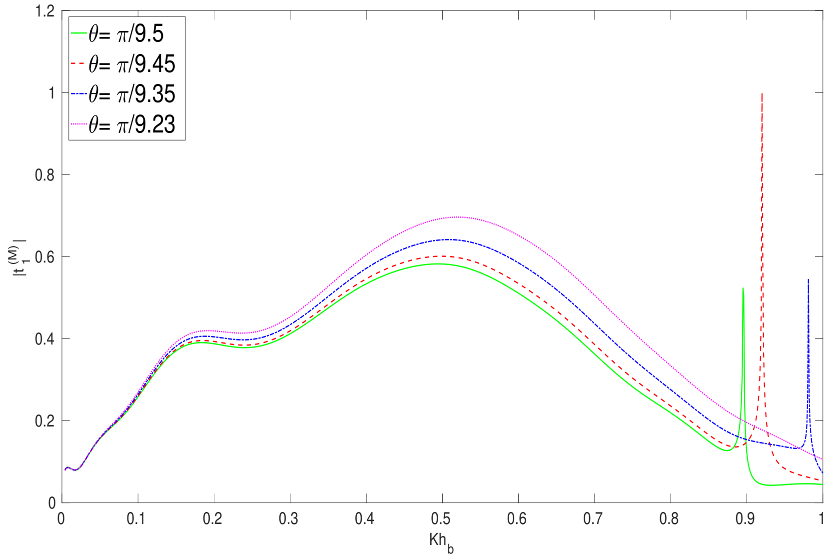

Figure 2.18: Transmission coefficient $|t_1^{(M)}|$ plotted against Kh_b for various angle of incidence θ corresponding to a propagating wave of mode M with $n = 3$, $\rho = 0.5$, $h_b/h_f = 2$, $a/h_b = 0.1$, $lh_b = 1$, $D/h_b^4 = 1$, $\epsilon/h_b = 0.001$

The curves in Fig. 2.15 are plotted for $\theta = 0$, $\pi/18$ and $\pi/10$ with $n = 3$. Whatever may the incident angle be, the first-order reflection coefficient $|R_1^{(M)}|$ does not exhibit spike type of curves as observed in Figs. 2.12, 2.13, 2.14 because of the occurrence of reflection of waves for the free surface mode due to an oblique wave of wavenumber M

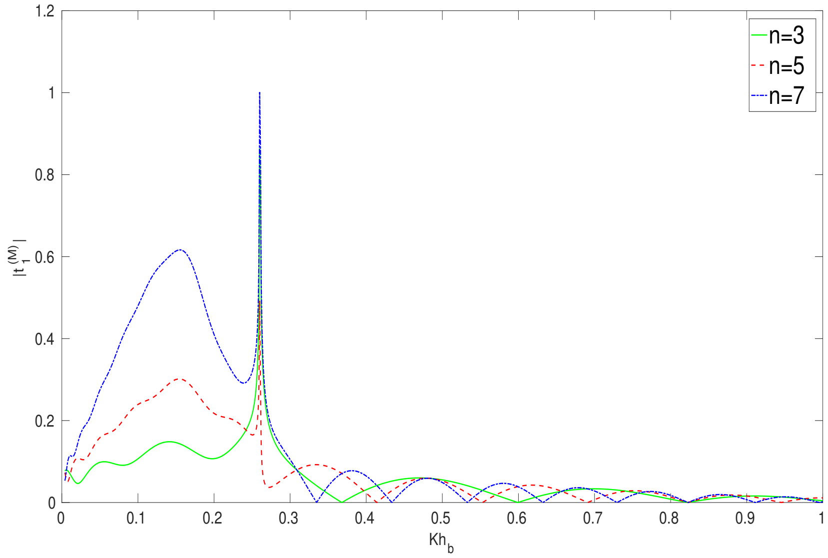

Figure 2.19: Transmission coefficient $|t_1^{(M)}|$ plotted against Kh_b for different number of ripples corresponding to a propagating wave of mode M with $D/h_b^4 = 1$, $\epsilon/h_b = 0.001$, $\theta = \pi/15$, $\rho = 0.5$, $h_b/h_f = 2$, $a/h_b = 0.1$, $lh_b = 1$

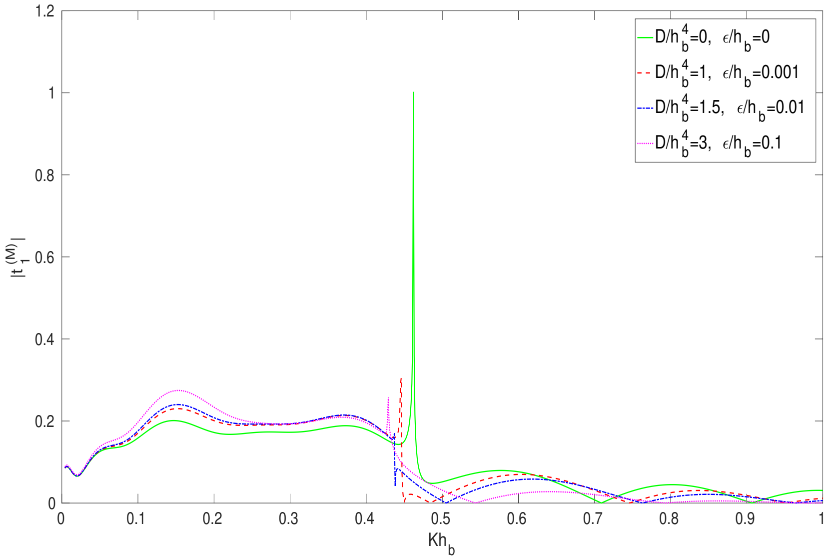

Figure 2.20: Transmission coefficient $|t_1^{(M)}|$ plotted against Kh_b for different elastic parameter values corresponding to a propagating wave of mode M with $\theta = \pi/12$, $n = 3$, $\rho = 0.5$, $h_b/h_f = 2$, $a/h_b = 0.1$, $lh_b = 1$

incident on the undulation. Figure 2.15 shows that, with the angle of incidence increasing, a reduction in the peak value of the first-order reflection coefficient $|R_1^{(M)}|$ occurs.

The curves in Figs. 2.13, 2.16 and 2.19 are plotted for different numbers of bed ripples with $\theta = \pi/15$. It is clear from Fig. 2.16 that, if the number of ripples increases, the peak value of the reflection coefficient $|R_1^{(M)}|$ increases. Figures 2.13 and 2.19, respectively, establish the fact that there exist cut-off values for reflection and transmission of waves which results in the occurrence of conversion of energy from mode M to mode m corresponding to different values of n.

The curves in Figs. 2.14, 2.17 and 2.20 are plotted for four different sets of elastic parameters $(D/h_b^4 = 0,\ \epsilon/h_b = 0)$, $(D/h_b^4 = 1,\ \epsilon/h_b = 0.001)$, $(D/h_b^4 = 1.5,\ \epsilon/h_b = 0.01)$ and $(D/h_b^4 = 3,\ \epsilon/h_b = 0.1)$, with $n = 3$ and $\theta = \pi/12$. Figure 2.17 clearly shows that, with an increase in the value of the elastic parameters, the peak values of $|R_1^{(M)}|$ also show an upward trend. The spikes noticed in Figs. 2.14 and 2.20 indicate the presence of cut-off frequency. Figures 2.14 and 2.20 establish that, with an increase in the values of the elastic parameters, a subsequent increase in the peak values of reflection coefficient $|r_1^{(M)}|$ and transmission coefficient $|t_1^{(M)}|$ is also noticed. A clear observation is that, for both free surface and interfacial modes, increase in the values of both reflection and transmission coefficients take place in response to the increase in the values of the elastic parameters of the bed. This may have resulted because of the interaction of waves in free surface mode and interfacial mode with the elastic sea-bed.

2.7 Energy identities

Energy conservation in the absence of dissipation mechanisms is an important feature of the model deployed in any problem. It is expressed through the energy conservation relation or energy identity which is, in this case, connected to the reflection and transmission coefficients. It can, furthermore, be used as a verification test on the solution methodology adopted for any particular problem. For a two-layer fluid, there exist two energy balance relations satisfied by the reflection and transmission coefficients corresponding to the incident waves of two different wave modes. For the present problem, modified Green's integral theorem is used to derive the energy identities. A similar kind of analysis as in Das et al. [24], Panda and Martha [74] and Sarangi and Mohapatra [84] is followed here to determine these identities.

When the incident wave is of mode m, we acquire the energy balance relation involving the reflection coefficients $r^{(m)}$and $R^{(m)}$ and the transmission coefficients $t^{(m)}$ and $T^{(m)}$ as (Das et al. [24])

$$|r^{(m)}|^2+|t^{(m)}|^2+J\Big(|R^{(m)}|^2+|T^{(m)}|^2\Big) = 1, \tag{2.82}$$

where $J = \dfrac{J_M}{J_m}$ with

$$J_u = \mathrm{i}\Big[Du^5 + (1-\epsilon K)u\Big] \times \Big[\rho \int_{-h_f}^{0} [g(u,y)]^2 dy + \int_0^{h_b} [f(u,y)]^2 dy\Big], \quad u = m, M, \tag{2.83}$$

with $g(u, y) = u \cosh u(y + h_f) - K \sinh u(y + h_f)$, and $f(u, y)$ given by (2.9).

Similarly, when the incident wave is of mode M, the energy balance relation involving the coefficients $r^{(M)}, R^{(M)}, t^{(M)}$ and $T^{(M)}$ is acquired as

$$\frac{1}{J}\Big(|r^{(M)}|^2+|t^{(M)}|^2\Big) + |R^{(M)}|^2+|T^{(M)}|^2 = 1. \tag{2.84}$$

Kh_b	$\lvert r^{(m)}\rvert$	$\lvert R^{(m)}\rvert$	$\lvert t^{(m)}\rvert$	$\lvert T^{(m)}\rvert$	$\lvert r^{(m)}\rvert^2+\lvert t^{(m)}\rvert^2 +J\Big(\lvert R^{(m)}\rvert^2+\lvert T^{(m)}\rvert^2\Big)$
0.1	1.0599e − 02	2.9596e − 03	1.0000	4.4570e − 04	0.99910
0.2	1.3508e − 02	1.5405e − 03	1.0000	7.8157e − 03	0.98887
0.25	3.0110e − 02	2.0435e − 03	1.0000	1.1367e − 02	0.96882
0.35	2.1029e − 02	1.2269e − 03	1.0000	9.1941e − 03	0.96289
0.45	1.4209e − 01	7.2684e − 04	1.0000	1.1396e − 03	1.01880
0.5	1.5405e − 01	4.4386e − 04	1.0000	1.5918e − 03	1.02105
0.6	4.8417e − 02	3.9511e − 04	1.0000	2.3349e − 03	0.99350
0.9	1.0529e − 02	1.4372e − 04	1.0000	2.1288e − 04	0.99980
1	7.6540e − 03	8.0249e − 05	1.0000	4.3809e − 04	1.00040

Table 2.1: Numerical values of all reflection and transmission coefficients for energy identity relation (2.82)

When the incident wave is of mode m, the numerical values of $r^{(m)}, R^{(m)}, t^{(m)}, T^{(m)}$ and subsequently of the expression $|r^{(m)}|^2+|t^{(m)}|^2+J\Big(|R^{(m)}|^2+|T^{(m)}|^2\Big)$ are presented for various values of Kh_b in Table 2.1. In this case, the following values are considered: angle of incidence $\theta = 0$, depth ratio $h_b/h_f = 2$, amplitude of the sinusoidal ripples $a/h_b = 0.1$, ripple wavenumber $lh_b = 1$, total number of ripples $n = 3$, density ratio $\rho = 0.5$, and elastic parameters $D/h_b^4 = 1$, $\epsilon/h_b = 0.001$. It is noticed from the last column of Table 2.1 that the numerical values of $|r^{(m)}|^2+|t^{(m)}|^2+J\Big(|R^{(m)}|^2+|T^{(m)}|^2\Big)$ corresponding to various values of Kh_b is nearly equal to 1. This, consequently, implies that the energy balance relation or energy identity given in (2.82) is satisfied almost accurately.

Similarly, when the incident wave is of mode M, the numerical values of $r^{(M)}$, $R^{(M)}$, $t^{(M)}$, $T^{(M)}$ and subsequently of the expression $\frac{1}{J}\Big(|r^{(M)}|^2+|t^{(M)}|^2\Big) + |R^{(M)}|^2+|T^{(M)}|^2$ are presented for various values of Kh_b in Table 2.2. In this case, we consider the same set of

Kh_b	$\lvert r^{(M)}\rvert$	$\lvert R^{(M)}\rvert$	$\lvert t^{(M)}\rvert$	$\lvert T^{(M)}\rvert$	$\frac{1}{J}\left(\lvert r^{(M)}\rvert^2+\lvert t^{(M)}\rvert^2\right)$ $+\lvert R^{(M)}\rvert^2+\lvert T^{(M)}\rvert^2$
0.1	2.9969e − 01	1.1440e − 02	1.5493e − 01	1.0000	0.99100
0.2	1.3648e − 01	5.2674e − 03	2.3661e − 01	1.0000	0.99961
0.25	2.2163e − 01	3.8097e − 03	1.0161e − 01	1.0000	0.99976
0.35	1.6175e − 01	2.5590e − 04	4.5376e − 01	1.0000	0.99946
0.45	1.1101e − 01	1.7702e − 03	8.5036e − 02	1.0000	0.99998
0.5	7.2753e − 02	1.3814e − 03	1.3592e − 01	1.0000	0.99998
0.6	7.4022e − 02	3.7847e − 04	2.4389e − 01	1.0000	1.00000
0.9	3.6458e − 02	2.8533e − 04	2.8776e − 02	1.0000	1.00000
1	2.2467e − 02	4.4955e − 05	6.0989e − 02	1.0000	1.00000

Table 2.2: Numerical values of all reflection and transmission coefficients for energy identity relation (2.84)

values of the parameters listed for Table 2.1. It is noticed from the last column of Table 2.2 that the numerical value of $\frac{1}{J}\left(|r^{(M)}|^2+|t^{(M)}|^2\right)+|R^{(M)}|^2+|T^{(M)}|^2$ corresponding to various values of Kh_b is almost equal to 1. That implies that the energy balance relation or energy identity given in (2.84) is satisfied almost accurately.

2.8 Conclusion

The work in this chapter takes up the problem of oblique wave scattering by a small elastic bottom undulation in a two-layer fluid which has a free surface and uses linear water wave theory to find the solution. Considering Euler-Bernoulli beam equation, the elastic sea-bed is approximated as a thin elastic plate, whose thickness is assumed to be much smaller compared to its horizontal length. Consequently, the sea-bed can be idealized as a thin, linear elastic plate of uniform mass density and thickness. Under these circumstances, corresponding to any given frequency, there exist propagating waves at two different wavenumbers: the one with the smaller wavenumber corresponds to the interfacial wave mode and the other with the higher wavenumber corresponds to the free surface mode. Applying perturbation technique in association with Fourier transform, the first-order correction to the velocity potentials, the reflection and transmission coefficients are evaluated. The significance of the roles of different physical parameters on wave energy transfer from one mode to the other mode is demonstrated through graphical representation. The present work establishes the occurrence of the complex resonant interactions involving wave propagation over a rippled bottom due to free surface and interfacial modes. It is observed that the energy due to reflection and transmission corresponding to both free surface mode and interfacial mode increases when an increase in the elasticity of the bed is affected. A conclusion of significant consequence is that transfer of the incident wave energy of the smaller mode (interfacial mode) to the reflected and transmitted energy of the higher mode (free surface mode) is feasible for all possible incident angles. On the other hand, the energy transfer from the higher mode to the lower mode is possible only for the case when the angle of incidence is slightly less than the critical angle. One very important conclusion is that the energy balance equations involving the two reflection coefficients and two transmission coefficients for each mode are found to be satisfied almost accurately. The expectation here is that the results obtained in this work can be suitably used for a wider set of water wave scattering problems that occur in ocean and coastal engineering and any other discipline where a flexible sea-bed is considered. To sum it up, the importance of such an investigation stems from their applications in the construction of underwater pipe bridges, wave power devices, very large floating structures like floating oil storage bases, mobile offshore base for utilization of ocean space for various military operations, etc., where the significance of the free vibration due to the presence of the elastic sea-bed is usually taken into account. This type of investigation assumes immense significance since, while considering water waves passing over a deformable bottom, the constant depth water bounded below by a perfectly elastic soil of infinite depth has a shear which represents a soft marine sediment. A significant change in the wave characteristics is observed due to the elasticity of the bottom when the wave propagates over a deformable bottom. It has an immense impact on the water wave kinematics and dynamics in addition to demonstrating the elastic behaviour of the soil. In this context, study of wave propagation in a two-layer fluid over an undulating elastic bed is deemed essential in order to take into account the properties of soil beneath a horizontal sea-bed. It is expected that such problems with a deformable bed, inclusive of elasticity, will enable researchers to take up problems which take into account the characteristics of the infinite depth of soil beneath the bed, and the present study can probably provide the necessary background.

CHAPTER 3

PROPAGATION OF OBLIQUE WAVES OVER AN ELASTIC BOTTOM UNDULATION IN A TWO-LAYER FLUID FLOW THROUGH A CHANNEL

3.1 Introduction

In this chapter, a hydrodynamic model, with the incorporation of elasticity, is considered to study oblique incident waves propagating over a small undulation on an elastic sea-bed in a two-layer fluid, where the upper layer fluid is bounded above by a rigid lid, which approximates the free surface. The behaviour and properties of the roots of the dispersion relation are analyzed using counting argument and a contour plot. The same mathematical procedure, as applied in Chapter 2, is followed here to solve the boundary value problem. To validate the theory developed, two particular undulating bottom topography are taken up as examples in order to evaluate the hydrodynamic (reflection as well as transmission) coefficients which are represented through graphs. When the ratio of the wavenumber of the undulating bed and the wavenumber of the incident wave approaches two, the theory predicts the existence of resonance between the undulating elastic sea-bed and the interface of the layers.

3.2 Problem formulation

Small amplitude water waves under the action of gravity is considered to propagate in an inviscid, incompressible, immiscible two-layer fluid, which is bounded above by a rigid lid, over an elastic undulating topography for an irrotational motion. Due to the fact that the contribution of surface tension is not very significant, it is not taken into account in the formulation of the present problem. Euler-Bernoulli beam equation is considered here to approximate the elastic sea-bed as a thin elastic plate, as has already been considered in Chapter 2.

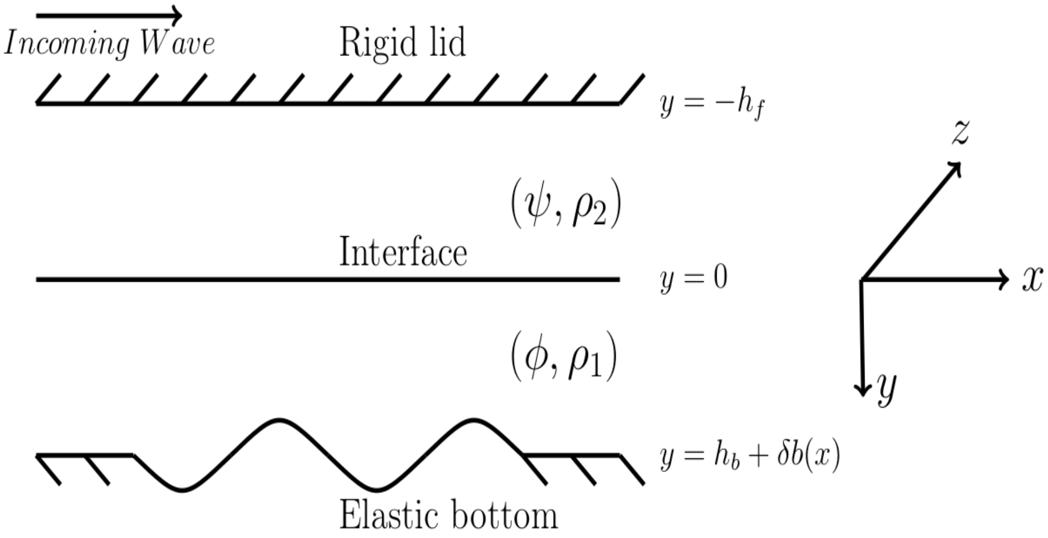

Figure 3.1: Schematic diagram of the problem

Taking a Cartesian coordinate system with the y-axis pointing vertically downward, and $y = -h_f$ and $y = 0$, respectively, representing the position of the horizontal rigid lid and the undisturbed interface, a small undulation $y = h_b + \delta b(x)$ on the elastic sea-bed, as described in Chapter 2, is considered. Assuming linear water wave theory and taking all these assumptions into account, the time-harmonic velocity potentials in the lower layer fluid of density ρ_1 and the upper layer fluid of density $\rho_2(<\rho_1)$ are, respectively, expressed as $\Phi(x, y, z, t) = \mathrm{Re}\{\phi(x, y) \exp(\mathrm{i}\gamma z) \exp(-\mathrm{i}\omega t)\}$ and $\Psi(x, y, z, t) = \mathrm{Re}\{\psi(x, y) \exp(\mathrm{i}\gamma z) \exp(-\mathrm{i}\omega t)\}$ for oblique waves.

The boundary value problems for potentials ψ and ϕ are set up as follows with the modified Helmholtz equation governing the process:

$$(\nabla^2_{x,y} - \gamma^2)\psi = 0 \text{ in the upper fluid,} \tag{3.1}$$

$$(\nabla^2_{x,y} - \gamma^2)\phi = 0 \text{ in the lower fluid.} \tag{3.2}$$

The linearized boundary condition at the rigid lid is

$$\frac{\partial \psi}{\partial y} = 0 \quad \text{on} \quad y = -h_f. \tag{3.3}$$

Let $\rho = \rho_2/\rho_1$. Then the matching conditions at the mean interface $y = 0$ have the following forms:

$$\begin{aligned} \frac{\partial \phi}{\partial y} &= \frac{\partial \psi}{\partial y}, \quad (3.4)\\ \rho\left(K\psi + \frac{\partial \psi}{\partial y}\right) &= K\phi + \frac{\partial \phi}{\partial y}, \quad (3.5)\end{aligned}$$

where $K = \omega^2/g$ and $\omega = 2\pi/T$. The conditions (3.4) and (3.5) ensure that the normal velocity and pressure, respectively, maintain continuity at the interface. The linearized boundary condition on the undulating elastic sea-bed is given by Eq. (2.6).

By utilizing the knowledge of linear theory applicable for a two-layer fluid, the representation of a train of progressive waves propagating along the positive x-direction is given by

$$\begin{aligned} \psi(x,y) &= -\exp(\mathrm{i}x\sqrt{u^2-\gamma^2})\cosh u(y+h_f) \quad \text{in} \quad -h_f \le y \le 0, \quad (3.6)\\ \phi(x,y) &= \exp(\mathrm{i}x\sqrt{u^2-\gamma^2}) f(u,y) \quad \text{in} \quad 0 \le y \le h_b, \quad (3.7)\end{aligned}$$

where $f(u,y) = \dfrac{\sinh uh_f[K\sinh u(h_b-y) + (Du^4+1-\epsilon K)u\cosh u(h_b-y)]}{K\cosh uh_b + (Du^4+1-\epsilon K)u\sinh uh_b}$, (3.8)

with the wave obliquely incident at an angle θ to the undulating elastic bed; $\gamma = u\sin\theta$, and u satisfying the following dispersion relation:

$$\triangle(u) \equiv 0, \quad \text{with} \quad (3.9)$$

$$\begin{aligned} \triangle(u) &= K^2\sinh uh_b\sinh uh_f + Ku(Du^4+1-\epsilon K)\cosh uh_b\sinh uh_f + \rho K^2 u\cosh uh_b\\ &\times\cosh uh_f + \rho Ku(Du^4+1-\epsilon K)\sinh uh_b\cosh uh_f - Ku\cosh uh_b\sinh uh_f - u^2\\ &\times(Du^4+1-\epsilon K)\sinh uh_b\sinh uh_f + \rho uK\cosh uh_b\sinh uh_f + \rho u^2(Du^4+1-\epsilon K)\\ &\times\sinh uh_b\sinh uh_f. \quad (3.10)\end{aligned}$$

Regarding the roots of dispersion relation (3.9), it may be noted that dispersion relation (3.9) gives rise to the following roots: (i) a positive real root μ corresponding to the propagating modes, (ii) two pairs of complex conjugate roots, in the form $p \pm \mathrm{i}q$ and $-(p \pm \mathrm{i}q)$ corresponding to the non-propagating modes, and (iii) an infinitely many purely imaginary roots corresponding to the evanescent modes. It may be noted that the negatives of all these roots also happen to be roots of (3.9) since they are also wavenumbers representing the waves traveling in the other direction. Due to the fact that the dispersion relation (3.9) has exactly one positive real root, it implies that there exists only one wave mode propagating along the positive x-direction at the interface (say, interfacial mode). Table 3.1 clearly shows that the value of the wavenumber μ increases steadily corresponding to an increase in the values of the elastic parameters of the ocean bed for different values of Kh_b. This table shows the values of μ for some selected values of Kh_b corresponding to various sets of values of the elastic parameters.

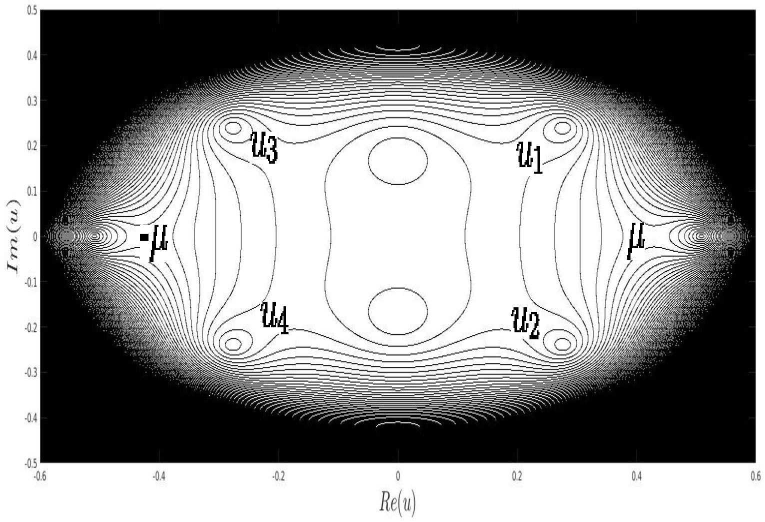

Figure 3.2: Roots of dispersion relation (3.9) with $h_b/h_f = 2$, $E = 6 \times 10^9$ Pa, $\nu = 0.3$, $\rho_1 = 1025$ kg/m^3, $\rho_0 = 2650$ kg/m^3, $h_0 = 0.1$ m, $g = 9.81$ m/s^2 and $T = 8$ s

Kh_b	$D/h_b^4 = 0$, $\epsilon/h_b = 0$	$D/h_b^4 = 1$, $\epsilon/h_b = 0.001$	$D/h_b^4 = 1.5$, $\epsilon/h_b = 0.01$	$D/h_b^4 = 3$, $\epsilon/h_b = 0.1$
0.15	0.794409	0.802748	0.805548	0.811021
0.25	1.083073	1.100592	1.103724	1.108109
0.35	1.351824	1.372819	1.374777	1.377105
0.45	1.614651	1.634456	1.635480	1.636609

Table 3.1: Values of the wavenumber μ corresponding to various elastic parameter values and Kh_b

It is obvious that dispersion relation (3.9) is complex in nature and therefore, its roots are computed numerically with the help of contour plots in order to understand the behaviours of the wavenumbers (Fig. 3.2). For computational purpose, the values of different physical parameters are considered as follows: depth ratio $h_b/h_f = 2$, time period $T = 8$ s, lower layer fluid density $\rho_1 = 1025$ kg/m^3, elastic material density of the bottom $\rho_0 = 2650$ kg/m^3, density ratio of the layers as $\rho = 0.5$, Young's modulus of the elastic material $E = 6 \times 10^9$ Pa, Poisson's ratio $\nu = 0.3$, thickness of the elastic plate $h_0 = 0.1$ m, $g = 9.81$ m/s^2. Here the nature of the roots of (3.9) is found by following a simple counting argument which was followed by Fox and Squire [32]. Figure 3.2 presents the behaviour of the roots of the dispersion relation for the present problem and it shows that two real roots, denoted by $\pm\mu$, lie on the real axis and two pairs of complex roots, which occur as positive and negative of a complex conjugate pair, namely, u_1, u_2, u_3, u_4, are located in such a way that there is one root in each of the quadrants. Table 3.2 presents different values of four complex roots u_1, u_2, u_3, u_4 corresponding to various elastic parameter values.

u_i	$E = 6 \times 10^9$ Pa	$E = 7 \times 10^9$ Pa	$E = 8 \times 10^9$ Pa
u_1	0.277295 + 0.240049i	0.268048 + 0.230356i	0.260373 + 0.222304i
u_2	0.277295 − 0.240049i	0.268048 − 0.230356i	0.260373 − 0.222304i
u_3	−0.277295 + 0.240049i	−0.268048 + 0.230356i	−0.260373 + 0.222304i
u_4	−0.277295 − 0.240049i	−0.268048 − 0.230356i	−0.260373 − 0.222304i

Table 3.2: Complex roots of dispersion relation (3.9) corresponding to various elastic parameter values

Progressive waves of mode μ, following Eqs. (3.6) and (3.7), take the forms

$$\psi(x,y) = -\exp\left(\mathrm{i}x\sqrt{\mu^2-\gamma^2}\right)\cosh\mu(y+h_f) \quad \text{in} \quad -h_f \le y \le 0, \tag{3.11}$$

$$\phi(x,y) = \exp\left(\mathrm{i}x\sqrt{\mu^2-\gamma^2}\right)f(\mu,y) \quad \text{in} \quad 0 \le y \le h_b, \tag{3.12}$$

with the constraint $\gamma < \mu$ in order that existence of these progressive waves is guaranteed.

If the incident wave of mode μ makes an acute angle θ with the x-axis, then the wave has the following form:

$$\psi_0(x,y) = -\exp\left(\mathrm{i}\mu x\cos\theta\right)\cosh\mu(y+h_f) \quad \text{in} \quad -h_f \le y \le 0, \tag{3.13}$$

$$\phi_0(x,y) = \exp\left(\mathrm{i}\mu x\cos\theta\right)f(\mu,y) \quad \text{in} \quad 0 \le y \le h_b. \tag{3.14}$$

In this case, the following is satisfied:

$$\gamma = \mu \sin\theta. \tag{3.15}$$

With the knowledge that the wave train undergoes reflection by, and transmission over the undulating bottom topography, the asymptotic behaviours of potentials ψ and ϕ, respectively, take the following forms:

$$\psi(x,y) \sim \begin{cases} \psi_0(x,y) + R\psi_0(-x,y), & \text{as } x \to -\infty, \\ T\psi_0(x,y), & \text{as } x \to \infty, \end{cases} \tag{3.16}$$

$$\phi(x,y) \sim \begin{cases} \phi_0(x,y) + R\phi_0(-x,y), & \text{as } x \to -\infty, \\ T\phi_0(x,y), & \text{as } x \to \infty. \end{cases} \tag{3.17}$$

In (3.16) and (3.17), the coefficients R and T are, respectively, the reflection coefficient and transmission coefficient corresponding to an obliquely incident wave of mode μ, and they are required to be evaluated.

The boundary condition satisfied at the uneven bottom $y = h_b + \delta b(x)$ is then approximated (ignoring the terms with higher powers of δ) by Eq. (2.21). Employing perturbation technique for calculating these coefficients up to first-order with the assumption of a small variation at the bottom, we proceed to solve the problem. Next task is to calculate the relevant first-order potentials ϕ_1 and ψ_1 and also the associated reflection and transmission coefficients.

3.3 Solution procedure

3.3.1 Perturbation method

We consider an incident wave of mode μ obliquely incident at an angle $\theta(< \pi/2)$ to the undulating elastic sea-bed under consideration. If there exists no bottom distortion, it is obvious that this wave train propagates with no disturbance. Subsequently, this results in only the transmission of waves taking place in the direction of the positive x-axis. This consideration, along with the boundary condition (2.21) in an appropriate form, allows us to write the velocity potentials ψ and ϕ, the reflection coefficient R and the transmission coefficient T appropriately in perturbation series in terms of a small perturbation parameter δ as (in a similar manner as in Chapter 2)

$$\psi = \psi_0 + \delta\psi_1 + O(\delta^2), \tag{3.18}$$
$$\phi = \phi_0 + \delta\phi_1 + O(\delta^2), \tag{3.19}$$

$$
\begin{aligned}
R &= \delta R_1 + O(\delta^2), && (3.20)\\
T &= 1 + \delta T_1 + O(\delta^2), && (3.21)
\end{aligned}
$$

where ψ_0 and ϕ_0 are, respectively, given by Eqs. (3.13) and (3.14).

However, it is observed that this type of perturbation expansion given by (3.18)-(3.21) is not valid in the case of Bragg resonance for which the reflection coefficient takes values higher than that of the undulation parameter δ (Mei [68]). The phenomenon of Bragg resonance is already discussed in Chapter 2.

We now substitute the relations (3.18)-(3.21) into (3.1)-(3.5), (3.16)-(3.17) and (2.21) with $\gamma = \mu \sin\theta$. By carrying out the comparison of the first-order terms of the perturbation parameter δ from those equations, the coupled BVP for the first-order velocity potentials ψ_1 and ϕ_1 can be expressed as follows:

$$
\begin{aligned}
(\nabla^2_{x,y} - \gamma^2)\psi_1 &= 0 \quad \text{in} \quad -h_f \le y \le 0, && (3.22)\\
(\nabla^2_{x,y} - \gamma^2)\phi_1 &= 0 \quad \text{in} \quad 0 \le y \le h_b, && (3.23)\\
\frac{\partial \psi_1}{\partial y} &= 0 \quad \text{on} \quad y = -h_f, && (3.24)\\
\frac{\partial \phi_1}{\partial y} &= \frac{\partial \psi_1}{\partial y} \quad \text{on} \quad y = 0, && (3.25)\\
\rho\Big(K\psi_1 + \frac{\partial \psi_1}{\partial y}\Big) &= K\phi_1 + \frac{\partial \phi_1}{\partial y} \quad \text{on} \quad y = 0, && (3.26)
\end{aligned}
$$

$$
K\phi_1 + \Big\{D\Big(\frac{\partial^2}{\partial x^2} - \gamma^2\Big)^2 + 1 - \epsilon K\Big\}\frac{\partial \phi_1}{\partial y} = q(x) \quad \text{on} \quad y = h_b, \qquad (3.27)
$$

$$
\begin{aligned}
\text{where } q(x) = f(\mu, h_b)\Big[D\Big(\frac{\partial^2}{\partial x^2} - \gamma^2\Big)^2 + 1 - \epsilon K\Big]\Big\{\mathrm{i}\mu\cos\theta \frac{\partial}{\partial x}\Big(b(x)e^{\mathrm{i}\mu x\cos\theta}\Big)\\
-\mu^2\sin^2\theta\, b(x)e^{\mathrm{i}\mu x\cos\theta}\Big\} - Kb(x)e^{\mathrm{i}\mu x\cos\theta}\Big[\frac{df(\mu,y)}{dy}\Big]_{y=h_b}, \qquad (3.28)
\end{aligned}
$$

with the asymptotic forms

$$
\psi_1(x,y) \sim \begin{cases} R_1\psi_0(-x,y), & \text{as } x \to -\infty,\\ T_1\psi_0(x,y), & \text{as } x \to \infty, \end{cases} \qquad (3.29)
$$

$$
\phi_1(x,y) \sim \begin{cases} R_1\phi_0(-x,y), & \text{as } x \to -\infty,\\ T_1\phi_0(x,y), & \text{as } x \to \infty. \end{cases} \qquad (3.30)
$$

3.3.2 Formation of boundary value problems for ϕ_1 and ψ_1

The coupled boundary value problem for ϕ_1 and ψ_1, described by Eqs. (3.22)-(3.30), is decomposed into the following two independent BVPs for ψ_1 and ϕ_1:
BVP-I for $\psi_1(x, y)$ is as follows:

$$\begin{aligned}
(\nabla^2_{x,y} - \gamma^2)\psi_1 &= 0 \quad \text{in} \quad -h_f \le y \le 0, && (3.31)\\
\frac{\partial \psi_1}{\partial y} &= 0 \quad \text{on} \quad y = -h_f, && (3.32)\\
\frac{\partial \psi_1}{\partial y} &= \zeta(x) \quad \text{on} \quad y = 0, && (3.33)
\end{aligned}$$

where $\zeta(x)$ is known and ψ_1 has the following far-field behaviour:

$$\psi_1(x, y) \sim \begin{cases} -R_1 \cosh u(y + h_f)e^{-\mathrm{i}\mu x \cos\theta}, & \text{as } x \to -\infty, \\ -T_1 \cosh u(y + h_f)e^{\mathrm{i}\mu x \cos\theta}, & \text{as } x \to \infty. \end{cases} \tag{3.34}$$

BVP-II for $\phi_1(x, y)$ is as follows:

$$\begin{aligned}
(\nabla^2_{x,y} - \gamma^2)\phi_1 &= 0 \quad \text{in} \quad 0 \le y \le h_b, && (3.35)\\
\frac{\partial \phi_1}{\partial y} &= \zeta(x) \quad \text{on} \quad y = 0, && (3.36)\\
K\phi_1 + \Big\{D\Big(\frac{\partial^2}{\partial x^2} - \gamma^2\Big) + 1 - \epsilon K\Big\}\frac{\partial \phi_1}{\partial y} &= q(x) \quad \text{on} \quad y = h_b, && (3.37)
\end{aligned}$$

with the asymptotic behaviour

$$\phi_1(x, y) \sim \begin{cases} R_1 f(\mu, y)e^{-\mathrm{i}\mu x \cos\theta}, & \text{as } x \to -\infty, \\ T_1 f(\mu, y)e^{\mathrm{i}\mu x \cos\theta}, & \text{as } x \to \infty. \end{cases} \tag{3.38}$$

Now by using Eqs. (3.33) and (3.36), Eq. (3.26) takes the following form:

$$K(\phi_1 - \rho\psi_1) = (\rho - 1)\zeta(x) \quad \text{on} \quad y = 0. \tag{3.39}$$

3.3.3 Fourier transform technique

Application of Fourier transform, as was followed in Chapter 2, to Eqs. (3.31)-(3.33) gives rise to the following transformed BVP for $\overline{\psi_1}$:

$$\begin{aligned}
\overline{\psi_1}_{yy} - \hat{\beta}^2\overline{\psi_1} &= 0 \quad \text{in} \quad -h_f \le y \le 0, && (3.40)\\
\overline{\psi_1}_y &= 0 \quad \text{on} \quad y = -h_f, && (3.41)\\
\overline{\psi_1}_y &= \bar{\zeta}(\beta) \quad \text{on} \quad y = 0, && (3.42)
\end{aligned}$$

where $\hat{\beta}^2 = \beta^2 + \gamma^2$, and $\bar{\zeta}(\beta)$ denotes the Fourier transform of $\zeta(x)$. The above problem as defined by (3.40)-(3.42) is solved to obtain the solution as

$$\overline{\psi_1}(\hat{\beta}, y) = \frac{\cosh \hat{\beta}(y + h_f)}{\sinh \hat{\beta} h_f} \frac{\bar{\zeta}(\beta)}{\hat{\beta}}. \tag{3.43}$$

Similarly, application of Fourier transform to Eqs. (3.35)-(3.37) gives the following transformed BVP for $\overline{\phi_1}$:

$$\begin{aligned} \overline{\phi_1}_{yy} - \hat{\beta}^2 \overline{\phi_1} &= 0 \quad \text{in} \quad 0 \le y \le h_b, && (3.44)\\ \overline{\phi_1}_y &= \bar{\zeta}(\beta) \quad \text{on} \quad y = 0, && (3.45)\\ K\overline{\phi_1} + (D\hat{\beta}^4 + 1 - \epsilon K)\overline{\phi_1}_y &= \bar{q}(\beta) \quad \text{on} \quad y = h_b, && (3.46) \end{aligned}$$

where $\bar{q}(\beta)$ denotes the Fourier transform of $q(x)$. The solution of the problem given by (3.44)-(3.46) is evaluated as

$$\overline{\phi_1}(\hat{\beta}, y) = \frac{\hat{\beta}\bar{q}(\beta)\cosh \hat{\beta} y + \bar{\zeta}(\beta)\Big[K \sinh \hat{\beta}(y - h_b) - (D\hat{\beta}^4 + 1 - \epsilon K)\hat{\beta}\cosh \hat{\beta}(y - h_b)\Big]}{\hat{\beta}\Big[K \cosh \hat{\beta} h_b + (D\hat{\beta}^4 + 1 - \epsilon K)\hat{\beta} \sinh \hat{\beta} h_b\Big]}. \tag{3.47}$$

By applying Fourier transform to Eq. (3.39), we get

$$K(\overline{\phi_1} - \rho\overline{\psi_1}) = (\rho - 1)\bar{\zeta}(\beta) \quad \text{on} \quad y = 0. \tag{3.48}$$

Substitution of Eqs. (3.43) and (3.47) into Eq. (3.48) gives $\bar{\zeta}(\beta)$ as

$$\bar{\zeta}(\beta) = \frac{K\hat{\beta}\bar{q}(\beta)\sinh(\hat{\beta} h_f)}{\triangle(\hat{\beta})}, \tag{3.49}$$

where the form of $\triangle(\hat{\beta})$ is given by (3.10). From Eq. (3.9), it is observed that $\triangle(\hat{\beta})$ can have one and only one non-zero positive root μ on the real axis of β. Substituting $\bar{\zeta}(\beta)$ into Eqs. (3.43) and (3.47), and then affecting the inverse transform, the velocity potentials $\psi_1(x, y)$ and $\phi_1(x, y)$ are, respectively, evaluated as

$$\begin{aligned} \psi_1(x, y) &= \frac{K}{2\pi} \int_{-\infty}^{\infty} \frac{\cosh \hat{\beta}(y + h_f)}{\triangle(\hat{\beta})} \bar{q}(\beta) e^{\mathrm{i}\beta x} \mathrm{d}\beta, && (3.50)\\ \phi_1(x, y) &= \frac{1}{2\pi} \int_{-\infty}^{\infty} \frac{[\cosh \hat{\beta} y + \frac{K \sinh \hat{\beta} h_f}{\triangle(\hat{\beta})} G(\hat{\beta}, y)]}{[K \cosh \hat{\beta} h_b + (D\hat{\beta}^4 + 1 - \epsilon K)\hat{\beta} \sinh \hat{\beta} h_b]} \bar{q}(\beta) e^{\mathrm{i}\beta x} \mathrm{d}\beta, && (3.51) \end{aligned}$$

where $G(\hat{\beta}, y) = K \sinh \hat{\beta}(y - h_b) - (D\hat{\beta}^4 + 1 - \epsilon K)\hat{\beta} \cosh \hat{\beta}(y - h_b)$.

Here the Fourier transform of $q(x)$, i.e., $\bar{q}(\beta)$, is defined as

$$\bar{q}(\beta) = S(\mu, \beta) \int_{-\infty}^{\infty} e^{\mathrm{i}(\mu \cos\theta - \beta)x} b(x) \mathrm{d}x, \tag{3.52}$$

where the function S is defined as follows:

$$\begin{aligned} S(\mu, \beta) = f(\mu, h_b) \Big[D \Big\{ & \mu \cos\theta (\mu \cos\theta - \beta)^5 - \mu^2 (4 \cos^2\theta + 1)(\mu \cos\theta - \beta)^4 \\ & + 2\mu^3 \cos\theta (3 + 2\cos^2\theta)(\mu \cos\theta - \beta)^3 - 2\mu^4 (4\cos^2\theta + 1)(\mu\cos\theta - \beta)^2 \\ & + 5\mu^5 \cos\theta(\mu\cos\theta - \beta) - \mu^6 \Big\} + (1 - \epsilon K)(\mu^2 \cos^2\theta - \beta\mu\cos\theta - \mu^2) \Big] \\ & + \frac{\mu K^2 \sinh \mu h}{K \cosh \mu h_b + (D\mu^4 + 1 - \epsilon K)\mu \sinh \mu h_b}. \end{aligned} \tag{3.53}$$

The fact that $\triangle(\hat{\beta})$ has only one non-zero root at $\hat{\beta} = \mu$ on the positive real axis of β corresponding to $\beta_1 = \sqrt{\mu^2 - \gamma^2}$ implies that each of the integrals in (3.50) and (3.51) contains a pole at β_1. Subsequently, the path of each integral in (3.50) and (3.51) is indented below the poles at β_1.

3.4 Determination of reflection and transmission coefficients

We now evaluate the reflection coefficient R_1 and transmission coefficient T_1 which arise due to the oblique wave of mode μ incident on the elastic undulating bed (here $\gamma = \mu \sin\theta$). We let $x \to \pm\infty$ in Eqs. (3.50) or (3.51) and then compare with Eqs. (3.34) or (3.38).

For evaluating R_1, letting $x \to -\infty$ in either (3.50) or (3.51), the behaviour of the potentials $\psi_1(x, y)$ or $\phi_1(x, y)$ is examined by affecting a rotation of the path of the integral, which involves $\bar{q}(-\beta)$, into a suitable contour in the first quadrant in order that the residue at the pole β_1 may be incorporated. Similarly, when the integral involves $\bar{q}(\beta)$ in Eqs. (3.50) or (3.51), integration can be carried out along a suitable contour in the fourth quadrant in order that this integral makes no contribution as $x \to -\infty$. Subsequently, after comparing the newly evaluated integral with Eqs. (3.34) or (3.38), the final expression for R_1 is obtained as

$$\begin{aligned} R_1 &= -\frac{\mathrm{i}K\bar{q}(-\mu\cos\theta)}{\cos\theta \triangle'(\mu)} \\ &= -\frac{\mathrm{i}K S(\mu, -\mu\cos\theta)}{\cos\theta\triangle'(\mu)} \int_{-\infty}^{\infty} e^{2\mathrm{i}\mu x \cos\theta} b(x) \mathrm{d}x, \end{aligned} \tag{3.54}$$

where S is given by Eq. (3.53).

In a similar manner, the evaluation of T_1 can be achieved by assuming $x \to \infty$ in (3.50) or (3.51). When $x \to \infty$, it is possible to obtain the behaviour of the potentials $\psi_1(x, y)$ or $\phi_1(x, y)$ in a similar way as was done for the case $x \to -\infty$. Since the integral involving the term $\bar{q}(-\beta)$ makes no contribution as $x \to \infty$ (as explained earlier), comparison of the resultant integral with Eqs. (3.34) or (3.38) gives us the final expression for T_1 as follows:

$$\begin{aligned} T_1 &= -\frac{\mathrm{i}K\bar{q}(\mu\cos\theta)}{\cos\theta\triangle'(\mu)} \\ &= -\frac{\mathrm{i}KS(\mu,\mu\cos\theta)}{\cos\theta\triangle'(\mu)}\int_{-\infty}^{\infty} b(x)\mathrm{d}x. \end{aligned} \tag{3.55}$$

It is clear that these first-order reflection and transmission coefficients given by Eqs. (3.54) and (3.55) still remain in integral form containing the shape function $b(x)$, and can be calculated only when the shape of the bottom undulation of the elastic bed is given explicitly. The next section presents a study of reflection and transmission due to some particular sinusoidal forms of $b(x)$.

3.5 Particular undulating bottom profiles

Two particular forms of the function $b(x)$ each of which represents an irregular bottom topography are considered in this section. The utility of such bed forms is already described in Chapter 2 while considering such undulating bed shapes. Due to the physical significance of such bed topographies containing sinusoidal ripples, enormous importance has been accorded to such topographies and in view of this, the following appropriate examples are considered to substantiate the results obtained in the earlier sections.

3.5.1 Undulating bottom profile-I

The same shape function $b(x)$ as used in Chapter 2 in the following form represents a patch of sinusoidal ripples of amplitude a at the sea-bed:

$$b(x) = \begin{cases} a\sin lx, & -\frac{n\pi}{l} \le x \le \frac{n\pi}{l}, \\ 0, & \text{otherwise}, \end{cases} \tag{3.56}$$

where l denotes the ripple wavenumber in the region $-\frac{n\pi}{l} \le x \le \frac{n\pi}{l}$ and n, a positive integer, gives the number of ripples in this particular patch of ripples.

R_1, the first-order reflection coefficient, which arises due to the wave of mode μ being obliquely incident on the elastic undulating bed, is now acquired through the substitution of $b(x)$ from Eq. (3.56) into Eq. (3.54). Subsequently, the required coefficient is found to be

$$R_1 = (-1)^{n+1} \frac{2alKS(\mu, -\mu\cos\theta)}{\cos\theta \triangle'(\mu)} \frac{\sin(\frac{2\mu n\pi\cos\theta}{l})}{l^2 - 4\mu^2\cos^2\theta}. \tag{3.57}$$

In a similar manner, the transmission coefficient T_1 can be calculated by the substitution of $b(x)$ from Eq. (3.56) into Eq. (3.55) to get

$$T_1 = 0. \tag{3.58}$$

The expression for R_1 given in Eq. (3.57) illustrates that R_1 is an oscillatory function corresponding to a certain given number of ripples on the undulating sea-bed. Moreover, Eq. (3.57) shows that, with the wavenumber of the sinusoidal elastic bed becoming approximately two times the interface wavenumber along the x-axis, i.e., when $l = 2\mu\cos\theta$, the reflection coefficient turns unbounded. It predicts existence of resonance between the undulating elastic bed and the interface of the layers. From Eq. (3.57), it can be observed that R_1 takes the following limiting value near resonance:

$$R_1 = \frac{aKS(\mu, -\mu\cos\theta)}{2\mu\cos^2\theta\triangle'(\mu)} n\pi. \tag{3.59}$$

It can be clearly observed that, with $2\mu\cos\theta/l$ approaching 1 and n becoming large, R_1 becomes inexhaustible which contradicts the fact that it is a very small quantity, being a first-order correction. Therefore, the present work considers only those cases that eliminate these two situations to avoid the possible contradiction in the case of resonance.

For this example, the first-order reflection coefficient R_1 is clearly seen as a constant multiple of n with which it increases linearly. Despite of the fact that the theory does not hold when $l = 2\mu\cos\theta$, i.e., for the case of Bragg resonance, it is worthwhile mentioning that a substantial amount of reflected wave energy by such an undulating bottom is very likely to occur around this singularity.

3.5.2 Undulating bottom profile-II

Another particular form of the shape function representing a patch of sinusoidal ripples with amplitude a but with two different wanumbers is considered at the sea-bed as follows (Mohapatra and Bora [71]):

$$b(x) = \begin{cases} a\sin l_1 x, & -L_3 \le x \le 0, \\ a\sin l_2 x, & 0 \le x \le L_4, \\ 0, & \text{otherwise.} \end{cases} \tag{3.60}$$

In order to maintain the continuity of the bed elevation, L_3 and L_4 can be considered as

$$L_3 = -\frac{n_1\pi}{l_1}, \quad L_4 = \frac{n_2\pi}{l_2}, \tag{3.61}$$

where n_1 and n_2 are two positive integers. The patches $-L_3 \leq x \leq 0$ and $0 \leq x \leq L_4$, respectively, contain $n_1/2$ ripples with wavenumber l_1 and $n_2/2$ ripples with wavenumber l_2. For calculating the corrected first-order coefficients R_1 and T_1, $b(x)$ given by (3.60) is substituted into Eqs. (3.54) and (3.55) to get

$$\begin{aligned} R_1 &= -\frac{\mathrm{i}KS(\mu,-\mu\cos\theta)}{\cos\theta\triangle'(\mu)}\left[\frac{al_1}{l_1^2-4\mu^2\cos^2\theta}\left\{(-1)^{n_1}e^{2\mathrm{i}\mu\cos\theta L_3}-1\right\}\right. \\ &\left.+\frac{al_2}{l_2^2-4\mu^2\cos^2\theta}\left\{1-(-1)^{n_2}e^{2\mathrm{i}\mu\cos\theta L_4}\right\}\right], \qquad (3.62) \\ T_1 &= -\frac{\mathrm{i}aKS(\mu,\mu\cos\theta)}{\cos\theta\triangle'(\mu)}\left[\left\{\frac{(-1)^{n_1}-1}{l_1}\right\}+\left\{\frac{1-(-1)^{n_2}}{l_2}\right\}\right]. \qquad (3.63) \end{aligned}$$

As a special instance, if $n_1 = n_2 = n$ as well as $l_1 = l_2 = l$ are considered in Eqs. (3.62) and (3.63), respectively, those get reduced to Eqs. (3.57) and (3.58), where all the ripples have the same wavenumber l.

Here also it is observed, just as in the previous example, that when the wavenumber of the bed takes value approximately twice the interface wavenumber, i.e., when $l_1 = 2\mu\cos\theta$ and $l_2 = 2\mu\cos\theta$, a resonant interaction is observed between the sea-bed and interface. Eq. (3.62) indicates that under such condition, R_1 takes the limiting value in the following form:

$$R_1 = \frac{aKS(\mu,-\mu\cos\theta)}{4\mu\cos^2\theta\triangle'(\mu)}(n_1+n_2)\pi. \tag{3.64}$$

For this bottom profile also, the first-order reflection coefficient R_1 can be seen as a constant multiple of the number of ripples $(n_1+n_2)/2$ and it increases linearly with n_1 and n_2. Despite the theory breaking down for the instance when either $l_1 = 2\mu\cos\theta$ or $l_2 = 2\mu\cos\theta$, a substantial amount of reflected energy due to the presence of the undulating elastic sea-bed will get created in the neighbourhood of these singularities.

3.6 Validation

To validate our result, we consider the results of Mohapatra and Bora [71] to be compared with our result when the elasticity of the sea-bed is removed from the system. Mathematically, it is derived in Appendix B that when the values of both elastic parameters D and ϵ are taken as 0, then the sea-bed can be considered as a rigid one. Appendix B also elaborates the equivalence of bottom boundary condition used in the present work and that

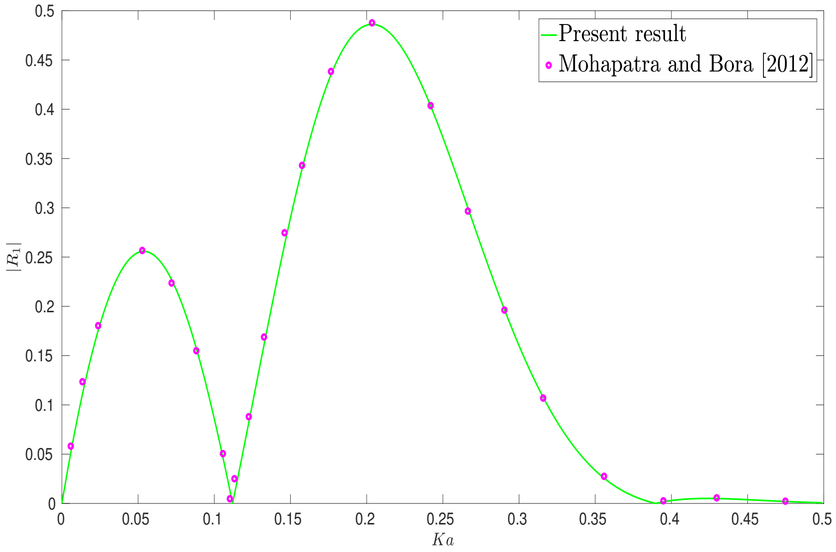

Figure 3.3: Comparison between present work and the work of Mohapatra and Bora [71]

in Mohapatra and Bora [71]. Here we take the example of the bottom undulation given in subsection 3.5.1 and consider the lower layer depth as $h_b = 10a$, upper layer depth as $h_f = 10a$, the density ratio as $\rho = 0.95$, the ripple wavenumber as $la = 0.52$, the angle of incidence as $\theta = 0$ and the sum of ripples of the bottom undulation as $n = 2$. Figure 3.3 presents the plots of the reflection coefficient $|R_1|$ against Ka for the work of Mohapatra and Bora [71] with Fig. 2 and the present work from which an excellent agreement can be inferred. This implies that the present model is valid and can be applied to various relevant problems in coastal and offshore engineering.

3.7 Results for reflection and transmission coefficients

In order to examine the effects of various parameters used in the present work, such as the angle of incidence, the number of ripples of the undulating bottom, the elastic parameters etc., on the scattering corrections R_1 and T_1 for two particular forms of bottom undulations as considered in the previous section, an appropriate MATLAB program is used. Behaviour of the first-order reflection and transmission coefficients arising out of the interaction of an oblique incident wave with an undulating elastic sea-bed in specific form are presented and analyzed in graphical form through a number of figures corresponding to different dimensionless parameters. For convenience, we introduce the following dimensionless parameters:

$$\begin{cases} \mu^* = \mu h_b, \;\; K^* = K h_b, \\ D^* = \frac{D}{h_b^4}, \;\; \epsilon^* = \dfrac{\epsilon}{h_b}, \\ a^* = \frac{a}{h_b}, \;\; l^* = l h_b. \end{cases}$$

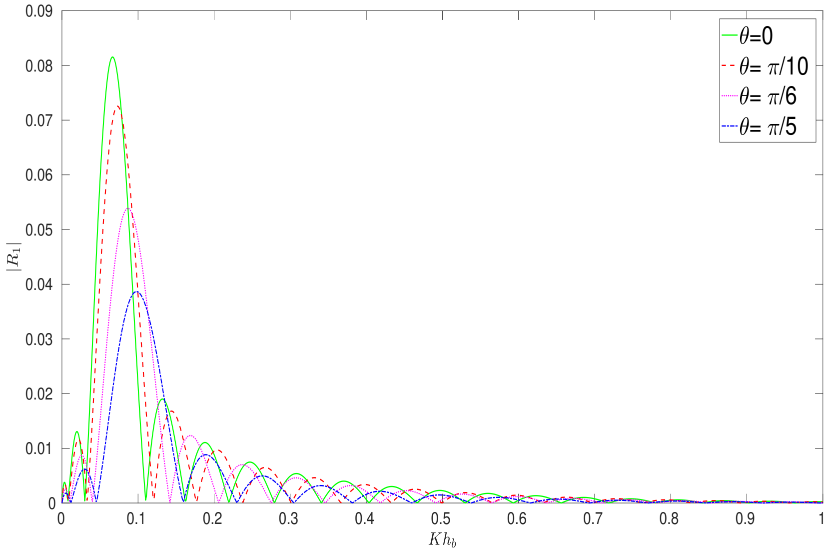

Figure 3.4: Reflection coefficient $|R_1|$ for different angle of incidence against Kh_b with $n = 3$, $h_b/h_f = 2$, $a/h_b = 0.1$, $lh_b = 1$, $\rho = 0.5$, $D/h_b^4 = 0.1$, $\epsilon/h_b = 0.1$

The examples considered in the previous section, that is, the rippled elastic sea-bed, is considered very important mainly due to its competence in reflecting incident wave energy in water wave problems. Figures 3.4-3.8 demonstrate the first-order reflection coefficient $|R_1|$ for a wave train with wavenumber μ (interfacial mode) corresponding to various parameters. We consider Eq. (3.57) and compute $|R_1|$ corresponding to an oblique wave of wavenumber μ incident at an angle θ to the elastic sinusoidal ripple bed with wavenumber l and n ripples. In this case, we take the depth ratio h_b/h_f as 2, the amplitude of the sinusoidal ripples as $a/h_b = 0.1$, the density ratio as $\rho = 0.5$ and the elastic parameters fixed at $D/h_b^4 = 0.1$, $\epsilon/h_b = 0.1$ (barring Fig. 3.6 and Fig. 3.7). The curves in Fig. 3.4 are plotted corresponding to four values of θ, namely, $\theta = 0$, $\pi/10$, $\pi/6$ and $\pi/5$. Here, the number of ripples (n) in the undulating sea-bed is fixed at 3 and ripple wavenumber at $lh_b = 1$. For $\theta = 0$, i.e., for normal incidence, $|R_1|$ attains its maximum value at 0.081531, that is, at $\mu h_b \cos\theta = 0.507096$ (when $Kh_b = 0.067$). In other words, the maximum value of $|R_1|$ occurs for the case of the ripple wavenumber lh_b of the sea-bed taking a value approximately twice the interface wavenumber $\mu h_b \cos\theta$ along the x-axis. Similar result is observed when θ is non-zero too. From Fig. 3.4, the oscillatory behaviour of $|R_1|$ with respect to Kh_b is observed. When there is an increase in the angle of incidence, there is a reduction in the peak value of $|R_1|$. It is observed that the value of $|R_1|$ is the highest when the incident wave falls normally on the undulating bed. A further observation is that the reflected energy generated by the normal incident wave is higher compared to that for the oblique incident wave.

Different curves in Fig. 3.5 present $|R_1|$ corresponding to ripple number $n = 1, 3, 5$ in the sinusoidal elastic sea-bed with the following fixed values of various parameters: $D/h_b^4 = 0.1$, $\epsilon/h_b = 0.1$, $\theta = \pi/6$, $lh_b = 1$. This figure shows that, with an increase in the number of ripples, $\mu h_b \cos\theta$ converges to some value in the vicinity of $lh_b/2$. In addition, the peak value of $|R_1|$ also has an increasing trend. But for the case when the number of ripples is taken to be reasonably large, $|R_1|$ turns out to be unbounded for some specific values of Kh_b which is due to Bragg resonance. In this case, the reflection coefficient takes much larger values than the perturbation parameter δ. It clearly means that the perturbation expansion discussed in the previous section is not valid, based on the observation made by Mei [68]. Figure 3.5 shows that when there occurs an increase in the number of ripples, the oscillatory nature of $|R_1|$ with respect to Kh_b is visibly clear with the observation of an increasing number of zeros although the general feature of $|R_1|$ does not exhibit any change. It can be inferred that such an oscillating behaviour appears because of the interaction of the incident wave with the undulating elastic sea-bed and the interface.

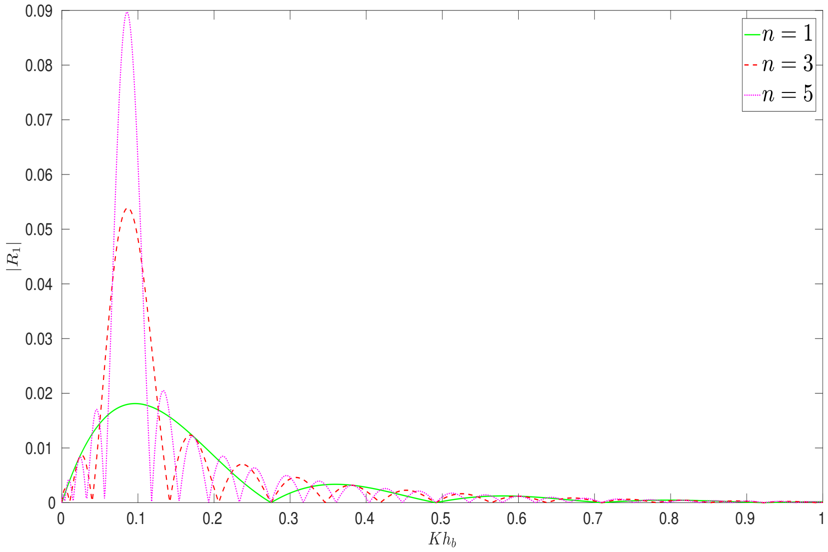

Figure 3.5: Reflection coefficient $|R_1|$ for different ripple numbers against Kh_b with $\theta = \pi/6$, $h_b/h_f = 2$, $a/h_b = 0.1$, $lh_b = 1$, $\rho = 0.5$, $D/h_b^4 = 0.1$, $\epsilon/h_b = 0.1$

Different curves in Fig. 3.6 present the first-order reflection coefficient $|R_1|$ corresponding to various elastic parameters ($D/h_b^4 = 0$, $\epsilon/h_b = 0$); ($D/h_b^4 = 1$, $\epsilon/h_b = 0.001$);

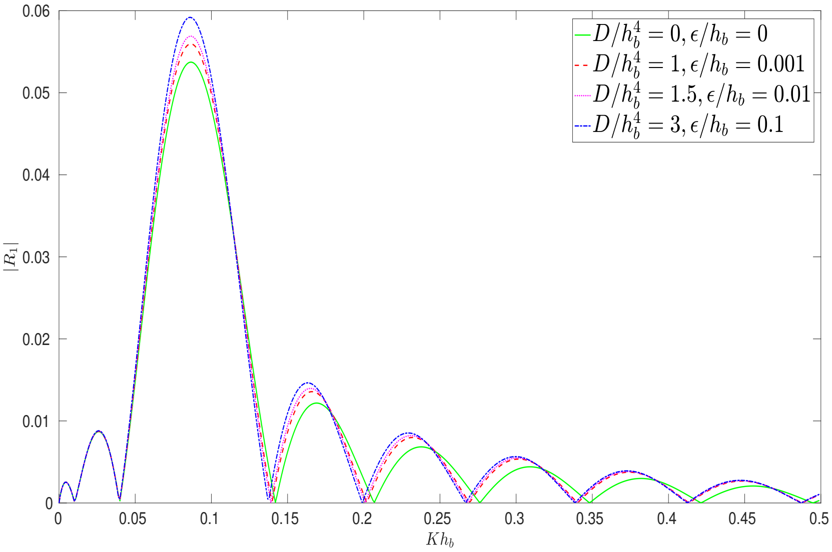

Figure 3.6: Reflection coefficient $|R_1|$ for different elastic parameters against Kh_b with $\theta = \pi/6$, $n = 3$, $\rho = 0.5$, $h_b/h_f = 2$, $a/h_b = 0.1$, $lh_b = 1$

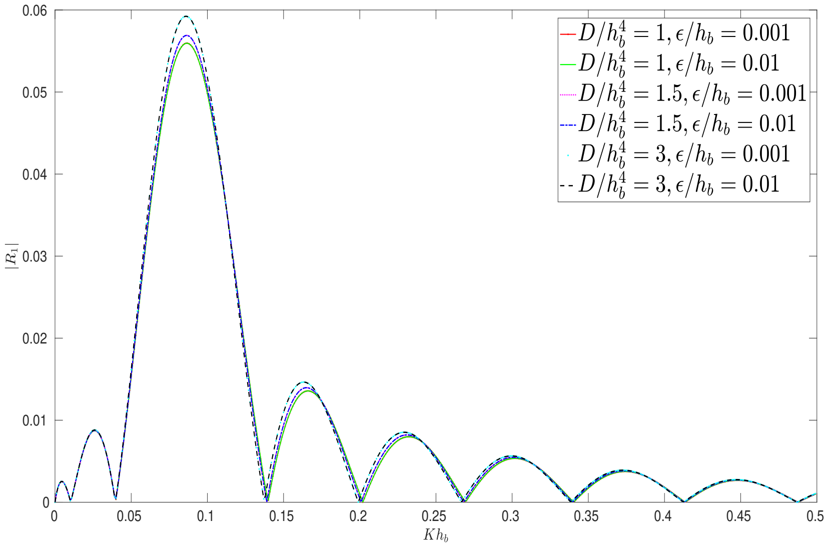

Figure 3.7: Reflection coefficient $|R_1|$ for different elastic parameters against Kh_b with $\theta = \pi/6$, $n = 3$, $\rho = 0.5$, $h_b/h_f = 2$, $a/h_b = 0.1$, $lh_b = 1$

$(D/h_b^4 = 1.5,\ \epsilon/h_b = 0.01)$ and $(D/h_b^4 = 3,\ \epsilon/h_b = 0.1)$ with $\theta = \pi/6$, $n = 3$ and $lh_b = 1$. It shows that, if the value of the elastic parameters of the bed increases, the peak value of $|R_1|$ increases. This shows that the energy generated by reflection in some sense depends to a great extent on the variation in elastic parameter values. The peak values of $|R_1|$ corresponding to the different elastic parameters $(D/h_b^4 = 0,\ \epsilon/h_b = 0)$; $(D/h_b^4 = 1,\ \epsilon/h_b = 0.001)$; $(D/h_b^4 = 1.5,\ \epsilon/h_b = 0.01)$ and $(D/h_b^4 = 3,\ \epsilon/h_b = 0.1)$

are found for the values $\mu h_b = 0.584304,\ 0.583157,\ 0.584273$ and 0.587080, respectively. Therefore, as noticed earlier too, here also the reflection coefficient attains the peak value when the wavenumber lh_b of the undulating elastic sea-bed takes values approximately twice the interface wavenumber $\mu h_b \cos\theta$ along the x-axis. It is also a remarkable fact that if the bed is impermeable (i.e., when the elastic parameters are taken to be 0), the reflected energy is smaller than the reflected energy generated by an undulating flexible sea-bed. From these curves in Fig. 3.7, we observe that the role of the parameter D/h_b^4 is much more significant than that of the other parameter ϵ/h_b. It may point towards consideration of higher values of D/h_b^4 for getting maximum reflected energy. However, very high values of elasticity may bring in difficulty in maintaining appropriate and controllable elasticity of the sea-bed. Therefore, it is suggested that moderate values of elasticity is suitable for effective use in coastal engineering.

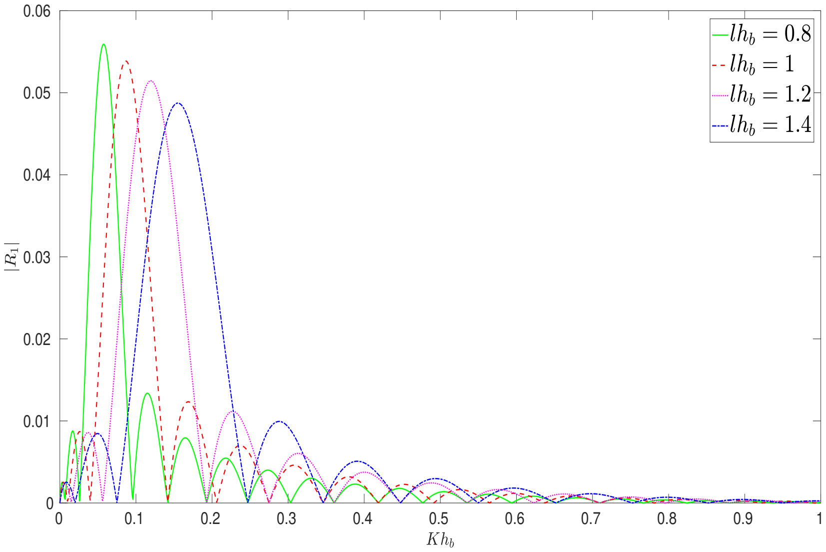

Figure 3.8: Reflection coefficient $|R_1|$ for different sea-bed wavenumber against Kh_b with $\theta = \pi/6,\ n = 3,\ \rho = 0.5,\ h_b/h_f = 2,\ a/h_b = 0.1,\ D/h_b^4 = 0.1,\ \epsilon/h_b = 0.1$

Different curves in Fig. 3.8 present $|R_1|$ plotted against wavenumber Kh_b of the incident wave corresponding to wavenumbers $lh_b = 0.8,\ 1,\ 1.2,\ 1.4$ of the undulating elastic sea-bed. Here the following values are considered: $D/h_b^4 = 0.1,\ \epsilon/h_b = 0.1,\ \theta = \pi/6$ and $n = 3$. The peak values of the reflection coefficient $|R_1|$ is observed to have appeared corresponding to lower values of Kh_b. The main fact behind this type of occurrence is that $|R_1|$ attains maximum only when $lh_b = 2\mu h_b \cos\theta$. This figure shows that, when the ripple wavenumbers increase, $|R_1|$ decreases, and it, moreover, becomes less than that for the large ripple bed wavenumbers. This implies that, in the event of an obliquely incident wave propagating over an elastic undulating bed having a small ripple wavenumber, a considerable amount of reflected energy is generated.

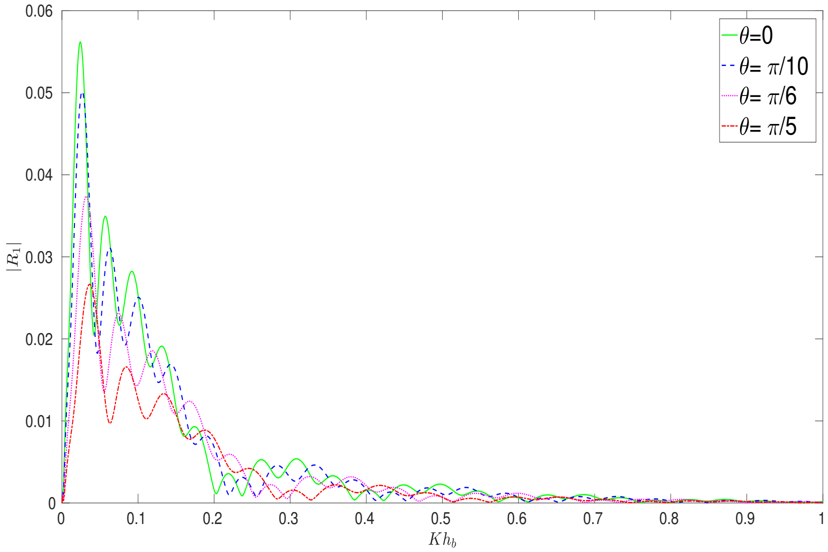

Figure 3.9: Reflection coefficient $|R_1|$ for different angle of incidence against Kh_b with $\rho = 0.5$, $h_b/h_f = 2$, $a/h_b = 0.1$, $n_1 = 2$, $n_2 = 3$, $l_1h_b = 1$, $l_2h_b = 0.5$, $D/h_b^4 = 0.1$, $\epsilon/h_b = 0.1$

We now refer to the second specific patch of sinusoidal bottom undulation, which is taken up in subsection 3.5.2, with the ripple patches of having two different wavenumbers l_1 and l_2. Figures 3.9-3.13 present the non-dimensionalized first-order reflection and transmission coefficients $|R_1|$ and $|T_1|$ due to a progressive wave train with wavenumber μ obliquely incident at an angle θ to the positive x-axis. Here the ripple wavenumbers l_1 and l_2 each has n_1 and n_2 ripples, respectively, in the patch. The following parameter values are considered: $h_b/h_f = 2$, $a/h_b = 0.1$, $\rho = 0.5$ and elastic parameters are fixed at $D/h_b^4 = 0.1$, $\epsilon/h_b = 0.1$ (except for Figs. 3.12 and 3.13). The curves in Fig. 3.9 present $|R_1|$ against Kh_b for four different angles of incidence, namely, $\theta = 0$, $\pi/10$, $\pi/6$ and $\pi/5$, with $l_1h_b = 1$, $l_2h_b = 0.5$, $n_1 = 2$ and $n_2 = 3$. This figure shows that, for normal incidence, the first maximum value of $|R_1|$ is found to be 0.056206, which corresponds to $\mu h_b = 0.296289$ (when $Kh_b = 0.024$). Similarly, $|R_1|$ attains its second maximum value of 0.034953 which corresponds to $\mu h_b = 0.465109$ (when $Kh_b = 0.057$). In Fig. 3.10, $|R_1|$ is plotted against Kh_b corresponding to $l_1h_b = 1$, $l_2h_b = 0.5$, $n_1 = 2$ and $n_2 = 4$, where the number of ripples in the second part of the patch is increased from 3 to 4. Fig. 3.10 establishes that for $\theta = 0$, $|R_1|$ attains its first maximum value of 0.06783 corresponding to $\mu h_b = 0.28336$ (when $Kh_b = 0.022$). The next maximum value of of $|R_1|$ is 0.037387 which is found at $\mu h_b = 0.419987$ (when $Kh_b = 0.047$). It can be inferred from this figure that for any θ lying in $0 \le \theta < \pi/2$, the reflection coefficient $|R_1|$ attains two peak values occurring for each case of the ripple wavenumbers l_1h_b and l_2h_b of the undulating elastic sea-bed becoming approximately twice the interface wavenumber. It is seen from those

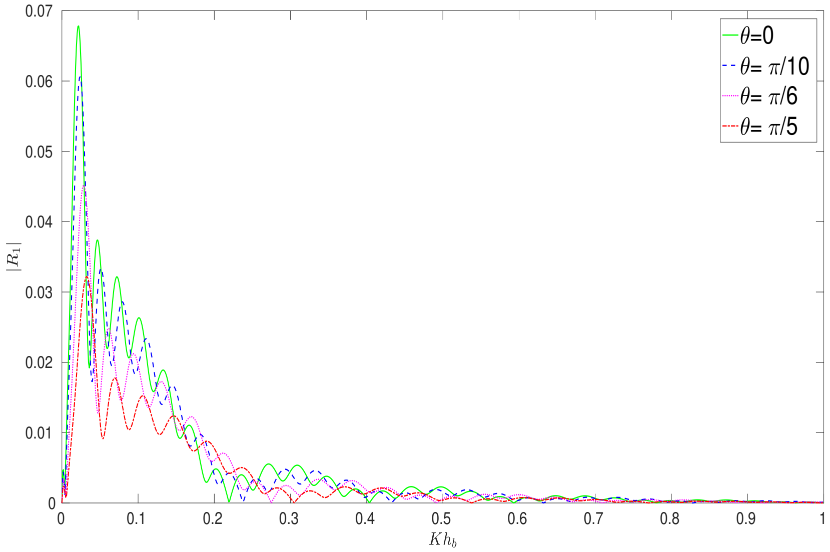

Figure 3.10: Reflection coefficient $|R_1|$ for different angle of incidence against Kh_b with $\rho = 0.5$, $h_b/h_f = 2$, $a/h_b = 0.1$, $n_1 = 2$, $n_2 = 4$, $l_1h_b = 1$, $l_2h_b = 0.5$, $D/h_b^4 = 0.1$, $\epsilon/h_b = 0.1$

figures that the occurrence of an increase in the angle of incidence forces a reduction in $|R_1|$. However, when the numbers of ripples n_1 and n_2 increase, the peak value of $|R_1|$ is observed to increase with its oscillatory behaviour against Kh_b becoming pronounced. This oscillating nature is observed to have occurred due to the resonance situation taking place due to the incident wave interacting with the undulating elastic bottom which has different wavenumbers, and also with the interface.

Different curves in Fig. 3.11 show the reflection coefficient against wavenumber Kh_b of the incident wave corresponding to different number of ripples on the undulating elastic bed. The following parameter values are considered: $D/h_b^4 = 0.1$, $\epsilon/h_b = 0.1$, $\theta = \pi/6$, $l_1h_b = 1$ and $l_2h_b = 0.5$. There is a clear indication that, with an increase in the number of ripples, there is an increase in the peak value of $|R_1|$ and its oscillatory behaviour is clearly noticeable. Different curves in Fig. 3.12 correspond to $|R_1|$ plotted against Kh_b corresponding to various elastic parameters ($D/h_b^4 = 0$, $\epsilon/h_b = 0$); ($D/h_b^4 = 1$, $\epsilon/h_b = 0.001$); ($D/h_b^4 = 1.5$, $\epsilon/h_b = 0.01$) and ($D/h_b^4 = 3$, $\epsilon/h_b = 0.1$) for $\theta = \pi/6$, $l_1h_b = 1$, $l_2h_b = 0.5$, $n_1 = 2$ and $n_2 = 3$. It shows that, if the elastic parameters of the bed take increasing values, the peak value of $|R_1|$ increases. The rate of increase of the reflection coefficient is quite imperceptible corresponding to various values of Kh_b. This shows that the produced reflected energy is independent of the changes in the values of the elastic parameter of the bed given by Eq. (3.60). Furthermore, the rate of change for the values of the reflection coefficient of the sinusoidal bed with two wavenumbers is largely ineffective as compared to the reflection coefficient of the sinusoidal bed having one wavenumber.

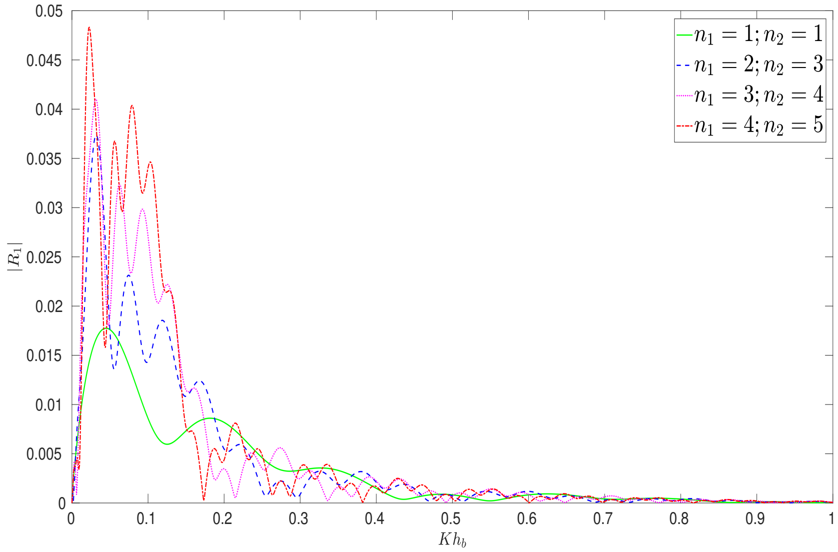

Figure 3.11: Reflection coefficient $|R_1|$ for different ripple numbers against Kh_b with $\rho = 0.5$, $h_b/h_f = 2$, $a/h_b = 0.1$, $l_1h_b = 1$, $l_2h_b = 0.5$, $\theta = \pi/6$, $D/h_b^4 = 0.1$, $\epsilon/h_b = 0.1$

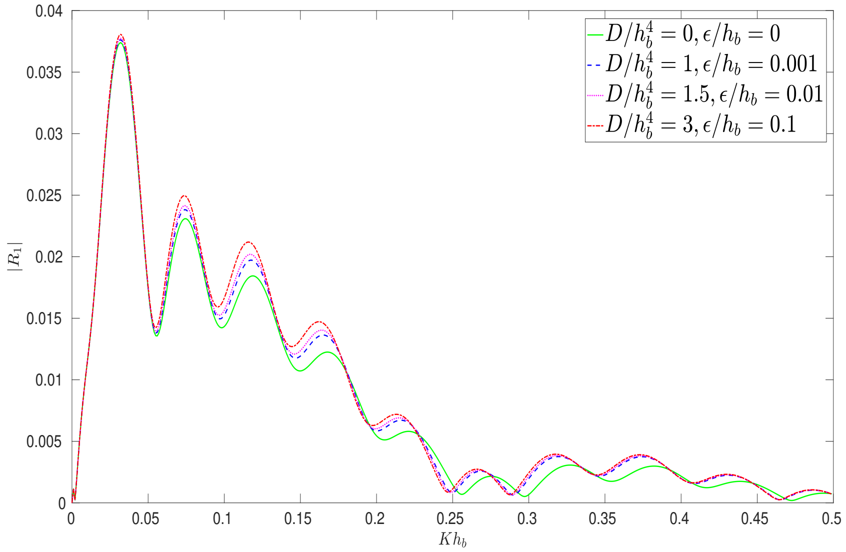

Figure 3.12: Reflection coefficient $|R_1|$ for different elastic parameters against Kh_b with $\rho = 0.5$, $h_b/h_f = 2$, $a/h_b = 0.1$, $l_1h_b = 1$, $l_2h_b = 0.5$, $n_1 = 2$, $n_2 = 3$, $\theta = \pi/6$

This implies that the elastic sea-bed under consideration does not show any significant effect on the reflected energy due to the bottom undulation described by two patches of two different wavenumbers instead of the one with one wavenumber. Similar behaviour is observed when $n_2 = 3$ is changed to $n_2 = 4$ keeping $n_1 = 2$ unchanged.

Figure 3.13 presents the transmission coefficient $|T_1|$ against Kh_b corresponding to various elastic parameters ($D/h_b^4 = 0$, $\epsilon/h_b = 0$); ($D/h_b^4 = 1$, $\epsilon/h_b = 0.001$); ($D/h_b^4 =$

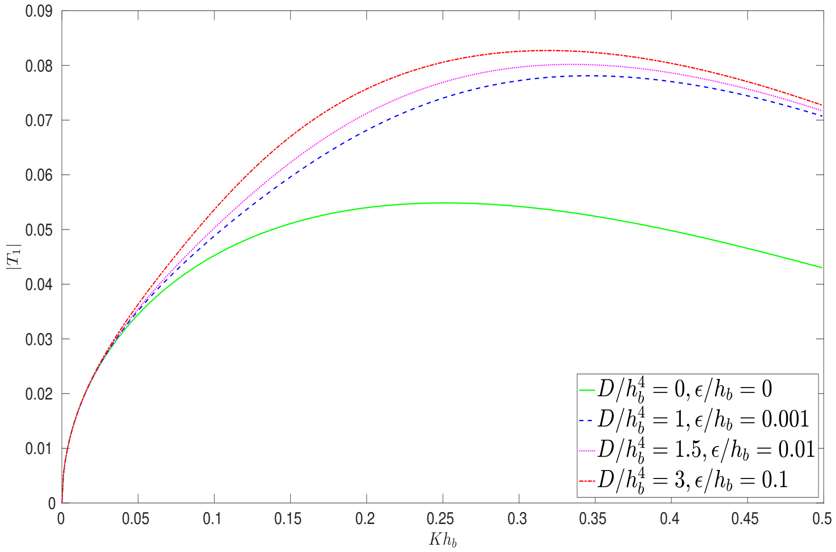

Figure 3.13: Transmission coefficient $|T_1|$ for different elastic parameters plotted against Kh_b with $\rho = 0.5$, $h_b/h_f = 2$, $a/h_b = 0.1$, $l_1 h_b = 1$, $l_2 h_b = 0.5$, $n_1 = 2$, $n_2 = 4$, $\theta = \pi/6$

1.5, $\epsilon/h_b = 0.01$) and ($D/h_b^4 = 3$, $\epsilon/h_b = 0.1$) for $\theta = \pi/6$, $l_1 h_b = 1$, $l_2 h_b = 0.5$, $n_1 = 2$ and $n_2 = 3$. This figure depicts that, as the value of the elastic parameters of the sea-bed increases, the peak value of $|T_1|$ also increases which shows that, with an oblique incident wave propagating over an elastic bed with a patch of undulation, there is a fair possibility of considerable amount of transmitted energy being produced. From Fig. 3.13, the non-oscillating behaviour of the transmitted energy with respect to Kh_b is clearly noticed. An observation can be made that the amount of reflected energy produced is less than the transmitted energy. It is clear that it happens due to the sea-bed being elastic.

To sum it up: in this chapter, we discuss a hydroelastic model for studying the propagation of oblique water waves over an undulating elastic sea-bed, for a two-layer fluid flow through a channel. As far as our knowledge in concerned, no investigation of this type of problems having an undulating elastic bed in connection with a two-layer fluid flow has been taken up till date. However, the present work bears certain similarities with that of Mohapatra and Bora [71]. One basic similarity observed in both these works is that, for any given frequency, there exists a time-harmonic wave propagating along the interface. Figure 3.4 illustrates that the value of the first-order reflection coefficient $|R_1|$ decreases corresponding to an increase in the angle of incidence. On the other hand, $|R_1|$ takes increasing values when the number of ripples of the sinusoidal elastic sea-bed is increased. The same characteristics were observed in the work by Mohapatra and Bora [71] too. But the numerical approximations of the coefficients are not the same due to the difference of various physical considerations, including the consideration of elasticity in the bed, in those works.

3.8 Conclusion

In this chapter, employing linear water wave theory, scattering of obliquely incident waves by a small elastic bottom undulation in a two-layer fluid is investigated. With the upper layer bounded above by a rigid lid, a channel flow comes into existence. For convenience as well as the adoption of similar consideration by several other researchers, the elastic sea-bed thickness is assumed to be relatively less than the wavelength of the propagating wave. Under these circumstances, propagating waves exist only at one wavenumber for any given frequency. By application of perturbation technique in association with Fourier transform, the BVP is split into suitable ones and the first-order velocity potentials, along with the relevant reflection and transmission coefficients, are evaluated and discussed. Demonstration of the results is carried out by considering two special types of bottom undulation on the elastic sea-bed. An important observation is the occurrence of complex resonance during the bed-interface interaction when the ratio of the ripple wavenumber of the bottom undulation and the interface wavenumber becoming very close to 2. Another noteworthy inference is that the reflected energy gets reduced corresponding to an increase in the angle of incidence. The reflected energy is found to be the highest for the normal incidence of the waves. It is observed that, when the wave train encounters the sea-bed, the reflected energy increases corresponding to an increase in the elasticity of the bed. Due to the flexibility of the sea-bed, the reflected energy is found to be smaller than the transmitted energy. Furthermore, the reflection coefficient increases when the number of ripples of the sinusoidal bottom undulation increases. It is observed that even a small number of ripples is effective enough to produce a considerable amount of reflected energy. It is to be noted that the formulation, procedure and solutions adopted and evaluated in this work are valid for small reflection and not effective for resonance cases. The results described for the present work is going to be of significant use for a variety of water wave scattering problems in ocean engineering and allied branches where a flexible sea-bed is required to be considered with the upper surface covered by a rigid lid.

CHAPTER 4

WATER WAVE SCATTERING BY AN ELASTIC SEA-BED OF VARYING DEPTH IN TWO SUPERPOSED FLUIDS COVERED BY AN ICE-SHEET

4.1 Introduction

A hydroelastic model is taken up in this chapter to investigate the propagation of normal incident waves over a small undulation located on an elastic sea-bed in a fluid flow for two superposed fluids where a floating ice-sheet covers the upper fluid. Here, both the floating ice-sheet and elastic sea-bed are approximated as thin elastic plates which follow the Euler-Bernoulli beam equation, as in the earlier problems. By assuming the fluid to be incompressible and inviscid following an irrotational motion, and then applying a perturbation technique, the first-order contribution to the velocity potentials in each layer is evaluated with the help of Fourier transform. Following that, the associated reflection and transmission coefficients are computed by carrying out the appropriate integration for integrals containing a shape function depicting the sea-bed undulation. The solutions of problems like these dealing with a deformable sea-bed will be beneficial in providing the required background to the researchers with respect to the incorporation of the characteristics of the infinite depth soil located below the sea-bed. This is in addition to its contribution in studying problems with a floating ice-sheet.

4.2 Formulation of scattering problem

Water wave propagation of small amplitude, in response to the action of gravity and assuming small-amplitude plate response, is considered in two incompressible, inviscid, immiscible superposed fluids undergoing an irrotational motion and flowing underneath

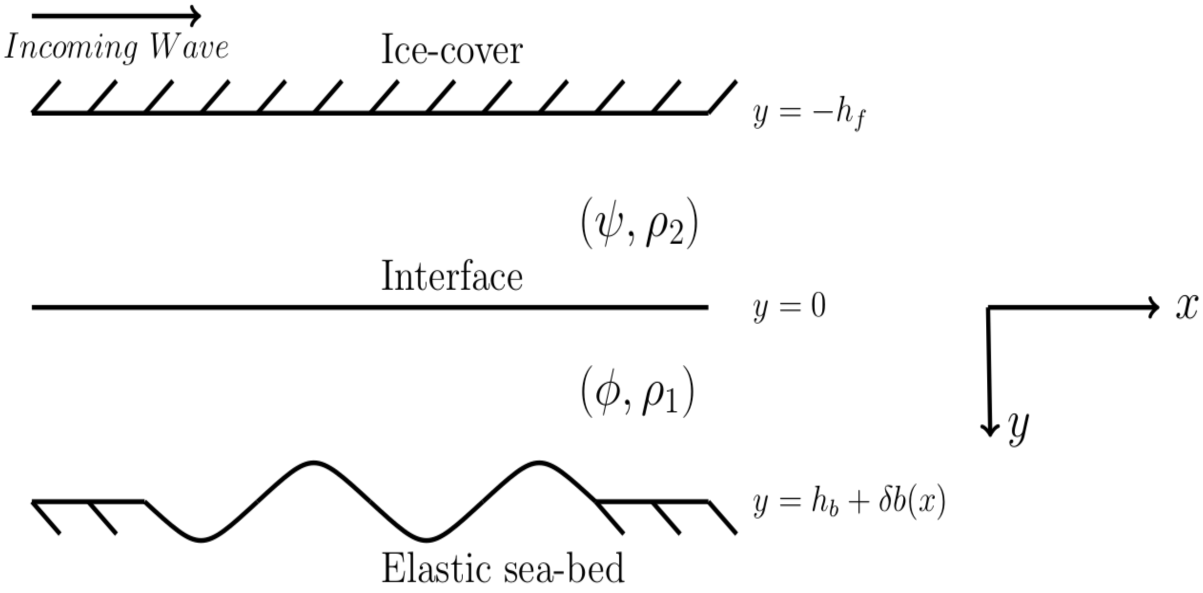

Figure 4.1: Schematic diagram depicting domain definition

an infinitely extended floating ice-sheet in horizontal directions in an ocean over an undulating elastic bed. Following Euler-Bernoulli beam equation, the floating ice-sheet and elastic sea-bed are considered to act as thin elastic plates, as has also been considered in the previous chapters.

A two-dimensional Cartesian coordinate system is adopted in such a way that the y-axis points in the vertical downward direction; $y = -h_f$ and $y = 0$, respectively, represent the location of the floating ice-sheet and the tranquil interface, as displayed in Fig. 4.1. It is assumed that a small undulation given by $y = h_b + \delta b(x)$, as described in Chapter 2, is located on the elastic sea-bed. Here, ρ_1 is the lower fluid density and $\rho_2(< \rho_1)$ is the upper fluid density and let the ratio $\rho_2/\rho_1(< 1)$ of the two fluid densities be designated by ρ. Adopting linear water wave theory and accounting for all the above assumptions, the time harmonic velocity potentials in the upper fluid and in the lower fluid can, respectively, be represented by $\Psi(x, y, t) = \text{Re}\{\psi(x, y) \exp(-\text{i}\omega t)\}$ and $\Phi(x, y, t) = \text{Re}\{\phi(x, y) \exp(-\text{i}\omega t)\}$ for normal wave incidence.

Now, the physical problem is modeled in which the velocity potentials ψ and ϕ, respectively, satisfy the Laplace's equation in the upper and lower fluids as follows:

$$\nabla^2_{x,y}\psi = 0, \ -\infty < x < \infty, \ -h_f \leq y \leq 0, \tag{4.1}$$

$$\nabla^2_{x,y}\phi = 0, \ -\infty < x < \infty, \ 0 \leq y \leq h_b + \delta b(x). \tag{4.2}$$

The relevant boundary condition at the upper surface, i.e., at the floating ice-sheet, is represented by

$$\left\{D_1\frac{\partial^4}{\partial x^4}+1-\epsilon_1 K\right\}\frac{\partial\psi}{\partial y}+K\psi=0 \quad \text{on} \quad y=-h_f, \tag{4.3}$$

where $D_1=(Q_1/\rho_1 g)$, $Q_1=E_1h_1^3/[12(1-\nu_1^2)]$ denoting the flexural rigidity of the ice-sheet; E_1 the Young's modulus; ν_1 the Poisson's ratio of the ice-sheet; $\epsilon_1=(\rho_f/\rho_2)h_1$ with ρ_f as the ice-sheet density and h_1 the ice-sheet thickness, which is considered to be very small.

The interfacial conditions at $y=0$ are given by

$$\frac{\partial\psi}{\partial y} = \frac{\partial\phi}{\partial y}, \tag{4.4}$$

$$K\psi+\frac{\partial\psi}{\partial y} = \frac{1}{\rho}\left(K\phi+\frac{\partial\phi}{\partial y}\right). \tag{4.5}$$

The boundary condition at the lower surface, i.e., at the elastic sea-bed, has the form

$$\left\{D_2\frac{\partial^4}{\partial x^4}+1-\epsilon_2 K\right\}\frac{\partial\phi}{\partial n}+K\phi=0 \quad \text{on} \quad y=h_b+\delta b(x), \tag{4.6}$$

with $D_2=(Q_2/\rho_2 g)$, where $Q_2=E_2h_2^3/[12(1-\nu_2^2)]$ is the flexural rigidity of the elastic sea-bed; E_2 and ν_2 are, respectively, Young's modulus and Poisson's ratio of the sea-bed; $\epsilon_2=(\rho_b/\rho_1)h_2$ where ρ_b denotes the elastic sea-bed density, h_2 denotes the elastic sea-bed thickness which is considered to be very small and $\frac{\partial}{\partial n}$ is the normal derivative to the sea-bed at any point (x,y).

The linearized condition (4.6), satisfied at the undulating bottom, can now be expressed (by ignoring the higher-order terms of δ) in the following form:

$$K\left[\phi+\delta b(x)\frac{\partial\phi}{\partial y}\right]+\left\{D_2\frac{\partial^4}{\partial x^4}+1-\epsilon_2 K\right\}\left[\frac{\partial\phi}{\partial y}-\delta\frac{\partial}{\partial x}\left\{b(x)\frac{\partial\phi}{\partial x}\right\}\right]+\ O(\delta^2)=0 \quad \text{on} \quad y=h_b. \tag{4.7}$$

Since the above converted condition is satisfied at a uniform depth instead of a varying depth, it will be much easier to solve the BVP now.

With the assumption of linear theory in two superposed fluids, progressive waves propagating in the two-layer fluid along the positive x-direction have the following forms in the respective layers:

$$\psi(x,y) = \exp(\pm iux)f_1(u,y) \quad \text{in} \quad -h_f\le y\le 0, \tag{4.8}$$

$$\phi(x,y) = \exp(\pm iux)f_2(u,y) \quad \text{in} \quad 0\le y\le h_b, \tag{4.9}$$

where

$$f_1(u,y) = \frac{(D_1u^4+1-\epsilon_1K)u\cosh u(y+h_f) - K\sinh u(y+h_f)}{(D_1u^4+1-\epsilon_1K)u\sinh uh_f - K\cosh uh_f}, \tag{4.10}$$

$$f_2(u,y) = \frac{K\sinh u(y-h_b) - (D_2u^4+1-\epsilon_2K)u\cosh u(y-h_b)}{K\cosh uh_b + (D_2u^4+1-\epsilon_2K)u\sinh uh_b}. \tag{4.11}$$

It is to be noted that the wavenumber u satisfies the following dispersion equation:

$$\triangle(u) \equiv 0, \tag{4.12}$$

where

$$\begin{aligned}\triangle(u) = &\Big[(D_1u^4+1-\epsilon_1K)u\tanh(uh_f) - K\Big]\Big[-(D_2u^4+1-\epsilon_2K)uK - K^2\tanh(uh_b)\\ &+(D_2u^4+1-\epsilon_2K)u^2\tanh(uh_b) + Ku\Big] - \rho\Big[(D_2u^4+1-\epsilon_2K)u\tanh(uh_b) + K\Big]\\ &\times\Big[(D_1u^4+1-\epsilon_1K)uK - K^2\tanh(uh_f) + (D_1u^4+1-\epsilon_1K)u^2\tanh(uh_f) - Ku\Big].\end{aligned} \tag{4.13}$$

It is obvious that $u = 0$ is a root of the dispersion equation (4.12) which has exactly two distinct positive and real zeros corresponding to a value of K, let them be m and M, where $0 < m < M$, in accordance with the propagating modes; four pairs of complex zeros that correspond to the non-propagating modes and also infinitely many purely imaginary zeros that relate to the evanescent modes. Since the existence of exactly two positive zeros m and M of (4.12) is evidently ensured, as also observed in the works of Saha and Bora [81] and Maiti and Mandal [60], there exist two wave modes (wavenumbers) with one propagating at the ice-sheet (say, flexural mode) and the other at the interface (say, interfacial mode), respectively, along the positive x-direction. Both wavenumbers exhibit increasing values when an increase in the values of the elastic parameter of the sea-bed is affected, and they decrease corresponding to increasing values of the elastic parameter of the floating ice-sheet.

The zeros of the complex dispersion equation (4.12) are evaluated through the use of contour plots for the purpose of interpreting the behaviours of the wavenumbers (as shown in Fig. 4.2). In order to compute these, the values of various parameters are considered in accordance with the following: upper layer depth $h_f = 10$ m, lower layer depth $h_b = 10$ m, $Kh_b = 0.5$, elastic parameters of the ice-sheet and the sea-bed are taken as $D_1/h_b^4 = 10^2$; $\epsilon_1/h_b = 0.0001$, and $D_2/h_b^4 = 10^2$, $\epsilon_2/h_b = 0.0001$, respectively, unless otherwise mentioned. A simple counting argument, as used in Fox and Squire [32], is followed here to find the nature of the zeros of (4.12). For finding the real zeros of

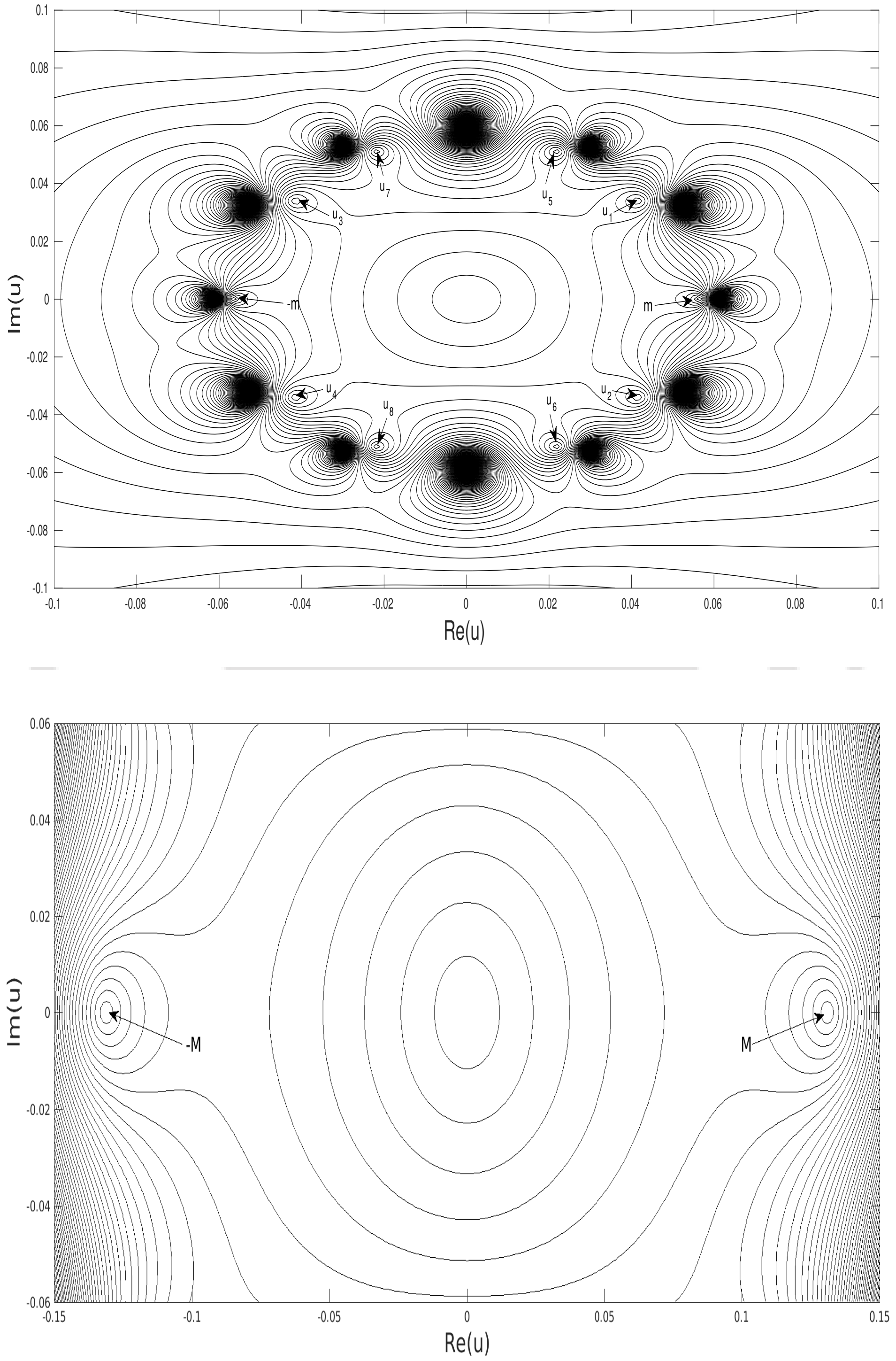

Figure 4.2: Contour plot of roots of dispersion relation (4.12)

the complex dispersion equation, Newton-Raphson method is used, and an initial guess for this method for each zero is acquired by utilizing a contour plot. From Fig. 4.2, it is noticed that two pairs of real zeros of opposite signs namely, $-m, m, -M$ and M, lie on the real axis and they can be referred to as the progressive wave modes in flexural modes and internal modes. The same feature related to those zeros was also observed by Das et al. [25] when they considered the flexural gravity wave motion over a poro-elastic bed in a two-layer fluid. Since the region of study is clearly symmetric about $x = 0$, it is considered to be sufficient to study the wave characteristics corresponding to $x \geq 0$ only. Figure 4.2 presents the nature of the complex zeros demonstrating that four pairs of complex zeros, occurring as positive and negative of a complex conjugate pair, namely, $u_1, u_2, u_3, u_4, u_5, u_6, u_7, u_8$, are located in such a way that there are two zeros in each of the quadrants. It needs to be mentioned that two pairs of complex zeros occur for the ice-sheet and another two pairs occur for the elastic sea-bed.

Progressive normal waves in correspondence with wavenumber m (flexural mode) can be represented by (where u in Eqs. (4.8) and (4.9) is replaced by m)

$$\begin{aligned} \psi_0(x,y) &= \exp(\pm imx) f_1(m,y) \quad \text{in } -h_f \leq y \leq 0, && (4.14)\\ \phi_0(x,y) &= \exp(\pm imx) f_2(m,y) \quad \text{in } \ 0 \leq y \leq h_b. && (4.15)\end{aligned}$$

Therefore, if a normal wave of wavenumber m proliferating from the negative x-direction interacts with the undulation of the sea-bed for a two-layer fluid flow, then reflection and and transmission occur for both flexural and interfacial modes. When the train of waves hits the bottom undulation, it experiences partial reflection and partial transmission, and accordingly the asymptotic behaviours of ψ and ϕ, respectively, can be expressed as

$$\psi(x,y) \sim \begin{cases} f_1(m,y)\Big[\exp(imx) + r^{(m)}\exp(-imx)\Big] + R^{(m)} f_1(M,y)\exp(-\mathrm{i}Mx), & x \to -\infty, \\[2ex] t^{(m)} f_1(m,y)\exp(imx) + T^{(m)} f_1(M,y)\exp(\mathrm{i}Mx), & x \to \infty, \end{cases} \tag{4.16}$$

$$\phi(x,y) \sim \begin{cases} f_2(m,y)\Big[\exp(imx) + r^{(m)}\exp(-imx)\Big] + R^{(m)} f_2(M,y)\exp(-\mathrm{i}Mx), & x \to -\infty, \\[2ex] t^{(m)} f_2(m,y)\exp(imx) + T^{(m)} f_2(M,y)\exp(\mathrm{i}Mx), & x \to \infty. \end{cases} \tag{4.17}$$

The undetermined coefficients $r^{(m)}$ and $R^{(m)}$ introduced in Eqs. (4.16) and (4.17), respectively, represent the reflection coefficients corresponding to the reflected waves of wavenumbers m and M for an incident wave of wavenumber m. In a similar manner,

$t^{(m)}$ and $T^{(m)}$, respectively, represent the transmission coefficients corresponding to the transmitted waves of wavenumbers m and M for an incident wave of wavenumber m.

Next, the progressive normal waves in correspondence with wavenumber M (interfacial mode) are given by

$$\psi_0(x,y) = \exp(\pm iMx) f_1(M,y) \quad \text{in} \quad -h_f \le y \le 0, \tag{4.18}$$

$$\phi_0(x,y) = \exp(\pm iMx) f_2(M,y) \quad \text{in} \quad 0 \le y \le h_b. \tag{4.19}$$

Accordingly, for a normal wave of wavenumber M, which is incident on the undulating sea-bed, the asymptotic forms of of ψ and ϕ, respectively, are as follows:

$$\psi(x,y) \sim \begin{cases} f_1(M,y)\Big[\exp(\mathrm{i}Mx) + R^{(M)}\exp(-\mathrm{i}Mx)\Big] + r^{(M)} f_1(m,y)\exp(-\mathrm{i}mx), \\ \hfill x \to -\infty, \\ t^{(M)} f_1(m,y)\exp(\mathrm{i}mx) + T^{(M)} f_1(M,y)\exp(\mathrm{i}Mx), \ x \to \infty, \end{cases} \tag{4.20}$$

$$\phi(x,y) \sim \begin{cases} f_2(M,y)\Big[\exp(\mathrm{i}Mx) + R^{(M)}\exp(-\mathrm{i}Mx)\Big] + r^{(M)} f_2(m,y)\exp(-\mathrm{i}mx), \\ \hfill x \to -\infty, \\ t^{(M)} f_2(m,y)\exp(\mathrm{i}mx) + T^{(M)} f_2(M,y)\exp(\mathrm{i}Mx), \ x \to \infty. \end{cases} \tag{4.21}$$

In Eqs. (4.20) and (4.21), the undetermined coefficients $r^{(M)}$ and $R^{(M)}$ represent the reflection coefficients related to the reflected wave of wavenumbers m and M, respectively, due to a normally incident waves of wavenumber M. Similarly, $t^{(M)}$ and $T^{(M)}$ represent the transmission coefficients corresponding to the transmitted waves of wavenumbers m and M, respectively, due to an incident wave of wavenumber M.

The process involved in evaluating the analytical values of these aforementioned coefficients for both the flexural and interfacial wave modes, for an arbitrary bottom topography, is not quite elementary. However, under the assumption of small bottom topography, a suitable perturbation expansion technique, as used in earlier chapters, can be used to obtain the first-order corrections to these undetermined coefficients.

The velocity potentials and the corresponding reflection and transmission coefficients for respective modes associated with the propagation of waves with different wavenumbers are going to be evaluated up to first-order in the following section.

4.3 Evaluation of velocity potentials and relevant coefficients

4.3.1 Perturbation method

Let a normal wave train of mode m be incident on the small undulation of an elastic sea-bed. For a sea-bed without any bottom distortion, the propagation of this wave train is not disturbed, i.e., only transmission takes place along the positive x-direction. However, when there some distortion is present on the sea-bed, the incident wave will undergo both reflection and transmission. With all available information and conditions, the velocity potentials ψ and ϕ, as well as the reflection coefficients $r^{(m)}$and $R^{(m)}$ and the transmission coefficients $t^{(m)}$ and $T^{(m)}$ can be written appropriately in perturbation series given by Eqs. (2.27)-(2.32) having perturbation parameter δ as was followed in Chapter 2.

Substituting the expansions presented by Eqs. (2.27)-(2.32) into Eqs. (4.1)-(4.5), (4.7), (4.16)-(4.17) and comparing the first-order terms of the perturbation parameter δ from both sides of the equations, a new coupled boundary value problem in first-order velocity potentials ψ_1 and ϕ_1 is formulated as follows:

$$\nabla^2_{x,y}\psi_1 = 0 \quad \text{in} \quad -h_f \le y \le 0, \tag{4.22}$$

$$\nabla^2_{x,y}\phi_1 = 0 \quad \text{in} \quad 0 \le y \le h_b, \tag{4.23}$$

$$K\psi_1 + \left\{D_1\frac{\partial^4}{\partial x^4} + 1 - \epsilon_1 K\right\}\frac{\partial \psi_1}{\partial y} = 0 \quad \text{on} \quad y = -h_f, \tag{4.24}$$

$$\frac{\partial \phi_1}{\partial y} = \frac{\partial \psi_1}{\partial y} \quad \text{on} \quad y = 0, \tag{4.25}$$

$$\rho\left(K\psi_1 + \frac{\partial \psi_1}{\partial y}\right) = K\phi_1 + \frac{\partial \phi_1}{\partial y} \quad \text{on} \quad y = 0, \tag{4.26}$$

$$K\phi_1 + \left\{D_2\frac{\partial^4}{\partial x^4} + 1 - \epsilon_2 K\right\}\frac{\partial \phi_1}{\partial y} = Q(x,y) \quad \text{on} \quad y = h_b. \tag{4.27}$$

Now we get

$$Q(x,h_b) = q(x) = f_2(m,h_b)\left[D_2\frac{\partial^4}{\partial x^4} + 1 - \epsilon_2 K\right]\left\{\mathrm{i}m\frac{\partial}{\partial x}\Big(b(x)\exp(\mathrm{i}mx)\Big)\right\} - Kb(x)\exp(\mathrm{i}mx)\left[\frac{\mathrm{d}}{\mathrm{d}y}\Big\{f_2(m,y)\Big\}\right]_{y=h_b}. \tag{4.28}$$

Moreover, $\psi_1(x,y)$ and $\phi_1(x,y)$ have following asymptotic forms:

$$\psi_1(x,y) \sim \begin{cases} r_1^{(m)} f_1(m,y)\exp(-\mathrm{i}mx) + R_1^{(m)} f_1(M,y)\exp(-\mathrm{i}Mx), & \text{as } x \to -\infty, \\ t_1^{(m)} f_1(m,y)\exp(\mathrm{i}mx) + T_1^{(m)} f_1(M,y)\exp(\mathrm{i}Mx), & \text{as } x \to \infty, \end{cases} \tag{4.29}$$

$$\phi_1(x,y) \sim \begin{cases} r_1^{(m)} f_2(m,y)\exp(-\mathrm{i}mx) + R_1^{(m)} f_2(M,y)\exp(-\mathrm{i}Mx), \ \text{as } x \to -\infty, \\ \\ t_1^{(m)} f_2(m,y)\exp(\mathrm{i}mx) + T_1^{(m)} f_2(M,y)\exp(\mathrm{i}Mx), \quad \text{as } x \to \infty. \end{cases} \tag{4.30}$$

4.3.2 Boundary value problems in ψ_1 and ϕ_1

The boundary value problem for the first-order velocity potentials ψ_1 and ϕ_1, as presented by Eqs. (4.22)-(4.28), along with the asymptotic forms (4.29)-(4.30), is now split into two separate boundary value problems for ψ_1 and ϕ_1.

Boundary value problem I for ψ_1:

$$\nabla^2_{x,y}\psi_1 = 0 \quad \text{in} \quad -h_f \le y \le 0, \tag{4.31}$$

$$K\psi_1 + \left\{D_1\frac{\partial^4}{\partial x^4} + 1 - \epsilon_1 K\right\}\frac{\partial\psi_1}{\partial y} = 0 \quad \text{on} \quad y = -h_f, \tag{4.32}$$

$$\frac{\partial\psi_1}{\partial y} = \eta(x) \quad \text{on} \quad y = 0, \tag{4.33}$$

with known $\eta(x)$ on $y = 0$.

Further, ψ_1 possesses the following far-field behaviour:

$$\psi_1(x,y) \sim \begin{cases} r_1^{(m)} f_1(m,y)\exp(-\mathrm{i}mx) + R_1^{(m)} f_1(M,y)\exp(-\mathrm{i}Mx), \ \text{as } x \to -\infty, \\ \\ t_1^{(m)} f_1(m,y)\exp(\mathrm{i}mx) + T_1^{(m)} f_1(M,y)\exp(\mathrm{i}Mx), \quad \text{as } x \to \infty. \end{cases} \tag{4.34}$$

Boundary value problem II for ϕ_1:

$$\nabla^2_{x,y}\phi_1 = 0 \quad \text{in} \quad 0 \le y \le h_b, \tag{4.35}$$

$$\frac{\partial\phi_1}{\partial y} = \eta(x) \quad \text{on} \quad y = 0, \tag{4.36}$$

$$K\phi_1 + \left\{D_2\frac{\partial^4}{\partial x^4} + 1 - \epsilon_2 K\right\}\frac{\partial\phi_1}{\partial y} = q(x) \quad \text{on} \quad y = h_b, \tag{4.37}$$

with ϕ_1 having the asymptotic behaviour

$$\phi_1(x,y) \sim \begin{cases} r_1^{(m)} f_2(m,y)\exp(-\mathrm{i}mx) + R_1^{(m)} f_2(M,y)\exp(-\mathrm{i}Mx), \ \text{as } x \to -\infty, \\ \\ t_1^{(m)} f_2(m,y)\exp(\mathrm{i}mx) + T_1^{(m)} f_2(M,y)\exp(\mathrm{i}Mx), \quad \text{as } x \to \infty. \end{cases} \tag{4.38}$$

By utilizing Eqs. (4.33) and (4.36), Eq. (4.26) may now be described as follows:

$$K(\phi_1-\rho\psi_1)=(\rho-1)\eta(x) \quad \text{on} \quad y=0. \tag{4.39}$$

4.3.3 Application of Fourier transform

In order to solve the above two **Boundary value problems**, the technique of Fourier transform is adopted. Utilization of Fourier transform, as defined in Chapter 2, to Eqs. (4.31)-(4.33) gives rise to the following BVP for $\overline{\psi}_1$:

$$\begin{aligned}\overline{\psi}_{1yy}-\gamma^2\overline{\psi}_1 &= 0 \quad \text{in} \quad -h_f\le y\le 0, && (4.40)\\ K\overline{\psi}_1+\Big\{D_1\gamma^4+1-\epsilon_1K\Big\}\overline{\psi}_{1y} &= 0 \quad \text{on} \quad y=-h_f, && (4.41)\\ \overline{\psi}_{1y} &= \bar{\eta}(\gamma) \quad \text{on} \quad y=0, && (4.42)\end{aligned}$$

where $\bar{\eta}(\gamma)$ is the Fourier transform of $\eta(x)$. After following the usual procedures, the above BVP given by (4.40)-(4.42) is solved as

$$\overline{\psi}_1(\gamma,y)=\frac{[(D_1\gamma^4+1-\epsilon_1K)\gamma\cosh\gamma(y+h_f)-K\sinh\gamma(y+h_f)]}{(D_1\gamma^4+1-\epsilon_1K)\gamma\sinh\gamma h_f-K\cosh\gamma h_f}\frac{\bar{\eta}(\gamma)}{\gamma}. \tag{4.43}$$

In a similar manner, Eqs. (4.35)-(4.37) are converted to a BVP for $\overline{\phi}_1$ as follows:

$$\begin{aligned}\overline{\phi}_{1yy}-\gamma^2\overline{\phi}_1 &= 0 \quad \text{in} \quad 0\le y\le h_b, && (4.44)\\ \overline{\phi}_{1y} &= \bar{\eta}(\gamma) \quad \text{on} \quad y=0, && (4.45)\\ K\overline{\phi}_1+(D_2\gamma^4+1-\epsilon_2K)\overline{\phi}_{1y} &= \bar{q}(\gamma) \quad \text{on} \quad y=h_b, && (4.46)\end{aligned}$$

where the Fourier transform $\bar{q}(\gamma)$ of $q(x)$ is

$$\bar{q}(\gamma)=S(\gamma,m)\int_{-\infty}^{\infty}b(x)e^{i(m-\gamma)x}\mathrm{d}x, \tag{4.47}$$

with

$$S(\gamma,m)=-m\gamma^5D_2f_2(m,h_b)-m\gamma(1-\epsilon_2K)f_2(m,h_b)-K\left[\frac{\mathrm{d}}{\mathrm{d}y}\Big\{f_2(m,y)\Big\}\right]_{y=h_b}. \tag{4.48}$$

The solution of the BVP given by (4.44)-(4.46) is found as follows:

$$\overline{\phi}_1(\gamma,y)=\frac{\gamma\bar{q}(\gamma)\cosh\gamma y-\bar{\eta}(\gamma)[K\sinh\gamma(h_b-y)+(D_2\gamma^4+1-\epsilon_2K)\gamma\cosh\gamma(h_b-y)]}{\gamma[K\cosh\gamma h_b+(D_2\gamma^4+1-\epsilon_2K)\gamma\sinh\gamma h_b]}, \tag{4.49}$$

where $\bar{\eta}(\gamma)$ is determined by first applying Fourier transform to Eq. (4.39):

$$K(\overline{\phi}_1 - \rho\overline{\psi}_1) = (\rho - 1)\bar{\eta}(\gamma) \quad \text{on} \quad y = 0, \tag{4.50}$$

and then using (4.43) and (4.49) into Eq. (4.50) to get

$$\bar{\eta}(\gamma) = -\frac{K\gamma[(D_1\gamma^4 + 1 - \epsilon_1 K)\gamma \sinh \hat{\gamma} h_f + K\cosh \gamma h_f]\bar{q}(\gamma)}{\triangle(\gamma)}, \tag{4.51}$$

where the function $\triangle(\gamma)$ is of the form given by (4.13). It is observed from Eq. (4.12) that $\triangle(\gamma)$ possesses only two non-zero positive zeros m and M on the real γ-axis. Now upon substitution of $\bar{\eta}(\gamma)$ into Eqs. (4.43) and (4.49), and then employing inverse Fourier transform, the expressions for $\psi_1(x, y)$ and $\phi_1(x, y)$ are acquired, respectively, in the following forms:

$$\psi_1(x, y) = \frac{K}{2\pi}\int_{-\infty}^{\infty} \frac{[K\sinh\gamma(y + h_f) - (D_1\gamma^4 + 1 - \epsilon_1 K)\gamma\cosh\gamma(y + h_f)]}{\triangle(\gamma)}\bar{q}(\gamma)e^{\mathrm{i}\gamma x}\mathrm{d}\gamma, \tag{4.52}$$

$$\phi_1(x, y) = \frac{1}{2\pi}\int_{-\infty}^{\infty} \frac{[\cosh\gamma y + \frac{K[(D_1\gamma^4+1-\epsilon_1 K)\sinh\gamma h_f + K\cosh\gamma h_f]}{\triangle(\gamma)}G(\gamma, y)]}{[K\cosh\gamma h_b + (D_2\gamma^4 + 1 - \epsilon_2 K)\gamma\sinh\gamma h_b]}\bar{q}(\beta)e^{\mathrm{i}\gamma x}\mathrm{d}\gamma, \tag{4.53}$$

where

$$G(\gamma, y) = (D_2\gamma^4 + 1 - \epsilon_2 K)\gamma\cosh\gamma(h_b - y) + K\sinh\gamma(h_b - y).$$

Since $\triangle(\gamma)$ has two non-zero positive zeros $\gamma_1 = m$ and $\gamma_2 = M$, respectively, on the positive real axis of γ, the above integrals in (4.52) and (4.53) contain two simple poles at γ_1 and γ_2. As a result, it is necessary that the path of integration in (4.52) and (4.53) is to be indented beneath the poles at $\gamma_1 = m$ and $\gamma_2 = M$.

4.3.4 Determination of relevant coefficients

The first-order reflection and transmission coefficients $r_1^{(m)}$, $t_1^{(m)}$and $R_1^{(m)}$, $T_1^{(m)}$ corresponding to the flexural and interfacial modes for a normally incident proliferating wave of mode m are calculated by integrating with respect to γ in Eqs. (4.52) or (4.53), and then by letting $x \to \pm\infty$ and then comparing with those in the asymptotic expressions for the velocity potentials from Eqs. (4.34) or (4.38) gives the values.

In order to obtain the first-order reflection coefficients, we consider $x \to -\infty$ in either Eq. (4.52) or Eq. (4.53). When $x \to -\infty$, the behaviour of $\psi_1(x, y)$ or $\phi_1(x, y)$ is studied through a rotation of the path of the integral, which contains the term $\bar{q}(-\gamma)$, into a contour in the first quadrant so that the residue terms at the poles γ_1 and γ_2 can be incorporated. Similarly, the path of the integral containing the term $\bar{q}(\gamma)$ in Eq. (4.52) or Eq. (4.53) is rotated into a contour, this time in the fourth quadrant, so that there is no contribution from this integral when $x \to -\infty$. Subsequently, after comparing the resultant integral with Eq. (4.34) or Eq. (4.38), the eventual expressions for $r_1^{(m)}$ and $R_1^{(m)}$ can, respectively, be obtained as

$$\begin{aligned} r_1^{(m)} &= \frac{iK\Big[K\cosh mh_f - (D_1m^4+1-\epsilon_1K)m\sinh mh_f\Big]\bar{q}(-m)}{\triangle'(m)} \\ &= \frac{iK\Big[K\cosh mh_f - (D_1m^4+1-\epsilon_1K)m\sinh mh_f\Big]S(-m,m)}{\triangle'(m)}\int_{-\infty}^{\infty} e^{2\mathrm{i}mx}b(x)\mathrm{d}x, \end{aligned} \tag{4.54}$$

$$\begin{aligned} R_1^{(m)} &= \frac{iK\Big[K\cosh Mh_f - (D_1M^4+1-\epsilon_1K)M\sinh Mh_f\Big]\bar{q}(-M)}{\triangle'(M)} \\ &= \frac{iK\Big[K\cosh Mh_f - (D_1M^4+1-\epsilon_1K)M\sinh Mh_f\Big]S(-M,m)}{\triangle'(M)} \\ &\times \int_{-\infty}^{\infty} e^{\mathrm{i}(m+M)x}b(x)\mathrm{d}x. \end{aligned} \tag{4.55}$$

Adopting a similar procedure, the first-order transmission coefficients are evaluated by letting $x \to \infty$ in either Eq. (4.52) or Eq. (4.53). As $x \to \infty$, the behaviour of $\psi_1(x,y)$ or $\phi_1(x,y)$ is studied in a similar manner as done for the case $x \to -\infty$. Because of the fact that the integral containing the term $\bar{q}(-\gamma)$ makes no contribution when $x \to \infty$, subsequently by comparison of the resultant integral with expressions in Eq. (4.34) or Eq. (4.38), the coefficients $t_1^{(m)}$ and $T_1^{(m)}$ can, respectively, be expressed as follows:

$$\begin{aligned} t_1^{(m)} &= \frac{iK\Big[K\cosh mh_f - (D_1m^4+1-\epsilon_1K)m\sinh mh_f\Big]\bar{q}(m)}{\triangle'(m)} \\ &= \frac{iK\Big[K\cosh mh_f - (D_1m^4+1-\epsilon_1K)m\sinh mh_f\Big]S(m,m)}{\triangle'(m)}\int_{-\infty}^{\infty} b(x)\mathrm{d}x, \end{aligned} \tag{4.56}$$

$$\begin{aligned} T_1^{(m)} &= \frac{iK\Big[K\cosh Mh_f - (D_1M^4+1-\epsilon_1K)M\sinh Mh_f\Big]\bar{q}(M)}{\triangle'(M)} \\ &= \frac{iK\Big[K\cosh Mh_f - (D_1M^4+1-\epsilon_1K)M\sinh Mh_f\Big]S(M,m)}{\triangle'(M)} \\ &\times \int_{-\infty}^{\infty} e^{\mathrm{i}(m-M)x}b(x)\mathrm{d}x. \end{aligned} \tag{4.57}$$

As the next step forward, a train of normal waves of mode M is considered to be incident on the undulating elastic sea-bed. Then, the coefficients $r_1^{(M)}$, $R_1^{(M)}$, $t_1^{(M)}$ and $T_1^{(M)}$ are calculated by following the same procedure that was applied earlier for wave mode m. In this case, these coefficients are found as

$$\begin{aligned} r_1^{(M)} &= \frac{iK\Big[K\cosh mh_f - (D_1m^4+1-\epsilon_1K)m\sinh mh_f\Big]S(-m,M)}{\triangle'(m)} \\ &\times \int_{-\infty}^{\infty} e^{\mathrm{i}(M+m)x} b(x)\mathrm{d}x, \qquad (4.58) \\ R_1^{(M)} &= \frac{iK\Big[K\cosh Mh_f - (D_1M^4+1-\epsilon_1K)M\sinh Mh_f\Big]S(-M,M)}{\triangle'(M)} \\ &\times \int_{-\infty}^{\infty} e^{2\mathrm{i}Mx} b(x)\mathrm{d}x, \qquad (4.59) \\ t_1^{(M)} &= \frac{iK\Big[K\cosh mh_f - (D_1m^4+1-\epsilon_1K)m\sinh mh_f\Big]S(m,M)}{\triangle'(m)} \\ &\times \int_{-\infty}^{\infty} e^{\mathrm{i}(M-m)x} b(x)\mathrm{d}x, \qquad (4.60) \\ T_1^{(M)} &= \frac{iK\Big[K\cosh Mh_f - (D_1M^4+1-\epsilon_1K)M\sinh Mh_f\Big]S(M,M)}{\triangle'(M)} \\ &\times \int_{-\infty}^{\infty} b(x)\mathrm{d}x. \qquad (4.61) \end{aligned}$$

It can be observed that all these above coefficients are expressed in integral form which contains the uneven bed shape function $b(x)$, and hence these can be computed for a given shape function. In the next section, the consequence of reflection and transmission is going to be investigated by considering a sinusoidal ripple bed.

4.4 Special form of the undulating sea-bed

Here, we consider the same special sinusoidal form of the shape function $b(x)$ for the uneven bottom surface, as was considered as Eq. (2.75) in Chapter 2.

Suppose that the normal proliferating waves with wavenumber m (flexural mode) encounter the small undulation located on the elastic sea-bed under consideration. The first-order reflection and transmission coefficients $r_1^{(m)}$, $R_1^{(m)}$, $t_1^{(m)}$ and $T_1^{(m)}$, corresponding to the flexural and interfacial modes due to a normally incident propagating wave of mode m, are calculated by substituting $b(x)$ from Eq. (2.75) into Eqs. (4.54)-(4.57). In this case, the coefficient $t_1^{(m)}$ vanishes identically and the rest three coefficients are found as

$$\begin{aligned} r_1^{(m)} &= (-1)^n \frac{2aKl\Big[K\cosh mh_f - (D_1m^4 + 1 - \epsilon_1 K)m\sinh mh_f\Big]}{\triangle'(m)} \\ &\quad\times \frac{S(-m,m)\sin(\frac{2mn\pi}{l})}{l^2 - 4m^2}, \end{aligned} \tag{4.62}$$

$$\begin{aligned} R_1^{(m)} &= (-1)^n \frac{2aKl\Big[K\cosh Mh_f - (D_1M^4 + 1 - \epsilon_1 K)M\sinh Mh_f\Big]}{\triangle'(M)} \\ &\quad\times \frac{S(-M,m)\sin\left(\frac{(m+M)n\pi}{l}\right)}{l^2 - (m+M)^2}, \end{aligned} \tag{4.63}$$

$$\begin{aligned} T_1^{(m)} &= (-1)^n \frac{2aKl\Big[K\cosh Mh_f - (D_1M^4 + 1 - \epsilon_1 K)M\sinh Mh_f\Big]}{\triangle'(M)} \\ &\quad\times \frac{S(M,m)\sin\left(\frac{(m-M)n\pi}{l}\right)}{l^2 - (m-M)^2}. \end{aligned} \tag{4.64}$$

Next, the normal propagating waves with wavenumber M (interfacial mode) is considered to be incident on the bottom undulation. Following a similar procedure, the first-order reflection and transmission coefficients $r_1^{(M)}$, $R_1^{(M)}$, $t_1^{(M)}$ and $T_1^{(M)}$ for the normally incident proliferating wave of mode M are calculated by putting $b(x)$ into Eqs. (4.58)-(4.61). This time the coefficient $T_1^{(M)}$ vanishes identically and the other three coefficients are found as follows:

$$\begin{aligned} r_1^{(M)} &= (-1)^n \frac{2aKl\Big[K\cosh mh_f - (D_1m^4 + 1 - \epsilon_1 K)m\sinh mh_f\Big]}{\triangle'(m)} \\ &\quad\times \frac{S(-m,M)\sin\left(\frac{(m+M)n\pi}{l}\right)}{l^2 - (m+M)^2}, \end{aligned} \tag{4.65}$$

$$\begin{aligned} R_1^{(M)} &= (-1)^n \frac{2aKl\Big[K\cosh Mh_f - (D_1M^4 + 1 - \epsilon_1 K)M\sinh Mh_f\Big]}{\triangle'(M)} \\ &\quad\times \frac{S(-M,M)\sin(\frac{2Mn\pi}{l})}{l^2 - 4M^2}, \end{aligned} \tag{4.66}$$

$$\begin{aligned} t_1^{(M)} &= (-1)^n \frac{2aKl\Big[K\cosh mh_f - (D_1m^4 + 1 - \epsilon_1 K)m\sinh mh_f\Big]}{\triangle'(m)} \\ &\quad\times \frac{S(m,M)\sin\left(\frac{(M-m)n\pi}{l}\right)}{l^2 - (M-m)^2}. \end{aligned} \tag{4.67}$$

It can be observed from Eqs. (4.62)-(4.67) that, for a fixed number of ripples n, an oscillatory nature is exhibited in these first-order coefficients. Additionally, it is noticed from (4.62) that in the event of the ripple wavenumber l and the incident wavenumber m satisfying the relation $l = 2m$, the theory adopted here ceases and consequently, generation of a large amount of reflected wave energy created by the undulating sea-bed is visible in the neighbourhood of this singularity. The implication is that resonant interaction occurs between the incident wave and the sinusoidal ripples. Furthermore, resonant interaction can occur between the incident wave and the ripple bed, specifically when $l = m + M$ and $l = m - M$, respectively, in (4.63) and (4.64). Similarly, resonance due to an incident wave of wavenumber M can be taken up. It is seen that with occurrence of resonance, the highest peak value of each coefficient has a linear variation with respect to ripple number n. Moreover, those coefficients are also dependent on the values of elasticity parameters D_1, ϵ_1 of the ice-sheet and D_2, ϵ_2 of the elastic sea-bed.

The computation of the coefficients given by (4.62)-(4.67) is performed with an eye to investigate the role of various parameters in the variation of wave energy in response to reflection and transmission.

4.5 Results and discussion

By devising an appropriate MATLAB program, the influence of various parameters such as elastic parameters of the ice-sheet and the sea-bed, the number of ripples of the undulation etc. on reflection as well as transmission coefficients, for a patch of sinusoidal ripples on an elastic sea-bed, is examined. The essential goal of the present investigation is to identify the pattern of incident wave energy distribution between the reflected and transmitted waves. The graphs and the related interpretation for the evaluated first-order reflection and transmission coefficients corresponding to the interfacial and flexural wave mode are presented for various values of different non-dimensional parameters. For computing purpose, the following values are considered: $\rho = 0.5$, $h_b/h_f = 1$, $lh_b = 1$, $a/h_b = 0.1$, $\epsilon_1/h_b = 0.0001, \epsilon_2/h_b = 0.0001$, unless otherwise mentioned.

In Figs. 4.3-4.11, the reflection and transmission coefficients are demonstrated versus non-dimensional wavenumber Kh_b for the variation of various parameters in accordance with a normally incident wave of mode m (flexural mode) on the undulating sea-bed. In Figs. 4.3-4.5, the graphs are plotted for various number of ripples (n) where the values of the elastic parameters of the ice-sheet and the sea-bed are considered as $D_1/h_b^4 = 1$ and $D_2/h_b^4 = 1$, respectively. From Fig. 4.3, it is noted that the utmost values of the reflection coefficient $|r_1^{(m)}|$ due to the flexural wave influence for an incident wave of mode m (i.e., for flexural wave mode) striking the undulation normally increases in accordance with an increase in the values of n. Further, it seems obvious from Figs. 4.4 and 4.5 that the utmost values for both the reflection and transmission coefficients of the waves, due to the interfacial wave influence for a normally incident proliferating wave of wavenumber

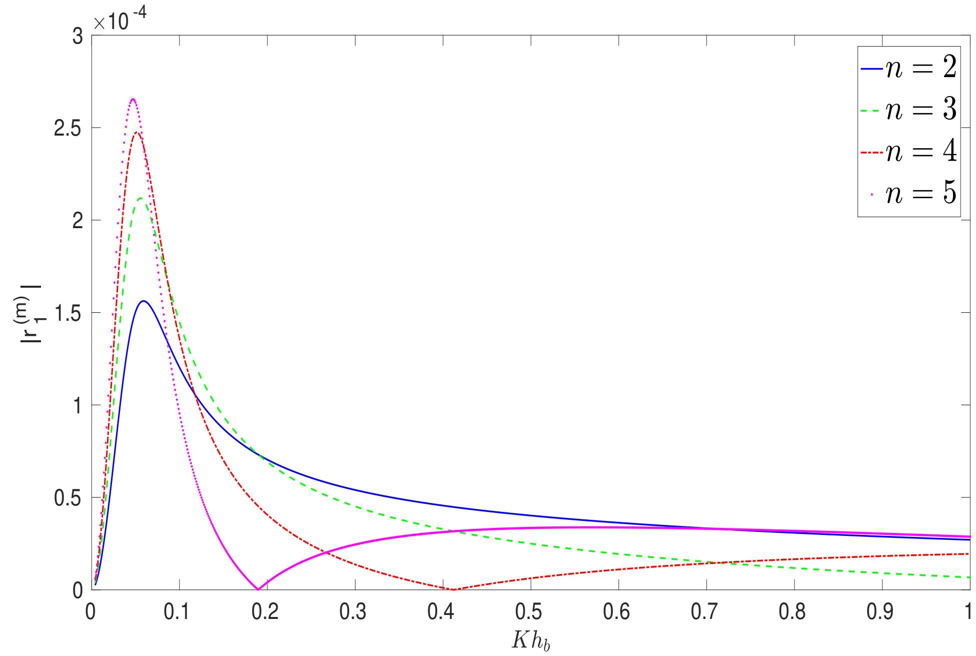

Figure 4.3: Variation of $|r_1^{(m)}|$ versus Kh_b for different number of ripples corresponding to flexural wave mode with $\rho = 0.5$, $h_b/h_f = 1$, $lh_b = 1$, $a/h_b = 0.1$, $D_1/h_b^4 = 1$, $D_2/h_b^4 = 1$, $\epsilon_1/h_b = 0.0001, \epsilon_2/h_b = 0.0001$.

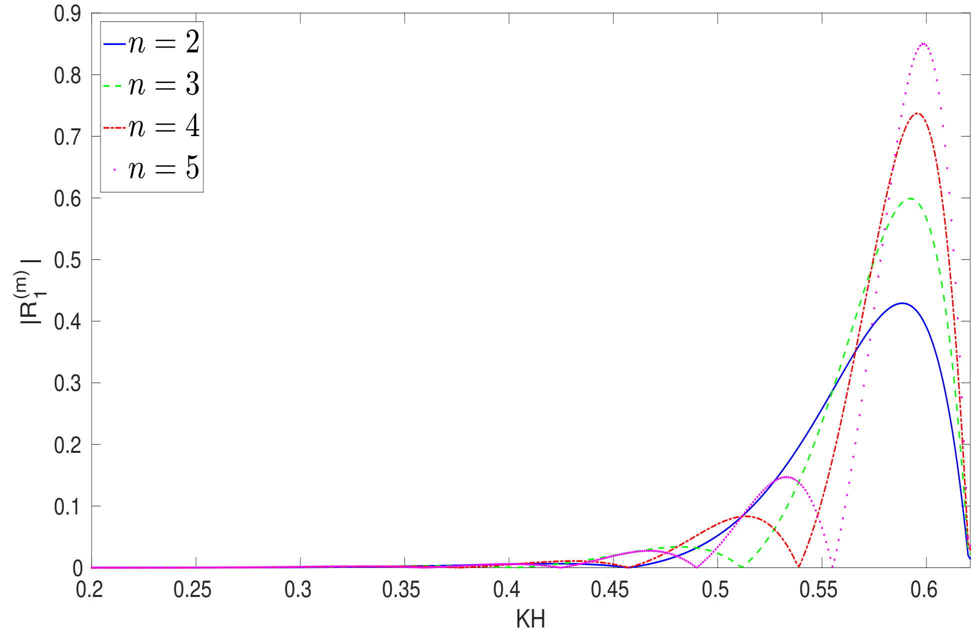

Figure 4.4: Variation of $|R_1^{(m)}|$ versus Kh_b for different number of ripples corresponding to flexural wave mode with $\rho = 0.5$, $h_b/h_f = 1$, $lh_b = 1$, $a/h_b = 0.1$, $D_1/h_b^4 = 1$, $D_2/h_b^4 = 1$, $\epsilon_1/h_b = 0.0001, \epsilon_2/h_b = 0.0001$

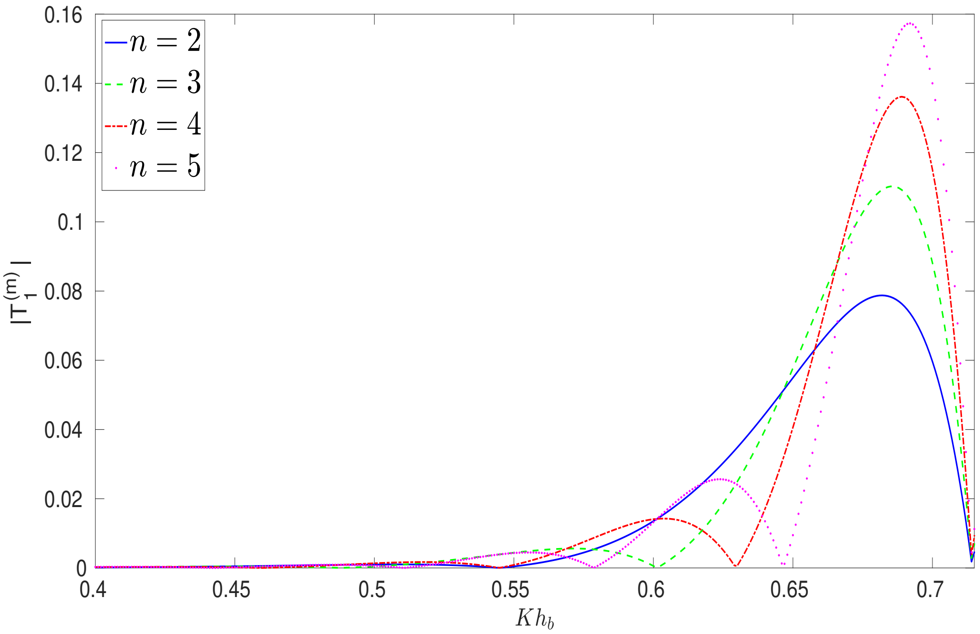

Figure 4.5: Variation of $|T_1^{(m)}|$ versus Kh_b for different number of ripples corresponding to flexural wave mode with $\rho = 0.5$, $h_b/h_f = 1$, $lh_b = 1$, $a/h_b = 0.1$, $D_1/h_b^4 = 1$, $D_2/h_b^4 = 1$, $\epsilon_1/h_b = 0.0001, \epsilon_2/h_b = 0.0001$

m, increase when the value of n increases. It is worthwhile to note that if the value of n rises, then the coefficients corresponding to reflection and transmission turn out to be unbounded for some specific values of Kh_b. This is what Bragg resonance is - as mentioned earlier. If the value of n rises, the graphs of reflection coefficient $|R_1^{(m)}|$ and transmission coefficient $|T_1^{(m)}|$, with regard to Kh_b, show a significant oscillatory pattern with the increase of number of zeros. Such an oscillatory behaviour arises as a result of the proliferating incident wave interacting multiple times with the undulating elastic sea-bed, the ice-sheet and the interface. Figure 4.4 shows that the utmost values of the first-order reflection coefficient are higher as compared to those in the example of Maiti and Mandal [60]. This may have resulted because of the association of an elastic sea-bed instead of an impermeable sea-bed.

Figures 4.6-4.8 show the curves for reflection and transmission coefficients $|r_1^{(m)}|$, $|R_1^{(m)}|$ and $|T_1^{(m)}|$ corresponding to different sets of values of the elastic parameters of the ice-sheet, namely, $D_1/h_b^4 = 1, 2, 3$ and 4, $n = 4$ and elastic parameter of the sea-bed taken as $D_2/h_b^4 = 1$. It can be seen from Fig. 4.6 that, the values of the reflection coefficient $|r_1^{(m)}|$ for waves with wavenumber m, i.e., for flexural mode, due to a normal incident wave of wavenumber m, reduce for increasing values of the elastic parameter D_1/h_b^4 of the ice-sheet. Next, Figs. 4.7 and 4.8, respectively, demonstrate the first-order reflection and transmission coefficients of interfacial wave mode, i.e., for wavenumber M due to a

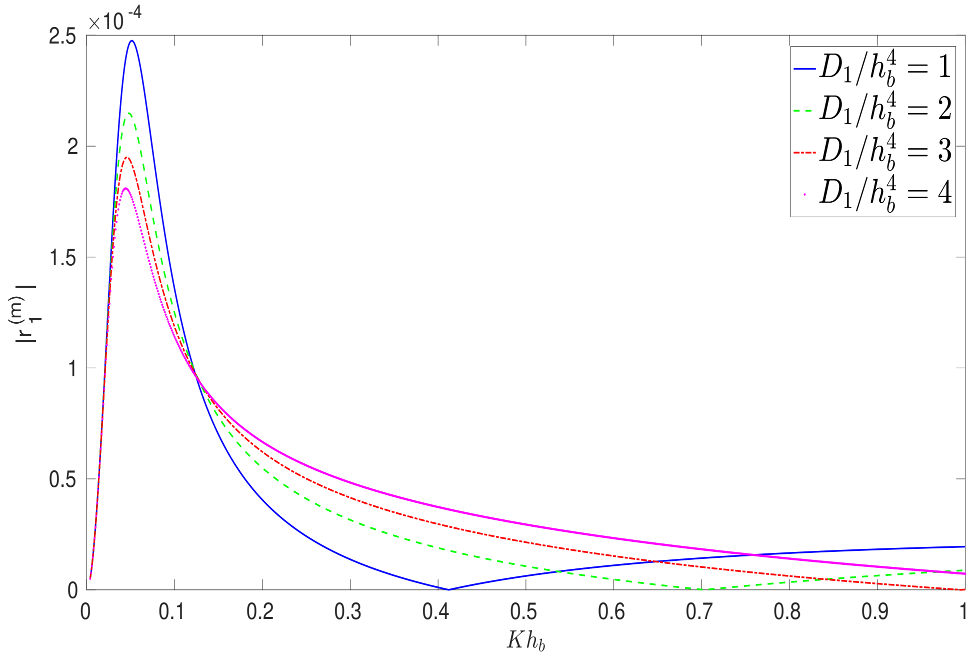

Figure 4.6: Variation of $|r_1^{(m)}|$ versus Kh_b for different ice parameter values corresponding to flexural wave mode with $\rho = 0.5$, $h_b/h_f = 1$, $lh_b = 1$, $a/h_b = 0.1$, $n = 4$, $D_2/h_b^4 = 1$, $\epsilon_1/h_b = 0.0001, \epsilon_2/h_b = 0.0001$

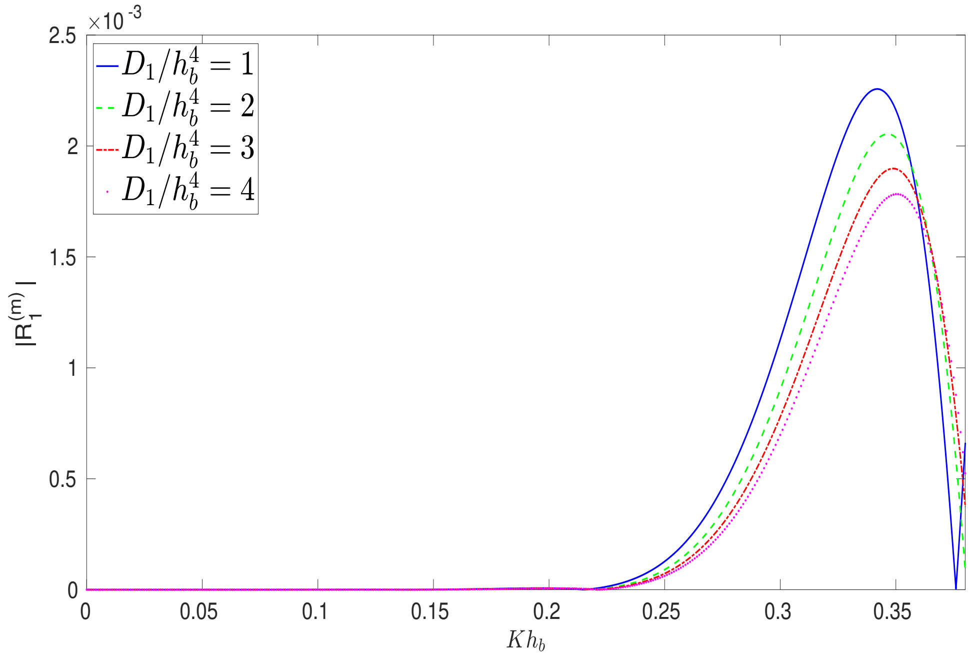

Figure 4.7: Variation of $|R_1^{(m)}|$ versus Kh_b for different ice parameter values corresponding to flexural wave mode with $\rho = 0.5$, $h_b/h_f = 1$, $lh_b = 1$, $a/h_b = 0.1$, $n = 4$, $D_2/h_b^4 = 1$, $\epsilon_1/h_b = 0.0001, \epsilon_2/h_b = 0.0001$

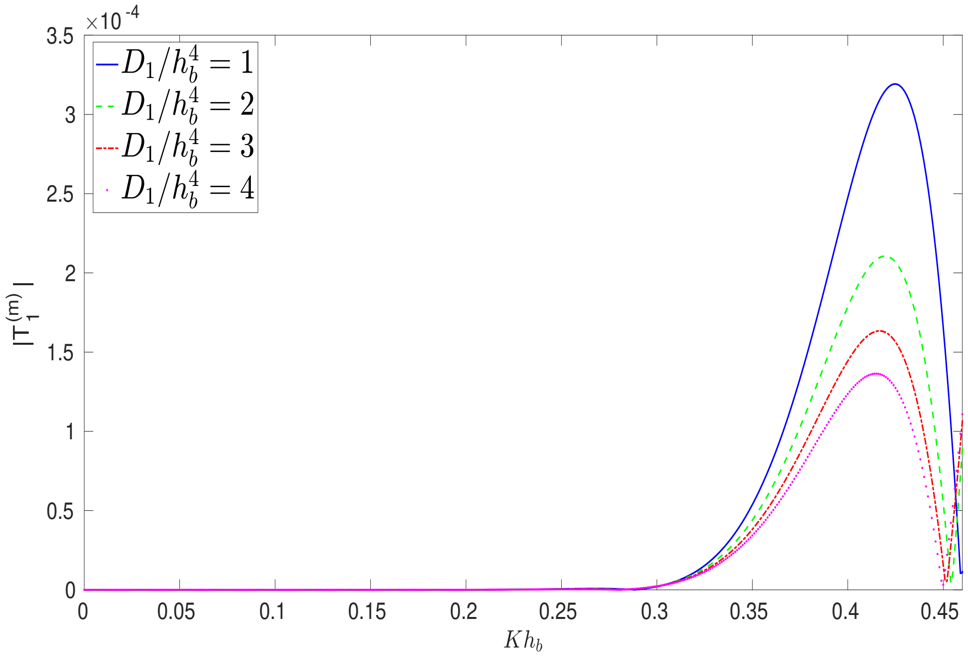

Figure 4.8: Variation of $|T_1^{(m)}|$ versus Kh_b for different ice parameter values corresponding to flexural wave mode with $\rho = 0.5$, $h_b/h_f = 1$, $lh_b = 1$, $a/h_b = 0.1$, $n = 4$, $D_2/h_b^4 = 1$, $\epsilon_1/h_b = 0.0001, \epsilon_2/h_b = 0.0001$

normal incident proliferating wave of wavenumber m. It is exhibited that, for increasing values of the elastic parameter of the ice-sheet, both $|R_1^{(m)}|$ and $|T_1^{(m)}|$ decrease. Non-zero values of both the first-order reflection coefficient and the first-order transmission coefficient exist due to the reflected waves and the transmitted waves, respectively, with wavenumber M corresponding to various values of the elastic parameter of the ice-sheet. It establishes that energy conversion is always possible between the interfacial wave mode and the flexural wave mode to some extent. It is also observed from Figs. 4.6 and 4.7 that the reflection coefficient corresponding to the reflected wave of wavenumber M, i.e., for the case of interfacial wave mode, is greater than that of the reflected wave with wavenumber m, i.e., for the case of flexural wave mode. Another important observation is that corresponding to increasing values of the elastic parameter of the ice-sheet, the rate of change of the transmission coefficients and reflection coefficients is found to be higher for both flexural and interfacial modes. Thus it can be inferred that, for a train of normal propagating wave incident on the undulating elastic sea-bed, the energy associated with both reflection and transmission is very sensitive if some variation of the elastic parameter of the ice-sheet is affected.

The curves presented in Figs. 4.9-4.11 correspond to five different values of elastic parameter of the sea-bed: $D_2/h_b^4 = 0, 1, 3, 4.5$ and 5.5 (where $D_2/h_b^4 = 0$ is associated with the value $\epsilon_2/h_b = 0$, while for other values of D_2/h_b^4, the associated value of ϵ_2/h_b

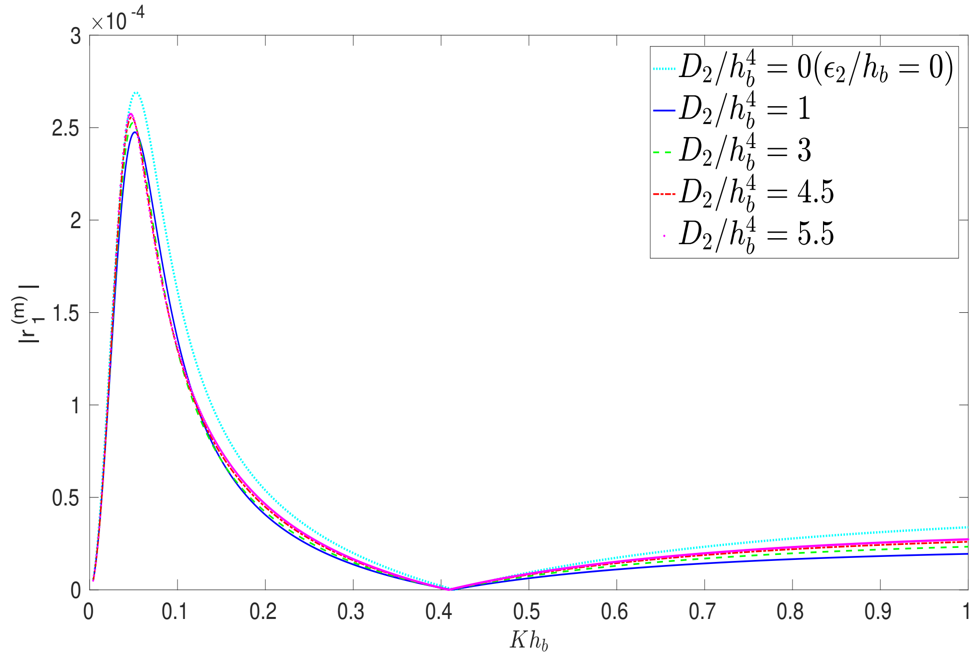

Figure 4.9: Variation of $|r_1^{(m)}|$ versus Kh_b for different sea-bed elastic parameter values corresponding to flexural wave mode with $\rho = 0.5$, $h_b/h_f = 1$, $lh_b = 1$, $a/h_b = 0.1$, $n = 4$, $D_1/h_b^4 = 1$, $\epsilon_1/h_b = 0.0001, \epsilon_2/h_b = 0.0001$

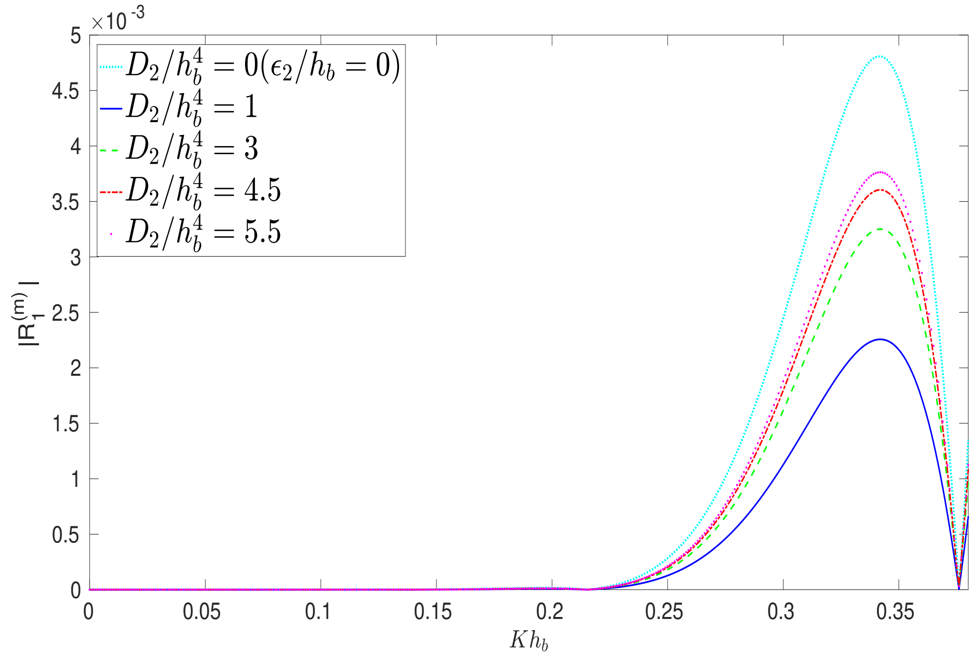

Figure 4.10: Variation of $|R_1^{(m)}|$ versus Kh_b for different sea-bed elastic parameter values corresponding to flexural wave mode with $\rho = 0.5$, $h_b/h_f = 1$, $lh_b = 1$, $a/h_b = 0.1$, $n = 4$, $D_1/h_b^4 = 1$, $\epsilon_1/h_b = 0.0001, \epsilon_2/h_b = 0.0001$

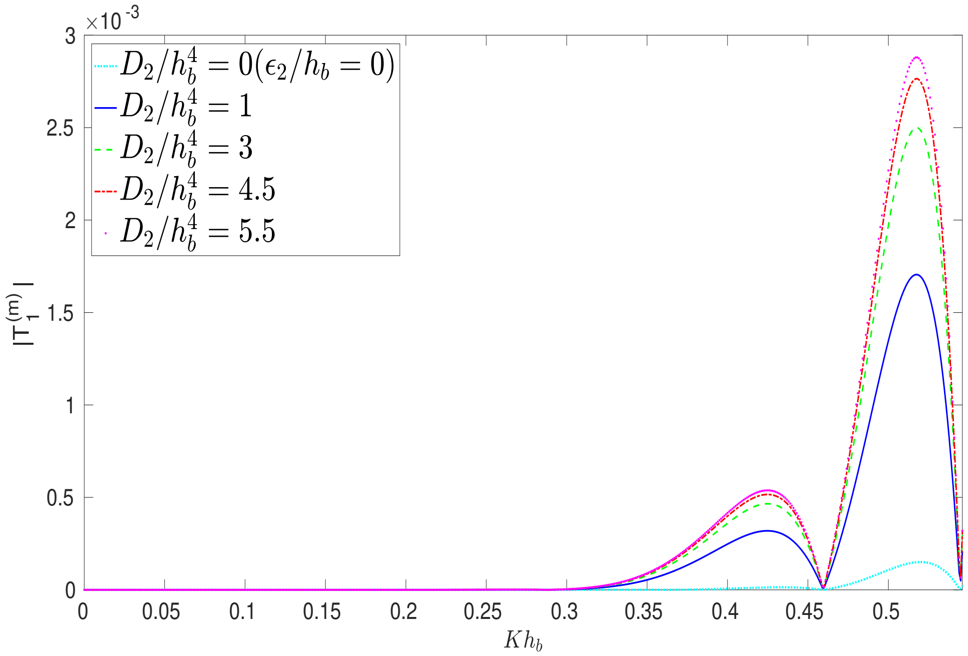

Figure 4.11: Variation of $|T_1^{(m)}|$ versus Kh_b for different sea-bed elastic parameter values corresponding to flexural wave mode with $\rho = 0.5$, $h_b/h_f = 1$, $lh_b = 1$, $a/h_b = 0.1$, $n = 4$, $D_1/h_b^4 = 1$, $\epsilon_1/h_b = 0.0001, \epsilon_2/h_b = 0.0001$

is considered as 0.0001, as mentioned earlier) with $n = 4$ and the value of the elastic parameter of the ice-sheet considered as $D_1/h_b^4 = 1$. It is to be noted that the case $D_2/h_b^4 = 0, \epsilon_2/h_b = 0$ implies a rigid sea-bed. Figure 4.9 depicts that, for increasing values of the elastic parameters of the sea-bed, there is always an increase in the reflection coefficient $|r_1^{(m)}|$. It can be observed from Figs. 4.10 and 4.11 that, as we keep on increasing the value of elastic parameter D_2/h_b^4 of the sea-bed, we observe a gradual increment in $|R_1^{(m)}|$ and $|T_1^{(m)}|$. However, the non-zero values of both $|R_1^{(m)}|$ and $|T_1^{(m)}|$ with wavenumber M for different elastic specifications of the sea-bed indicate that conversion of some amount of energy is feasible from one wavenumber to the other. Another important remark is that when an increase in the value of the elastic parameter of the sea-bed is affected, then the rate of change of both reflection and transmission coefficients is higher for flexural wave mode. This implies that the energy due to reflection and transmission is very sensitive in response to the variation in the values of the elastic parameter of the sea-bed when the incident wave of flexural mode encounters the undulating elastic sea-bed. Moreover, it can be inferred that, with increasing values of elastic parameter of the sea-bed, the value of first-order reflection and transmission coefficients become much higher.

From Figs. 4.3-4.11, it is worthwhile to note that the number of zeros of reflection and transmission coefficients is less than those in the example of Maiti and Mandal [60]. It very likely happens due to the presence of the elastic sea-bed. A common observation in these figures is the oscillating behaviour of the coefficient which is a function of the wavenumber Kh_b.

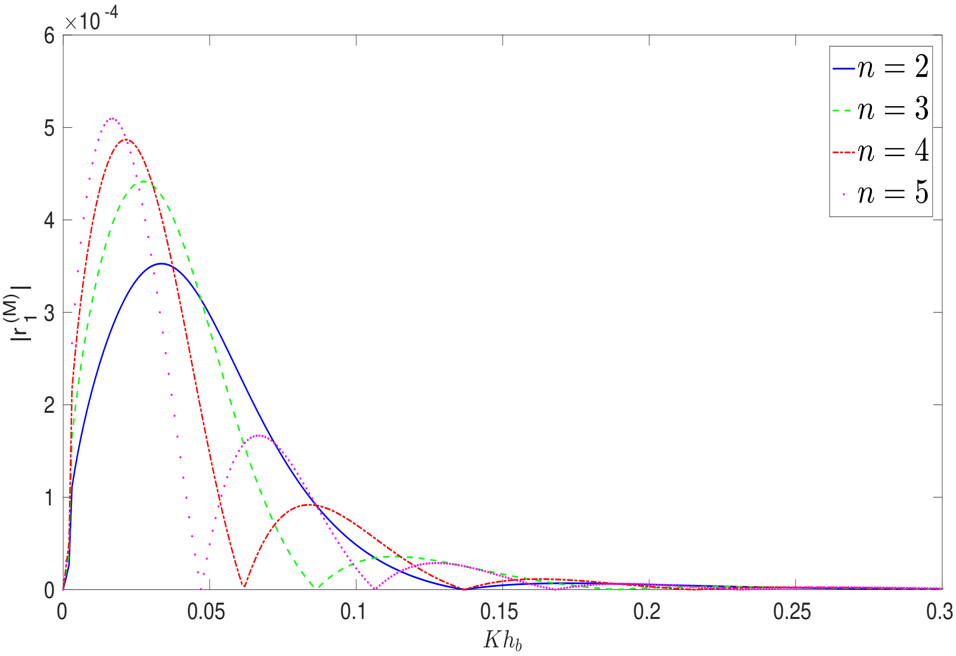

Figure 4.12: Variation of $|r_1^{(M)}|$ versus Kh_b for different number of ripples corresponding to interfacial wave mode with $\rho = 0.5$, $h_b/h_f = 1$, $lh_b = 1$, $a/h_b = 0.1$, $D_1/h_b^4 = 1$, $D_2/h_b^4 = 1$, $\epsilon_1/h_b = 0.0001, \epsilon_2/h_b = 0.0001$

The case of a normally proliferating incident wave of wavenumber M (interfacial mode) represents a delightful circumstance due to the involvement of the elasticity of the sea-bed, where the energy conversion takes place from one wave mode to the other. Correspondingly, Figs. 4.12-4.20 present the coefficients $|r_1^{(M)}|$, $|R_1^{(M)}|$ and $|t_1^{(M)}|$ plotted with respect to Kh_b by considering density ratio $\rho = 0.5$, depth ratio $h_b/h_f = 1$, ripple wavenumber $lh_b = 1$, amplitude of the sinusoidal ripples $a/h_b = 0.1$ and non-dimensional parameters $\epsilon_1/h_b = 0.0001, \epsilon_2/h_b = 0.0001$. The curves presented in Figs. 4.12-4.14 depict the coefficients for various sets of values of number of ripples with the values of the elastic parameters of the ice-sheet and the sea-bed fixed at $D_1/h_b^4 = 1$ and $D_2/h_b^4 = 1$, respectively. It is clear from Figs. 4.12 and 4.14 that, as we keep on increasing the number of ripples, a gradual increment is observed in the peak values of $|r_1^{(M)}|$ and $|t_1^{(M)}|$. Figure 4.13 establishes that if an increase in the values of n is affected, then there is always an increase in the peak values of $|R_1^{(M)}|$ corresponding to a normal incident wave of wavenumber M (i.e., for the case of interfacial mode). But for this case, the reflection coefficient $|R_1^{(M)}|$ takes values higher than those of the reflection coefficient $|r_1^{(M)}|$. This occurs since the interface is somewhat beneath the floating ice-sheet of the fluid and therefore, the reflected energy of flexural wave influence is smaller than that due to the interfacial wave movement. It

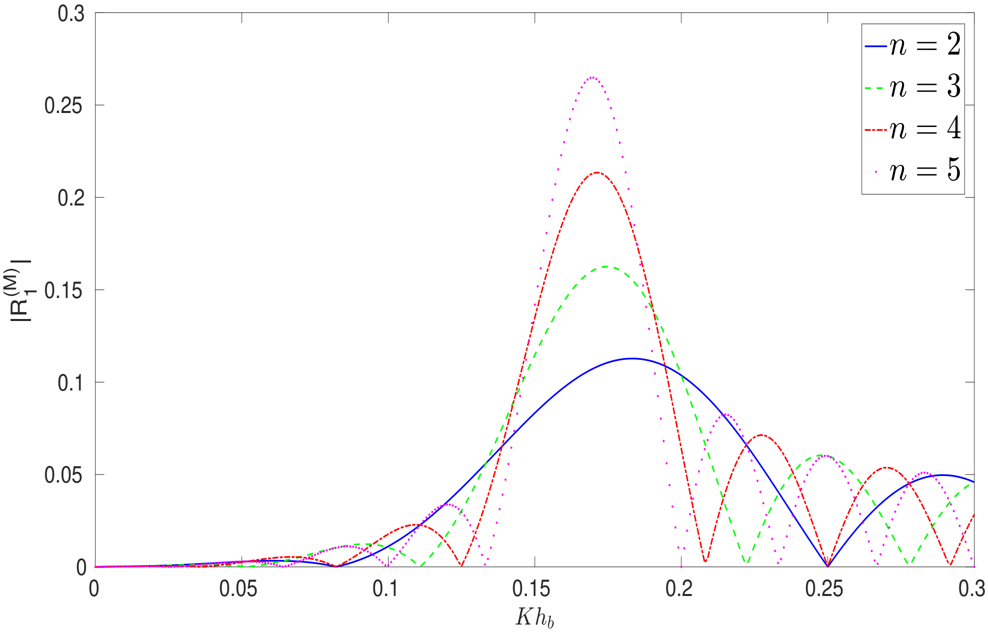

Figure 4.13: Variation of $|R_1^{(M)}|$ versus Kh_b for different number of ripples corresponding to interfacial wave mode with $\rho = 0.5$, $h_b/h_f = 1$, $lh_b = 1$, $a/h_b = 0.1$, $D_1/h_b^4 = 1$, $D_2/h_b^4 = 1$, $\epsilon_1/h_b = 0.0001, \epsilon_2/h_b = 0.0001$

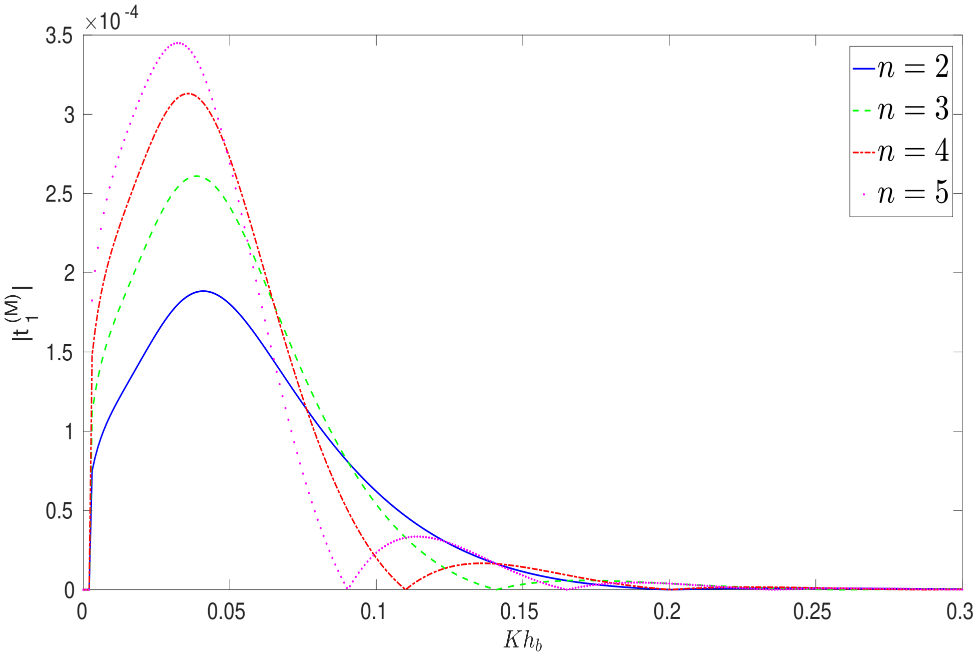

Figure 4.14: Variation of $|t_1^{(M)}|$ versus Kh_b for different number of ripples corresponding to interfacial wave mode with $\rho = 0.5$, $h_b/h_f = 1$, $lh_b = 1$, $a/h_b = 0.1$, $D_1/h_b^4 = 1$, $D_2/h_b^4 = 1$, $\epsilon_1/h_b = 0.0001, \epsilon_2/h_b = 0.0001$

is noticed that when n becomes large, then the reflection and transmission coefficients turn out to be inexhaustible for some specific values of Kh_b, which represents nothing but occurrence of Bragg resonance, as also observed in the earlier problems.

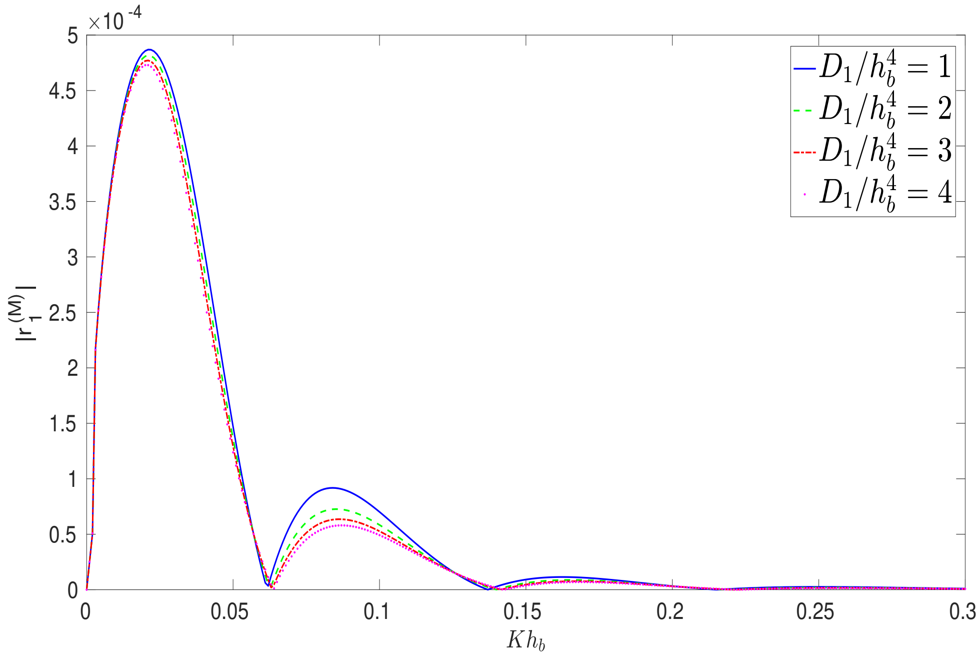

Figure 4.15: Variation of $|r_1^{(M)}|$ versus Kh_b for different ice parameter values corresponding to interfacial wave mode with $\rho = 0.5$, $h_b/h_f = 1$, $lh_b = 1$, $a/h_b = 0.1$, $n = 4$, $D_2/h_b^4 = 1$, $\epsilon_1/h_b = 0.0001$, $\epsilon_2/h_b = 0.0001$

The curves in Figs. 4.15-4.17 present the coefficients for various sets of values of the elastic parameter of the ice-sheet, namely, $D_1/h_b^4 = 1, 2, 3$ and 4, with $n = 4$ and elastic parameter of the sea-bed as $D_2/h_b^4 = 1$. Figures 4.15 and 4.16 clearly show that when the value of the elastic parameter D_1/h_b^4 of the ice-sheet increases, the values of $|r_1^{(M)}|$ and $|R_1^{(M)}|$ decrease. One important observation is that, according to an increase in value of the elastic parameter of the ice-sheet, the rate of decrement of the first-order reflection coefficients is quite insensitive. This is due to the fact that since the interface is somewhat below the ice-sheet, not much effect on the interfacial wave is observed due to the changes in the elastic parameter of the ice-sheet. Consequently, the floating ice-sheet does not have much effect on the reflection coefficients due to the interfacial wave movement and the flexural wave influence in the fluid region for the normally incident wave of mode M proliferating along the interface. Figure 4.17 depicts a reduction in the values of $|t_1^{(M)}|$ according to an increase in the elastic parameter of the ice-sheet. Thus the elastic parameter of the ice-sheet influences transmission coefficient significantly in connection with the case of interfacial wave mode.

Figures 4.18-4.20 demonstrate the reflection and transmission coefficients for different

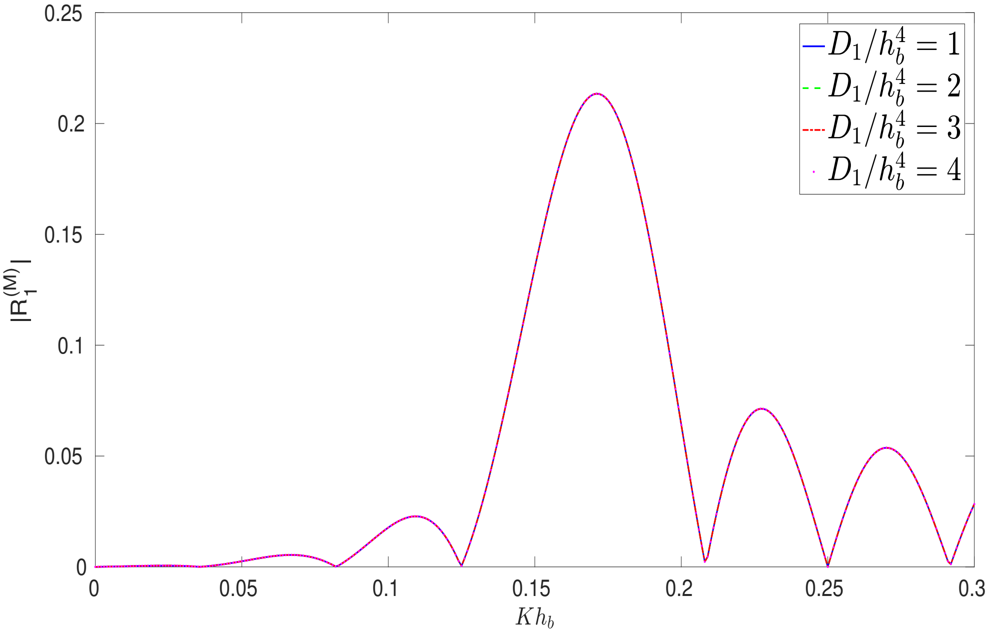

Figure 4.16: Variation of $|R_1^{(M)}|$ versus Kh_b for different ice parameter values corresponding to interfacial wave mode with $\rho = 0.5$, $h_b/h_f = 1$, $lh_b = 1$, $a/h_b = 0.1$, $n = 4$, $D_2/h_b^4 = 1$, $\epsilon_1/h_b = 0.0001, \epsilon_2/h_b = 0.0001$

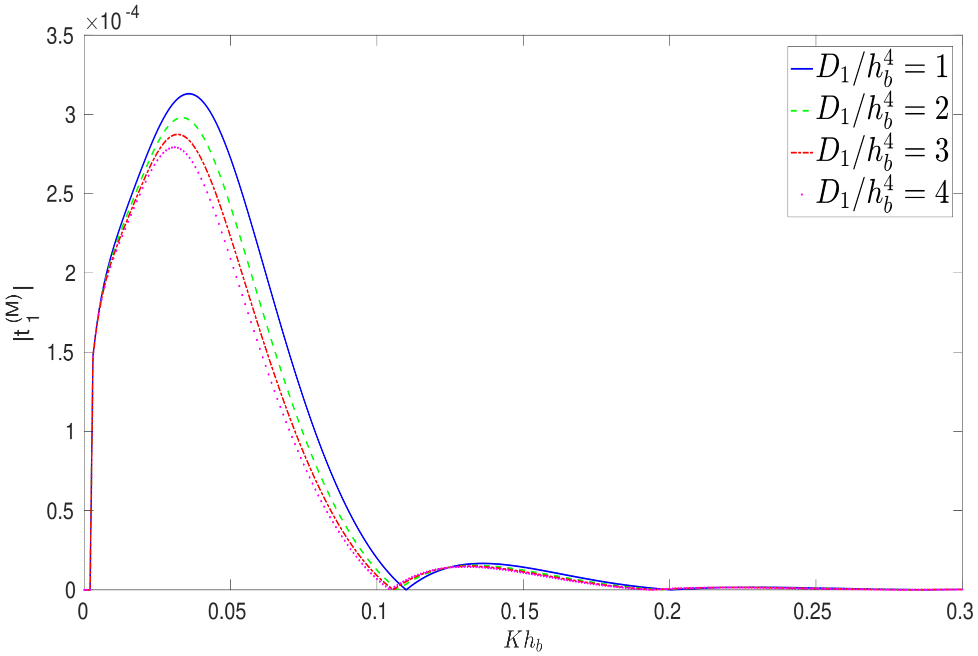

Figure 4.17: Variation of $|t_1^{(M)}|$ versus Kh_b for different ice parameter values corresponding to interfacial wave mode with $\rho = 0.5$, $h_b/h_f = 1$, $lh_b = 1$, $a/h_b = 0.1$, $n = 4$, $D_2/h_b^4 = 1$, $\epsilon_1/h_b = 0.0001, \epsilon_2/h_b = 0.0001$

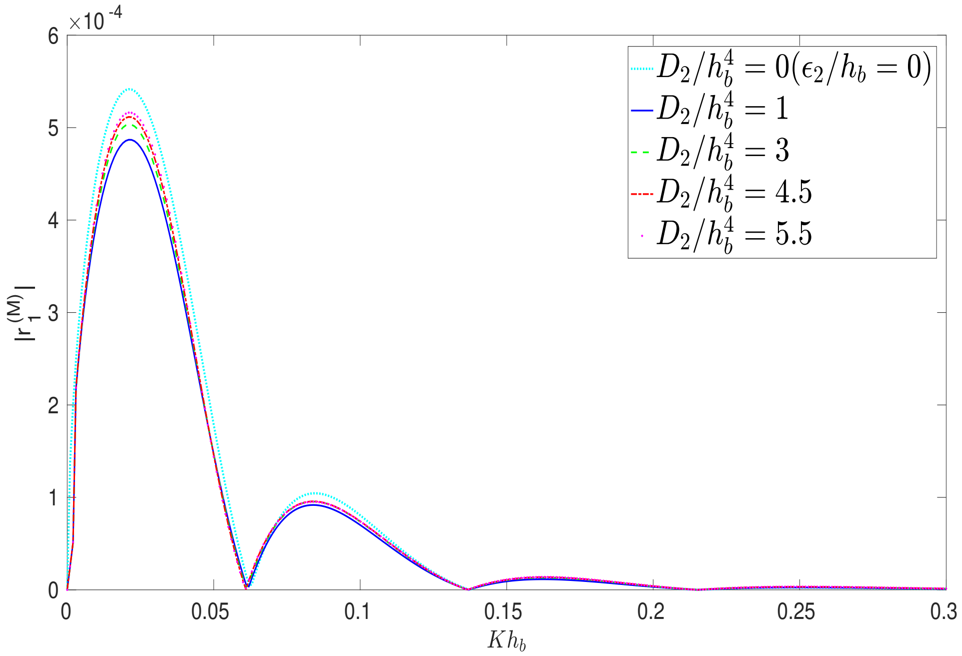

Figure 4.18: Variation of $|r_1^{(M)}|$ versus Kh_b for different sea-bed elastic parameter values corresponding to interfacial wave mode with $\rho = 0.5$, $h_b/h_f = 1$, $lh_b = 1$, $a/h_b = 0.1$, $n = 4$, $D_1/h_b^4 = 1$, $\epsilon_1/h_b = 0.0001, \epsilon_2/h_b = 0.0001$

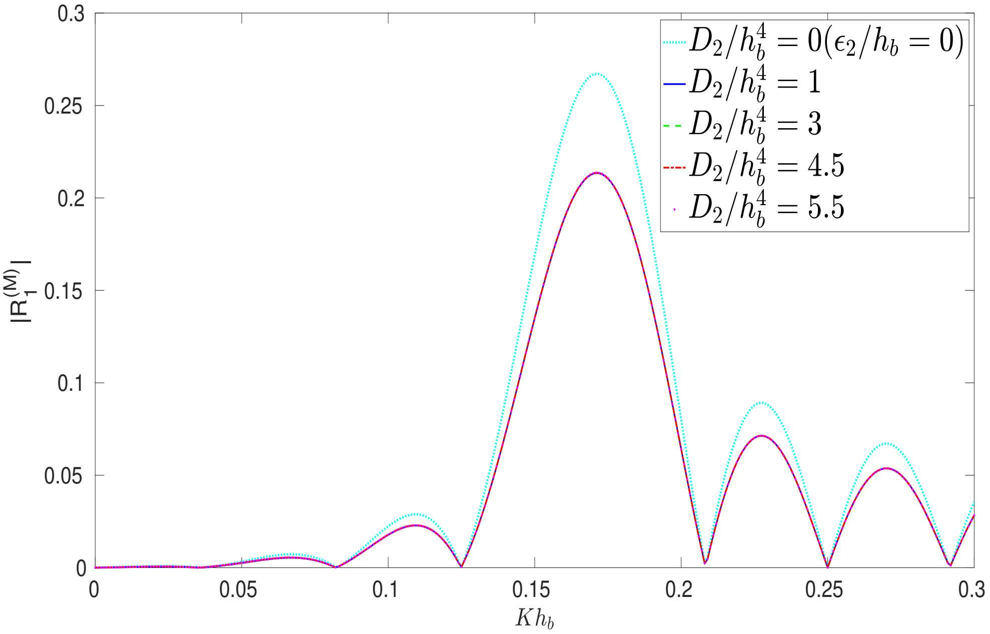

Figure 4.19: Variation of $|R_1^{(M)}|$ versus Kh_b for different sea-bed elastic parameter values corresponding to interfacial wave mode with $\rho = 0.5$, $h_b/h_f = 1$, $lh_b = 1$, $a/h_b = 0.1$, $n = 4$, $D_1/h_b^4 = 1$, $\epsilon_1/h_b = 0.0001, \epsilon_2/h_b = 0.0001$

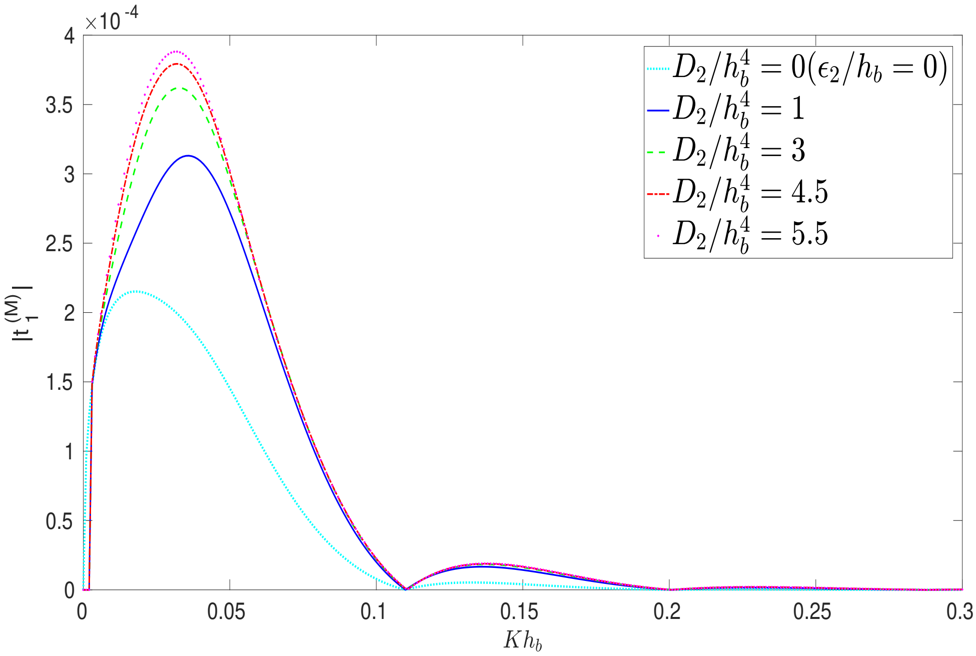

Figure 4.20: Variation of $|t_1^{(M)}|$ versus Kh_b for different sea-bed elastic parameter values corresponding to interfacial wave mode with $\rho = 0.5$, $h_b/h_f = 1$, $lh_b = 1$, $a/h_b = 0.1$, $n = 4$, $D_1/h_b^4 = 1$, $\epsilon_1/h_b = 0.0001, \epsilon_2/h_b = 0.0001$

values of the the elastic parameter D_2/h_b^4 of the sea-bed. For this case, n is taken as 4 and the value of the elastic parameter of the ice-sheet is considered as $D_1/h_b^4 = 1$. Figures 4.18 and 4.19 show that an increase in the value of the elastic parameters of the sea-bed brings an increase in the values of reflection coefficients $|r_1^{(M)}|$ and $|R_1^{(M)}|$. One important observation is that, with an increase in the values of the elastic parameter of the sea-bed, the increasing rate of the first-order reflection coefficients is found to be quite imperceptible. It means that the elastic sea-bed does not command significant influence on the reflected wave energy as a result of the interfacial wave movement and the flexural wave influence in the fluid for the normally incident wave train with wavenumber M proliferating at the interface. On the other hand, Fig. 4.20 shows that the transmission coefficient $|t_1^{(M)}|$ increases corresponding to an increase in the value of the elastic parameter of the sea-bed. However, non-zero values of both first-order reflection and transmission coefficients for a train of propagating waves of mode M suggest that some conversion of reflected as well as transmitted energy is almost always possible from interfacial wave mode to the flexural wave mode. A present observation is that increasing the elastic parameters of the sea-bed can significantly increase the values of reflection and transmission coefficients for both flexural and interfacial modes. It may happen due to the interaction of waves in flexural and interfacial modes with the undulating elastic sea-bed. One observation from Figs. 4.9-4.11 and 4.18-4.20 is that when the sea-bed is considered as a rigid one, then the wave reflection is higher and the wave transmission is lower. It is concluded that interfacial wave gets influenced more as compared to the flexural wave when a rigid sea-bed is considered. It may be due to the fact that the sea-bed is located underneath the interface of the fluid whereas the ice-sheet is above the interface.

To put it concisely, in this work we present a hydroelastic model to treat the water wave propagation over a small bottom undulation located on an elastic sea-bed, for two superposed fluids flowing underneath a floating ice-sheet. There is an observation that an increase in the values of the elastic parameter of the ice-sheet is associated with a reduction in the values of the reflection coefficient $|r_1^{(m)}|$. On the other hand, increase in the values of the reflection and transmission coefficients in both modes is noticed if the number of ripples of the undulating elastic sea-bed increases. It can also be observed that an increase in the values of the elastic parameter of the sea-bed results in the increase in the values of the reflection and transmission coefficients for both modes.

4.6 Conclusion

In this chapter, we take up the problem of normally incident water wave scattering by a small undulation located on an elastic sea-bed in two superposed fluids flowing underneath an infinitely extended floating ice-sheet. Considering the well-known Euler-Bernoulli beam equation, both the ice-sheet and elastic sea-bed are considered as thin elastic plates, where the horizontal length of such a plate is considered to be much larger in comparison to its thickness. Under such circumstances, there exist propagating waves at two distinct wavenumbers for any given frequency: the one with the smaller wavenumber along the floating ice-sheet corresponding to the flexural mode and the other one with the higher wavenumber along the interface corresponding to the interfacial mode. The first-order velocity potentials and the reflection and transmission coefficients are found by applying the technique of perturbation in conjunction with Fourier transform. Wave energy conversion from one wave mode to the other is exhibited by providing graphical representation corresponding to various physical parameters of the system. The complex resonant interactions are demonstrated concerning wave propagation in an ice-covered two superposed fluids flowing over a rippled elastic sea-bed as a result of action of flexural and interfacial modes. The energy related to reflection and transmission in accordance with both flexural and interfacial mode is observed to reduce when the elasticity of the ice-sheet increases. On the other hand, an opposite trend is observed for reflected and transmitted energy when the elasticity of the sea-bed increases. Furthermore, it is worthwhile to note that the peak values of the reflection and transmission coefficients go upward when the total number of ripples of the bottom undulation on the sea-bed increases. This outcome may bear a significant implication for both coastal protection and of possible ripple growth on an erodible bed involving a two-layer ocean covered by a thin ice-sheet. For an interfacial wave mode, the reflection corresponding to the flexural wave influence and interfacial wave movement is not influenced by the variations in the elastic parameter of the floating ice-sheet. Since the interface is quite below the ice-sheet, the interfacial wave is not much influenced by the changes in the elastic parameter of the floating ice-sheet. At the same time, the transmission in accordance with the interfacial wave mode is significantly affected. A remarkable significance is observed in the conversion of incident wave energy to the reflected and transmitted energy taking place between the higher mode (interfacial mode) and the smaller mode (flexural mode) because of the non-zero values of reflection and transmission coefficients arising out of the flexural wave movement and the interfacial wave influence in the fluid region. It is expected that the results developed in this work may be utilized in an appropriate manner for tackling a large class of water wave scattering problems that appear in various disciplines of ocean engineering. The model developed here, based on a physical problem, and its associated results will certainly be helpful in the development of wave power devices, underwater pipe bridges, mobile offshore base, VLFS like floating oil storage bases for oceanographic purposes in connection with different advanced evolutions in the marine environment. The conclusions drawn from the present study will be immensely helpful in the selection of the site for various large floating offshore infrastructures and to understand the pattern of coupling between waves and sea ice under various bed characteristics, especially elasticity.

CHAPTER 5

WATER WAVE SCATTERING BY TWO THIN VERTICAL SUBMERGED POROUS BARRIERS LOCATED ABOVE A POROUS SEA-BED

5.1 Introduction

In this chapter, the problem of oblique water wave scattering by two fully submerged parallel porous barriers with the wave propagating over a porous sea-bed in a homogenous fluid is solved with the help of linear water wave theory. The porous barriers are assumed to follow the theory of thin plates, and the wave propagation through the porous structure follows porous wave-maker theory. Methods of eigenfunction expansion and least square are employed to acquire the complete analytical solution for the interaction of water waves with submerged porous barriers. The reflection and transmission coefficients as well as the energy loss are computed and examined corresponding to various values of parameters such as porous-effect parameter, the submergence depth of barriers from the free surface, the angle of incidence, the porosity of the sea-bed. The present approach is expected to be of great significance in the designing and construction of different types of effective wave absorbers utilized in sea for studying reflection as well as dissipation of wave energy in coastal regions and hence, in general, for the purpose of activities in coastal as well as offshore engineering.

5.2 Formulation of the scattering problem

Propagation of water waves of a comparatively small amplitude under the action of gravity in an inviscid, incompressible and homogeneous fluid with an irrotational motion over a porous sea-bed is considered here. Let $x = 0$ and $x = L$, respectively, be the locations of two fully submerged thin vertical porous barriers of different heights in a water region of constant depth h with the y-axis pointing vertically upwards. For all the problems from this chapter onward, the same orientation of the coordinate system will be considered. Further, the positive x-axis is defined in the direction of the normal on the first porous barrier towards the second porous barrier, the z-axis along the transverse direction of the porous barriers. Let $y = 0$ and $y = -h$, respectively, represent the undisturbed free surface and the location of the porous sea-bed. d_1 and d_3, respectively, are taken as the distances of the lower vertical tips of the first and second porous barriers from the free surface; d_2 and d_4, respectively, as the respective distances of the upper vertical tips. In order to solve the boundary value problem, the whole fluid domain is divided into three regions: region A, the domain in front of the first porous barrier, i.e., $-\infty < x < 0,\ -h < y < 0$; region B, the domain between two porous barriers, i.e., $0 < x < L,\ -h < y < 0$; and region C, the domain behind the second porous barrier, i.e., $L < x < \infty,\ -h < y < 0$. Adopting linear water wave theory and utilizing all these assumptions, the time harmonic velocity potentials are defined as $\Psi_1(x, y, z, t) = \psi_1(x, y) \exp(\mathrm{i}lz - \mathrm{i}\omega t)$ in region A, $\Psi_2(x, y, z, t) = \psi_2(x, y) \exp(\mathrm{i}lz - \mathrm{i}\omega t)$ in region B and $\Psi_3(x, y, z, t) = \psi_3(x, y) \exp(\mathrm{i}lz - \mathrm{i}\omega t)$ in region C, respectively (Fig. 5.1) with l being the component of the incident wavenumber k_0 (surface mode) along the z-axis defined by $l = k_0 \sin\theta$, where θ is the angle of incidence on the x-axis and ω is the angular wave frequency of the incoming waves.

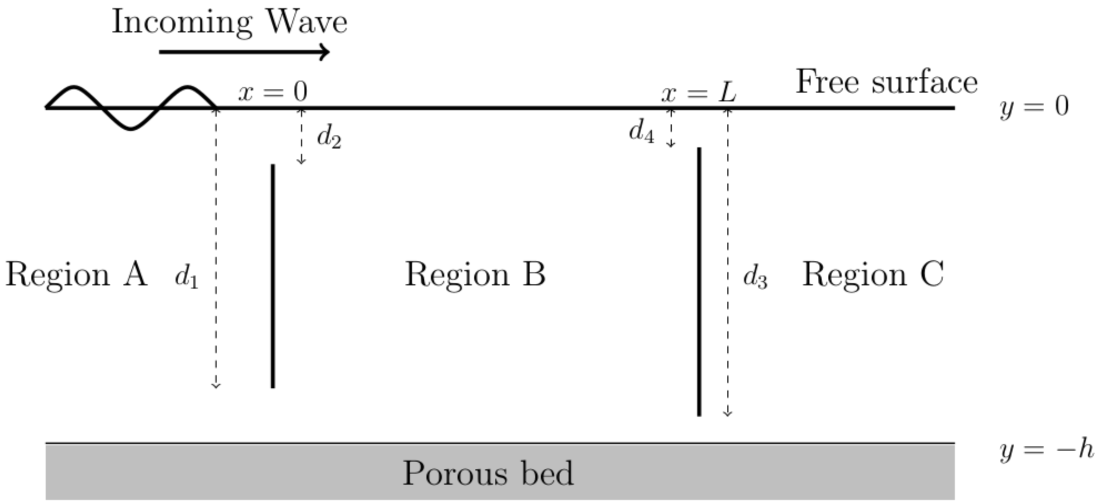

Figure 5.1: Diagram of the problem depicting the structure, the fluid and the sea-bed

In regions A, B and C, the velocity potentials $\psi_j,\ j = 1, 2, 3$ satisfy the modified Helmholtz equation

$$\frac{\partial^2 \psi_j}{\partial x^2} + \frac{\partial^2 \psi_j}{\partial y^2} - l^2 \psi_j \quad = \quad 0. \tag{5.1}$$

The linearized mean free surface boundary condition has the following standard expression:

$$\frac{\partial \psi_j}{\partial y} - K\psi_j = 0 \quad \text{on} \quad y = 0, \quad j = 1, 2, 3, \tag{5.2}$$

with $\omega = \dfrac{2\pi}{T}$, where T is the time period.

The very important linearized boundary condition at the porous sea-bed is given by

$$\frac{\partial \psi_j}{\partial y} + G\psi_j = 0, \quad \text{on} \quad y = -h, \ j = 1, 2, 3, \tag{5.3}$$

where the term $G = \dfrac{\mathrm{i}\rho_h \omega b_c}{v_d}$ is the porosity parameter of the sea-bed (Chwang [17]), with b_c as the coefficient which has the dimension of length, ρ_h the uniform fluid density and v_d the coefficient of dynamic viscosity. The parameter G can be written in general as $G = G_r + \mathrm{i}G_i$ (Yu [100]), where G_r denotes the real part and G_i denotes the imaginary part. It is to be noted that the porosity parameter usually has a complex value in order to account for both resistance and inertial effect (Yu and Chwang [101]). However, the porosity G of the sea-bed in the current work is taken as a real number (in a similar manner as in Martha et al. [66], Maiti and Mandal [62]) by taking into account only the resistance effects and neglecting the inertial terms. Further, consideration of G as real is to ensure that the progressive wave propagates at the far field (see Maiti and Mandal [62]). However, both resistance and inertial effects are taken into account for the barriers. Here, the fluid motions are considered in such a way that the associated boundary condition on the porous sea-bed, as utilized in this work, shall be valid based on the porosity parameter G only, which has a dimension of $(\text{length})^{-1}$. In other words, the porous sea-bed is considered just as a boundary, and the motion beyond it is not considered.

It is to be noted that the governing equations and different boundary conditions for each region as stated above are also accompanied by some other important conditions, usually known as matching conditions, along the common boundary of any two adjacent regions. These conditions are necessary to ensure the continuity of pressure and horizontal velocity across the boundaries. Velocity potentials ψ_j, $j = 1, 2, 3$, satisfy the following conditions along the vertical boundaries $x = 0$ and $x = L$ (Chwang [17],Yu [100]):

$$\frac{\partial \psi_1}{\partial x} = \frac{\partial \psi_2}{\partial x} = \mathrm{i}k_0\mathcal{G}_1(\psi_1 - \psi_2); \quad x = 0, -d_1 < y < -d_2, \tag{5.4}$$

$$\frac{\partial \psi_1}{\partial x} = \frac{\partial \psi_2}{\partial x}; \ x = 0, \ (-h < y < -d_1) \cup (-d_2 < y < 0), \tag{5.5}$$

$$\psi_1 = \psi_2; \ x = 0, \ (-h < y < -d_1) \cup (-d_2 < y < 0), \tag{5.6}$$

$$\frac{\partial \psi_2}{\partial x} = \frac{\partial \psi_3}{\partial x} = \mathrm{i}k_0\mathcal{G}_2(\psi_2 - \psi_3); \quad x = L, -d_3 < y < -d_4, \tag{5.7}$$

$$\frac{\partial \psi_2}{\partial x} = \frac{\partial \psi_3}{\partial x}; \; x = L, \; (-h < y < -d_3) \cup (-d_4 < y < 0), \tag{5.8}$$

$$\psi_2 = \psi_3; \; x = L, \; (-h < y < -d_3) \cup (-d_4 < y < 0), \tag{5.9}$$

where $\mathcal{G}_1$ and $\mathcal{G}_2$ are, respectively, the dimensionless porous-effect parameters of first and second barriers placed at $x = 0$ and $x = L$. Here, $\mathcal{G}_1$ and $\mathcal{G}_2$ are taken as complex numbers taking into account both resistance and inertial effects. The energy dissipation due to the resistance effect of the barrier is relevant to the real part of the porous-effect parameter. But the phase shift due to the inertial effect of the barrier is relevant to the imaginary part of the porous-effect parameter.

5.3 Analytical solutions

By using the method of separation of variables, velocity potential $\psi_1(x, y)$ in region A can be written in the following form:

$$\psi_1(x, y) = [e^{\mathrm{i}K_0 x} + R_0 e^{-\mathrm{i}K_0 x}] Z_0(h, y) + \sum_{n=1}^{\infty} R_n e^{-\mathrm{i}K_n x} Z_n(h, y), \tag{5.10}$$

where R_0 is the complex reflection coefficient and all R_n, $n = 1, 2, \ldots$, represent the decaying modes of the wave reflection; $K_n = (k_n^2 - l^2)^{\frac{1}{2}}$. Using boundary condition (5.3), the depth-dependent function $Z_n(h, y)$ can be obtained as

$$Z_n(h, y) = \frac{k_n \cosh k_n(h + y) - G \sinh k_n(h + y)}{k_n \cosh k_n h - G \sinh k_n h}, \quad n = 0, 1, 2, ..., \tag{5.11}$$

where k_n satisfies the dispersion relation

$$K(k_n - G \tanh k_n h) = k_n(k_n \tanh k_n h - G). \tag{5.12}$$

The above dispersion relation (5.12) has exactly one positive real root k_0 that indicates the propagating mode; and an infinite number of purely imaginary roots $k_n = \mathrm{i}\kappa_n$, $n = 1, 2, ...$, that correspond to a set of evanescent modes (Fig. 5.2). Further, the negative values of all of these also happen to be roots which actually represent wavenumbers of the waves travelling in the negative direction. The fact that (5.12) has exactly one positive real root k_0 leads to the existence of one mode of wave propagating at the free surface, called the surface mode, along the positive x-direction. The evanescent modes of the potential with the infinite sum is truncated at $n = N$ to get

$$\psi_1(x, y) = [e^{\mathrm{i}K_0 x} + R_0 e^{-\mathrm{i}K_0 x}] Z_0(h, y) + \sum_{n=1}^{N} R_n e^{-\mathrm{i}K_n x} Z_n(h, y). \tag{5.13}$$

In region B also, following a similar procedure, the spatial velocity potential $\psi_2(x, y)$ is expressed, after truncation at $n = N$, as

$$\psi_2(x, y) = \sum_{n=0}^{N} [A_n e^{\mathrm{i}K_n x} + B_n e^{-\mathrm{i}K_n (x-L)}] Z_n(h, y), \tag{5.14}$$

where A_n and B_n are arbitrary constants.

Similarly in region C, the spatial velocity potential $\psi_3(x, y)$ is expressed as

$$\psi_3(x, y) = \sum_{n=0}^{N} T_n e^{\mathrm{i}K_n (x-L)} Z_n(h, y), \tag{5.15}$$

where T_0 is the complex transmission coefficient and all T_n, $n = 1, 2, \ldots,$ represent the decaying modes of transmission. It is to be noted that the loss of energy due to water wave interaction with the barriers is computed by utilizing the following well-known relation (in a similar manner as in Liu and Li [58]):

$$\text{Energy loss} = (1 - |R_0|^2 - |T_0|^2) \times 100\%. \tag{5.16}$$

The roots of dispersion relation (5.12) are computed numerically by using contour plots in order to apprehend the behaviours of the wavenumbers (Fig. 5.2). For computational purpose, different physical parameters are taken as: time period $T = 5$ s, the porous effect parameter of the bed $Gh = 0.1$, $g = 9.81$ m/s^2, unless otherwise mentioned.

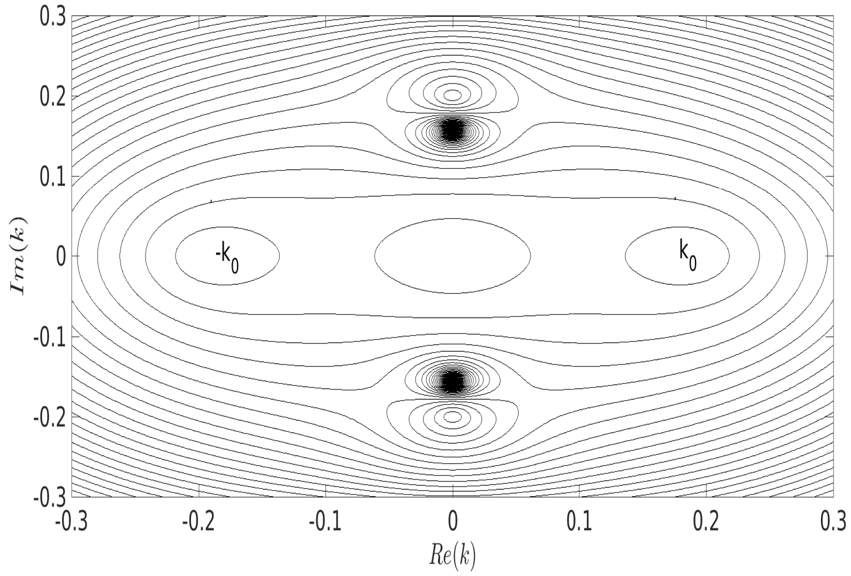

Figure 5.2: Roots of dispersion relation (5.12) with $Gh = 0.1$, $g = 9.81$ m/s^2 and $T = 5$ s

Following Fox and Squire [32], the nature of the roots of the dispersion relation is found by applying a simple counting argument. In order to apply Newton–Raphson method for computing all the roots of the dispersion relation due to the porous sea-bed, the required initial guess for each root is acquired by using a contour plot. Figure 5.2 shows the behaviour of the roots of the dispersion relation for wave propagation over the porous sea-bed.

The horizontal velocity components $\frac{\partial\psi_1}{\partial x}$ and $\frac{\partial\psi_2}{\partial x}$ follow the continuity condition along $x = 0, -h < y < 0$ (from Eqs. (5.4) and (5.5)) so as to give

$$R_n = \begin{cases} 1 - A_n + B_n e^{\mathrm{i}K_nL}, & \text{for } n = 0, \\ B_n e^{\mathrm{i}K_nL} - A_n, & \text{for } n = 1, 2, \dots, N. \end{cases} \tag{5.17}$$

Also the second equality of Eq. (5.4) leads to

$$\sum_{n=0}^{N}(K_n + 2k_0\mathcal{G}_1)A_nZ_n - \sum_{n=0}^{N} K_nB_ne^{\mathrm{i}k_nL}Z_n - 2k_0\mathcal{G}_1Z_0 = 0,\ -d_2 < y < -d_1. \tag{5.18}$$

Similarly, Eq. (5.6) results in

$$2Z_0 - \sum_{n=0}^{N} 2A_nZ_n = 0,\ (-h < y < -d_1) \cup (-d_2 < y < 0). \tag{5.19}$$

Least square approach, as used by Dalrymple and Martin [23], is employed to find the undetermined coefficients in Eqs. (5.18) and (5.19). For this purpose, a new quantity $\mathcal{L}(y)$ is defined as follows:

$$\mathcal{L}(y) = \begin{cases} \sum_{n=0}^{N}(K_n + 2k_0\mathcal{G}_1)A_nZ_n - \sum_{n=0}^{N} K_nB_ne^{\mathrm{i}k_nL}Z_n - 2k_0\mathcal{G}_1Z_0, & -d_2 < y < -d_1, \\ \\ 2Z_0 - \sum_{n=0}^{N} 2A_nZ_n, & (-h < y < -d_1) \cup (-d_2 < y < 0). \end{cases} \tag{5.20}$$

This method requires that

$$\int_{-h}^{0} |\mathcal{L}(y)|^2 \mathrm{d}y \quad \text{is minimum} \tag{5.21}$$

holds to satisfy $\mathcal{L}(y) = 0$ in $-h < y < 0$.

Subsequently, minimizing the above integral in Eq. (5.21) with respect to each A_m ($m = 0, 1, \dots, N$), we obtain the following integral equation:

$$\int_{-h}^{0} \mathcal{L}^*(y)\frac{\partial\mathcal{L}(y)}{\partial A_m}\mathrm{d}y = 0,\ m = 0, 1, 2, \dots N, \tag{5.22}$$

where $\mathcal{L}^*(y)$ is the corresponding complex conjugate of $\mathcal{L}(y)$.

After carrying out integration with respect to y, the following system of linear equations arises:

$$\sum_{n=0}^{N} S^{(1)}_{m,n} A^*_n + \sum_{n=0}^{N} T^{(1)}_{m,n} B^*_n = r^{(1)}_m, \ m = 0, 1, 2, \ldots, N, \tag{5.23}$$

where

$$S^{(1)}_{m,n} = (K^*_n + 2k_0\mathcal{G}^*_1)(K_m + 2k_0\mathcal{G}_1)\int_{-d_1}^{-d_2} Z_m Z_n \mathrm{d}y + 4\left[\int_{-h}^{-d_1} Z_m Z_n \mathrm{d}y + \int_{-d_2}^{0} Z_m Z_n \mathrm{d}y\right], \tag{5.24}$$

$$T^{(1)}_{m,n} = -K^*_n \zeta^*_n (K_m + 2k_0\mathcal{G}_1)\int_{-d_1}^{-d_2} Z_m Z_n \mathrm{d}y, \tag{5.25}$$

$$r^{(1)}_m = 2k_0\mathcal{G}^*_1(K_m + 2k_0\mathcal{G}_1)\Big[\int_{-d_1}^{-d_2} Z_m Z_0 \mathrm{d}y\Big] + 4\Big[\int_{-h}^{-d_1} Z_m Z_0 \mathrm{d}y + \int_{-d_2}^{0} Z_m Z_0 \mathrm{d}y\Big], \tag{5.26}$$

with $\zeta_n = e^{\mathrm{i}K_nL}$ and $*$ denoting the complex conjugate of the corresponding quantity.

Using the continuity condition along the boundary $x = L, -h < y < 0$ for the horizontal velocity components $\frac{\partial\psi_2}{\partial x}$ and $\frac{\partial\psi_3}{\partial x}$ (from Eqs. (5.7) and (5.8)), the following is obtained:

$$T_n \ = \ A_n e^{\mathrm{i}K_nL} - B_n, \ \text{for } n = 0, 1, 2, \ldots, N. \tag{5.27}$$

Using the second equality of Eq. (5.7), we obtain the following:

$$\sum_{n=0}^{N} K_n e^{\mathrm{i}k_nL} A_n Z_n - \sum_{n=0}^{N} (K_n + 2k_0\mathcal{G}_2) B_n Z_n = 0, \ -d_4 < y < -d_3. \tag{5.28}$$

Further, Eq. (5.9) leads to

$$\sum_{n=0}^{N} 2B_n Z_n = 0, \ (-h < y < -d_3) \cup (-d_4 < y < 0). \tag{5.29}$$

Application of least square approach leads to another system of linear equations as follows:

$$\sum_{n=0}^{N} S^{(2)}_{m,n} A^*_n + \sum_{n=0}^{N} T^{(2)}_{m,n} B^*_n = 0, \ m = 0, 1, 2, \ldots, N, \tag{5.30}$$

where

$$S^{(2)}_{m,n} = -K_n^*\zeta_n^*(K_m + 2k_0\mathcal{G}_2)\int_{-d_3}^{-d_4} Z_mZ_n\mathrm{d}y, \tag{5.31}$$

$$T^{(2)}_{m,n} = (K_n^* + 2k_0\mathcal{G}_2^*)(K_m + 2k_0\mathcal{G}_2)\int_{-d_3}^{-d_4} Z_mZ_n\mathrm{d}y + 4\left[\int_{-h}^{-d_3} Z_mZ_n\mathrm{d}y + \int_{-d_4}^{0} Z_mZ_n\mathrm{d}y\right]. \tag{5.32}$$

Now we develop the following complex matrix system by combining the system of equations given by Eqs. (5.23) and (5.30):

$$\mathcal{H}\mathcal{X} = \mathcal{B},$$

where $\mathcal{H}$ is a matrix of size $(2N+2)\times(2N+2)$, $\mathcal{X} = [A_0^*, A_1^*, \dots, A_N^*, B_0^*, B_1^*, \dots, B_N^*]^T$ is an unknown quantity, and $\mathcal{B} = [r_0^{(1)}, r_1^{(1)}, \dots, r_N^{(1)}, \underbrace{0, \dots, 0}_{\text{N+1}}]^T$.

By solving the above system of equations, the unknown coefficients A_n^* and B_n^* are obtained. With determination of these coefficients, the reflection coefficient $|R_0|$ and transmission coefficient $|T_0|$ as well as energy loss are computed.

5.4 Validation

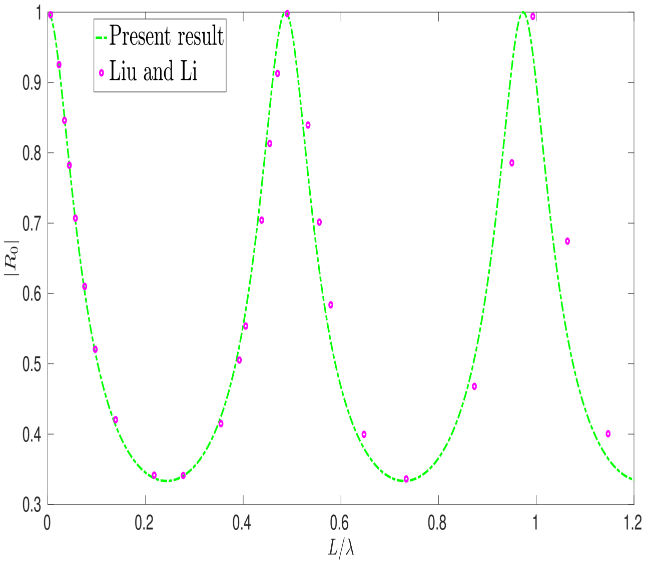

Figure 5.3: Validation of present result with an existing result of Liu and Li [58]

In order to go ahead with various investigations in our work, we wish to validate one of our results with some available established result at the outset so that the efficiency of our model gets validated. In this direction, we compare our result with that of Liu and Li [58]. If the porosity of the sea-bed is removed from the system which results in $Gh = 0$, and by taking $d_1 = d_3$, $d_2 = d_4 = 0$ and $\mathcal{G}_2 = 0$, the present configuration reduces to the one in the problem by Liu and Li [58] with Fig. 5.(a). In Fig. 5.3, the plots of the reflection coefficient against L/λ with $d_1/h = 1, Kh = 1.6, \mathcal{G}_1 = 0.5$ are shown for the result of both Liu and Li [58] and the present one, and from this, an excellent agreement can be inferred.

Based on this outcome, various subsequent investigations in our work are carried out by accepting the present model to be an effective one. As a result, there is a very strong conviction to believe that this model will be of practical use for tackling various problems in coastal and offshore engineering for such configurations.

5.5 Results and discussion

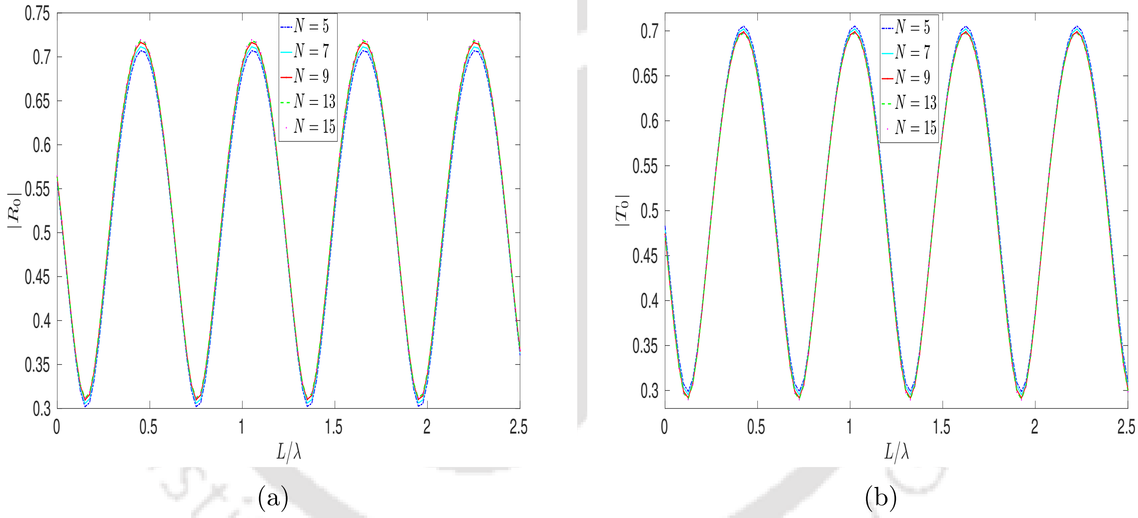

(a) (b)

Figure 5.4: Convergence of (a) reflection coefficient $|R_0|$ and (b) transmission coefficient $|T_0|$ versus L/λ for various number of evanescent modes with $d_2 = d_4 = 0.5h$, $d_1 = d_3 = d_2 + 0.5h$, $\mathcal{G}_1 = 0.5 = \mathcal{G}_2$

A MATLAB program is devised to examine the effects of the structural parameters on reflection coefficient, transmission coefficient and energy loss. Here we produce the results through graphical presentation and present the related explanation corresponding to the reflection and transmission coefficients found due to varying values of different dimensionless parameters. It is to be noted that the square root singularity of the fluid velocity found at the barrier tips can be assimilated in the solution so as to increase the convergence remarkably (discussed in Porter and Evans [75] and Li et al. [54]). Further, another significant fact is that all square integrable functions satisfy the least-square approach utilized in this solution strategy and therefore, the above-mentioned square-root singularity can be handled in a simple manner (detailed discussion in Kelman and Chester [47]). Various researchers, e.g., Das and Bora [26], Liu and Li [58], utilized this procedure to tackle wave scattering and trapping problems because of its faster convergence. Moreover, it was found that the geometry and configuration of the porous barriers played a crucial role in determining the number of terms N with an eye to attain the desired efficiency.

While considering two fully submerged parallel vertical porous barriers, for demonstrating the convergence of the numerical results, the coefficients $|R_0|$ and $|T_0|$ are plotted against L/λ, where λ is the wavelength of the incident wave, in Fig. 5.4 for various $N = 5, 7, 9, 13, 15$. For $N = 13$ and 15, both $|R_0|$ and $|T_0|$ exhibit excellent agreement. Subsequently, $N = 15$ is considered in the numerical computation for all discussions. For computational purpose, values of different physical parameters are taken as follows: time period $T = 5$ s, $g = 9.81$ m/s^2, $\theta = 0°$ (only the normal incidence), porosity of the sea-bed $Gh = 0.25$, $d_2 = d_4 = 0.2h$, $d_1 = d_3 = 0.5h$, $\mathcal{G}_1 = 0.5 = \mathcal{G}_2$ and $N = 15$, unless otherwise mentioned.

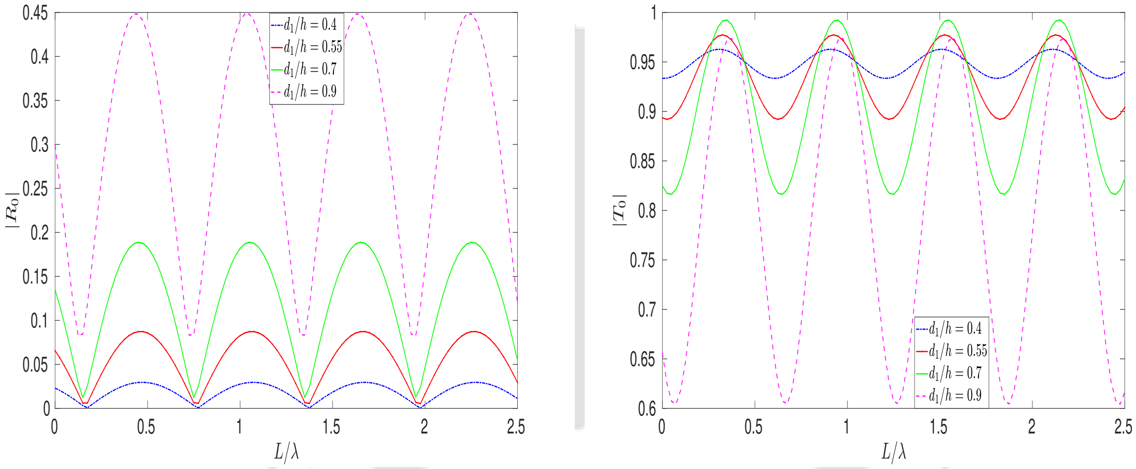

(a) (b)

Figure 5.5: Effect of (a) reflection coefficient $|R_0|$ and (b) transmission coefficient $|T_0|$ versus L/λ for various drafts of the lower tip of the first barrier with $\mathcal{G}_1 = \mathcal{G}_2 = 0.5$, $d_2 = 0.2h$, $d_3 = d_1$, $d_4 = d_2$, $\theta = 0^0$ and $N = 15$

In Fig. 5.5(a,b), the reflection and transmission coefficients are plotted versus L/λ, which represents the distance between the porous barriers, for various values of draft d_1/h corresponding to the first barrier. For these figures, the following values are considered: $\mathcal{G}_1 = \mathcal{G}_2 = 0.5$, $d_2 = 0.2h$, $d_3 = d_1$, $d_4 = d_2$. From Fig. 5.5, it is observed that the reflection coefficient increases and the transmission coefficient decreases corresponding to an increase in the values of d_1/h. Both the maximum and minimum values of $|R_0|$ occur at some specific values of L/λ. It is observed that higher oscillation occurs for higher values of d_1/h. However, both coefficients follow a certain oscillatory pattern for all values of d_1/h. Further, higher reflection occurs when the barriers are of greater height. It is worthwhile to note that, when the both porous barriers of greater height are fully submerged and they are close to the porous sea-bed, sufficient portion of the incident wave energy, concentrated near the sea-bed, is reflected by the porous barriers, and some other portion of the incident wave energy gets dissipated while passing through the porous barriers.

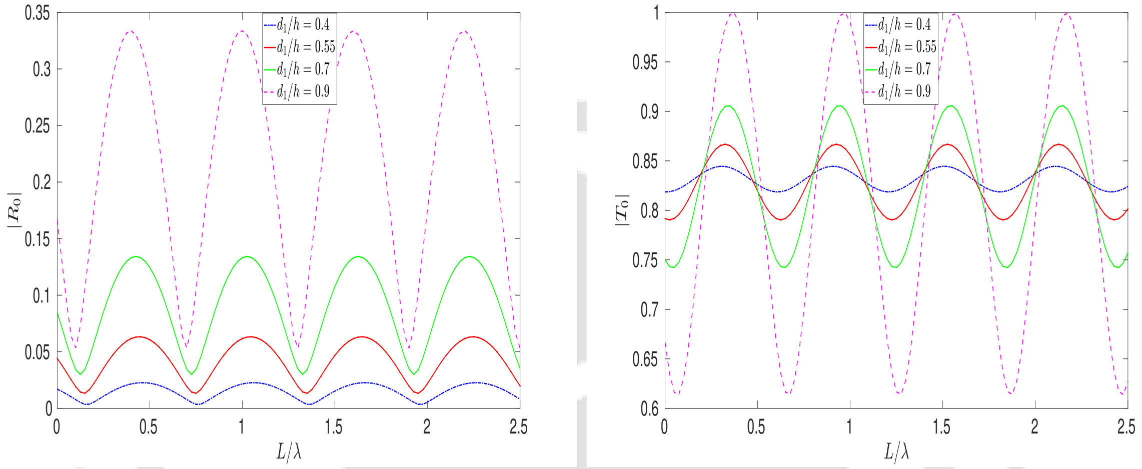

(a) (b)

Figure 5.6: Effect of (a) reflection coefficient $|R_0|$ and (b) transmission coefficient $|T_0|$ versus L/λ for various drafts of the lower tip of the first barrier with $\mathcal{G}_1 = 0.5+i, \mathcal{G}_2 = 0.5$, $d_2 = 0.2h$, $d_3 = d_1$, $d_4 = d_2$, $\theta = 0^0$ and $N = 15$

In Fig. 5.6(a,b), the reflection and transmission coefficients are plotted versus L/λ for various draft d_1/h with the inclusion of an imaginary quantity to $\mathcal{G}_1$ by taking $\mathcal{G}_1 = 0.5+\text{i}$, whereas $\mathcal{G}_2$ is taken as 0.5. It is found that, corresponding to an increase in d_1/h, the reflection coefficient acquires higher values. By comparison of Fig. 5.5(a) with Fig. 5.6(a), a clear observation is that the higher values of reflection coefficient get reduced (in Fig. 5.6(a)) corresponding to the larger values of d_1/h, i.e., for the case when $\mathcal{G}_1$ possesses both resistance and inertial effect. Therefore, it can be concluded that the imaginary part of $\mathcal{G}_1$, attributed to the inertial effect, is responsible for a significant contribution in attenuating the reflected energy by the submerged porous barriers. However, by comparing Figs. 5.5(b) and 5.6(b), it is observed that the maximum values of transmission coefficient increase for larger values of d_1/h.

Figure 5.7(a,b) presents the reflection and transmission coefficients plotted versus L/λ for various drafts d_1/h with the inclusion of an imaginary quantity to $\mathcal{G}_2$ by taking $\mathcal{G}_2 = 0.5 + \text{i}$, whereas $\mathcal{G}_1$ is taken as 0.5. It is found that, corresponding to an increase in d_1/h, the reflection coefficient increases whereas the transmission coefficient decreases. By

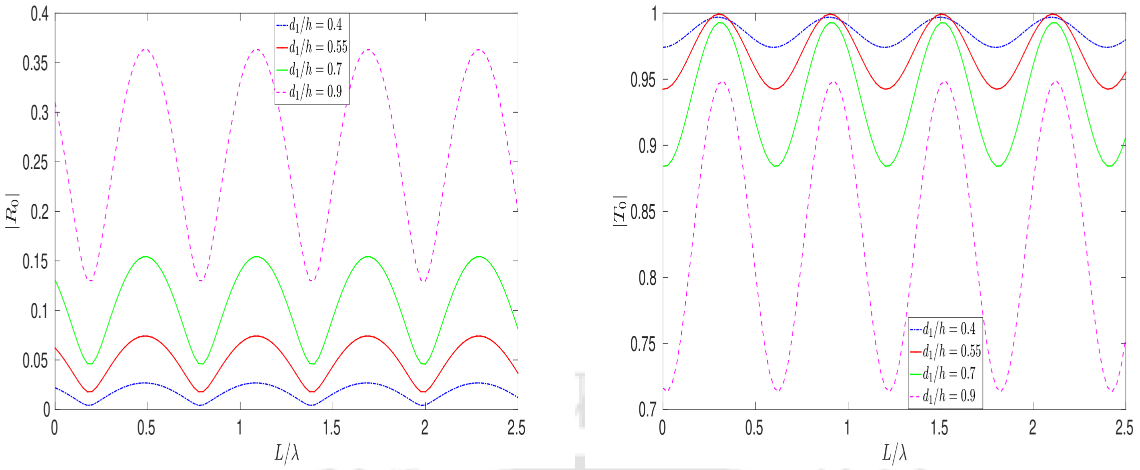

(a) (b)

Figure 5.7: Effect of (a) reflection coefficient $|R_0|$ and (b) transmission coefficient $|T_0|$ versus L/λ for various drafts of the lower tip of the first barrier with $\mathcal{G}_1 = 0.5, \mathcal{G}_2 = 0.5+i$, $d_2 = 0.2h$, $d_3 = d_1$, $d_4 = d_2$, $\theta = 0^0$ and $N = 15$

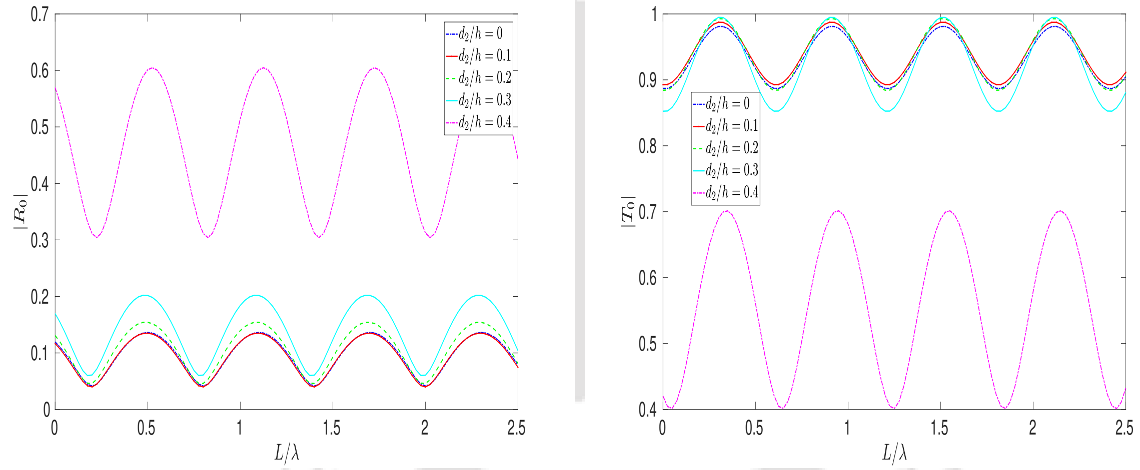

(a) (b)

Figure 5.8: Effect of (a) reflection coefficient $|R_0|$ and (b) transmission coefficient $|T_0|$ versus L/λ for various drafts of the upper tip of the first barrier with $\mathcal{G}_1 = 0.5, \mathcal{G}_2 = 0.5+\mathrm{i}$, $d_1 = d_2 + 0.5h$, $d_3 = d_1$, $d_4 = d_2$, $\theta = 0^0$ and $N = 15$

comparing Figs. 5.5(a) and 5.7(a), it can be noted that the amplitude of the oscillation of reflection coefficient reduces, but the decreasing rate of the reflection coefficient is quite inappreciable. This means that the imaginary part of $\mathcal{G}_2$, attributed to the inertial effect, does not have any significant effect in attenuating the wave transmission by the porous barrier. By comparing Fig. 5.5(b) with Fig. 5.7(b), it is also noticed that the decreasing rate of the transmission coefficient is quite insignificant. In other words, the

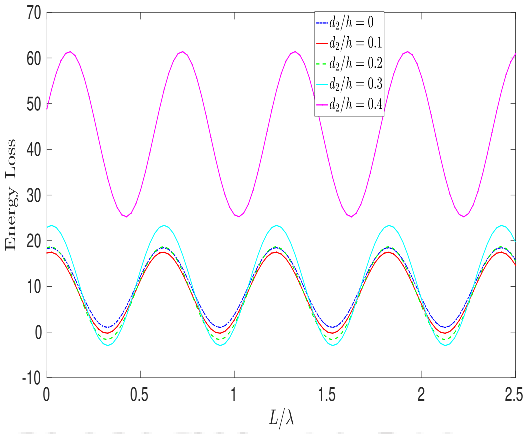

Figure 5.9: Energy loss (in %) versus L/λ for various drafts of the upper tip of the first barrier with $\mathcal{G}_1 = 0.5, \mathcal{G}_2 = 0.5 + \mathrm{i}$, $d_1 = d_2 + 0.5h$, $d_3 = d_1$, $d_4 = d_2$, $\theta = 0^0$ and $N = 15$

wave characteristics are not affected by alternating the position of the porous barriers.

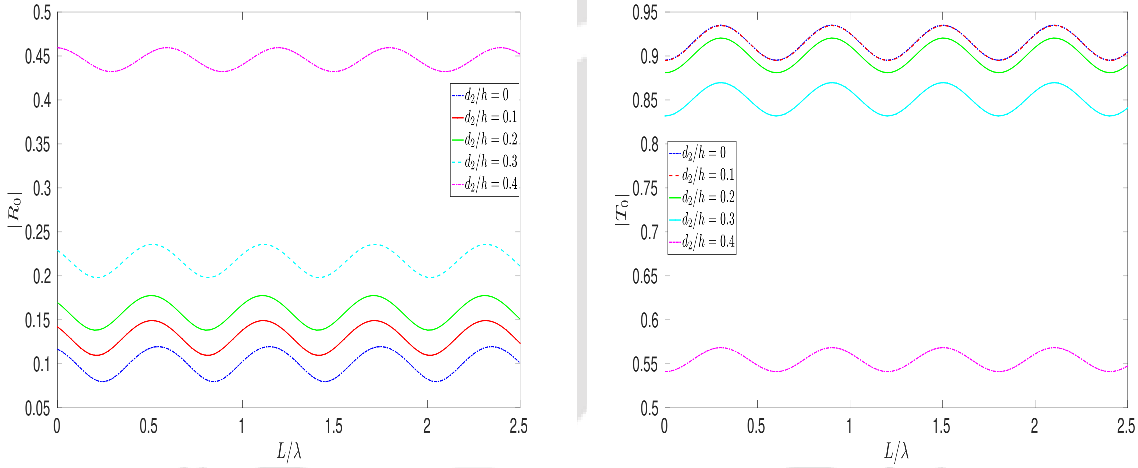

(a) (b)

Figure 5.10: Effect of (a) reflection coefficient $|R_0|$ and (b) transmission coefficient $|T_0|$ versus L/λ for various drafts of the upper tip of the first barrier with $\mathcal{G}_1 = 0.5, \mathcal{G}_2 = 0.5+\mathrm{i}$, $d_1 = d_2 + 0.6h$, $d_3 = 0.5h$, $d_4 = 0.2h$, $\theta = 0^0$ and $N = 15$

Figure 5.8(a,b) depicts the behaviours of reflection and transmission coefficients $|R_0|$ and $|T_0|$ with respect to the non-dimensional depth of the upper tip of the first porous barrier plotted versus L/λ by taking fixed length of porous barriers inside water. For these figures, the following values are considered: $\mathcal{G}_1 = 0.5, \mathcal{G}_2 = 0.5 + \mathrm{i}$, $d_1 = d_2 + 0.5h$, $d_3 = d_1$, $d_4 = d_2$. It is observed that $|R_0|$ increases as the value of d_2/h increases. The maximum and minimum values of $|R_0|$ is found to be much higher for $d_2/h = 0.4$, i.e., when both the porous barriers are fully submerged and they just touch the porous sea-bed. Similarly, a reverse pattern is observed for the case of $|T_0|$. Since the incident wave

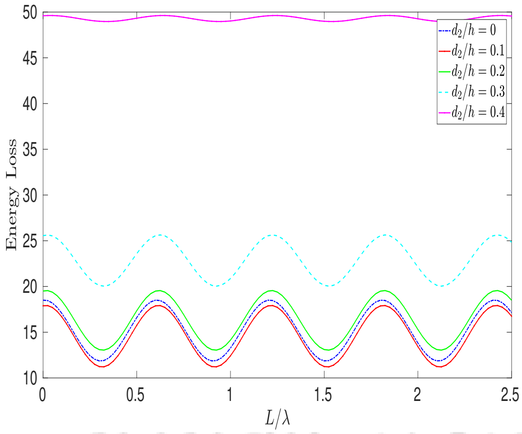

Figure 5.11: Energy loss (in %) versus L/λ for various drafts of the upper tip of the first barrier with $\mathcal{G}_1 = 0.5, \mathcal{G}_2 = 0.5 + \mathrm{i}$, $d_1 = d_2 + 0.6h$, $d_3 = 0.5h$, $d_4 = 0.2h$, $\theta = 0^0$ and $N = 15$

interacts with the porous barriers over the porous sea-bed, occurrence of certain phase change is observed in all the waves. For the mutual interaction of all these incident, reflected and transmitted waves, a certain oscillatory pattern is followed by the reflection coefficient and transmission coefficients corresponding to various values of d_2/h. From Fig. 5.9, it is noticed that when $d_2/h = 0.4$ (when both the porous barriers just touch the porous sea-bed), energy loss is more as compared to the other values of d_2/h.

Figure 5.10(a,b) and Fig. 5.11, respectively, show the behaviours of reflection and transmission coefficients and energy loss with respect to the non-dimensional depth of the upper tip of the first porous barrier by fixing the location of the second porous barrier (when it is submerged) and varying the location of the first porous barrier vertically within the water region. For these figures, the following values are considered: $\mathcal{G}_1 = 0.5, \mathcal{G}_2 = 0.5 + \mathrm{i}$, $d_1 = d_2 + 0.6h$, $d_3 = 0.5h$, $d_4 = 0.2h$. It is noticed that the reflection coefficient increases corresponding to an increase in the value of d_2/h, and the maximum and minimum values of reflection coefficient are higher when $d_2/h = 0.4$, i.e., when the first porous barrier is totally submerged and it just touches the porous sea-bed. The occurrence of maxima/minima in wave reflection is very likely due to the constructive/destructive interference of the incident and reflected waves in the presence of the porous barriers. The transmission coefficient follows a completely reverse pattern of the reflection coefficient. Here, the reflection coefficient, transmission coefficient and energy loss follow oscillatory patterns for various values of d_2/h. As the incident wave interacts with the porous barriers, certain phase change occurs in the incident, reflected and transmitted waves and subsequently, the mutual interaction of these waves leads to the oscillatory trend in the reflection coefficient, transmission coefficient and energy loss. From Fig. 5.11, it is noticed that, for the case of the first porous barrier totally submerged in water and just touching the porous bottom, the energy loss is higher.

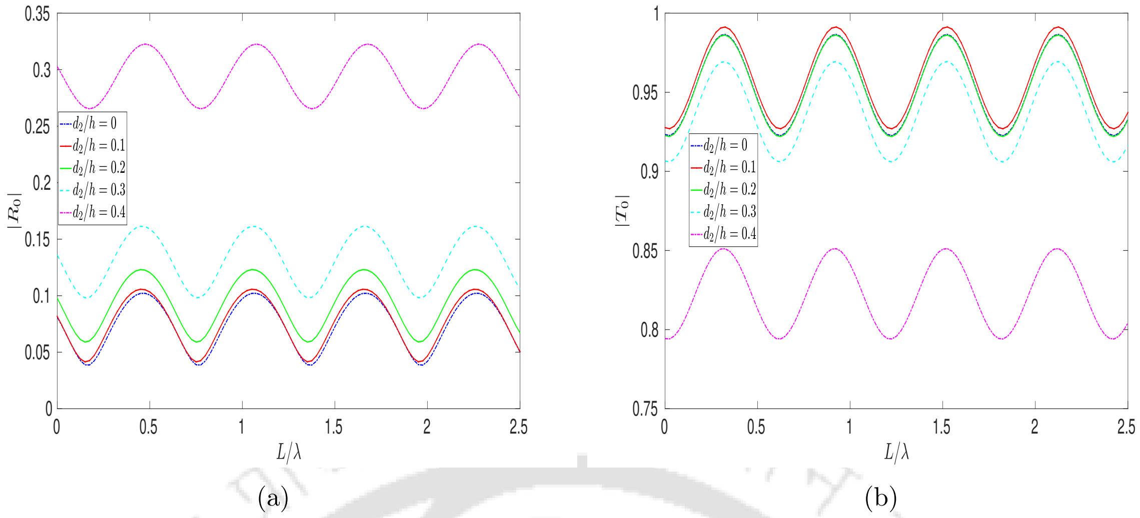

Figure 5.12: Effect of (a) reflection coefficient $|R_0|$ and (b) transmission coefficient $|T_0|$ versus L/λ for various drafts of the upper tip of the first barrier with $\mathcal{G}_1 = 0.5+\mathrm{i}, \mathcal{G}_2 = 0.5$, $d_1 = d_2 + 0.6h$, $d_3 = 0.5h$, $d_4 = 0.2h$, $\theta = 0^0$ and $N = 15$

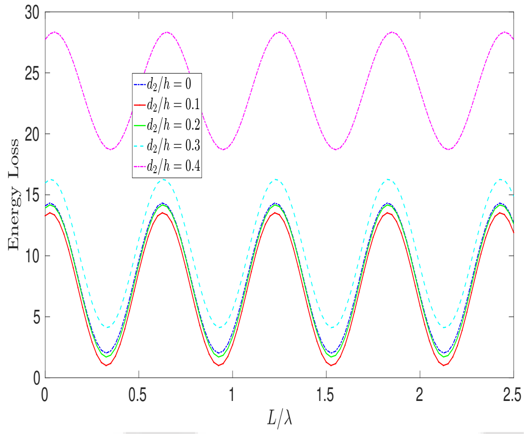

Figure 5.13: Energy loss (in %) versus L/λ for various drafts of the upper tip of the first barrier with $\mathcal{G}_1 = 0.5 + \mathrm{i}, \mathcal{G}_2 = 0.5$, $d_1 = d_2 + 0.6h$, $d_3 = 0.5h$, $d_4 = 0.2h$, $\theta = 0^0$ and $N = 15$

In Fig. 5.12(a,b), the behaviours of reflection and transmission coefficients are investigated by fixing the location of the second porous barrier (when it is submerged) and varying the location of the first porous barrier vertically inside water. For these figures, the following values are considered: $\mathcal{G}_1 = 0.5 + \mathrm{i}, \mathcal{G}_2 = 0.5$, $d_1 = d_2 + 0.6h$, $d_3 = 0.5h$, $d_4 = 0.2h$. The main difference of this result with that from Fig. 5.10(a,b) is the different types of values chosen for $\mathcal{G}_1$ and $\mathcal{G}_2$. For Fig. 5.10(a,b), $\mathcal{G}_1$ has a real value and $\mathcal{G}_2$ has a complex value while for Fig. 5.12(a,b), it is exactly the opposite. It is noticed that the reflection coefficient increases corresponding to an increase in the values of d_2/h. The maximum and minimum values of reflection coefficient are higher when $d_2/h = 0.4$, i.e., for the case of the first porous barrier totally submerged and it just touching the porous bed. The transmission coefficient follows a completely reverse pattern of the reflection coefficient. From Fig. 5.13, it is noticed that, when the first porous barrier just touches the porous bed, energy loss is less as compared to the previous configuration. By comparing Fig. 5.11 with Fig. 5.13, occurrence of a significant increment in energy loss is observed with the inclusion of an imaginary part to the porous-effect parameter of the second porous barrier for the situation when the second porous barrier is totally submerged, i.e., when inertial effects are taken into account. Here, a certain oscillatory pattern is followed by the reflection coefficient, transmission coefficient and energy loss for the various values of d_2/h.

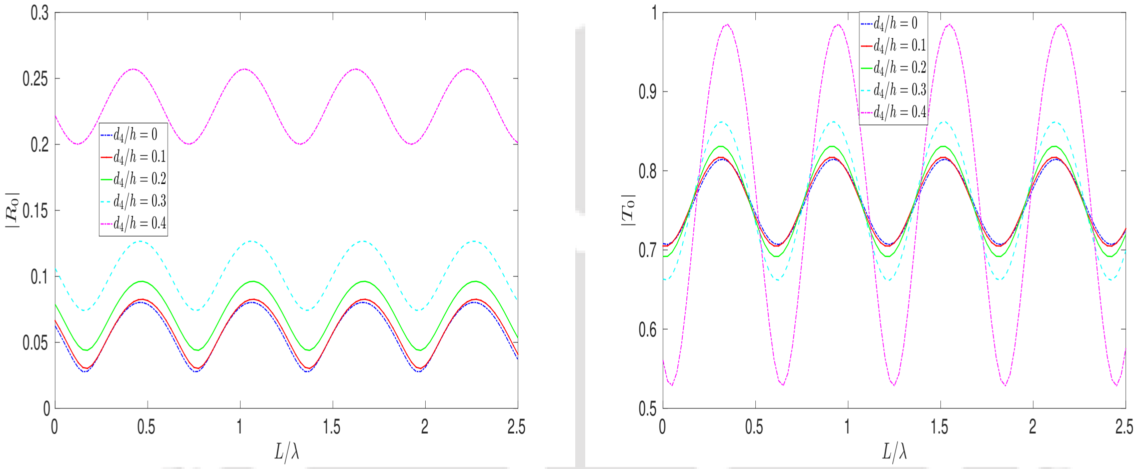

(a) (b)

Figure 5.14: Effect of (a) reflection coefficient $|R_0|$ and (b) transmission coefficient $|T_0|$ versus L/λ for various drafts of the upper tip of the second barrier with $\mathcal{G}_1 = 0.5, \mathcal{G}_2 = 0.5 + \mathrm{i}$, $d_3 = d_4 + 0.6h$, $d_1 = 0.5h$, $d_2 = 0.2h$, $\theta = 0^0$ and $N = 15$

Figures 5.14(a,b) and 5.15 present another investigation with respect to the non-dimensional depth of the upper tip of the second porous barrier by fixing the location of the first porous barrier (when it is submerged) and varying the location of the second porous barrier vertically inside water. Here the behaviours of reflection coefficient, transmission coefficient and energy loss are discussed for the following values of parameters: $\mathcal{G}_1 = 0.5, \mathcal{G}_2 = 0.5 + \mathrm{i}$, $d_3 = d_4 + 0.5h$, $d_1 = 0.5h$, $d_2 = 0.2h$. It is noticed that the reflection coefficient increases corresponding to an increase of the values of d_4/h. It is found that, corresponding to an increase in the values in d_4/h, the oscillatory bahaviour of transmission coefficient magnifies. Also, it is worthwhile to note that, for some specific values of L/λ, the maximum and minimum values of both the reflection coefficient and transmission coefficients are obtained for $d_4/h = 0.4$, i.e., when the second porous barrier just touches the sea-bed. Also the maximum and minimum values of energy loss

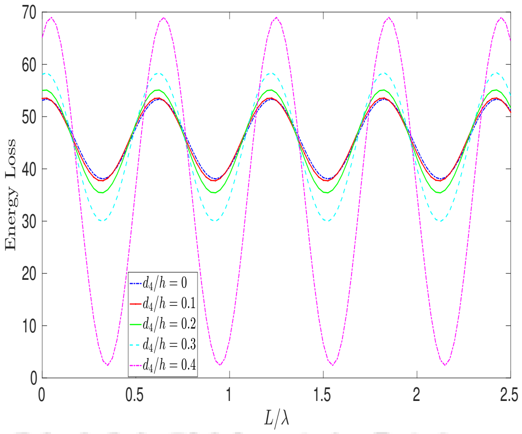

Figure 5.15: Energy loss (in %) versus L/λ for various drafts of the upper tip of the second barrier with $\mathcal{G}_1 = 0.5, \mathcal{G}_2 = 0.5 + \mathrm{i}$, $d_3 = d_4 + 0.6h$, $d_1 = 0.5h$, $d_2 = 0.2h$, $\theta = 0^0$ and $N = 15$

occur when $d_4/h = 0.4$. Here also, an oscillatory pattern is observed with respect to the reflection coefficient, transmission coefficient and energy loss for various values of d_4/h.

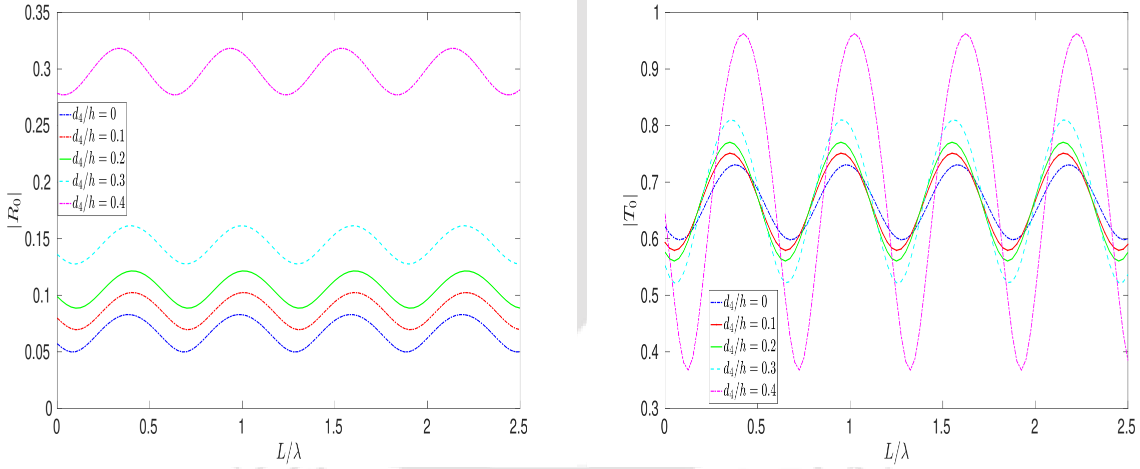

(a) (b)

Figure 5.16: Effect of (a) reflection coefficient $|R_0|$ and (b) transmission coefficient $|T_0|$ versus L/λ for various drafts of the upper tip of the second barrier with $\mathcal{G}_1 = 0.5 + \mathrm{i}, \mathcal{G}_2 = 0.5$, $d_3 = d_4 + 0.6h$, $d_1 = 0.5h$, $d_2 = 0.2h$, $\theta = 0^0$ and $N = 15$

In Figs. 5.16(a,b) and 5.17, the same investigation is carried out by fixing the location of the first porous barrier (when it is submerged) and varying the location of the second porous barrier vertically inside water region. Here the behaviours of reflection and transmission coefficients are analyzed for the following parameter values: $\mathcal{G}_1 = 0.5 + \mathrm{i}, \mathcal{G}_2 = 0.5$, $d_3 = d_4 + 0.6h$, $d_1 = 0.5h$, $d_2 = 0.2h$. It is noticed that the reflection coefficient increases corresponding to an increase in the values of d_4/h. Both maximum and minimum values

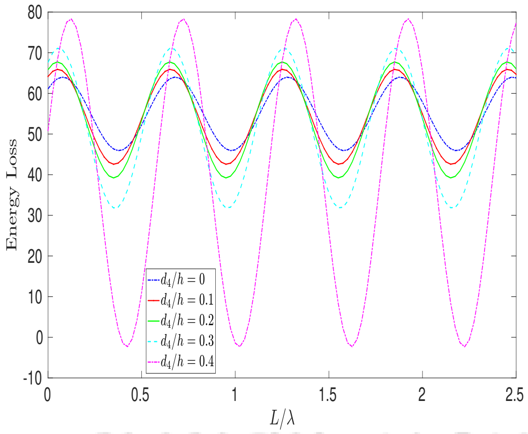

Figure 5.17: Energy loss (in %) versus L/λ for various drafts of the upper tip of the second barrier with $\mathcal{G}_1 = 0.5 + \mathrm{i}, \mathcal{G}_2 = 0.5$, $d_3 = d_4 + 0.6h$, $d_1 = 0.5h$, $d_2 = 0.2h$, $\theta = 0^0$ and $N = 15$

of reflection coefficient and transmission coefficient occur when $d_4/h = 0.4$, i.e., when the second porous barrier just touches the porous sea-bed. Here also, the reflection coefficient, transmission coefficient and energy loss follow a certain oscillatory pattern for various values of d_4/h. Similarly, the maximum and minimum values of energy loss are obtained for $d_4/h = 0.4$. By comparing Figs. 5.15 and 5.17, the occurrence of a reasonable decrement in energy loss is observed with the inclusion of an imaginary part to the porous effect parameter of the second porous barrier for the situation when the first porous barrier is totally submerged. For fixed properties of the first porous barrier, energy dissipation is less as compared to the energy dissipation due to fixed properties of the second porous barrier. Therefore, it is observed that a suitable positioning of the barriers is required in order to reduce the waveload and to create a tranquility zone.

In Fig. 5.18(a,b), the effect of angle of incidence is investigated for the case of submergence of both the barriers in water. Here the behaviours of reflection and transmission coefficients are examined for the following values of parameters: $\mathcal{G}_1 = 0.5 + \mathrm{i}, \mathcal{G}_2 = 0.5$, $d_2 = d_4 = 0.2h$, $d_1 = d_3 = d_4 + 0.5h$. It is found that the maximum and minimum values of reflection occur in the case of normal incidence (i.e., $\theta = 0°$). It is noticed from the above figures that the reflection coefficient and transmission coefficient follow an oscillatory pattern. One interesting fact is that, with the barriers adjacent to each other, the amplitude of oscillation in the reflection coefficient is less, but the analogous transmission is quite large. It occurs because of the ineffectiveness of the second porous barrier when both the barriers are adjacent to one another.

In Fig. 5.19(a,b), the reflection and transmission coefficients are plotted versus L/λ corresponding to various values of porosity of the sea-bed. For these figures, the following values are considered: $\mathcal{G}_1 = 0.5 = \mathcal{G}_2$, $d_2 = d_4 = 0.5h$, $d_1 = d_3 = d_4 + 0.5h$. It is observed that the reflection coefficient increases corresponding to an increase in porosity

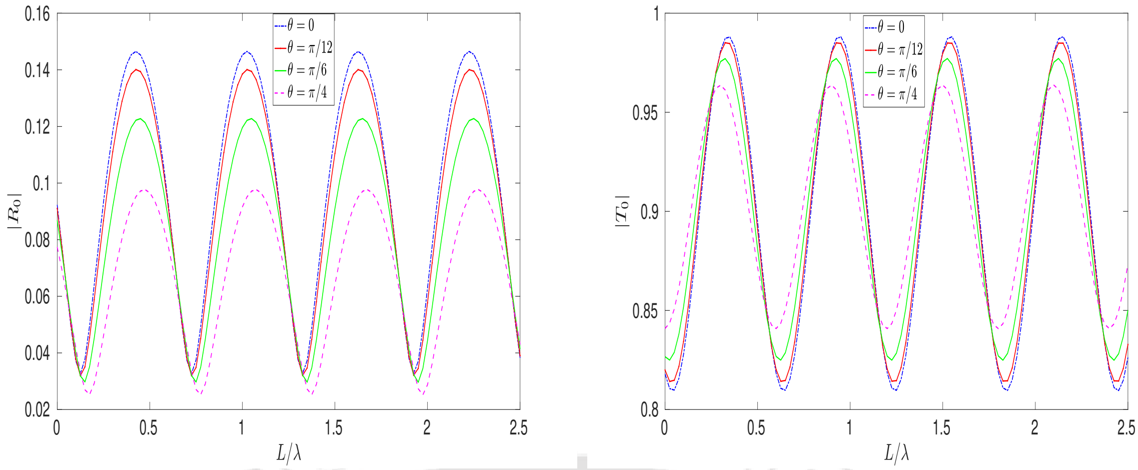

(a) (b)

Figure 5.18: Effect of (a) reflection coefficient $|R_0|$ and (b) transmission coefficient $|T_0|$ versus L/λ for different values of angle of incidence with $\mathcal{G}_1 = 0.5 + \mathrm{i}, \mathcal{G}_2 = 0.5$, $d_2 = d_4 = 0.2h$, $d_1 = d_3 = d_4 + 0.5h$ and $N = 15$

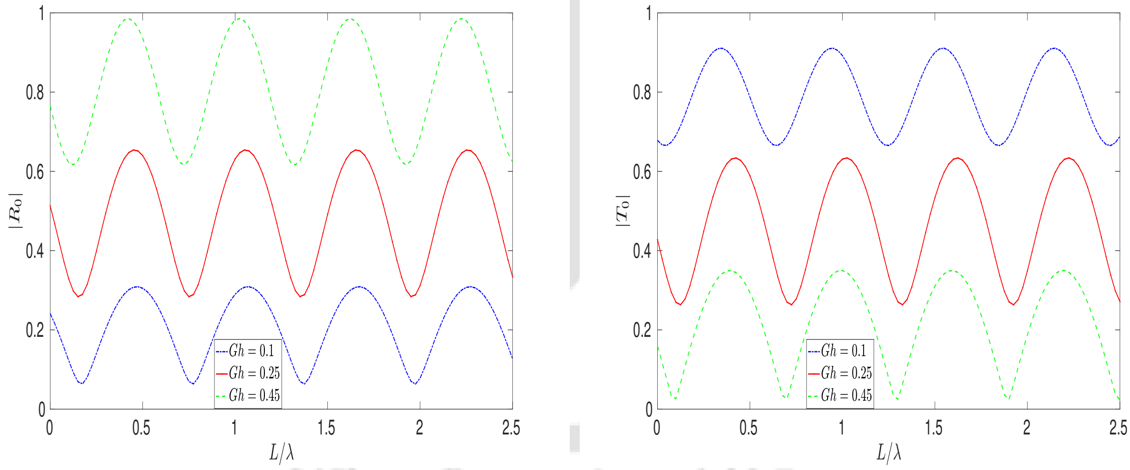

(a) (b)

Figure 5.19: Effect of (a) reflection coefficient $|R_0|$ and (b) transmission coefficient $|T_0|$ versus L/λ for different values of porosity of the sea-bed with $\mathcal{G}_1 = 0.5 = \mathcal{G}_2$, $d_2 = d_4 = 0.5h$, $d_1 = d_3 = d_4 + 0.5h$ and $N = 15$

G of the sea-bed. On the other hand, transmission coefficient decreases corresponding to an increase in porosity G. It is worthwhile to note that major portion of the incident wave energy gets dissipated through the porous sea-bed.

5.6 Conclusion

This chapter takes up the problem of scattering of oblique water waves by two fully submerged porous barriers of different porosity propagating over a porous sea-bed in an infinite channel of finite depth, having a free surface and uses linearized wave theory to obtain the results. It is to be noted that the motion of the fluid below the porous sea-bed is not considered in this work. Under these circumstances, corresponding to any given frequency, there exists exactly one propagating wave which corresponds to the free-surface wave mode. For the presence of the porous sea-bed, the roots of the dispersion relation are investigated by using a contour plot. Applying eigenfunction expansion method in association with least square approach, the physical problem under consideration is formulated as an appropriate boundary value problem (BVP) involving region-wise velocity potentials. Subsequently, by using the matching boundary conditions along the vertical boundaries, the reflection and transmission coefficients and energy loss are computed by solving a system of linear equations. The significance of the roles of different physical parameters such as porosity of the barriers, distance of the barriers from the mean free surface, the position of the barriers and porosity of the sea-bed on the process of scattering is analyzed graphically. There is a glimpse of periodic oscillation in every graph. Further, the study reveals that when the height of a porous barrier is fixed, lower reflection and higher transmission can be acquired by affecting an increase in the inertial effect of the porous barrier. Further, higher energy loss is found by attenuating the inertial effect of the submerged porous barriers. It is worthwhile to note that when the porous barriers of greater height just touch the porous sea-bed, maximum energy loss occurs. Therefore, it can be concluded that a suitable positioning of the barriers is required in order to reduce the waveload and to create a tranquility zone. For wave scattering by submerged barriers, with an increment in porosity of the sea-bed, wave reflection increases and transmission decreases. Thus, it can be concluded that wave energy is significantly dissipated for higher porosity of the sea-bed. It should be noted that the presence of the porous sea-bed is instrumental for a sufficient portion of the wave energy getting dissipated when the wave interacts with the porous barriers. The solution of this physical problem is likely to be helpful in devising mechanism for reducing the waveload for purposes of different advanced evolutions in the marine environment. The expectation here is that the results obtained in this work can be suitably used for a wider set of water wave scattering problems that occur in ocean engineering, especially when the sea-bed is considered to be porous and thin vertical porous barriers are used as breakwaters. Excellent agreement is observed when an obtained result is compared with an available established result.

CHAPTER 6

SCATTERING OF WATER WAVES BY TWO SUBMERGED POROUS BARRIERS LOCATED ABOVE AN ELASTIC SEA-BED

6.1 Introduction

In this chapter, a hydroelastic model, due to an elastic sea-floor, is presented for studying the scattering of oblique water waves by two totally submerged vertical porous barriers, placed at some distance from each other, in a homogeneous fluid. The complete analytical solution, under the assumption of small-amplitude theory and structural response, is acquired by employing eigenfunction expansion and least square method for the problem of flexural gravity waves interacting with submerged porous barriers. Subsequently, numerical computation for the reflection and transmission coefficients and energy loss are carried out and discussed for different values of the wavenumber, elasticity of the sea-floor, porous barrier and structural parameters. Significant variation in the elastic specification of the sea-floor commands considerable influence when the propagating wave impinges upon the submerged vertical porous barriers. The porous barriers are expected to reduce the wave impact and thereby help in creating a tranquility zone in the coastal regions for various activities taking place without much hindrance. Certain description in this work may be same or similar to those in earlier chapters. It has been kept here to get a proper flow in reading the whole chapter.

6.2 Formulation of scattering problem

Propagation of water wave of small amplitude, in response to the action of gravity and under the assumption of small-amplitude plate response, is considered in an incompressible, inviscid and homogeneous fluid undergoing an irrotational motion and flowing over an elastic sea-floor. Here the elastic sea-floor is considered just as a boundary and motion beyond it is not considered. Following Euler-Bernoulli beam equation, the elastic sea-floor is considered to act as a thin elastic plate, as has already been considered in earlier relevant chapters.

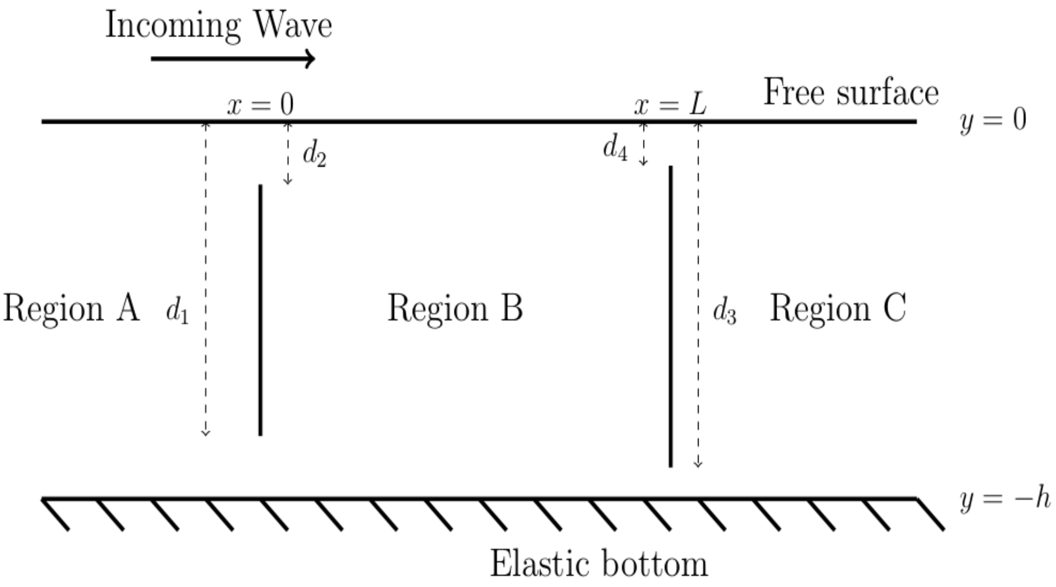

Figure 6.1: Schematic diagram of the problem

A Cartesian coordinate system is adopted in such a way that the y-axis points in the vertical upward direction; $y=-h$ and $y=0$, respectively, represent the location of the elastic sea-floor and free surface, as displayed in Fig. 6.1. Here, two fully submerged thin vertical porous barriers of different heights are placed at $x=0$ and $x=L$, respectively. Assume d_1 and d_3, respectively, to represent the distances of the lower vertical tips of the first and second porous barriers, and d_2 and d_4, respectively, the distances of the upper vertical tips, from the free surface. The whole fluid domain under consideration is partitioned into three sub-domains, namely, $x<0$, $-h<y<0$ as region A, $0<x<L$, $-h<y<0$ as region B, and $x>L$, $-h<y<0$ as region C. Adopting small amplitude theory and accounting for all the above assumptions, the velocity potentials in each region A, B and C, respectively, can be represented by $\Psi_1(x,y,z,t)=\psi_1(x,y)e^{(\mathrm{i}lz-\mathrm{i}\omega t)}$, $\Psi_2(x,y,z,t)=\psi_2(x,y)e^{(\mathrm{i}lz-\mathrm{i}\omega t)}$ and $\Psi_3(x,y,z,t)=\psi_3(x,y)e^{(\mathrm{i}lz-\mathrm{i}\omega t)}$. Here $l=k_I\sin\theta$ is the component of the incident wave number k_I (surface mode) along the z-axis with θ denoting the angle of the incidence on the x-axis.

As such, the velocity potentials ψ_j, $j=1,2,3$, in regions A, B and C, respectively, satisfy modified Helmholtz equation as follows:

$$\frac{\partial^2\psi_j}{\partial x^2}+\frac{\partial^2\psi_j}{\partial y^2}-l^2\psi_j=0. \tag{6.1}$$

The boundary condition at the mean free surface $y=0$ is given by

$$\frac{\partial\psi_j}{\partial y}-K\psi_j=0, \qquad j=1,2,3. \tag{6.2}$$

The elastic sea-floor condition can be written as (based on Saha and Bora [81])

$$K\psi_j+\Big\{\mathcal{D}\Big(\frac{\partial^2}{\partial x^2}-l^2\Big)^2+1-\epsilon K\Big\}\frac{\partial\psi_j}{\partial y}=0, \quad \text{on} \quad y=-h,\ j=1,2,3, \tag{6.3}$$

where $\mathcal{D}=\frac{Q}{\rho_h g}$ with Q as the flexural rigidity of the elastic sea-floor given by $Q=Eh_0^3/[12(1-\nu^2)]$; E and ν, respectively, are Young's modulus and Poisson's ratio, $\epsilon=(\rho_0/\rho_h)h_0$; ρ_h is the density of water, ρ_0 is the density of the elastic plate, h_0 is thickness of the elastic plate, which is considered to be very small compared to depth h.

In addition to the governing equations and various boundary conditions as already mentioned above, there are several matching conditions which are satisfied across the vertical boundaries. ψ_j, $j=1,2,3$ satisfy the following across $x=0$ and $x=L$ (Chwang [17],Yu [100]):

$$\begin{aligned}
\frac{\partial\psi_1}{\partial x} &= \frac{\partial\psi_2}{\partial x}=\mathrm{i}k_I\mathcal{G}_1(\psi_1-\psi_2); \quad x=0,-d_1<y<-d_2, && (6.4)\\
\frac{\partial\psi_1}{\partial x} &= \frac{\partial\psi_2}{\partial x};\ x=0,\ (-h<y<-d_1)\cup(-d_2<y<0), && (6.5)\\
\psi_1 &= \psi_2;\ x=0,\ (-h<y<-d_1)\cup(-d_2<y<0), && (6.6)\\
\frac{\partial\psi_2}{\partial x} &= \frac{\partial\psi_3}{\partial x}=\mathrm{i}k_I\mathcal{G}_2(\psi_2-\psi_3); \quad x=L,-d_3<y<-d_4, && (6.7)\\
\frac{\partial\psi_2}{\partial x} &= \frac{\partial\psi_3}{\partial x};\ x=L,\ (-h<y<-d_3)\cup(-d_4<y<0), && (6.8)\\
\psi_2 &= \psi_3;\ x=L,\ (-h<y<-d_3)\cup(-d_4<y<0), && (6.9)
\end{aligned}$$

where $\mathcal{G}_1$ and $\mathcal{G}_2$, respectively, denote the non-dimensional porous-effect parameters, which are complex in nature, associated with the barriers at $x=0$ and $x=L$, respectively.

6.3 Solution of the BVPs

Applying the separation of variables technique, velocity potential $\psi_1(x,y)$ can be written as

$$\psi_1(x,y)=\sum_{n=I}^{II}[e^{\mathrm{i}K_nx}+R_ne^{-\mathrm{i}K_nx}]Z_n(h,y)+\sum_{n=III}^{IV}R_ne^{-\mathrm{i}K_nx}Z_n(h,y)+\sum_{n=1}^{\infty}R_ne^{-\mathrm{i}K_nx}Z_n(h,y), \tag{6.10}$$

where R_n represents the complex reflection coefficient and $K_n=(k_n^2-l^2)^{\frac{1}{2}}$. Here it is assumed that $R_{IV}=0$ due to the boundedness of the velocity potential at negative infinity. The depth-dependent function $Z_n(h,y)$ has the following form upon utilizing (6.3):

$$Z_n(h,y)=\frac{(\mathcal{D}k_n^4+1-\epsilon K)k_n\cosh k_n(h+y)-K\sinh k_n(h+y)}{(\mathcal{D}k_n^4+1-\epsilon K)k_n\sinh k_nh-K\cosh k_nh}, n=I,...,IV,1,2,..., \tag{6.11}$$

where k_n satisfies the dispersion relation

$$[k_n^2(\mathcal{D}k_n^4+1-\epsilon K)+K^2]\tanh k_nh-Kk_n(\mathcal{D}k_n^4+2-\epsilon K)=0. \tag{6.12}$$

Dispersion relation (6.12) has a pair of distinct positive real roots k_n, $n=I,II$, that indicate the propagating modes; two pairs of complex roots k_n, $n=III,...,VI$ in the form $a\pm ib$ and $-(a\pm ib)$ which correspond to the non-propagating modes and an infinite number of purely imaginary roots $k_n=\mathrm{i}\kappa_n$, $n=1,2,\ldots,$ that correspond to a set of evanescent modes (Fig. 6.2). For the sake of ensuring the validity of the boundedness property of the velocity potential, the contribution from the roots k_V and k_{VI} is to be avoided. Since the existence of exactly two positive real roots k_I and k_{II} of (6.12) (Mohapatra and Sahoo [73]) is evidently ensured, there exist two wave modes (wavenumbers) - one wave propagating along the free surface (surface mode) and other one along the elastic sea-floor (flexural mode) along the positive x-direction. It is to be noted that the root k_I of dispersion relation (6.12), without loss of generality, can be considered to be the same as the wavenumber of the incident wave as denoted earlier. The number of evanescent modes of the potential is required to be truncated at some finite $n=N$ so as to get

$$\psi_1(x,y)=\sum_{n=I}^{II}[e^{\mathrm{i}K_nx}+R_ne^{-\mathrm{i}K_nx}]Z_n(h,y)+\sum_{n=III}^{IV}R_ne^{-\mathrm{i}K_nx}Z_n(h,y)+\sum_{n=1}^{N}R_ne^{-\mathrm{i}K_nx}Z_n(h,y). \tag{6.13}$$

Similarly, the spatial velocity potential $\psi_2(x,y)$ in region B has the following expression, after truncating at $n = N$:

$$\psi_2(x, y) = \sum_{n=I,..,IV,1}^{N} [A_n e^{\mathrm{i}K_n x} + B_n e^{-\mathrm{i}K_n(x-L)}] Z_n(h, y), \tag{6.14}$$

with A_n and B_n as arbitrary constants.

Following a similar procedure, the spatial velocity potential $\psi_3(x, y)$ in region C can be written as

$$\psi_3(x, y) = \sum_{n=I,..,IV,1}^{N} T_n e^{\mathrm{i}K_n(x-L)} Z_n(h, y), \tag{6.15}$$

where T_n is the complex transmission coefficient. Here it is assumed that $T_{IV} = 0$ due to the boundedness of the velocity potential at infinity. It is worth mentioning that the energy loss due to the interaction of the waves with the porous barriers can be determined by using the relation as follows:

$$\text{Energy loss} = (1 - |R_I|^2 - |T_I|^2) \times 100\%. \tag{6.16}$$

The zeros of the complex dispersion relation (6.12) are evaluated numerically through the use of contour plots for the purpose of interpreting the behaviours of the wavenumbers (Fig. 6.2). In order to compute these, values of various parameters are considered in accordance with the following: time period $T = 5$ s, depth $h = 20$ m, density of the homogeneous fluid $\rho_h = 1025$ kg/m^3, elastic material density of the plate $\rho_0 = 2650$ kg/m^3, Young's modulus of the elastic material of the elastic plate $E = 6 \times 10^8$ Pa, Poisson's ratio $\nu = 0.3$, thickness of the elastic plate $h_0 = 1$ m, $g = 9.81$ m/s^2, respectively, unless otherwise mentioned. To find the nature and value of the roots of (6.12), a similar approach as followed in the earlier chapters is adopted. Figure 6.2 represents the nature of the complex zeros demonstrating that two pairs of complex zeros, occurring as positive and negative of a complex conjugate pair, namely, $k_{III}, k_{IV}, k_V, k_{VI}$, are located in such a way that there is one zero in each of the quadrants. It is required to be mentioned that two pairs of complex zeros occur for the elastic sea-floor. For computational purpose, only the roots that lie in the first and fourth quadrants are chosen in order that the velocity potentials ψ_1 and ψ_3 remain bounded.

The horizontal velocity components $\frac{\partial \psi_1}{\partial x}$ and $\frac{\partial \psi_2}{\partial x}$ follow the continuity condition along $x = 0, -h < y < 0$, using Eqs. (6.4) and (6.5), thereby giving

$$\begin{aligned} R_n &= 1 - A_n + B_n e^{\mathrm{i}K_n L}, \text{ for } n = I, II, III, && (6.17)\\ R_n &= B_n e^{\mathrm{i}K_n L} - A_n, \text{ for } n = 1, 2, \cdots, N, && (6.18)\\ R_n &= 0, \text{ for } n = IV. && (6.19) \end{aligned}$$

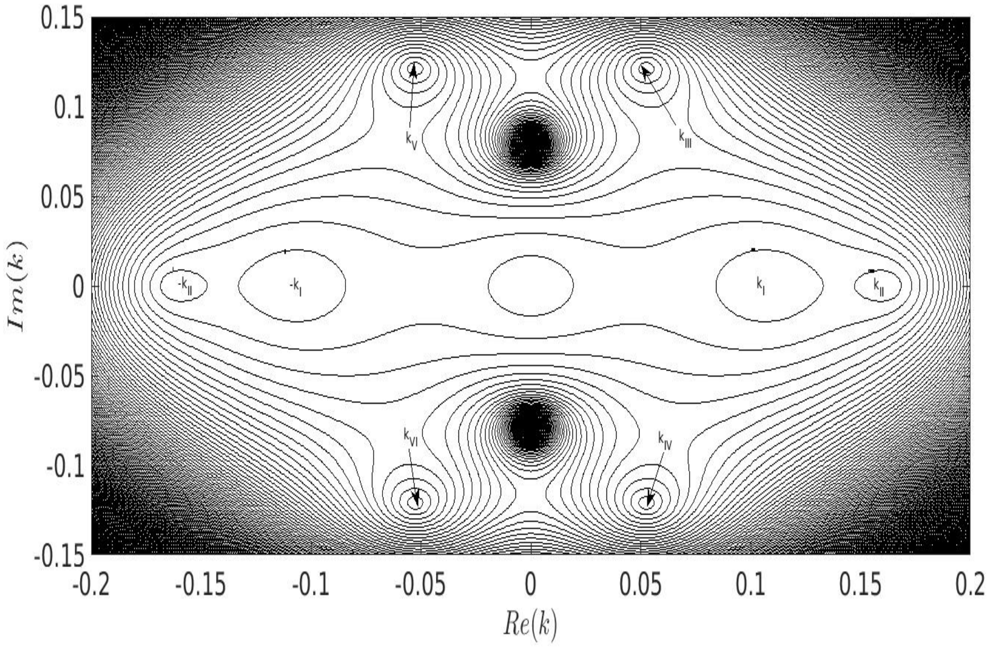

Figure 6.2: Roots of the dispersion relation with $h = 20$ m, $E = 6 \times 10^8$ Pa, $\nu = 0.3$, $\rho = 1025$ kg/m^3, $\rho_0 = 2650$ kg/m^3, $h_0 = 1$ m, $g = 9.81$ m/s^2 and $T = 5$ s

The second equality in Eq. (6.4) gives

$$\sum_{n=I,II,III,1}^{N} (K_n + 2k_I \mathcal{G}_1) A_n Z_n - \sum_{n=I,II,III,1}^{N} K_n B_n e^{\mathrm{i}k_n L} Z_n + (K_{IV} + k_1 \mathcal{G}_1) A_{IV} Z_{IV}$$
$$-(K_{IV} - k_1 \mathcal{G}_1) e^{\mathrm{i}k_{IV} L} B_{IV} Z_{IV} - 2k_I \mathcal{G}_1 \sum_{n=I}^{II} Z_n = 0, \; -d_2 < y < -d_1. \quad (6.20)$$

Similarly, Eq. (6.6) results in

$$\sum_{n=I,II,III,1}^{N} 2A_n Z_n + A_{IV} Z_{IV} + e^{\mathrm{i}k_{IV} L} B_{IV} Z_{IV} - \sum_{n=I}^{II} 2Z_n = 0,$$
$$(-h < y < -d_1) \cup (-d_2 < y < 0). \quad (6.21)$$

To evaluate the undetermined coefficients appearing in Eqs. (6.20) and (6.21), we adopt the method of least square approach as used in Chapter 5. In order to implement this, a notation $\mathcal{L}(y)$ is introduced as follows:

$$\mathcal{L}(y)=\begin{cases}\sum\limits_{n=I,II,III,1}^{N}(K_n+2k_I\mathcal{G}_1)A_nZ_n-\sum\limits_{n=I,II,III,1}^{N}K_nB_ne^{\mathrm{i}k_nL}Z_n+(K_{IV}+k_1\mathcal{G}_1)A_{IV}Z_{IV}\\ -(K_{IV}-k_1\mathcal{G}_1)e^{\mathrm{i}k_{IV}L}B_{IV}Z_{IV}-2k_I\mathcal{G}_1\sum\limits_{n=I}^{II}Z_n,\\ \\ \sum\limits_{n=I,II,III,1}^{N}2A_nZ_n+A_{IV}Z_{IV}+e^{\mathrm{i}k_{IV}L}B_{IV}Z_{IV}-\sum\limits_{n=I}^{II}2Z_n.\end{cases}\tag{6.22}$$

It may be noted that the quantity $\mathcal{L}(y)$ is similar to the one used in Chapter 5, but not the same.

The requirement is that the relation

$$\int_{-h}^{0}|\mathcal{L}(y)|^2\mathrm{d}y=\text{minimum}\tag{6.23}$$

must be valid for $\mathcal{L}(y)=0$ in $-h<y<0$.

Next, the above integral is minimized with respect to each coefficient A_m $(m=I,II,III,IV,1,2,\ldots,N)$ to get the following integral equation:

$$\int_{-h}^{0}\mathcal{L}^*(y)\frac{\partial\mathcal{L}(y)}{\partial A_m}\mathrm{d}y=0,\ \ m=I,II,III,IV,1,2,\ldots,N,\tag{6.24}$$

where $\mathcal{L}^*(y)$ denotes the complex conjugate of $\mathcal{L}(y)$.

Integrating with respect to the variable y, we obtain the following system of linear equations:

$$\sum_{n=I,II,III,1}^{N}S^{(1)}_{m,n}A_n^*+\mathcal{S}^{(1)}_{m,IV}A_{IV}^*+\sum_{n=I,II,III,1}^{N}T^{(1)}_{m,n}B_n^*+\mathcal{T}^{(1)}_{m,IV}B_{IV}^*=r^{(1)}_m,\ \ m\neq IV,\tag{6.25}$$

$$\sum_{n=I,II,III,1}^{N}S^{(2)}_{m,n}A_n^*+\mathcal{S}^{(2)}_{m,IV}A_{IV}^*+\sum_{n=I,II,III,1}^{N}T^{(2)}_{m,n}B_n^*+\mathcal{T}^{(2)}_{m,IV}B_{IV}^*=r^{(2)}_m,\ \ m=IV,\tag{6.26}$$

where

$$S^{(1)}_{m,n}=(K_n^*+2k_I\mathcal{G}_1^*)(K_m+2k_I\mathcal{G}_1)\int_{-d_1}^{-d_2}Z_mZ_n\mathrm{d}y+4\left[\int_{-h}^{-d_1}Z_mZ_n\mathrm{d}y+\int_{-d_2}^{0}Z_mZ_n\mathrm{d}y\right],\tag{6.27}$$

$$S^{(2)}_{m,n} = (K_n^* + 2k_I\mathcal{G}_1^*)(K_m + k_I\mathcal{G}_1)\int_{-d_1}^{-d_2} Z_m Z_n \mathrm{d}y + 2\Big[\int_{-h}^{-d_1} Z_m Z_n \mathrm{d}y + \int_{-d_2}^{0} Z_m Z_n \mathrm{d}y\Big], \tag{6.28}$$

$$\mathcal{S}^{(1)}_{m,IV} = (K_{IV}^* + 2k_I\mathcal{G}_1^*)(K_m + k_I\mathcal{G}_1)\int_{-d_1}^{-d_2} Z_m Z_{IV} \mathrm{d}y + 2\Big[\int_{-h}^{-d_1} Z_m Z_{IV} \mathrm{d}y + \int_{-d_2}^{0} Z_m Z_{IV} \mathrm{d}y\Big], \tag{6.29}$$

$$\mathcal{S}^{(2)}_{m,IV} = (K_{IV}^* + k_I\mathcal{G}_1^*)(K_{IV} + k_I\mathcal{G}_1)\int_{-d_1}^{-d_2} Z_{IV}^2 \mathrm{d}y + \Big[\int_{-h}^{-d_1} Z_{IV}^2 \mathrm{d}y + \int_{-d_2}^{0} Z_{IV}^2 \mathrm{d}y\Big], \tag{6.30}$$

$$T^{(1)}_{m,n} = -K_n^*\zeta_n^*(K_m + 2k_I\mathcal{G}_1)\int_{-d_1}^{-d_2} Z_m Z_n \mathrm{d}y, \tag{6.31}$$

$$T^{(2)}_{m,n} = -K_n^*\zeta_n^*(K_{IV} + k_I\mathcal{G}_1)\int_{-d_1}^{-d_2} Z_{IV} Z_n \mathrm{d}y, \tag{6.32}$$

$$\mathcal{T}^{(1)}_{m,IV} = -(K_{IV}^* - k_I\mathcal{G}_1^*)(K_m + 2k_I\mathcal{G}_1)\zeta_n^*\int_{-d_1}^{-d_2} Z_m Z_{IV} \mathrm{d}y + 2\zeta_{IV}^*\Big[\int_{-h}^{-d_1} Z_m Z_{IV} \mathrm{d}y + \int_{-d_2}^{0} Z_m Z_{IV} \mathrm{d}y\Big], \tag{6.33}$$

$$\mathcal{T}^{(2)}_{m,IV} = -(K_{IV}^* - k_I\mathcal{G}_1^*)(K_{IV} + k_I\mathcal{G}_1)\zeta_{IV}^*\int_{-d_1}^{-d_2} Z_{IV}^2 \mathrm{d}y + \zeta_{IV}^*\Big[\int_{-h}^{-d_1} Z_{IV}^2 \mathrm{d}y + \int_{-d_2}^{0} Z_{IV}^2 \mathrm{d}y\Big], \tag{6.34}$$

$$r^{(1)}_m = 2k_I\mathcal{G}_1^*(K_m + 2k_I\mathcal{G}_1)\sum_{n=I}^{II}\Big[\int_{-d_1}^{-d_2} Z_m Z_n \mathrm{d}y\Big] + 4\sum_{n=I}^{II}\Big[\int_{-h}^{-d_1} Z_m Z_n \mathrm{d}y + \int_{-d_2}^{0} Z_m Z_n \mathrm{d}y\Big], \tag{6.35}$$

$$r^{(2)}_m = 2k_I\mathcal{G}_1^*(K_{IV} + k_I\mathcal{G}_1)\sum_{n=I}^{II}\Big[\int_{-d_1}^{-d_2} Z_{IV} Z_n \mathrm{d}y\Big] + 2\sum_{n=I}^{II}\Big[\int_{-h}^{-d_1} Z_{IV} Z_n \mathrm{d}y + \int_{-d_2}^{0} Z_{IV} Z_n \mathrm{d}y\Big], \tag{6.36}$$

with $\zeta_n = e^{\mathrm{i}K_n L}$ and $*$ of any quantity standing for its corresponding complex conjugate.

Now utilization of the continuity condition along the boundary $x = L, -h < y < 0$

with respect to the horizontal velocity components $\frac{\partial\psi_2}{\partial x}$ and $\frac{\partial\psi_3}{\partial x}$ (Eqs. (6.7) and (6.8)) gives the following:

$$\begin{aligned} T_n &= A_n e^{\mathrm{i}K_nL} - B_n, \text{ for } n = I, II, III, 1, 2, \ldots, N, && (6.37)\\ T_n &= 0, \text{ for } n = IV. && (6.38)\end{aligned}$$

The second equality of Eq. (6.7) gives rise to

$$\sum_{n=I,II,III,1}^{N} K_n e^{\mathrm{i}k_nL} A_n Z_n - \sum_{n=I,II,III,1}^{N} (K_n + 2k_I\mathcal{G}_2)B_nZ_n - 2k_I\mathcal{G}_2B_{IV}Z_{IV} = 0, \quad -d_4 < y < -d_3. \qquad (6.39)$$

Furthermore, Eq. (6.9) gives

$$\sum_{n=I,..,IV,1}^{N} 2B_nZ_n = 0, \ (-h < y < -d_3) \cup (-d_4 < y < 0). \qquad (6.40)$$

By utilizing the method of least square, another system of linear equations arises as follows:

$$\begin{aligned} \sum_{n=I,..,III,1}^{N} P^{(1)}_{m,n}A^*_n + \sum_{n=I,..,III,1}^{N} Q^{(1)}_{m,n}B^*_n + \mathcal{Q}^{(1)}_{m,IV}B^*_{IV} &= 0, \ m \neq IV, && (6.41)\\ \sum_{n=I,..,III,1}^{N} P^{(2)}_{m,n}A^*_n + \sum_{n=I,..,III,1}^{N} Q^{(2)}_{m,n}B^*_n + \mathcal{Q}^{(2)}_{m,IV}B^*_{IV} &= 0, \ m = IV, && (6.42)\end{aligned}$$

where

$$P^{(1)}_{m,n} = -K^*_n\zeta^*_n(K_m + 2k_I\mathcal{G}_2)\int_{-d_3}^{-d_4} Z_mZ_n\mathrm{d}y, \qquad (6.43)$$

$$P^{(2)}_{m,n} = -2K^*_n\zeta^*_nk_I\mathcal{G}_2\int_{-d_3}^{-d_4} Z_{IV}Z_n\mathrm{d}y, \qquad (6.44)$$

$$Q^{(1)}_{m,n} = (K^*_n + 2k_I\mathcal{G}^*_2)(K_m + 2k_I\mathcal{G}_2)\int_{-d_3}^{-d_4} Z_mZ_n\mathrm{d}y + 4\left[\int_{-h}^{-d_3} Z_mZ_n\mathrm{d}y + \int_{-d_4}^{0} Z_mZ_n\mathrm{d}y\right], \qquad (6.45)$$

$$Q^{(2)}_{m,n} = 2k_I\mathcal{G}_2(K^*_n + 2k_I\mathcal{G}^*_2)\int_{-d_3}^{-d_4} Z_{IV}Z_n\mathrm{d}y + 4\left[\int_{-h}^{-d_3} Z_{IV}Z_n\mathrm{d}y + \int_{-d_4}^{0} Z_{IV}Z_n\mathrm{d}y\right], \qquad (6.46)$$

$$\mathcal{Q}^{(1)}_{m,IV} = 2k_I\mathcal{G}_2(K_m + 2k_I\mathcal{G}_2)\int_{-d_3}^{-d_4} Z_mZ_{IV}\mathrm{d}y + 4\left[\int_{-h}^{-d_3} Z_mZ_{IV}\mathrm{d}y + \int_{-d_4}^{0} Z_mZ_{IV}\mathrm{d}y\right], \qquad (6.47)$$

$$\mathcal{Q}^{(2)}_{m,IV} = 4k_I^2\mathcal{G}_2^*\mathcal{G}_2\int_{-d_3}^{-d_4} Z_{IV}^2 \mathrm{d}y + 4\left[\int_{-h}^{-d_3} Z_{IV}^2 \mathrm{d}y + \int_{-d_4}^{0} Z_{IV}^2 \mathrm{d}y\right]. \tag{6.48}$$

When the systems of equations (6.25)-(6.26) and (6.41)-(6.42) are combined, the following complex matrix system is obtained:

$$\mathcal{A}\mathcal{X} = \mathcal{B}, \tag{6.49}$$

with $\mathcal{A}$ being a matrix of size $(2N+8)\times(2N+8)$, $\mathcal{X} = [A_I^*, A_{II}^*, \ldots, A_N^*, B_I^*, B_{II}^*, \ldots, B_N^*]^T$ an unknown quantity, $\mathcal{B} = [r_I^{(1)}, r_{II}^{(1)}, r_{III}^{(1)}, r_{IV}^{(2)}, r_1^{(1)}, \ldots, r_N^{(1)}, \underbrace{0, \ldots, 0}_{\text{N+4}}]^T$.

Once the above system of equations is solved, the unknown coefficients A_n^* and B_n^* can be obtained, and subsequently, the reflection coefficient $|R_I|$ and transmission coefficient $|T_I|$ due to the surface wave mode and the energy loss can be determined.

6.4 Results and discussion

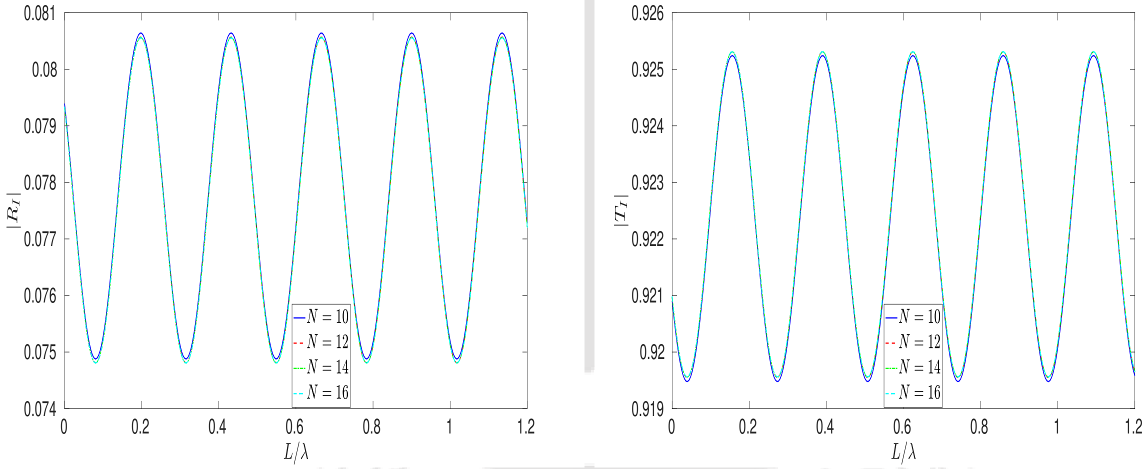

(a) (b)

Figure 6.3: Convergence of (a) reflection coefficient $|R_I|$ and (b) transmission coefficient $|T_I|$ versus L/λ for various number of evanescent modes with $d_2 = d_4 = 0.2h$, $d_1 = d_3 = 0.5h$, $\mathcal{G}_1 = 0.5 = \mathcal{G}_2$

For demonstrating the convergence of the results, we carry out some test and Fig. 6.3 presents the coefficients $|R_I|$ and $|T_I|$ plotted against L/λ, with λ denoting the wavelength of the incident wave, corresponding to different values of N. For $N = 12, 14$ and 16, both reflection and transmission coefficients are evidently in excellent agreement. Subsequently, $N = 16$ can be considered ideal for the purpose of all discussions here. For computational purpose, the following values are considered unless otherwise stated: depth $h = 20$ m, time period $T = 5$ s, density of the homogeneous fluid $\rho = 1025$ kg/m^3, density of the elastic material of the sea-floor $\rho_0 = 2650$ kg/m^3, Young's modulus of the elastic plate $E = 6 \times 10^8$ Pa, Poisson's ratio $\nu = 0.3$, thickness of the elastic plate $h_0 = h/20$, acceleration due to gravity $g = 9.81$ m/s^2, angle of incidence $\theta = 0°$, $d_2 = d_4 = 0.2h$, $d_1 = d_3 = 0.5h$, $\mathcal{G}_1 = 0.5 = \mathcal{G}_2$ and $N = 16$.

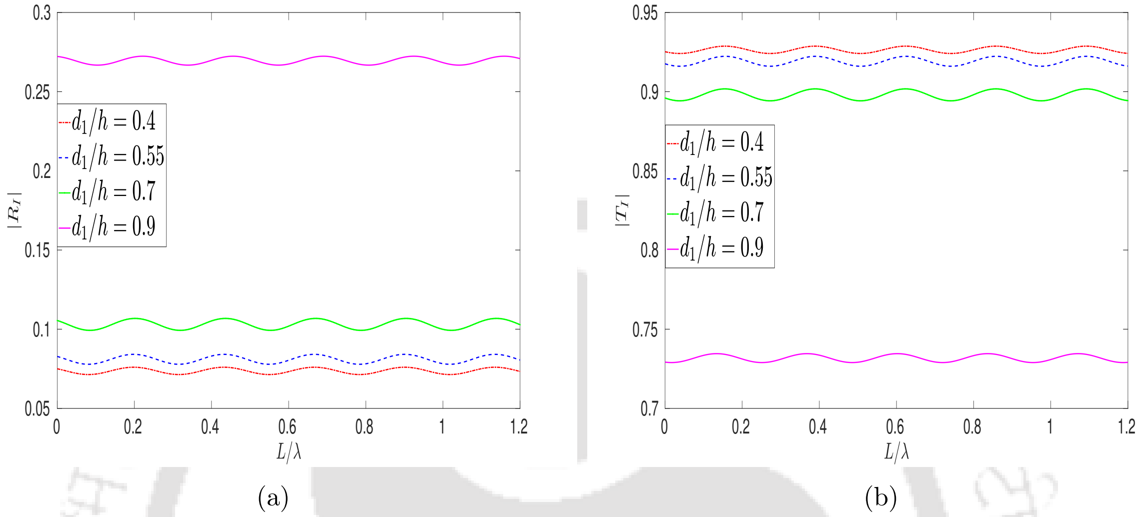

Figure 6.4: Effect of (a) reflection coefficient $|R_I|$ and (b) transmission coefficient $|T_I|$ versus L/λ for various drafts of the lower tip of the first barrier with $\mathcal{G}_1 = \mathcal{G}_2 = 0.5$, $d_2 = 0.2h$, $d_3 = d_1$, $d_4 = d_2$, $\theta = 0^0$ and $N = 16$

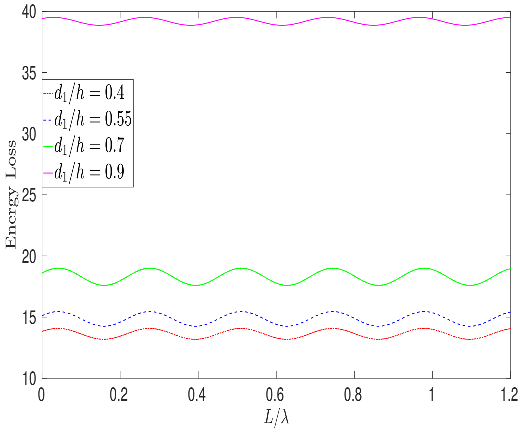

Figure 6.5: Energy loss (in %) versus L/λ for various drafts of the lower tip of the first barrier with $\mathcal{G}_1 = \mathcal{G}_2 = 0.5$, $d_2 = 0.2h$, $d_3 = d_1$, $d_4 = d_2$, $\theta = 0^0$ and $N = 16$

Figure 6.4(a,b) shows the reflection and transmission coefficients and Fig. 6.5 shows the energy loss plotted versus L/λ for different values of d_1/h for the first porous barrier, where structural parameters of the barriers are taken as $\mathcal{G}_1 = \mathcal{G}_2 = 0.5$, $d_2 = 0.2h$, $d_3 = d_1$, $d_4 = d_2$. From Fig. 6.4, it can be noticed that an increase in the value of d_1/h, i.e., of the

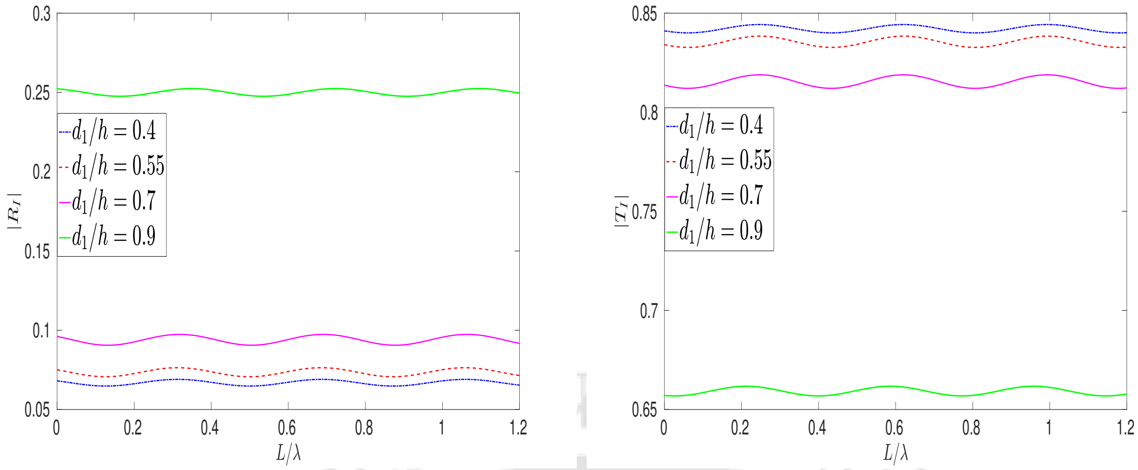

(a) (b)

Figure 6.6: Effect of (a) reflection coefficient $|R_I|$ and (b) transmission coefficient $|T_I|$ versus L/λ for various drafts of the lower tip of the first barrier with $\mathcal{G}_1 = 0.5 + \mathrm{i}, \mathcal{G}_2 = 0.5$, $d_2 = 0.2h$, $d_3 = d_1$, $d_4 = d_2$, $\theta = 0^0$ and $N = 16$

submerged height of the barrier, results in an increase in the reflection coefficient and a reduction in the transmission coefficient. The optimum values (i.e., maxima and minima) of $|R_I|$ and $|T_I|$ are found at specific values of L/λ for some fixed values of d_1/h. One important observation is that higher reflection occurs for both barriers of greater height while lower reflection occurs for lesser height. Figure 6.5 establishes that energy loss becomes higher with an increase in d_1/h, and the maximum energy loss is noticed when $d_1/h = 0.9$ which is the case when both the submerged porous barriers of greater height are closer to the elastic sea-floor. Exactly the opposite phenomenon occurs when the barriers are nearer to the free surface. However, it is found that the reflection and transmission coefficients and also the energy loss exhibit oscillatory patterns corresponding to all values of d_1/h. This happens, because when both submerged porous barriers are nearer to the elastic sea-floor, a large amount of the wave energy concentrated in the vicinity of the elastic sea-floor gets reflected by the barrier while some amount of the wave energy gets dissipated when the waves pass through the porous barriers.

Figure 6.6(a,b) presents the reflection and transmission coefficients plotted against L/λ with an addition of imaginary part to $\mathcal{G}_1$ by considering $\mathcal{G}_1 = 0.5 + \mathrm{i}$, whereas $\mathcal{G}_2$ is taken as 0.5. From Figs. 6.4 and 6.6, it is clearly visible that the amplitude of oscillation of the reflection and transmission coefficients reduces. Since we know that damping reduces the amplitude of the oscillation, therefore it confirms the occurrence of damping in the neighbourhood of the first porous barrier due to the presence of the imaginary part in $\mathcal{G}_1$, which is attributed to the inertial effect as mentioned earlier.

Figure 6.7(a,b) shows the reflection and transmission coefficients plotted against L/λ

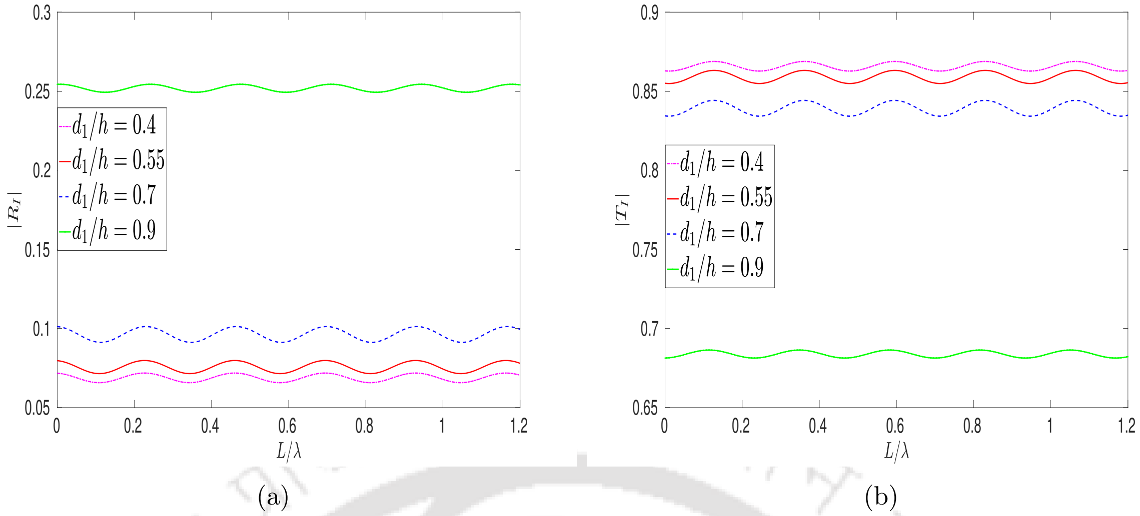

Figure 6.7: Effect of (a) reflection coefficient $|R_I|$ and (b) transmission coefficient $|T_I|$ versus L/λ for various drafts of the lower tip of the first barrier with $\mathcal{G}_1 = 0.5, \mathcal{G}_2 = 0.5 + \mathrm{i}$, $d_2 = 0.2h$, $d_3 = d_1$, $d_4 = d_2$, $\theta = 0^0$ and $N = 16$

with an addition of imaginary part to $\mathcal{G}_2$ by considering $\mathcal{G}_2 = 0.5 + \mathrm{i}$, whereas $\mathcal{G}_1$ is taken as 0.5. From Figs. 6.6(a) and 6.7(a), the clear observation is that the higher values of reflection coefficient reduce according to higher values of d_1/h, but the rate of reduction of the reflection coefficient is not sensitive at all. This is due to the inertial effect of $\mathcal{G}_2$ not having much influence in reducing the wave reflection by the barrier. Similarly, a reduction in the value of transmission coefficient is observed when the value of d_1/h increases.

Figure 6.8(a,b) presents the behaviours of reflection and transmission coefficients due to an adjustment of the position of the second porous barrier so that it is fully submerged while affecting a change of the position of the first porous barrier vertically inside water. Here, the following structural values are taken: $\mathcal{G}_1 = 0.5, \mathcal{G}_2 = 0.5 + \mathrm{i}$, $d_1 = d_2 + 0.5h$, $d_3 = 0.5h$, $d_4 = 0.2h$. It can be observed that as we keep on increasing the values of d_2/h, we observe a gradual reduction with a shift in the optimum values in both the reflection and transmission coefficients. Due to the wave energy dissipation by the elastic sea-floor, a uniform decrement in reflected wave energy is observed. When the interaction of the incident wave with the porous barriers takes place in the presence of the elastic sea-floor, then a certain phase shift occurs in the incident, reflected and transmitted waves. If the value of d_2/h is raised, the coefficients show a significant oscillatory nature which arises as a result of the mutual interaction of these waves. Figure 6.9 tells that, when $d_2/h = 0$ (i.e., when the first porous barrier touches the mean free surface), energy dissipation or energy loss is less than that for other values of d_2/h. Further, when the first porous barrier is closer to the elastic sea-floor, then energy loss is observed to be more.

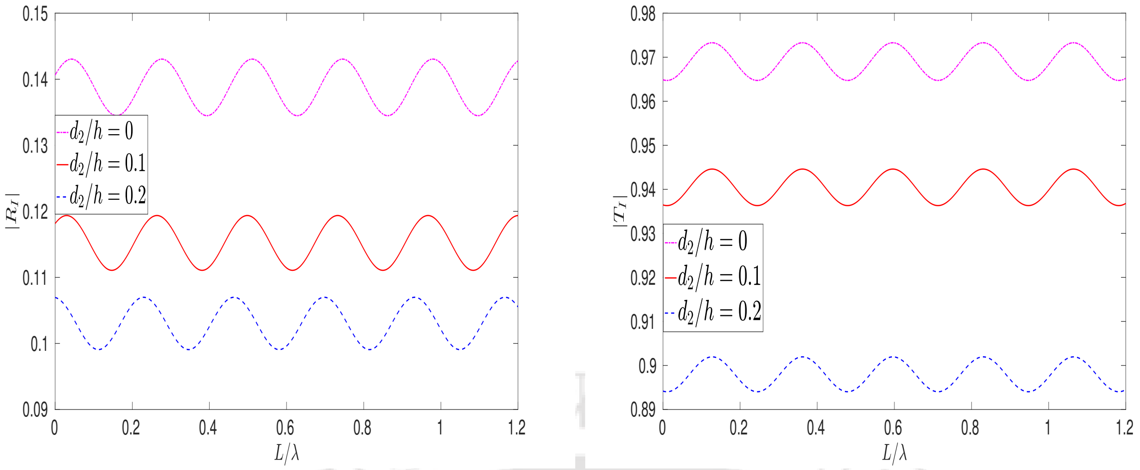

(a) (b)

Figure 6.8: Effect of (a) reflection coefficient $|R_I|$ and (b) transmission coefficient $|T_I|$ versus L/λ for various drafts of the upper tip of the first barrier with $\mathcal{G}_1 = 0.5, \mathcal{G}_2 = 0.5+\mathrm{i}$, $d_1 = d_2 + 0.5h$, $d_3 = 0.5h$, $d_4 = 0.2h$, $\theta = 0^0$ and $N = 16$

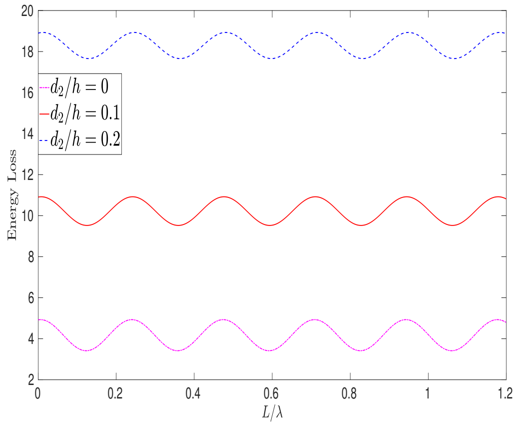

Figure 6.9: Energy loss (in %) versus L/λ for various drafts of the upper tip of the first barrier with $\mathcal{G}_1 = 0.5, \mathcal{G}_2 = 0.5 + \mathrm{i}$, $d_1 = d_2 + 0.5h$, $d_3 = 0.5h$, $d_4 = 0.2h$, $\theta = 0^0$ and $N = 16$

Figure 6.10(a,b) shows reflection and transmission coefficients by fixing the position of the second porous barrier such that it touches the free surface while changing the position of the first porous barrier in the vertical direction under the water region. Here, the following structural values are taken: $\mathcal{G}_1 = 0.5, \mathcal{G}_2 = 0.5 + \mathrm{i}$, $d_1 = d_2 + 0.5h$, $d_3 = 0.5h$, $d_4 = 0$. Figure 6.10 depicts that, for increasing values of d_2/h of the first barrier, there is always a reduction in the reflection and transmission coefficients. Further, it shows that the locations of the minima/maxima in the reflection curves get shifted to the left, and the minimum/maximum value of the reflection coefficient reduces with an increase in the value of d_2/h. It happens due to the effect of phase change of the reflected waves with

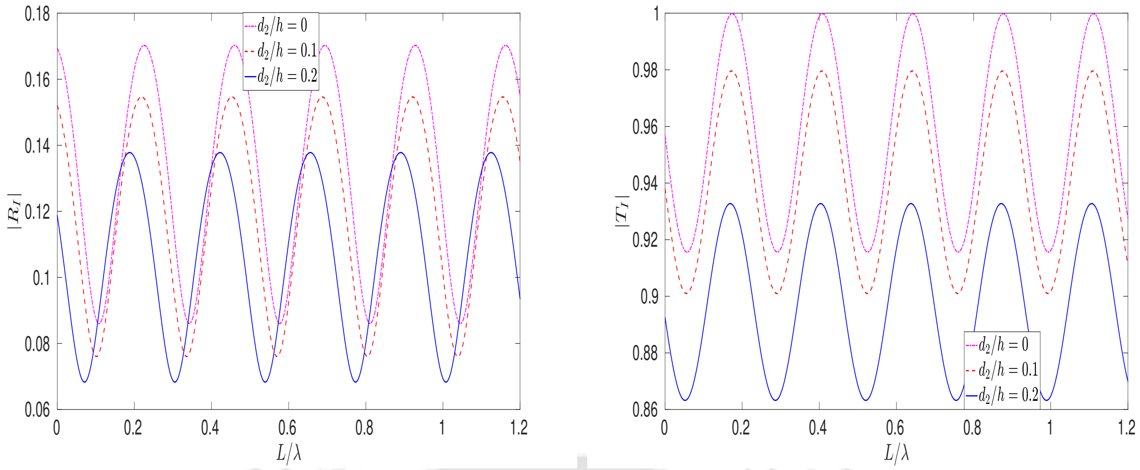

(a) (b)

Figure 6.10: Effect of (a) reflection coefficient $|R_I|$ and (b) transmission coefficient $|T_I|$ versus L/λ for various drafts of the upper tip of the first barrier with $\mathcal{G}_1 = 0.5, \mathcal{G}_2 = 0.5+\mathrm{i}$, $d_1 = d_2 + 0.5h$, $d_3 = 0.5h$, $d_4 = 0$, $\theta = 0^0$ and $N = 16$

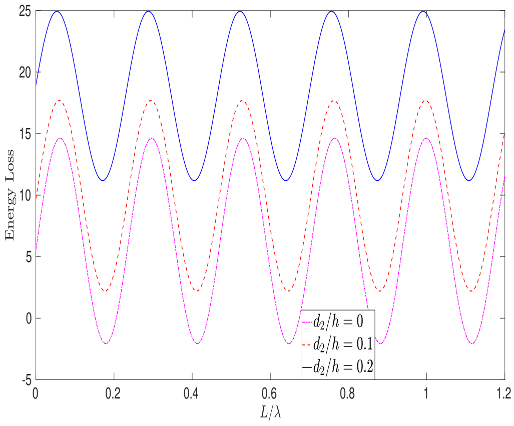

Figure 6.11: Energy loss (in %) versus L/λ for various drafts of the upper tip of the first barrier with $\mathcal{G}_1 = 0.5, \mathcal{G}_2 = 0.5 + \mathrm{i}$, $d_1 = d_2 + 0.5h$, $d_3 = 0.5h$, $d_4 = 0$, $\theta = 0^0$ and $N = 16$

the porous barriers in the vicinity of the elastic sea-floor. A common observation in these figures is the oscillating behaviour of the reflection coefficient, transmission coefficient and energy loss corresponding to different set of values of d_2/h. As observed earlier, energy loss is higher when the first porous barrier is closer to the elastic sea-floor.

Now we plot Figs. 6.12(a,b) and 6.13, respectively, for reflection coefficient, transmission coefficient and energy loss against L/λ by changing the porous-effect parameters from $\mathcal{G}_1 = 0.5, \mathcal{G}_2 = 0.5 + \mathrm{i}$ to $\mathcal{G}_1 = 0.5 + \mathrm{i}, \mathcal{G}_2 = 0.5$ for the same situation as considered for Figs. 6.10(a,b) and 6.11. It is noticed that reflection and transmission coefficients reduce corresponding to a shift in the optimum values when the value of d_2/h increases.

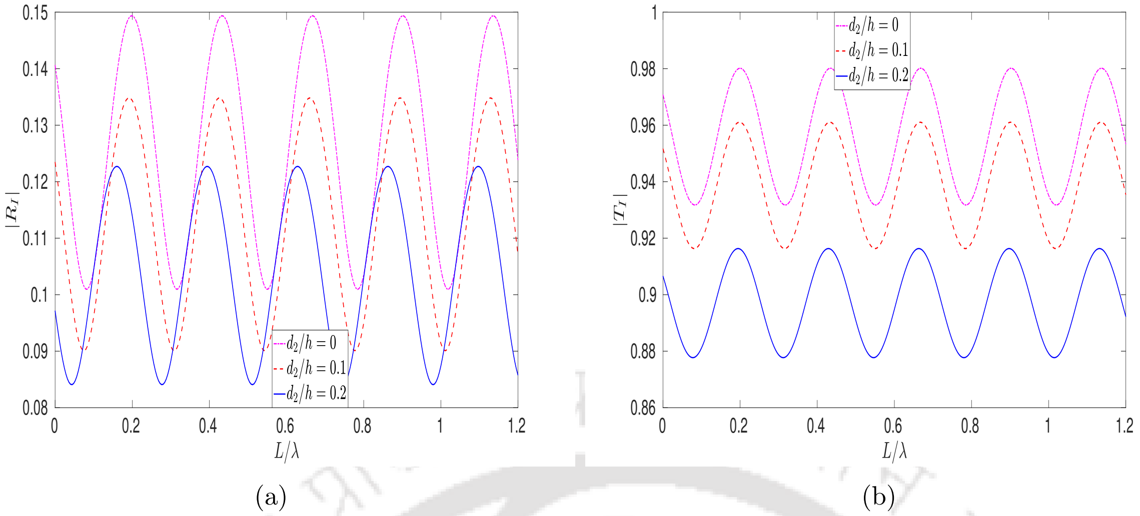

(a) (b)

Figure 6.12: Effect of (a) reflection coefficient $|R_I|$ and (b) transmission coefficient $|T_I|$ versus L/λ for various drafts of the upper tip of the first barrier with $\mathcal{G}_1 = 0.5+\mathrm{i}, \mathcal{G}_2 = 0.5$, $d_1 = d_2 + 0.5h$, $d_3 = 0.5h$, $d_4 = 0$, $\theta = 0^0$ and $N = 16$

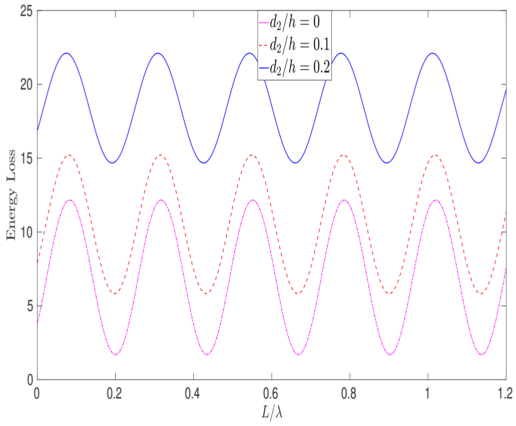

Figure 6.13: Energy loss (in %) versus L/λ for various drafts of the upper tip of the first barrier with $\mathcal{G}_1 = 0.5 + \mathrm{i}, \mathcal{G}_2 = 0.5$, $d_1 = d_2 + 0.5h$, $d_3 = 0.5h$, $d_4 = 0$, $\theta = 0^0$ and $N = 16$

Here also, all the coefficients are noticed to follow certain oscillatory patterns for different set of parameter values. It is clearly observed from Fig. 6.13 that, for the case of the first porous barrier located closer to the elastic sea-floor, the energy loss is less than that for the other values of d_2/h. When Figs. 6.11 and 6.13 are compared, an appreciable increase in energy loss is noticed when an imaginary part is incorporated to the otherwise real porous effect parameter of the second porous barrier for the case of submerged first porous barrier closer to the elastic sea-floor.

Figures 6.14(a,b) and 6.15, respectively, present another study of reflection and transmission coefficients and energy loss by fixing the position of the first porous barrier by

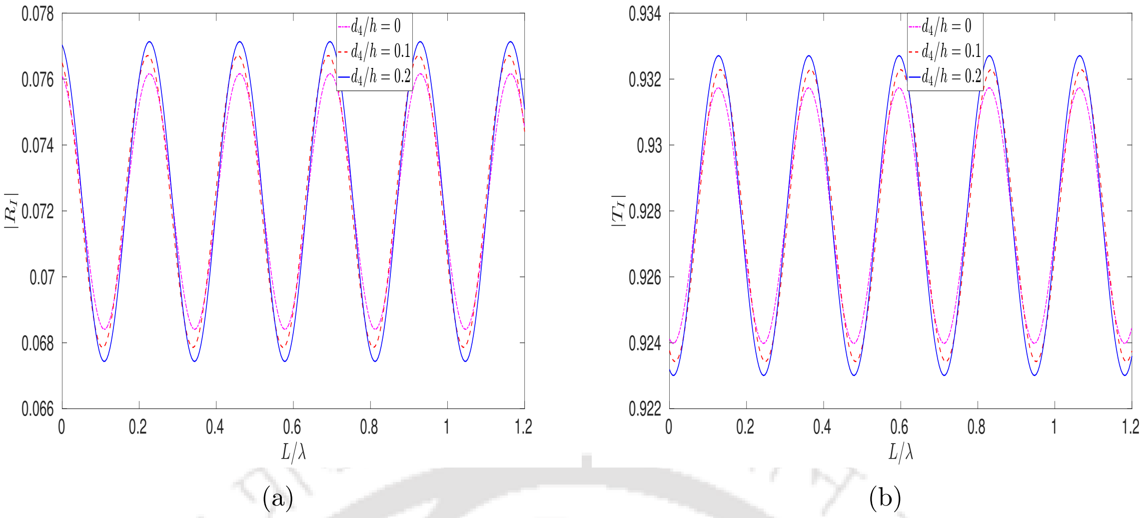

Figure 6.14: Effect of (a) reflection coefficient $|R_I|$ and (b) transmission coefficient $|T_I|$ versus L/λ for various drafts of the upper tip of the second barrier with $\mathcal{G}_1 = 0.5, \mathcal{G}_2 = 0.5 + \mathrm{i}$, $d_3 = d_4 + 0.5h$, $d_1 = 0.5h$, $d_2 = 0$, $\theta = 0^0$ and $N = 16$

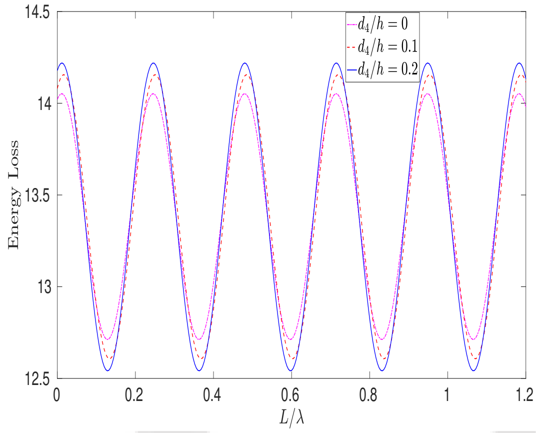

Figure 6.15: Energy loss (in %) versus L/λ for various drafts of the upper tip of the second barrier with $\mathcal{G}_1 = 0.5, \mathcal{G}_2 = 0.5 + \mathrm{i}$, $d_3 = d_4 + 0.5h$, $d_1 = 0.5h$, $d_2 = 0$, $\theta = 0^0$ and $N = 16$

making it touch the free surface while changing the position of the second porous barrier in the vertical direction under the water region. Here the following structural parameters are considered: $\mathcal{G}_1 = 0.5, \mathcal{G}_2 = 0.5 + \mathrm{i}$, $d_3 = d_4 + 0.5h$, $d_1 = 0.5h$, $d_2 = 0$. The maxima and minima of both the coefficients occur when $d_4/h = 0.2$, i.e., when the second porous barrier is closer to the elastic sea-floor. Reflection and transmission coefficient and energy loss exhibit certain oscillatory patterns corresponding to the different structural values of the second barrier i.e., d_4/h. The maximum/minimum values in wave reflection are due to the constructive/destructive interference of the incident and reflected waves in the presence of the porous barriers. A similar phenomenon of wave trapping by a permeable membrane barrier situated close to a wall is observed in the work of Koley and Sahoo [50]. When $d_4/h = 0.2$, the occurrence of maximum and minimum of energy dissipation or energy loss is observed.

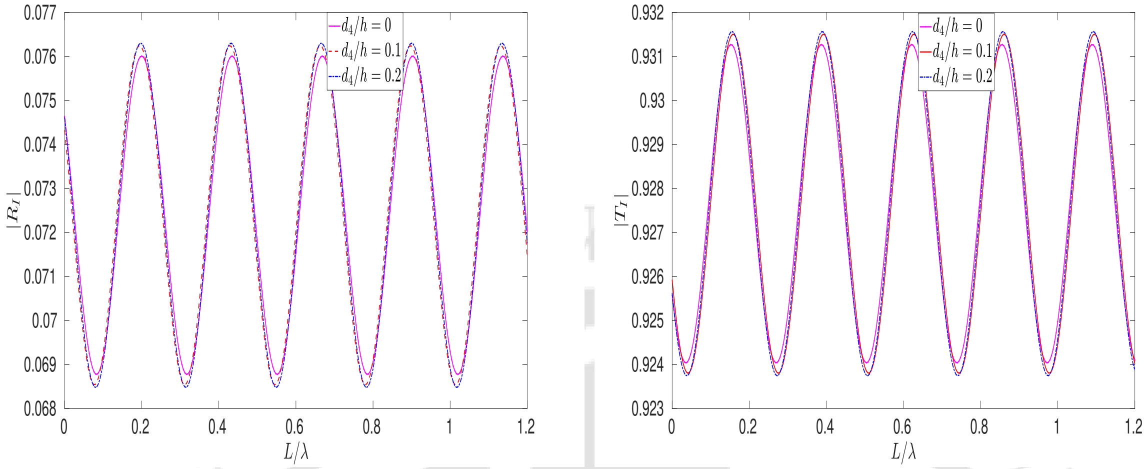

(a) (b)

Figure 6.16: Effect of (a) reflection coefficient $|R_I|$ and (b) transmission coefficient $|T_I|$ versus L/λ for various drafts of the upper tip of the second barrier with $\mathcal{G}_1 = 0.5 + \mathrm{i}, \mathcal{G}_2 = 0.5$, $d_3 = d_4 + 0.5h$, $d_1 = 0.5h$, $d_2 = 0$, $\theta = 0^0$ and $N = 16$

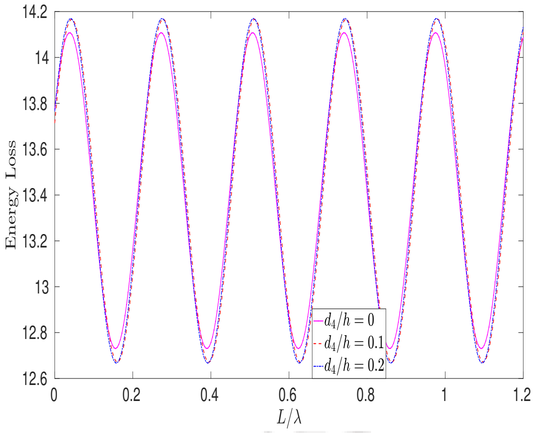

Figure 6.17: Energy loss (in %) versus L/λ for various drafts of the upper tip of the second barrier with $\mathcal{G}_1 = 0.5 + \mathrm{i}, \mathcal{G}_2 = 0.5$, $d_3 = d_4 + 0.5h$, $d_1 = 0.5h$, $d_2 = 0$, $\theta = 0^0$ and $N = 16$

In Figs. 6.16(a,b) and 6.17, the same study is performed by changing the values of $\mathcal{G}_1$ and $\mathcal{G}_2$ as follows: $\mathcal{G}_1 = 0.5 + \mathrm{i}, \mathcal{G}_2 = 0.5$. The values of some other relevant parameters are taken as $d_3 = d_4 + 0.5h$, $d_1 = 0.5h$, $d_2 = 0$. It may be noted that for Fig. 6.14(a,b), $\mathcal{G}_1$ is real and $\mathcal{G}_2$ is complex, but in case of Fig. 6.16(a,b), it is exactly the other way around. The optimum values for reflection and transmission are observed to occur for

$d_4/h = 0.2$, i.e., for the case in which the second porous barrier is placed closer to the elastic sea-floor. However, for the first porous barrier, wave reflection is found to be more than that for the second porous barrier. As seen earlier, all of reflection coefficient, transmission coefficient and energy loss follow certain oscillatory patterns corresponding to different values of d_4/h. Similarly, energy loss takes maximum and minimum values when $d_4/h = 0.2$. When we compare Figs. 6.15 and 6.17, it is found that the increment in energy loss is very negligible if an imaginary part is added to the porous-effect parameter of the second barrier. Maximum energy loss is observed when the first porous barrier is considered to be fixed. It is concluded that the wave energy dissipation due to the fixed location of first porous barrier is less in comparison to the energy dissipation due to the fixed location of the second porous barrier. Basically, it is required that both the porous barriers be positioned suitably so as to create a tranquility zone which reduces the wave impact.

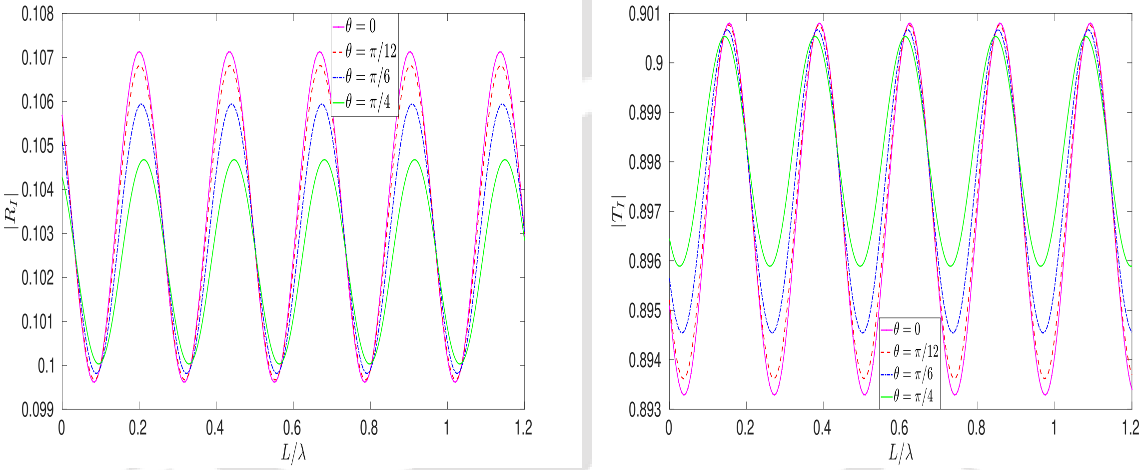

(a) (b)

Figure 6.18: Effect of (a) reflection coefficient $|R_I|$ and (b) transmission coefficient $|T_I|$ versus L/λ for different values of angle of incidence with $\mathcal{G}_1 = 0.5 + \mathrm{i}, \mathcal{G}_2 = 0.5$, $d_2 = d_4 = 0.2h$, $d_1 = d_3 = d_4 + 0.5h$ and $N = 16$

In Fig. 6.18(a,b), the effect of the angle of incidence on reflection and transmission coefficients is investigated when both the barriers are submerged in the water region. In this case, the following values of structural parameters are taken: $\mathcal{G}_1 = 0.5 + \mathrm{i}, \mathcal{G}_2 = 0.5$, $d_2 = d_4 = 0.2h$, $d_1 = d_3 = d_4 + 0.5h$. It is noticed that the optima in wave reflection take place in connection with the case of normal wave incidence. Further, it is observed from the figures that the reflection coefficient and transmission coefficient are oscillatory for different values of θ. It is important to note that, with the barriers placed close to each other, reflection coefficient shows a small magnitude of oscillation, but the analogous transmission coefficient happens to be reasonably high - the occurrence of which can probably be attributed to the inefficiency of the second porous barrier for such a location of the barriers.

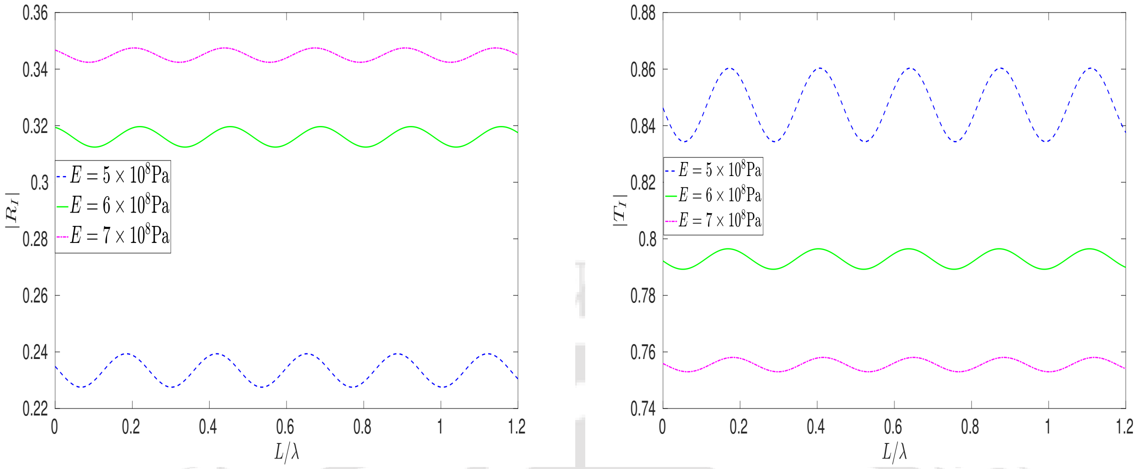

(a) (b)

Figure 6.19: Effect of (a) reflection coefficient $|R_I|$ and (b) transmission coefficient $|T_I|$ versus L/λ for different values of Young's modulus E of the elastic sea-floor with $\mathcal{G}_1 = 0.5 = \mathcal{G}_2$, $d_2 = d_4 = 0.5h$, $d_1 = d_3 = d_4 + 0.5h$ and $N = 16$

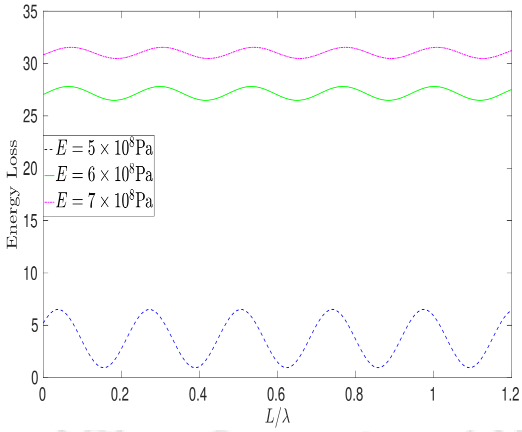

Figure 6.20: Energy loss (in %) versus L/λ for different values of Young's modulus E of the elastic sea-floor with $\mathcal{G}_1 = 0.5 = \mathcal{G}_2$, $d_2 = d_4 = 0.5h$, $d_1 = d_3 = d_4 + 0.5h$ and $N = 16$

In Figs. 6.19(a,b) and 6.20, reflection and transmission coefficients and energy loss are, respectively, plotted against L/λ for various values of Young's modulus E of the elastic sea-floor. This time, the values $\mathcal{G}_1 = 0.5 = \mathcal{G}_2$, $d_2 = d_4 = 0.5h$, $d_1 = d_3 = d_4 + 0.5h$ are considered. Figure 6.19 shows that the reflection coefficient takes increasing values and the transmission coefficient takes decreasing values corresponding to an increase in E. Thus, some incident wave energy is transferred to the elastic sea-floor. Consequently, a moderate elasticity E of the sea-floor seems helpful for use in coastal engineering problems for wave attenuation. However, Fig. 6.20 depicts that energy loss is higher for higher values of E of the elastic sea-floor. It is observed that, with both barriers fully submerged and closer to the sea-floor, the energy loss becomes higher. This is due to the fact that when the wave passes through the porous barriers, which are nearer to the sea-floor, a sufficient amount of the wave energy gets dissipated by the the sea-floor.

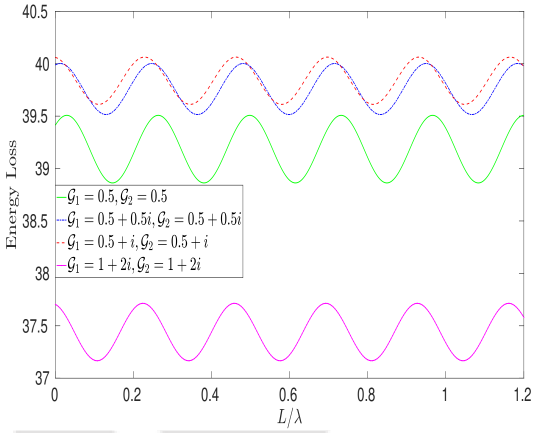

Figure 6.21: Energy loss (in %) versus L/λ for various porosities of the barriers with $d_2 = 0.2h$, $d_1 = 0.9h$, $d_4 = d_2$, $d_3 = d_1$ and $N = 16$

Figure 6.21 presents the energy loss plotted against L/λ for various values of porous-effect parameters of both barriers. The values $d_2 = 0.2h$, $d_1 = 0.9h$, $d_4 = d_2$, $d_3 = d_1$ are considered for computational purpose. Here, the energy loss follows an oscillatory pattern corresponding to various values of $\mathcal{G}_1$ and $\mathcal{G}_2$. It shows that the energy loss increases corresponding to increasing values of $\mathcal{G}_1$ and $\mathcal{G}_2$. Maximum energy loss is observed to be nearly 40% for the intermediate values of the porous-effect parameter with $\mathcal{G}_1 = \mathcal{G}_2 = 0.5 + \mathrm{i}$. The rate of energy loss or dissipation of energy increases when the inertial effects of the barriers increase but higher values of the imaginary part of the porous effect parameters (i.e., inertial effects) cause less energy loss for the incident waves at the porous barriers. It may be concluded from Fig. 6.21 that the energy loss is higher for moderate values of the porous-effect parameter of the porous barriers. Overall, it can be concluded that, if the porous barriers of reasonably greater height with moderate porosity are closer to the elastic sea-floor, then energy dissipation is higher and subsequently, this model can be considered to be very efficient for various applications in coastal engineering.

6.5 Conclusion

In this chapter, using linearized water wave theory, we take up the problem of oblique water wave scattering by a dual submerged porous barrier of different porosity over an elastic sea-floor. Considering the well-known Euler-Bernoulli beam equation, the elastic sea-floor is considered as a thin elastic plate where the horizontal length of such a plate is considered to be much larger in comparison to its thickness. Under such circumstances, there exist propagating waves at two distinct wavenumbers for any given frequency: the one with the smaller wavenumber along the free surface corresponding to the surface mode and the other one with the higher wavenumber along the elastic sea-floor corresponding to the flexural mode. The boundary value problem is solved with the help of eigenfunction expansion and least square methods. Numerical results are computed and examined for the reflection and transmission coefficients and energy loss to exhibit the effects of various structural parameters. It is important to note that the elasticity of sea-floor is responsible for a reasonable amount of the wave energy getting dissipated. For wave scattering by submerged barriers, with an increment in the elasticity of the sea-floor, wave reflection has an increasing trend, and the energy loss is observed to be higher. Therefore, the consideration of a moderate value of bed elasticity is likely to be helpful for wave attenuation in coastal and offshore engineering. Further, the study reveals that, for a fixed submergence depth of one of the porous barriers and corresponding to an increment of the inertial effect of the porous barrier, lower reflection and higher transmission are acquired. Moderate porosity of the submerged barriers results in higher energy loss. Occurrence of maximum energy loss is observed for the case of the submerged porous barriers of greater height placed closer to the elastic sea-floor. The inference is that, in order to reduce the waveload and to create a tranquility zone, positioning of the barriers in an appropriate manner is very essential. The physical problem and model described in this work are expected to provide the necessary information in choosing an appropriate mechanism to reduce waveload for a variety of marine problems. The results developed here may be utilized in a suitable manner for tackling a number of water wave scattering problems corresponding to porous breakwaters in the form of thin vertical barriers and involving an elastic sea-floor that may naturally appear in various disciplines of coastal and offshore engineering.

CHAPTER 7

SCATTERING OF OBLIQUE FLEXURAL GRAVITY WAVE BY A PAIR OF SUBMERGED VERTICAL POROUS BARRIERS DUE TO THE PRESENCE OF AN ICE-SHEET

7.1 Introduction

A hydrodynamic model, with incorporation of elasticity, is considered here to investigate oblique water wave scattering by two totally submerged vertical porous barriers, placed at some distance from each other, in a homogenous fluid. A thin ice-sheet, replacing the usual free surface, is considered as the upper surface. Numerical computation for the reflection and transmission coefficients, energy loss and wave forces are carried out and discussed for different values of parameters such as porous-effect parameter, the submergence depth of barriers from the ice-sheet, the angle of incidence, the elasticity of the floating ice-sheet. Present investigation demonstrates that the wave reflection is of oscillatory nature. It further shows that the minima in wave reflection occurs because of an increase in the inertial effect of the porous barrier. The vertical porous barriers are found to dissipate a significant portion of the wave energy when an increase in the inertial effect of the porous barriers is affected. The various parameters of the ice-sheet also play an important role in wave dissipation. The hydrodynamic force on the barriers also follows an oscillatory pattern and it increases when the length of the barrier is increased.

7.2 Formulation of the problem

Water wave propagation of small amplitude, in response to the action of gravity and small-amplitude plate response, is considered in an incompressible, inviscid and homogeneous fluid undergoing an irrotational motion and flowing underneath an infinitely extended floating ice-sheet in horizontal directions in an ocean. Following Euler-Bernoulli beam equation, the floating ice-sheet is considered to act as a thin elastic plate. The elastic plate (or the ice-sheet) is considered to be thin which implies that the horizontal length of the plate is much greater in comparison to the thickness of the plate. Interestingly, similarity of such works can be seen with that of linear water wave interaction with VLFS, as discussed in Chen et al. [14]. Throughout the present work, the mention of 'elastic plate' will mean 'ice-sheet'.

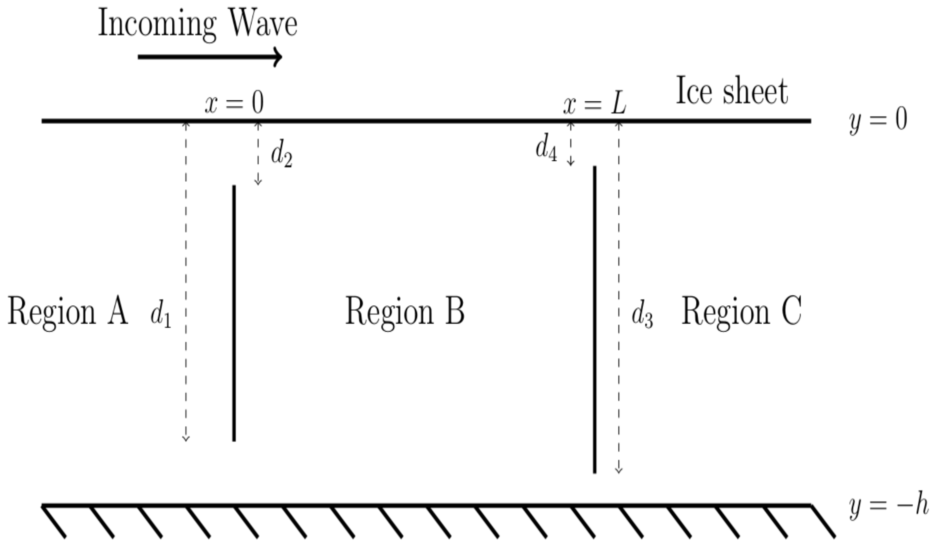

Figure 7.1: Schematic diagram of the problem

A Cartesian coordinate system is adopted in such a way that the y-axis points in the vertical upward direction; $y = -h$ and $y = 0$, respectively, represent the location of the sea-bed and floating ice-sheet; as displayed in Fig. 7.1. Here, two fully submerged thin vertical porous barriers of different heights are positioned at $x = 0$ and $x = L$. Assume d_1 and d_3, respectively, to represent the distances of the lower vertical tips of the first and second porous barriers from the ice-sheet and d_2 and d_4, respectively, are the distances of the upper vertical tips from the ice-sheet. The whole fluid domain under consideration is partitioned into three sub-domains, namely, $x < 0$, $-h < y < 0$ as region A, $0 < x < L$, $-h < y < 0$ as region B, and $x > L$, $-h < y < 0$ as region C. Adopting small amplitude theory and accounting for all the above assumptions, the velocity potentials in each region A, B and C, respectively, can be represented by $\Psi_1(x, y, z, t) = \psi_1(x, y)e^{(\mathrm{i}lz-\mathrm{i}\omega t)}$, $\Psi_2(x, y, z, t) = \psi_2(x, y)e^{(\mathrm{i}lz-\mathrm{i}\omega t)}$ and $\Psi_3(x, y, z, t) = \psi_3(x, y)e^{(\mathrm{i}lz-\mathrm{i}\omega t)}$.

As such the velocity potentials ψ_j, $j = 1, 2, 3$, in regions A, B and C, respectively, satisfy the modified Helmholtz equation as follows:

$$\frac{\partial^2\psi_j}{\partial x^2} + \frac{\partial^2\psi_j}{\partial y^2} - l^2\psi_j = 0. \qquad (7.1)$$

The linearized boundary condition on the ice sheet has the following form:

$$\left\{\mathcal{D}\Big(\frac{\partial^2}{\partial x^2}-l^2\Big)^2+1-\epsilon K\right\}\frac{\partial\psi_j}{\partial y}-K\psi_j=0, \quad \text{on} \quad y=0,\ j=1,2,3, \tag{7.2}$$

where $\mathcal{D}=\frac{F_r}{\rho_h g}$, F_r, the flexural rigidity of the ice-sheet given by $F_r=Eh_0^3/[12(1-\nu^2)]$; E and ν, respectively, are Young's modulus and Poisson's ratio, $\epsilon=(\rho_0/\rho_h)h_0$; ρ_0 is the density of the ice-sheet, h_0 is the small thickness of the ice-sheet.

The bottom boundary condition has the following form:

$$\frac{\partial\psi_j}{\partial y}=0, \quad \text{on} \quad y=-h,\ j=1,2,3. \tag{7.3}$$

Velocity potentials ψ_j satisfy the following boundary conditions across the vertical boundaries $x=0$ and $x=L$ (Chwang [17],Yu [100]):

$$\begin{aligned}
\frac{\partial\psi_1}{\partial x} &= \frac{\partial\psi_2}{\partial x}=\mathrm{i}k_0\mathcal{G}_1(\psi_1-\psi_2);\quad x=0,-d_1<y<-d_2, && (7.4)\\
\frac{\partial\psi_1}{\partial x} &= \frac{\partial\psi_2}{\partial x};\ x=0,\ (-h<y<-d_1)\cup(-d_2<y<0), && (7.5)\\
\psi_1 &= \psi_2;\ x=0,\ (-h<y<-d_1)\cup(-d_2<y<0), && (7.6)\\
\frac{\partial\psi_2}{\partial x} &= \frac{\partial\psi_3}{\partial x}=\mathrm{i}k_0\mathcal{G}_2(\psi_2-\psi_3);\quad x=L,-d_3<y<-d_4, && (7.7)\\
\frac{\partial\psi_2}{\partial x} &= \frac{\partial\psi_3}{\partial x};\ x=L,\ (-h<y<-d_3)\cup(-d_4<y<0), && (7.8)\\
\psi_2 &= \psi_3;\ x=L,\ (-h<y<-d_3)\cup(-d_4<y<0), && (7.9)
\end{aligned}$$

where $\mathcal{G}_1$ and $\mathcal{G}_2$, respectively, denote the non-dimensional porous-effect parameters, which are usually complex in nature, associated with the barriers placed at $x=0$ and $x=L$.

The asymptotic behaviours of the potentials ψ_1 and ψ_3 (there is no such representation for ψ_2 since it is associated with a bounded region) are given by

$$\begin{aligned}
\psi_1 &\to \frac{\cosh k_0(h+y)}{\cosh k_0h}\Big[e^{\mathrm{i}K_0x}+R_0e^{-\mathrm{i}K_0x}\Big] \text{ as } x\to-\infty, && (7.10)\\
\psi_3 &\to T_0\frac{\cosh k_0(h+y)}{\cosh k_0h}e^{\mathrm{i}K_0(x-L)} \text{ as } x\to\infty, && (7.11)
\end{aligned}$$

where the unknown quantities R_0 and T_0, respectively, are related to the amplitudes of the reflected and transmitted waves, and are, respectively, known as the reflection coefficient and transmission coefficient as defined earlier. In Eqs. (7.10) and (7.11), $K_0=(k_0^2-l^2)^{\frac{1}{2}}$ with k_0 satisfying $K-k_0(\mathcal{D}k_0^4+1-\epsilon K)\tanh k_0h=0$.

7.3 Derivation of analytical solutions

Employment of separation of variables technique gives velocity potential $\psi_1(x,y)$ in region A in the following form:

$$\psi_1(x,y) = \left[e^{\mathrm{i}K_0 x} + R_0 e^{-\mathrm{i}K_0 x}\right] Z_0(h,y) + \sum_{n=I}^{II} R_n e^{-\mathrm{i}K_n x} Z_n(h,y) + \sum_{n=1}^{\infty} R_n e^{-\mathrm{i}K_n x} Z_n(h,y), \tag{7.12}$$

where R_n is the complex reflection coefficient and $K_n = (k_n^2 - l^2)^{\frac{1}{2}}$. Here it is assumed that $R_{II} = 0$ due to the boundedness of the velocity potential at negative infinity. Using the boundary condition (7.3), the depth-dependent function $Z_n(h,y)$ is obtained as

$$Z_n(h,y) = \frac{\cosh k_n(h+y)}{\cosh k_n h}, \quad n = 0, I, II, 1, 2, ..., \tag{7.13}$$

with k_n satisfying the dispersion relation

$$K - k_n(\mathcal{D}k_n^4 + 1 - \epsilon K)\tanh k_n h = 0. \tag{7.14}$$

Dispersion relation (7.14) has (i) one positive real root k_0 (as in Bhattacharjee et. al. [10], Karmakar et. al. [45]) that indicates the propagating mode; (ii) two pairs of complex conjugate roots k_n, $n = I, II, III, IV$ in the form $a \pm ib$ and $-(a \pm ib)$, respectively, and (iii) also an infinite number of purely imaginary roots $k_n = \mathrm{i}\kappa_n$, $n = 1, 2, \ldots$, (Fig. 7.2). For the sake of ensuring the validity of the boundedness property of the velocity potential, it is assumed that the contribution from the roots k_{III} and k_{IV} be avoided. Since the existence of exactly one positive real root k_0 of (7.14) is evidently ensured, there exists only one wave mode (wavenumber) propagating at the ice-sheet (say, flexural mode) along the positive x-direction. We truncate the evanescent modes of the potential with the infinite sum at some finite $n = N$ to write $\psi_1(x,y)$ as

$$\begin{aligned}\psi_1(x,y) &= \left[e^{\mathrm{i}K_0 x} + R_0 e^{-\mathrm{i}K_0 x}\right] Z_0(h,y) + \sum_{n=I}^{II} R_n e^{-\mathrm{i}K_n x} Z_n(h,y) \\ &+ \sum_{n=1}^{N} R_n e^{-\mathrm{i}K_n x} Z_n(h,y).\end{aligned} \tag{7.15}$$

In region B also, following a similar procedure, the spatial velocity potential $\psi_2(x,y)$ takes the following form after truncating at $n = N$:

$$\psi_2(x,y) = \sum_{n=0,I,II,1}^{N} [a_n e^{\mathrm{i}K_n x} + b_n e^{-\mathrm{i}K_n (x-L)}] Z_n(h,y), \tag{7.16}$$

where a_n and b_n are arbitrary constants.

Likewise, the spatial velocity potential $\psi_3(x,y)$ in region C can be written as

$$\psi_3(x,y) = \sum_{n=0,I,II,1}^{N} T_n e^{\mathrm{i}K_n(x-L)} Z_n(h,y), \tag{7.17}$$

where T_n is the complex transmission coefficient. Here it is assumed that $T_{II} = 0$ in order to preserve the boundedness of the velocity potential at infinity.

The roots of the complex dispersion relation (7.14) are evaluated numerically through the use of contour plots for the purpose of interpreting the behaviours of the wavenumbers (as shown in Fig. 7.2). In order to compute these, except for ρ_0, E and h_0, the same set of values considered in Chapter 6 are used here. We take $\rho_0 = 922.5$ kg/m^3, $E = 6 \times 10^9$ Pa, $h_0 = 0.1$ m, for this work. Figure 7.2 presents the nature of the complex zeros demonstrating that two pairs of complex zeros, occurring as positive and negative of a complex conjugate pair, namely, $k_I, k_{II}, k_{III}, k_{IV}$, are located in such a way that there is one zero in each of the quadrants. It needs to be mentioned that two pairs of complex zeros occur for the ice-sheet. For computational purpose, only the roots that lie in the first and fourth quadrants are chosen in order that the velocity potentials ψ_1 and ψ_3 remain bounded.

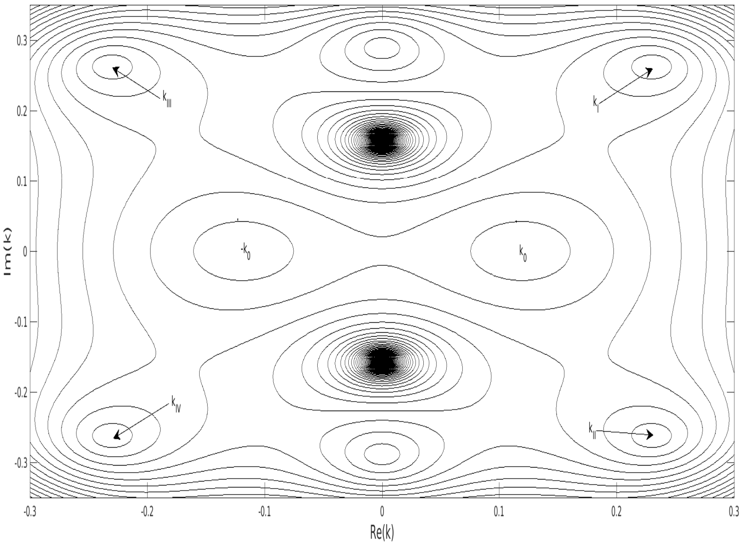

Figure 7.2: Contour plot of roots of the dispersion relation

The horizontal velocity components $\frac{\partial \psi_1}{\partial x}$ and $\frac{\partial \psi_2}{\partial x}$ follow the continuity conditions on $x = 0, -h < y < 0$ (using Eqs. (7.4) and (7.5)) giving

$$R_n \;=\; 1 - a_n + b_n e^{\mathrm{i}K_n L}, \text{ for } n = 0, I, \tag{7.18}$$

$$R_n = b_n e^{\mathrm{i}K_nL} - a_n, \text{ for } n = 1, 2, \cdots, N, \tag{7.19}$$

$$R_n = 0, \text{ for } n = II. \tag{7.20}$$

Also, the second equality in Eq. (7.4) leads to

$$\sum_{n=0}^{N}(K_n + 2k_0\mathcal{G}_1)a_nZ_n - \sum_{n=0}^{N} K_nb_ne^{\mathrm{i}k_nL}Z_n - 2k_0\mathcal{G}_1Z_0 = 0, \ -d_2 < y < -d_1. \tag{7.21}$$

Similarly, Eq. (7.6) results in

$$2Z_0 - \sum_{n=0}^{N} 2a_nZ_n = 0, \ (-h < y < -d_1) \cup (-d_2 < y < 0). \tag{7.22}$$

To evaluate the undetermined coefficients appearing in Eqs. (7.21) and (7.22), we adopt the method of least square approach as followed in earlier chapters. In order to implement this, a notation $\mathcal{L}(y)$ is defined as

$$\mathcal{L}(y) = \begin{cases} (K_n + 2k_0\mathcal{G}_1)a_nZ_n - \sum_{n=0}^{N} K_nb_ne^{\mathrm{i}k_nL}Z_n - 2k_0\mathcal{G}_1Z_0, -d_2 < y < -d_1, \\ \\ 2Z_0 - \sum_{n=0}^{N} 2a_nZ_n, \ (-h < y < -d_1) \cup (-d_2 < y < 0). \end{cases} \tag{7.23}$$

The requirement of the method is that the relation

$$\int_{-h}^{0} |\mathcal{L}(y)|^2 \mathrm{d}y = \text{minimum} \tag{7.24}$$

holds in satisfying $\mathcal{L}(y) = 0$ in $-h < y < 0$.

Next, the above integral is minimized with respect to each coefficient a_m $(m = 0, I, II, 1, 2, \ldots, N)$ to get the following integral equation:

$$\int_{-h}^{0} \mathcal{L}^*(y)\frac{\partial \mathcal{L}(y)}{\partial a_m}\mathrm{d}y = 0, \ m = 0, I, II, 1, 2, \ldots, N, \tag{7.25}$$

where $\mathcal{L}^*(y)$ denotes the complex conjugate of $\mathcal{L}(y)$.

Integrating with respect to the variable y, we obtain the following system of linear equations:

$$\sum_{n=0}^{N} S^{(1)}_{m,n}a^*_n + \sum_{n=0}^{N} T^{(1)}_{m,n}b^*_n = r^{(1)}_m, \ m = 0, I, II, 1, 2, \ldots, N, \tag{7.26}$$

where

$$
\begin{aligned}
S^{(1)}_{m,n} &= (K^*_n + 2k_0\mathcal{G}^*_1)(K_m + 2k_0\mathcal{G}_1)\int_{-d_1}^{-d_2} Z_m Z_n \mathrm{d}y + 4\Big[\int_{-h}^{-d_1} Z_m Z_n \mathrm{d}y \\
&+ \int_{-d_2}^{0} Z_m Z_n \mathrm{d}y\Big], \qquad (7.27)\\
T^{(1)}_{m,n} &= -K^*_n \zeta^*_n (K_m + 2k_0\mathcal{G}_1)\int_{-d_1}^{-d_2} Z_m Z_n \mathrm{d}y, \qquad (7.28)\\
r^{(1)}_{m} &= 2k_0\mathcal{G}^*_1(K_m + 2k_0\mathcal{G}_1)\Big[\int_{-d_1}^{-d_2} Z_m Z_0 \mathrm{d}y\Big] + 4\Big[\int_{-h}^{-d_1} Z_m Z_0 \mathrm{d}y \\
&+ \int_{-d_2}^{0} Z_m Z_0 \mathrm{d}y\Big], \qquad (7.29)
\end{aligned}
$$

with $\zeta_n = e^{\mathrm{i}K_n L}$ and $*$ of any quantity standing for its complex conjugate.

Now utilization of the continuity condition along the boundary $x = L, -h < y < 0$ with respect to the horizontal velocity components $\frac{\partial\psi_2}{\partial x}$ and $\frac{\partial\psi_3}{\partial x}$ (Eqs. (7.7) and (7.8)) gives the following:

$$
\begin{aligned}
T_n &= a_n e^{\mathrm{i}K_n L} - b_n, \text{ for } n = 0, I, 1, 2, \ldots, N, \qquad (7.30)\\
T_n &= 0, \text{ for } n = II. \qquad (7.31)
\end{aligned}
$$

The second equality of Eq. (7.7) gives rise to

$$\sum_{n=0}^{N} K_n e^{\mathrm{i}k_n L} a_n Z_n - \sum_{n=0}^{N}(K_n + 2k_0\mathcal{G}_2) b_n Z_n = 0, \ -d_4 < y < -d_3. \qquad (7.32)$$

Further, Eq. (7.9) gives the following equation:

$$\sum_{n=0}^{N} 2b_n Z_n = 0, \ (-h < y < -d_3) \cup (-d_4 < y < 0). \qquad (7.33)$$

Utilizing the method of least square gives another system of linear equations as follows:

$$\sum_{n=0}^{N} S^{(2)}_{m,n} a^*_n + \sum_{n=0}^{N} T^{(2)}_{m,n} b^*_n = 0, \ m = 0, I, II, 1, 2, \ldots, N, \qquad (7.34)$$

where

$$S^{(2)}_{m,n} = -K^*_n \zeta^*_n (K_m + 2k_0\mathcal{G}_2)\int_{-d_3}^{-d_4} Z_m Z_n \, \mathrm{d}y, \qquad (7.35)$$

$$
\begin{aligned}
T^{(2)}_{m,n} &= (K^*_n + 2k_0\mathcal{G}^*_2)(K_m + 2k_0\mathcal{G}_2)\int_{-d_3}^{-d_4} Z_m Z_n \mathrm{d}y + 4\Bigg[\int_{-h}^{-d_3} Z_m Z_n \,\mathrm{d}y \\
&+ \int_{-d_4}^{0} Z_m Z_n \,\mathrm{d}y\Bigg]. \qquad (7.36)
\end{aligned}
$$

When the systems of equations (7.26) and (7.34) are combined, the following complex matrix system is obtained:

$$\mathcal{H}\mathcal{X} = \mathcal{B}, \qquad (7.37)$$

with $\mathcal{H}$ being a matrix of size $(2N+6)\times(2N+6)$,

$\mathcal{X} = [a^*_0, a^*_I, \ldots, a^*_N, b^*_0, b^*_I, \ldots, b^*_N]^T$ is the unknown quantity, and

$\mathcal{B} = [r^{(1)}_0, r^{(1)}_I, r^{(1)}_{II}, r^{(1)}_1, \ldots, r^{(1)}_N, \underbrace{0, \ldots, 0}_{N+3}]^T$.

After solving (7.37), the unknown coefficients a^*_n and b^*_n are obtained, and subsequently it becomes possible to obtain the reflection and transmission coefficients $|R_0|$ and $|T_0|$ due to the flexural wave mode.

The energy loss due to water wave interaction with the porous barriers is determined by using the following relation:

$$\text{Energy loss} = (1 - |R_0|^2 - |T_0|^2) \times 100\%. \qquad (7.38)$$

The non-dimensional hydrodynamic force on the first porous barrier (i.e., the one placed at $x = 0, -d_1 < y < -d_2$) is obtained from

$$F_1 = \frac{\omega}{gh^2}\left|\int_{-d_1}^{-d_2} (\psi_1(0,y) - \psi_2(0,y))\mathrm{d}y\right|. \qquad (7.39)$$

The non-dimensional hydrodynamic force on the second porous barrier (i.e., the one placed at $x = L, -d_3 < y < -d_4$) is obtained from

$$F_2 = \frac{\omega}{gh^2}\left|\int_{-d_1}^{-d_2} (\psi_2(L,y) - \psi_3(L,y))\mathrm{d}y\right|. \qquad (7.40)$$

7.4 Comparison with existing result

In order that the computational results can be carried out throughout this work, it is deemed appropriate to connect at least one present result with that of some earlier work. In this direction, the result of Das and Bora [26] is considered here since it bears similarities with the present work to a reasonable level. It may further be noted that if there is no ice-sheet on the upper surface leaving with a free surface only, then the present configuration reduces to the problem of surface gravity wave scattering by a dual porous

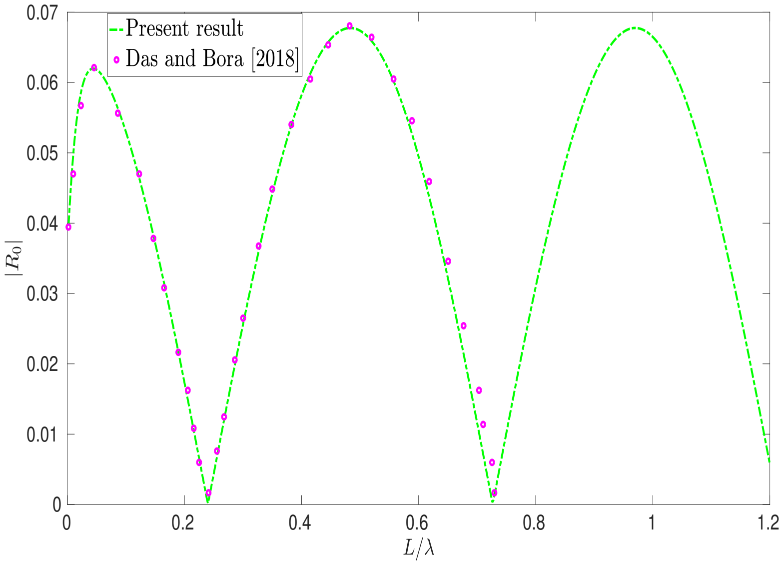

Figure 7.3: Validation between present result and existing results

barrier investigated by Das and Bora [26]. Considering $d_1 = d_3 = 0.4h$, $d_2 = d_4 = 0.2h$, $Kh = 1.6, \mathcal{G}_1 = 0.5 = \mathcal{G}_2$, $E = 0, \epsilon = 0$, it is evident from Fig. 7.3 that the results of Das and Bora [26] with Fig. 4.(a) and the present problem show very good agreement.

Based on these outcomes, a number of subsequent investigations is taken up by considering the present model to be an efficient one. Consequently, it is strongly believed that this model can be appropriately used for tackling problems involving an ice-sheet and porous breakwaters in the form of barriers in disciplines such as coastal and offshore engineering.

7.5 Results and discussion

For the purpose of demonstrating the convergence of the results, reflection coefficient $|R_0|$ and transmission coefficient $|T_0|$ are, respectively, plotted against the non-dimensional distance L/λ (where λ is the wavelength of the incident wave) between the barriers, in Fig. 7.4(a,b) for various values $N = 7, 9, 11, 13$. It is observed that, for $N = 7, 9, 11$ and 13, both $|R_0|$ and $|T_0|$ present very good agreement. Subsequently, $N = 13$ is considered to be ideal for the purpose of computation for all discussions here. For computational purpose, the following values are considered: the time period $T = 5$ s, $g = 9.81$ m/s^2, depth $h = 10$ m, the density of the homogeneous fluid $\rho_h = 1025$ kg/m^3, the elastic material density of the plate $\rho_0 = 922.5$ kg/m^3, the Young's modulus of the elastic material of the floating plate $E = 6 \times 10^9$ Pa, the thickness of the elastic plate $h_0 = 0.1$ m, $\theta = 0^\circ$ (only the normal incidence), and $N = 13$, unless otherwise mentioned.

Figure 7.5(a,b) shows the variation of the reflection and transmission coefficients

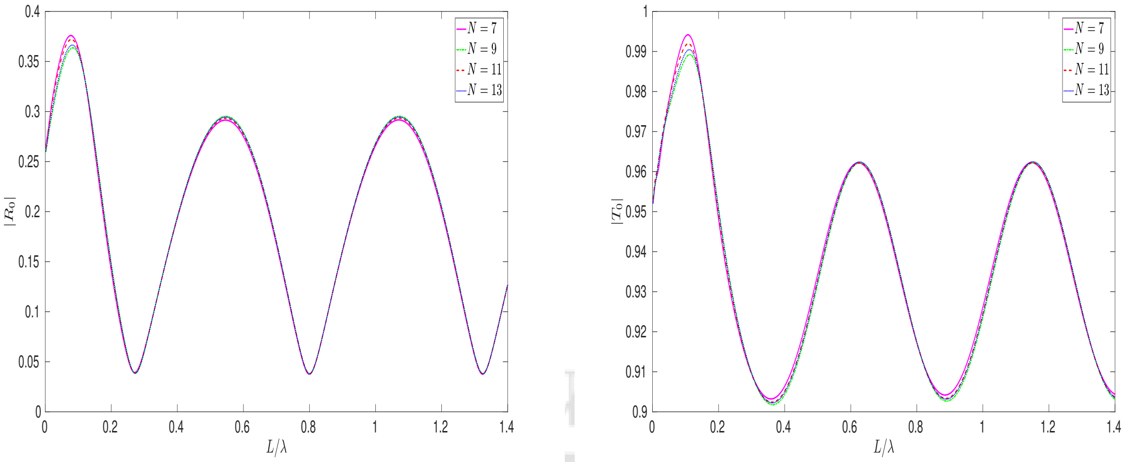

(a) (b)

Figure 7.4: Convergence of (a) reflection coefficient $|R_0|$ and (b) transmission coefficient $|T_0|$ versus L/λ for various number of evanescent modes with $d_2 = d_4 = 0$, $d_1 = d_2 + 0.5h, d_3 = d_4 + 0.5h, \mathcal{G}_1 = 0.5 = \mathcal{G}_2$

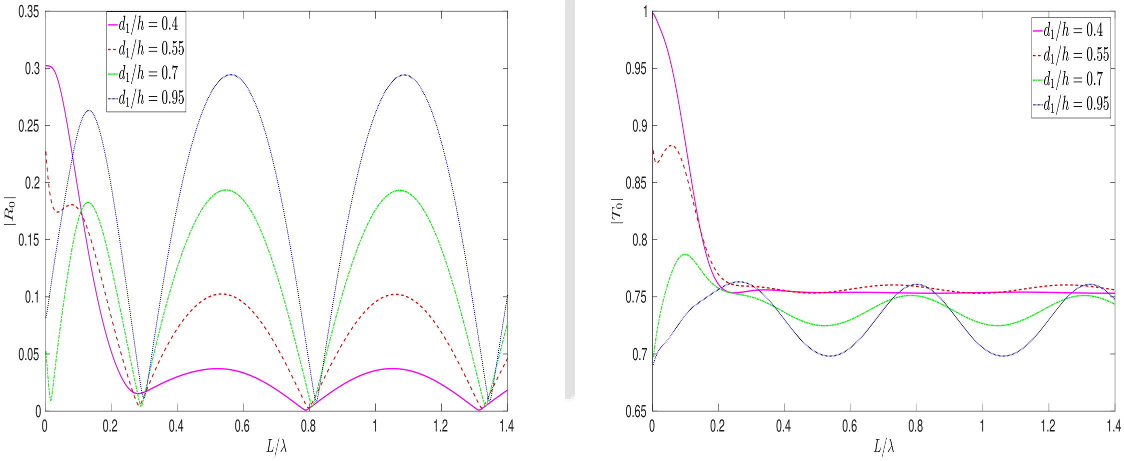

(a) (b)

Figure 7.5: Effect of (a) reflection coefficient $|R_0|$ and (b) transmission coefficient $|T_0|$ versus L/λ for various drafts of the lower tip of the first barrier with $\mathcal{G}_1 = \mathcal{G}_2 = 0.5$, $d_2 = 0.2h$, $d_3 = d_1$, $d_4 = d_2$, $\theta = 0^0$ and $N = 13$

against L/λ for different values of d_1/h of the first porous barrier where structural parameters of the barriers are taken as $\mathcal{G}_1 = \mathcal{G}_2 = 0.5$, $d_2 = 0.2h$, $d_3 = d_1$, $d_4 = d_2$. Figure 7.5 establishes that the reflection coefficient increases corresponding to an increase in d_1/h while an opposite trend is noticed with respect to the transmission coefficient. Also, one important observation is that higher reflection occurs for both barriers of greater height while lower reflection occurs for lesser height. When the length of the barriers increases, a major part of wave energy is reflected back by the barriers. It is noticed that higher oscillation for the coefficients occurs according to higher values of d_1/h. Both the maxima and minima in the values of $|R_0|$ are obtained corresponding to some particular values of L/λ with respect to the values of d_1/h. However, it is found that the reflection coefficient follows certain oscillatory patterns for all values of d_1/h.

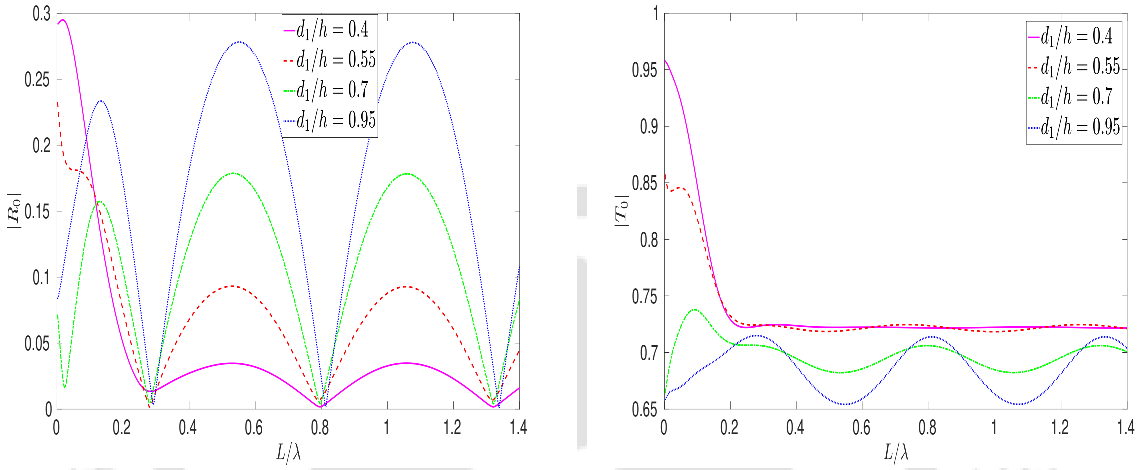

(a) (b)

Figure 7.6: Effect of (a) reflection coefficient $|R_0|$ and (b) transmission coefficient $|T_0|$ versus L/λ for various drafts of the lower tip of the first barrier with $\mathcal{G}_1 = 0.5 + \mathrm{i}, \mathcal{G}_2 = 0.5$, $d_2 = 0.2h$, $d_3 = d_1$, $d_4 = d_2$, $\theta = 0^0$ and $N = 13$

Figure 7.6(a,b) presents the reflection and transmission coefficients against L/λ with an addition of imaginary part to $\mathcal{G}_1$ by considering $\mathcal{G}_1 = 0.5 + \mathrm{i}$, whereas $\mathcal{G}_2$ is taken as 0.5. From Figs. 7.5(a) and 7.6(a), it is clearly visible that the amplitude of oscillation of the reflection coefficient reduces. Moreover, it can be inferred that, for complex values of the porous-effect parameter $\mathcal{G}_1$, a significant attenuation of the reflected wave energy by the submerged porous barriers is observed. It establishes the occurrence of damping in the neighbourhood of the first porous barrier due to the presence of the imaginary part in $\mathcal{G}_1$ which can be attributed to the inertial effect.

Figure 7.7(a,b) presents the curves for the reflection and transmission coefficients plotted against L/λ with an addition of imaginary part to $\mathcal{G}_2$ by considering $\mathcal{G}_2 = 0.5 + \mathrm{i}$, whereas $\mathcal{G}_1$ is taken as 0.5. By comparing Figs. 7.6(a) and 7.7(a), it is noticed that there is an increment in the amplitude of the oscillatory pattern of reflection coefficient, but the rate of increment of the reflected wave energy is not significant at all. In other words, complex values of the porous-effect parameter $\mathcal{G}_2$ do not have any significant impact on the attenuation of the reflected wave energy by the submerged porous barrier. In a similar manner, wave transmission decreases corresponding to the larger height of the barriers. One important observation, by comparing Figs. 7.6(b) and 7.7(b), is that the decreasing

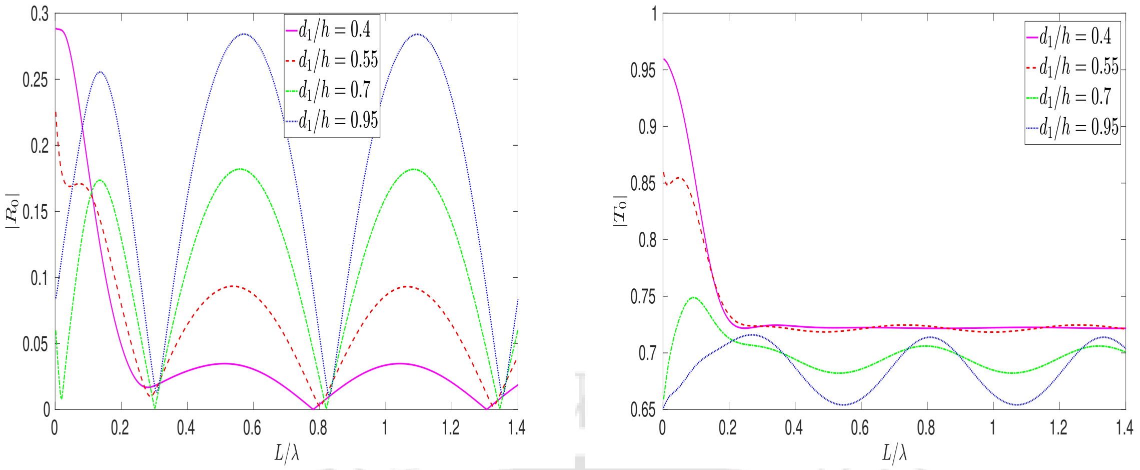

(a) (b)

Figure 7.7: Effect of (a) reflection coefficient $|R_0|$ and (b) transmission coefficient $|T_0|$ versus L/λ for various drafts of the lower tip of the first barrier with $\mathcal{G}_1 = 0.5, \mathcal{G}_2 = 0.5+\mathrm{i}$, $d_2 = 0.2h$, $d_3 = d_1$, $d_4 = d_2$, $\theta = 0^0$ and $N = 13$

rate of the transmitted wave energy is quite insensitive which implies that the wave transmission characteristics are not affected by the interchange of the positions of the porous barriers.

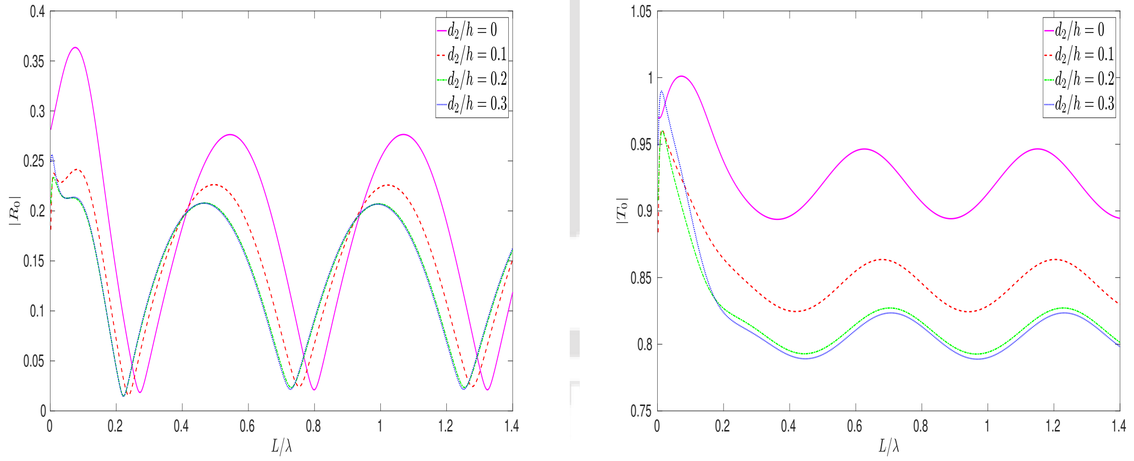

(a) (b)

Figure 7.8: Effect of (a) reflection coefficient $|R_0|$ and (b) transmission coefficient $|T_0|$ versus L/λ for various drafts of the upper tip of the first barrier with $\mathcal{G}_1 = 0.5, \mathcal{G}_2 = 0.5+\mathrm{i}$, $d_1 = d_2 + 0.5h$, $d_3 = 0.5h$, $d_4 = 0$, $\theta = 0^0$ and $N = 13$

Figures 7.8(a,b) and 7.9 present the variations of the reflection coefficient, transmission coefficient and energy loss with an adjustment of the position of the second porous barrier by making it touch the floating plate/ice-sheet while affecting a change of the position

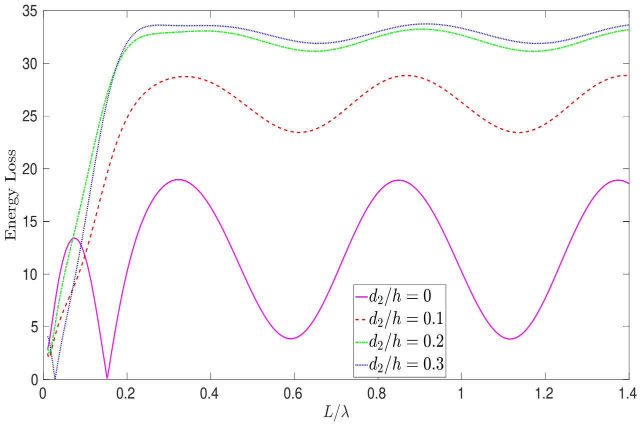

Figure 7.9: Energy loss (in %) versus L/λ for various drafts of the upper tip of the first barrier with $\mathcal{G}_1 = 0.5, \mathcal{G}_2 = 0.5 + \mathrm{i}$, $d_1 = d_2 + 0.5h$, $d_3 = 0.5h$, $d_4 = 0$, $\theta = 0^0$ and $N = 13$

of the first porous barrier in the vertical direction under the water region. Here, the following structural parameters of the barriers are taken: $\mathcal{G}_1 = 0.5, \mathcal{G}_2 = 0.5 + \mathrm{i}$, $d_1 = d_2 + 0.5h$, $d_3 = 0.5h$, $d_4 = 0$. It is noticed that the reflection and transmission coefficients both take reduced values corresponding to a shift in the optimum values when the value of d_2/h increases. Since the incident flexural gravity wave interacts with the porous barriers, occurrence of a specific phase change is observed for all of incident, reflected and transmitted waves. With regard to the mutual interaction amidst these waves, the reflection coefficient and transmission coefficient both follow a certain oscillatory pattern corresponding to various values of d_2/h. From Fig. 7.9, it is observed that, when $d_2/h = 0$ (when the first porous barrier touches the floating plate), energy loss is less than that for the other values of d_2/h. Further, it is also noticed that when the first porous barrier is closer to the bottom, energy loss is more. This is due to the fact that, when both porous barriers are nearer to the floating plate, a sufficient portion of the wave energy concentrated in the vicinity of the floating plate undergoes reflection by the plate while another portion gets dissipated while passing through the porous barriers. Again, now we plot Figs. 7.10(a,b) and 7.11 by changing the porous-effect parameters from $\mathcal{G}_1 = 0.5, \mathcal{G}_2 = 0.5 + \mathrm{i}$ to $\mathcal{G}_1 = 0.5 + \mathrm{i}, \mathcal{G}_2 = 0.5$ for the same situation as considered for Figs. 7.8(a,b) and 7.9. It is noticed that the reflection and transmission coefficients take reducing values corresponding to a shift in the optimum values for increasing values of d_2/h. Here, the same oscillatory pattern of the reflection coefficient and transmission coefficient follows corresponding to different set of values of d_2/h. From Fig. 7.11, it is noticed that, when the first porous barrier is closer to the floating plate, then energy loss is less than that for the other values of d_2/h. When Figs. 7.9 and 7.11 are compared, an appreciable increase in energy loss is observed when an imaginary part is incorporated to the otherwise real porous-effect parameter of the first porous barrier.

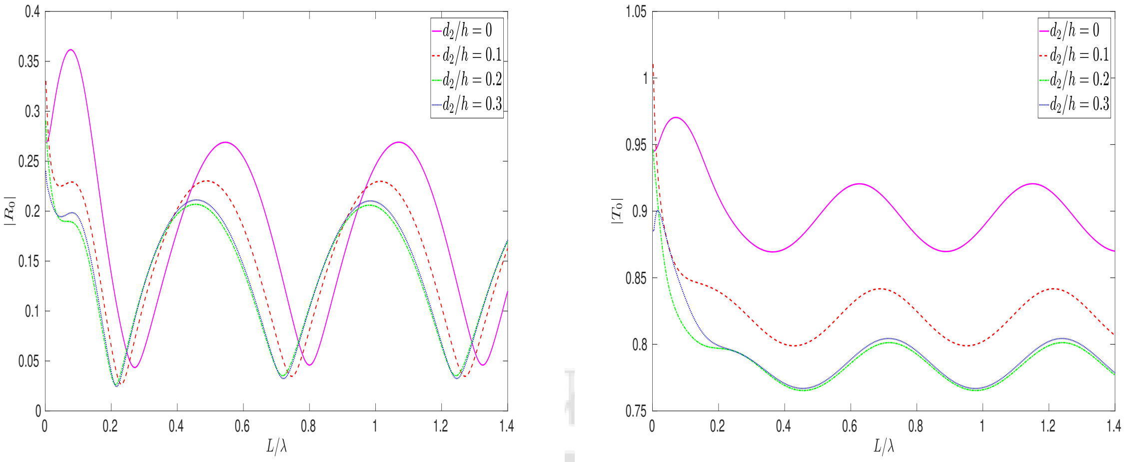

(a) (b)

Figure 7.10: Effect of (a) reflection coefficient $|R_0|$ and (b) transmission coefficient $|T_0|$ versus L/λ for various drafts of the upper tip of the first barrier with $\mathcal{G}_1 = 0.5+\mathrm{i}, \mathcal{G}_2 = 0.5$, $d_1 = d_2 + 0.5h$, $d_3 = 0.5h$, $d_4 = 0$, $\theta = 0^0$ and $N = 13$

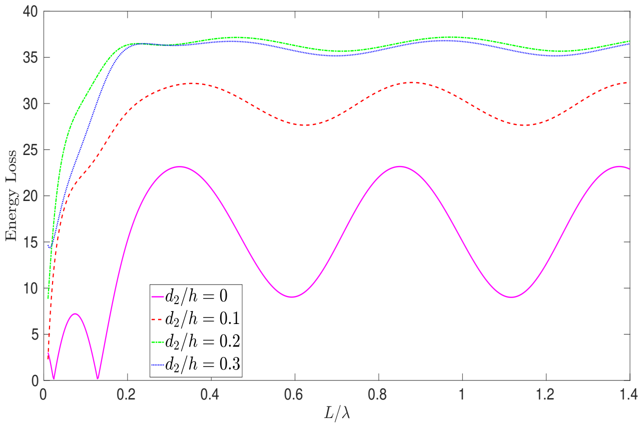

Figure 7.11: Energy loss (in %) versus L/λ for various drafts of the upper tip of the first barrier with $\mathcal{G}_1 = 0.5 + \mathrm{i}, \mathcal{G}_2 = 0.5$, $d_1 = d_2 + 0.5h$, $d_3 = 0.5h$, $d_4 = 0$, $\theta = 0^0$ and $N = 13$

In Figs. 7.12(a,b) and 7.13, another study is performed by fixing the position of the first porous barrier by making it touch the floating plate/ice-sheet while changing the position of the second porous barrier in the vertical direction under the water region. Here, the following structural parameters are considered: $\mathcal{G}_1 = 0.5, \mathcal{G}_2 = 0.5 + \mathrm{i}$, $d_3 = d_4 + 0.5h$, $d_1 = 0.5h$, $d_2 = 0$. It is noticed that the reflection and transmission coefficients take reducing values corresponding to deviation in the optimum values with increasing values of d_4/h. Since the incident flexural gravity wave interacts with the porous barrier, occurrence of certain phase change is observed in the incident, reflected and transmitted waves and further, in response to the mutual interaction of these waves, the reflection coefficient

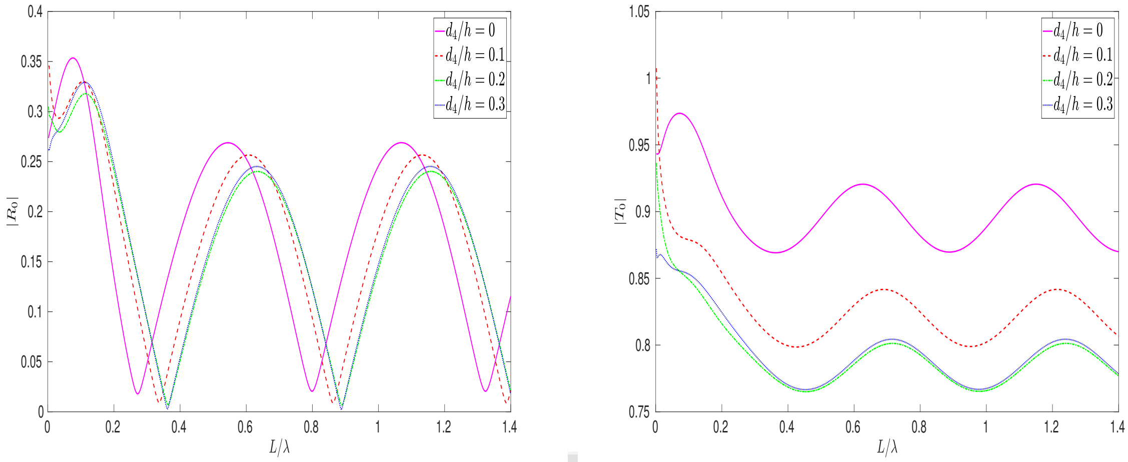

(a) (b)

Figure 7.12: Effect of (a) reflection coefficient $|R_0|$ and (b) transmission coefficient $|T_0|$ versus L/λ for various drafts of the upper tip of the second barrier with $\mathcal{G}_1 = 0.5, \mathcal{G}_2 = 0.5 + \mathrm{i}$, $d_3 = d_4 + 0.5h$, $d_1 = 0.5h$, $d_2 = 0$, $\theta = 0^0$ and $N = 13$

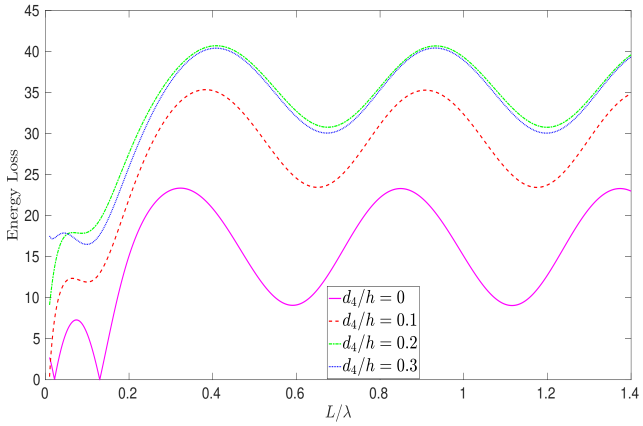

Figure 7.13: Energy loss (in %) versus L/λ for various drafts of the upper tip of the second barrier with $\mathcal{G}_1 = 0.5, \mathcal{G}_2 = 0.5 + \mathrm{i}$, $d_3 = d_4 + 0.5h$, $d_1 = 0.5h$, $d_2 = 0$, $\theta = 0^0$ and $N = 13$

and transmission coefficient exhibit a specific oscillatory pattern corresponding to various values of d_4/h. From Fig. 7.13, it is found that, when $d_4/h = 0$ (i.e., when the second porous barrier touches the floating plate), energy loss is less as compared to that for other values of d_4/h. Here the same observation, as for the first configuration, is noticed when the second barrier is placed nearer to the floating plate. Now, Figs. 7.14(a,b) and 7.15 are plotted by changing the porous-effect parameters from $\mathcal{G}_1 = 0.5, \mathcal{G}_2 = 0.5 + \mathrm{i}$ to $\mathcal{G}_1 = 0.5 + \mathrm{i}, \mathcal{G}_2 = 0.5$ for the same situation as considered for Figs. 7.12(a,b) and 7.13. Here, the reflection coefficient, transmission coefficient and energy loss are noticed to follow certain oscillatory patterns for various values of d_4/h. The maxima and minima for both reflection coefficient and transmission coefficient occur when $d_4/h = 0$, i.e., when the second porous barrier is nearer to the floating plate. Similarly, the occurrence of maximum and minimum values of energy loss is noticed when $d_4/h = 0$. Comparison of Figs. 7.13 and 7.15 clearly points to the occurrence of a significant decrement in energy loss with the incorporation of an imaginary part to the porous effect parameter of the first porous barrier for the case when second porous barrier is totally submerged. This is exactly the opposite of the observation from the comparison of Figs. 7.9 and 7.11.

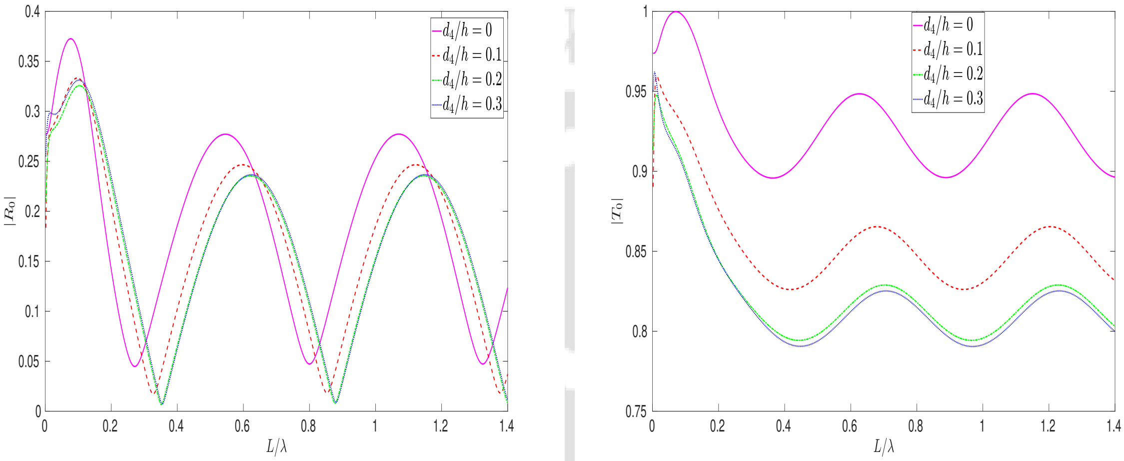

(a) (b)

Figure 7.14: Effect of (a) reflection coefficient $|R_0|$ and (b) transmission coefficient $|T_0|$ versus L/λ for various drafts of the upper tip of the second barrier with $\mathcal{G}_1 = 0.5 + \mathrm{i}, \mathcal{G}_2 = 0.5$, $d_3 = d_4 + 0.5h$, $d_1 = 0.5h$, $d_2 = 0$, $\theta = 0^0$ and $N = 13$

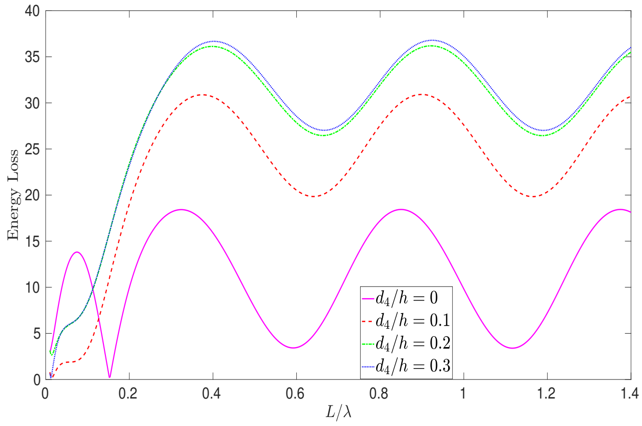

Figure 7.15: Energy loss (in %) versus L/λ for various drafts of the upper tip of the second barrier with $\mathcal{G}_1 = 0.5 + \mathrm{i}, \mathcal{G}_2 = 0.5$, $d_3 = d_4 + 0.5h$, $d_1 = 0.5h$, $d_2 = 0$, $\theta = 0^0$ and $N = 13$

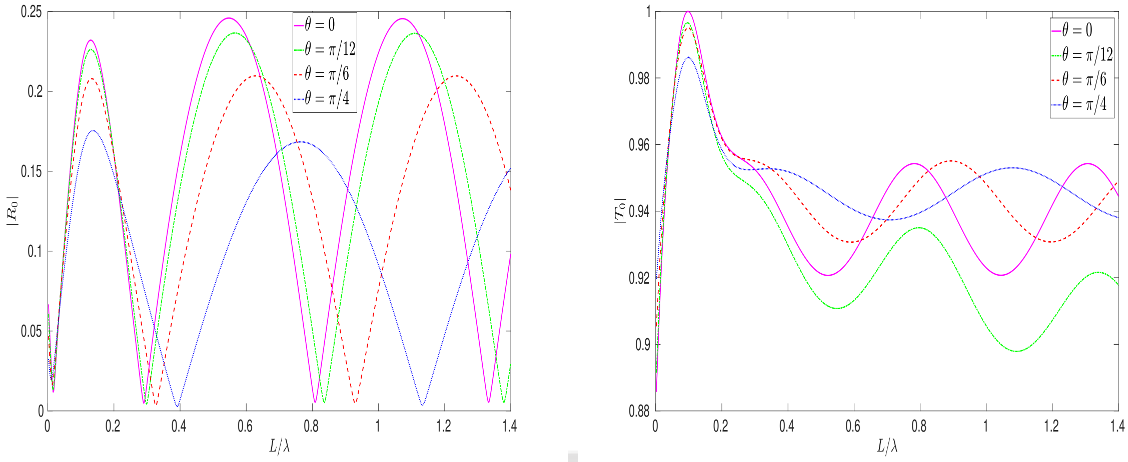

(a) (b)

Figure 7.16: Effect of (a) reflection coefficient $|R_0|$ and (b) transmission coefficient $|T_0|$ versus L/λ for different values of angle of incidence with $\mathcal{G}_1 = 0.5 = \mathcal{G}_2$, $d_2 = d_4 = 0.2h$, $d_1 = d_3 = d_4 + 0.5h$ and $N = 13$

In Figs. 7.16(a,b), the effect of the angle of incidence is investigated for the reflection and transmission coefficients when both the barriers are submerged in water. Here, the following structural parameters are taken: $\mathcal{G}_1 = 0.5 = \mathcal{G}_2$, $d_2 = d_4 = 0.2h$, $d_1 = d_3 = d_4 + 0.5h$. It is noticed that both maxima and minima for the reflection coefficient occur for normal incidence (i.e., for $\theta = 0°$). Further, it is seen from the figures that certain oscillatory patterns are followed by the reflection and transmission coefficients for different values of θ. It is important to note that, when the barriers are adjacent to each other, the reflection coefficient shows a small magnitude of oscillation, but the analogous transmission coefficient happens to be reasonably large. It occurs because of the inefficiency of the second porous barrier for such a location of the barriers.

Young's modulus is an interesting parameter since increasing it makes the ice less compliant and easier to break (i.e., a given wave amplitude produces a higher stress in the ice) which potentially increases the marginal ice zone width. But this also increases the attenuation, which could potentially reduce the marginal ice zone width (Williams et al. [98]). Williams et al. [97] showed that an appropriate choice of a value for the effective Young's modulus within the values from 5×10^9 Pa to 7×10^9 Pa was important from the wave modeling perspective. Figures 7.17(a,b) and 7.18, respectively, present plots of reflection and transmission coefficients, and energy loss according to different values of Young's modulus E of the floating ice-sheet. Here, the following structural parameters are considered: $\mathcal{G}_1 = 0.5 = \mathcal{G}_2$, $d_2 = d_4 = 0.2h$, $d_1 = d_3 = d_4 + 0.5h$. Figure 7.17 shows that the reflection coefficient takes increasing values according to an increase in Young's modulus E of the floating ice-sheet. Furthermore, transmission coefficient also increases

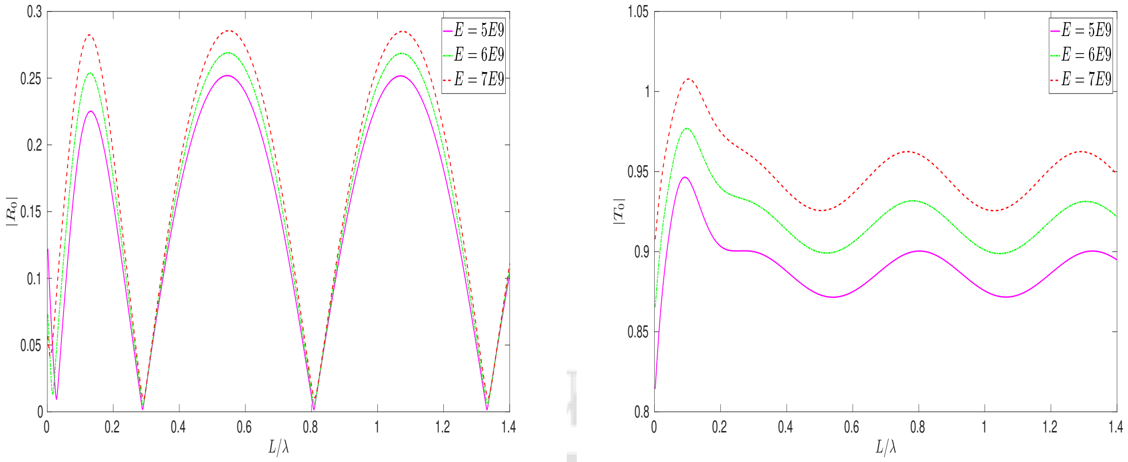

(a) (b)

Figure 7.17: Effect of (a) reflection coefficient $|R_0|$ and (b) transmission coefficient $|T_0|$ versus L/λ for different values of Young's modulus E of the ice-sheet with $\mathcal{G}_1 = 0.5 = \mathcal{G}_2$, $d_2 = d_4 = 0.2h$, $d_1 = d_3 = d_4 + 0.5h$ and $N = 13$

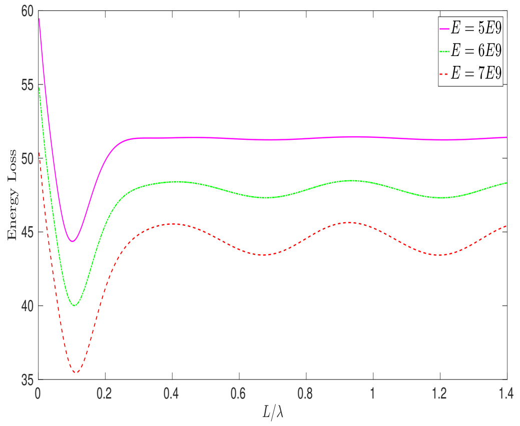

Figure 7.18: Energy loss (in %) versus L/λ for different values of Young's modulus E of the ice-sheet with $\mathcal{G}_1 = 0.5 = \mathcal{G}_2$, $d_2 = d_4 = 0.2h$, $d_1 = d_3 = d_4 + 0.5h$ and $N = 13$

corresponding to an increase in Young's modulus with the rate of increment being quite higher. Furthermore, Fig. 7.18 depicts that energy loss reduces when the value of Young's modulus E of the ice-sheet gets increased. According to an increment of E, the floating ice-sheet becomes more rigid and consequently, the wave cannot penetrate the floating plate and therefore, a very small amount of incident wave energy is transferred to the floating ice-sheet. Corresponding to an increase in E of the floating plate, a certain oscillatory pattern is followed by all of reflection coefficient, transmission coefficient and energy loss. In the presence of the floating ice-sheet, a sufficient portion of energy loss occurs because of the interference of the incident and reflected waves, and another part of the wave energy gets dissipated while passing through the porous barrier. Consequently, a moderate elasticity E of the floating ice-sheet can be considered to be helpful for use in coastal engineering for wave attenuation.

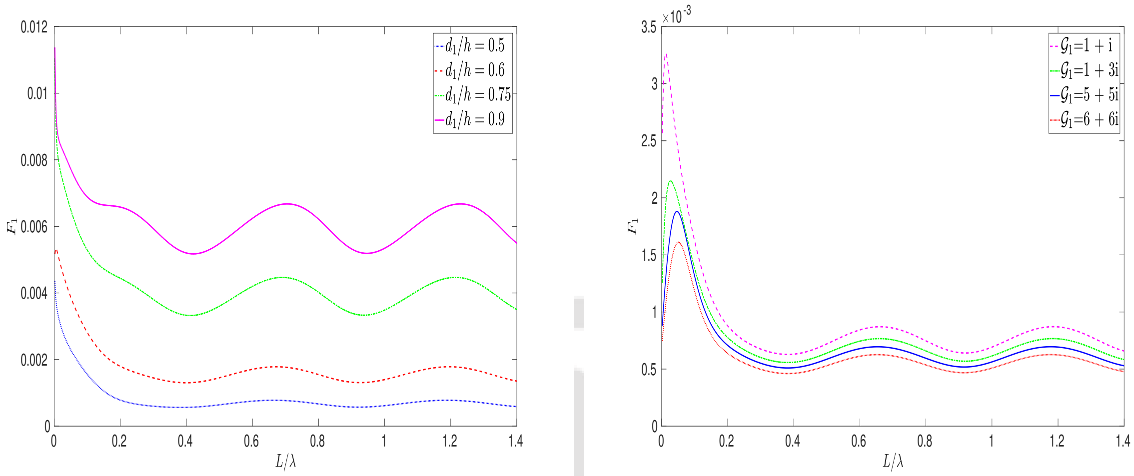

(a) (b)

Figure 7.19: Effect of force F_1 versus L/λ on the first barrier for (a) different values of d_1/h and (b) different values of $\mathcal{G}_1$

In Fig. 7.19(a), the effect of hydrodynamic force F_1 on the first porous barrier is plotted against L/λ corresponding to various values of the length of the first barrier, i.e., for d_1/h, where the following values are considered: $\mathcal{G}_1 = 0.5 = \mathcal{G}_2$, $d_2 = 0$, $d_4 = 0.2h$, $d_3 = d_4 + 0.5h$. Fig. 7.19(a) demonstrates that the hydrodynamic wave force acting on the barrier takes increasing values when the value of d_1/h increases. Oscillatory pattern in the wave force is observed corresponding to an increase in the length of the first barrier. In Fig. 7.19(b), the effect of hydrodynamic force on the first porous barrier is plotted against L/λ for various values of porous-effect parameter $\mathcal{G}_1$ of the first barrier. Here, the following structural values are taken: $\mathcal{G}_2 = 0.5$, $d_2 = 0$, $d_1 = 0.5h$, $d_4 = 0.2h$, $d_3 = d_4 + 0.5h$. It can be observed that the wave force takes reduced values corresponding to an increase in the value of $\mathcal{G}_1$. Here, the wave force follows an oscillatory nature corresponding to various values of $\mathcal{G}_1$. The wave force acting on the first barrier reduces because of the increment in wave energy dissipation and transmission by the porous barrier possessing greater porosity. Thus, it is observed that a suitable positioning of the barriers is required in order to reduce the waveload and create a tranquility zone.

Figure 7.20(a) shows the effect of hydrodynamic force F_2 on the second porous barrier for different values of length of the second barrier, i.e., for d_3/h. Here, the following structural values are taken: $\mathcal{G}_1 = 0.5 = \mathcal{G}_2$, $d_2 = 0.2h$, $d_1 = d_2 + 0.5h$, $d_4 = 0$. Figure 7.20(a) shows that the wave force takes increasing values corresponding to an increase in the values of d_3/h. Oscillatory behaviour by the wave force is observed corresponding to

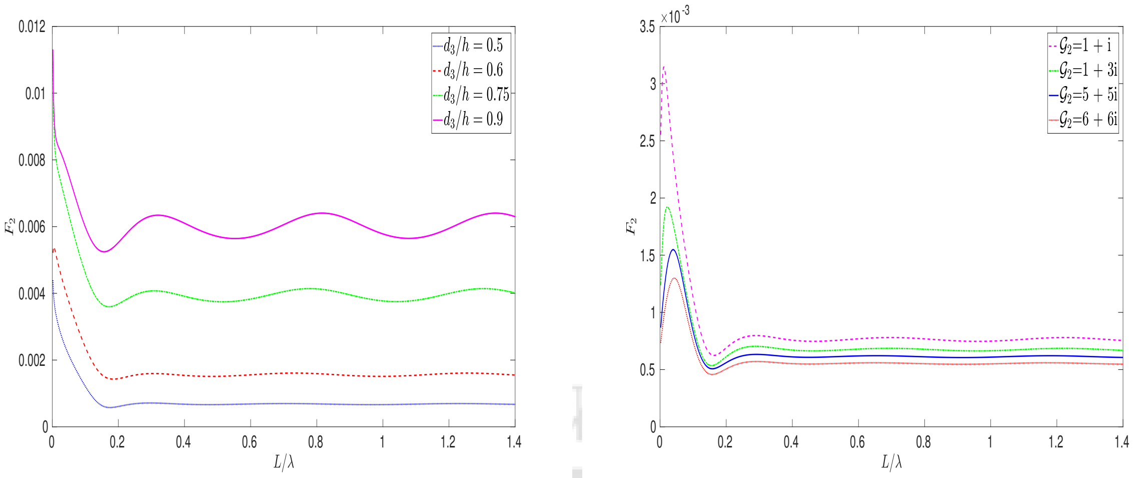

(a) (b)

Figure 7.20: Effect of force F_2 versus L/λ on the second barrier for (a) different values of d_3/h and (b) different values of $\mathcal{G}_2$

an increase in the length of the second barrier. In Fig. 7.20(b), the effect of hydrodynamic force on the second porous barrier is plotted against L/λ corresponding to various values of porous-effect parameter $\mathcal{G}_2$ of the second barrier. For these figures, the following values are considered: $\mathcal{G}_1 = 0.5$, $d_2 = 0.2h$, $d_1 = d_2 + 0.5h$, $d_3 = 0.5h$, $d_4 = 0$. A similar pattern as in Fig. 7.19(b) is also noticed in Fig. 7.20(b) which demonstrates the general pattern of the wave force, i.e., the wave force reduces corresponding to an increase in the values of porous-effect parameter of the second barrier due to an increment in wave energy dissipation and transmission by the barrier. Here, the wave force follows an oscillatory nature corresponding to higher values of the porous-effect parameter of the second barrier. However, by comparing Fig. 7.20(a) with Fig. 7.5(a), it is worthwhile to note that the optimum values in the reflection coefficient is associated with the optimum values in the hydrodynamic wave forces acting on the barriers.

7.6 Conclusion

In this chapter, using linearized water wave theory, we study the problem of oblique flexural gravity wave scattering by a dual submerged porous barrier of different porosity in an infinite channel of finite depth with an ice-sheet as the upper surface. Considering the well-known Euler-Bernoulli beam equation, the ice-sheet is considered as a thin elastic plate where the horizontal length of such a plate is considered to be much larger in comparison to its thickness. Under such circumstances, there exists propagating wave only at one wavenumber along the upper surface for any given frequency which corresponds to the flexural mode. The boundary value problem is solved with the help of eigenfunction expansion and least square methods as in Chapter 5. Results are computed and examined for the reflection and transmission coefficients, energy loss and hydrodynamic force to exhibit effects of the wave and various structural parameters. From all the graphical results, the following important observations are noted:

- When both porous barriers are nearer to the floating plate, i.e., the ice-sheet, a sufficient portion of the wave energy concentrated near the floating plate is found to be reflected by the plate and like-wise, a significant portion of the wave energy is dissipated when it passes through the porous barriers.
- Further, the study reveals that, for the fixed submergence depth of one of the porous barriers, corresponding to an increment of the inertial effect of the porous barrier, lower reflection and higher transmission are acquired.
- Energy loss reduces corresponding to an increase in the elasticity of the plate. In the presence of the floating ice-sheet, a sufficient portion of energy loss takes place as a consequence of the interference of the incident and reflected waves while another part of the wave energy is dissipated when it passes through the porous barriers. Therefore, a moderate plate elasticity is considered helpful for use in coastal engineering for wave attenuation.
- The wave force acting on either of the porous barriers takes increasing values when the length of the barrier is increased.
- The wave force acting on the barriers decreases because of the increment in wave energy dissipation and transmission by the porous barrier of higher porosity.

The inference is that, in order to reduce the waveload and to create a tranquility zone, positioning of the barriers in an appropriate manner is very essential. The physical problem and model described in this work are expected to provide benefit in choosing an appropriate mechanism to reduce waveload for a variety of marine problems. The results developed here may be utilized suitably for tackling a number of water wave scattering problems involving flexural gravity waves that appear in various disciplines of coastal and offshore engineering, mainly in polar regions.

CHAPTER 8

SCATTERING OF FLEXURAL GRAVITY WAVES BY A PAIR OF SUBMERGED VERTICAL POROUS BARRIERS LOCATED ABOVE A POROUS SEA-BED

8.1 Introduction

An analytical study is presented in this chapter to investigate the oblique flexural gravity wave scattering by two totally submerged vertical porous barriers, placed at some distance from each other, in a homogenous fluid by considering the sea-bed to be porous. A thin ice-sheet is considered as the upper surface. The complete analytical solution, under the assumption of small-amplitude theory and structural response, is acquired by employing eigenfunction expansion and least square method for the problem of flexural gravity waves interacting with submerged porous barriers as used in Chapter 7. Subsequently, computation for the reflection and transmission coefficients, energy loss and wave forces is carried out and discussed for different parameter values corresponding to the ice-sheet, porous sea-bed and porous barrier. The study reveals that nearly zero reflection and full transmission may occur for the case of an impermeable sea-bed and also for the real porosity parameter of the porous sea-bed for various structural parameters. Furthermore, wave transmission decreases significantly due to the energy dissipation by the porous sea-bed.

8.2 Formulation of the problem

This is an extension of the earlier problem discussed in Chapter 7. Here the impermeable sea-bed is replaced by a porous sea-bed. All other geometrical considerations are the same as the ones discussed in the previous chapter except the bottom boundary.

A Cartesian coordinate system is adopted in such a way that the y-axis points in

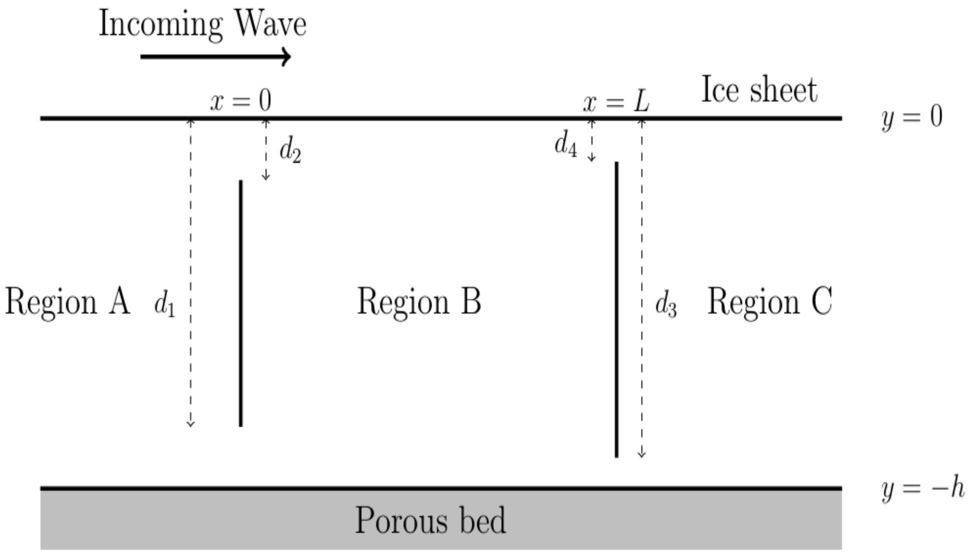

Figure 8.1: Schematic diagram of the problem

the vertical upward direction; $y = -h$ and $y = 0$, respectively, represent the location of the porous sea-bed and floating ice-sheet; as displayed in Fig. 8.1. Here, two fully submerged thin vertical porous barriers of different heights are located at $x = 0$ and $x = L$. Further, d_1 and d_3, respectively, represent the distances of the lower vertical tips of the first and second porous barriers from the ice-sheet while d_2 and d_4, respectively, represent the distances of the upper vertical tips from the ice-sheet. The whole fluid domain under consideration is partitioned into three sub-domains, namely, $x < 0$, $-h < y < 0$ as region A, $0 < x < L$, $-h < y < 0$ as region B, and $x > L$, $-h < y < 0$ as region C. Adopting small amplitude theory and accounting for all the above assumptions, the velocity potentials in each region A, B and C, respectively, can be represented by $\Psi_1(x, y, z, t) = \psi_1(x, y)e^{(\mathrm{i}lz - \mathrm{i}\omega t)}$, $\Psi_2(x, y, z, t) = \psi_2(x, y)e^{(\mathrm{i}lz - \mathrm{i}\omega t)}$ and $\Psi_3(x, y, z, t) = \psi_3(x, y)e^{(\mathrm{i}lz - \mathrm{i}\omega t)}$. The governing equations and upper surface boundary condition in each of the regions are the same as described in Chapter 7 (Eqs. (7.1) and (7.2)) except the bottom boundary condition.

The bottom boundary condition has the following form:

$$\frac{\partial \psi_j}{\partial y} + G\psi_j = 0, \quad \text{on} \quad y = -h, \ j = 1, 2, 3, \tag{8.1}$$

where G is the porosity parameter, which characterizes the sea-bed permeability. The detailed description of the porous sea-bed and its role is already presented in Chapter 5.

The matching conditions across the vertical boundaries $x = 0$ and $x = L$ are the same as the ones described in Chapter 7 (Eqs. (7.4) - (7.9)).

The asymptotic behaviours of the potentials ψ_1 and ψ_3 (there is no such representation for ψ_2 since it is associated with a bounded region) are given by

$$\psi_1 \rightarrow \frac{k_0\cosh k_0(h+y)-G\sinh k_0(h+y)}{k_0\cosh k_0h-G\sinh k_0h}\left[e^{\mathrm{i}K_0x}+R_0e^{-\mathrm{i}K_0x}\right] \quad \text{as } x\rightarrow-\infty, \tag{8.2}$$

$$\psi_3 \rightarrow \frac{k_0\cosh k_0(h+y)-G\sinh k_0(h+y)}{k_0\cosh k_0h-G\sinh k_0h}T_0e^{\mathrm{i}K_0(x-L)} \text{ as } x\rightarrow\infty, \tag{8.3}$$

where the unknown quantities R_0 and T_0, respectively, are the reflection and transmission coefficient. The radiation condition will be singular for certain values of the porosity parameter of the sea-bed, i.e, for the case of $G = k_0\coth k_0h$. In the present analysis, G is considered in such a way that $G = k_0\coth k_0h$ does not hold, and due to this, the solutions ψ_1 and ψ_3 remain bounded (in a similar manner in Behera et al. [6]). In Eqs. (8.2) and (8.3), $K_0 = (k_0^2-l^2)^{1/2}$ with k_0 satisfying $K(k_0-G\tanh k_0h)-(\mathcal{D}k_0^4+1-\epsilon K)(k_0^2\tanh k_0h-k_0G)=0$.

8.3 Derivation of analytical solutions

Employment of separation of variables technique gives velocity potential $\psi_1(x,y)$ in region A in the following form:

$$\begin{aligned}\psi_1(x,y) &= \left[e^{\mathrm{i}K_0x}+R_0e^{-\mathrm{i}K_0x}\right]Z_0(h,y)+\sum_{n=I}^{II}R_ne^{-\mathrm{i}K_nx}Z_n(h,y)\\ &+\sum_{n=1}^{\infty}R_ne^{-\mathrm{i}K_nx}Z_n(h,y),\end{aligned} \tag{8.4}$$

where R_n is the complex reflection coefficient and $K_n = (k_n^2-l^2)^{1/2}$. Here it is assumed that $R_{II} = 0$ due to the boundedness of the velocity potential at negative infinity. Using the boundary condition (8.1), the depth-dependent function $Z_n(h,y)$ is obtained as

$$Z_n(h,y) = \frac{k_n\cosh k_n(h+y)-G\sinh k_n(h+y)}{k_n\cosh k_nh-G\sinh k_nh}, \quad n=0,I,II,1,2,..., \tag{8.5}$$

with k_n satisfying the dispersion relation

$$K(k_n-G\tanh k_nh)-(\mathcal{D}k_n^4+1-\epsilon K)(k_n^2\tanh k_nh-k_nG)=0. \tag{8.6}$$

Dispersion relation (8.6) has (i) one positive real root k_0 that indicates the propagating mode; (ii) two pairs of complex conjugate roots k_n, $n = I, II, III, IV$ in the form $a\pm\mathrm{i}b$ and $-(a\pm\mathrm{i}b)$, respectively, and (iii) also an infinite number of purely imaginary roots $k_n = \mathrm{i}\kappa_n$, $n = 1,2,...$, (Fig. 8.2). For the sake of ensuring the validity of the boundedness property of the velocity potential, the contribution from the roots k_{III} and k_{IV} is avoided as in Chapter 7. Since the existence of exactly one positive real root k_0 of (8.6) is evidently ensured, there exists only one wave mode (wavenumber) propagating at the ice-sheet (say, flexural mode) along the positive x-direction. We truncate the evanescent modes of the potential with the infinite sum at some finite $n = N$ to write $\psi_1(x, y)$ as

$$\begin{aligned}\psi_1(x,y) &= \left[e^{\mathrm{i}K_0x} + R_0e^{-\mathrm{i}K_0x}\right]Z_0(h,y) + \sum_{n=I}^{II} R_ne^{-\mathrm{i}K_nx}Z_n(h,y)\\ &+ \sum_{n=1}^{N} R_ne^{-\mathrm{i}K_nx}Z_n(h,y). \qquad (8.7)\end{aligned}$$

In region B also, following a similar procedure, the spatial velocity potential $\psi_2(x, y)$ takes the following form:

$$\psi_2(x,y) = \sum_{n=0,I,II,1}^{N} [a_ne^{\mathrm{i}K_nx} + b_ne^{-\mathrm{i}K_n(x-L)}]Z_n(h,y), \qquad (8.8)$$

where a_n and b_n are arbitrary constants.

Likewise, the spatial velocity potential $\psi_3(x, y)$ in region C can be written as

$$\psi_3(x,y) = \sum_{n=0,I,II,1}^{N} T_ne^{\mathrm{i}K_n(x-L)}Z_n(h,y), \qquad (8.9)$$

where T_n is the complex transmission coefficient. Here it is assumed that $T_{II} = 0$ in order to preserve the boundedness of the velocity potential at infinity.

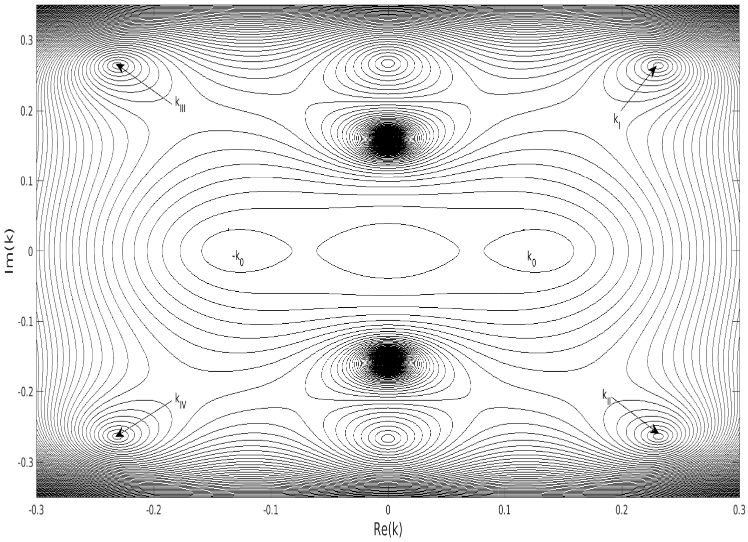

Figure 8.2: Contour plot of roots of the dispersion relation

The roots of the complex dispersion equation (8.6) are evaluated numerically through the use of contour plots for the purpose of interpreting the behaviours of the wavenumbers (Fig. 8.2). In order to compute these, the values of various parameters are considered in accordance with the following: time period $T = 5$ s, depth $h = 10$ m, density of the homogeneous fluid $\rho = 1025$ kg/m^3, elastic material density of the plate $\rho_0 = 922.5$ kg/m^3, the porosity of the sea-bed $Gh = 0.5$, Young's modulus of the elastic material of the floating plate $E = 6 \times 10^9$ Pa, Poisson's ratio $\nu = 0.3$, thickness of the elastic plate $h_0 = 0.1$ m, $g = 9.81$ m/s^2, respectively, unless otherwise mentioned. Figure 8.2 presents the nature of the complex roots demonstrating that two pairs of complex roots, occurring as positive and negative of a complex conjugate pair, namely, $k_I, k_{II}, k_{III}, k_{IV}$, are located in such a way that there is one root in each of the quadrants. It needs to be mentioned that two pairs of complex roots occur due to the presence of the ice-sheet. For computational purpose, only the roots that lie in the first and fourth quadrants are chosen in order that the velocity potentials ψ_1 and ψ_3 remain bounded.

The horizontal velocity components $\frac{\partial \psi_1}{\partial x}$ and $\frac{\partial \psi_2}{\partial x}$ follow continuity conditions across $x = 0$ (Eqs. (7.4) and (7.5)) giving

$$R_n = 1 - a_n + b_n e^{\mathrm{i}K_n L}, \text{ for } n = 0, I, \tag{8.10}$$

$$R_n = b_n e^{\mathrm{i}K_n L} - a_n, \text{ for } n = 1, 2, \cdots, N, \tag{8.11}$$

$$R_n = 0, \text{ for } n = II. \tag{8.12}$$

Using the continuity conditions along the boundary $x = L$ for the horizontal velocity components $\frac{\partial \psi_2}{\partial x}$ and $\frac{\partial \psi_3}{\partial x}$ (Eqs. (7.7) and (7.8)), the following are obtained:

$$T_n = a_n e^{\mathrm{i}K_n L} - b_n, \text{ for } n = 0, I, 1, 2, \ldots, N, \tag{8.13}$$

$$T_n = 0, \text{ for } n = II. \tag{8.14}$$

Now using the least square method with $Z_n(h, y)$ given by Eq. (8.5), as used in Chapter 7, we get the following complex matrix system:

$$\mathcal{A}\mathcal{X} = \mathcal{C}, \tag{8.15}$$

with $\mathcal{A}$ being a matrix of size $(2N+6) \times (2N+6)$, $\mathcal{X} = [a_0^*, a_I^*, \ldots, a_N^*, b_0^*, b_I^*, \ldots, b_N^*]^T$ – an unknown quantity, and $\mathcal{C} = [r_0^{(1)}, r_I^{(1)}, r_{II}^{(1)}, r_1^{(1)}, \ldots, r_N^{(1)}, \underbrace{0, \ldots, 0}_{\text{N+3}}]^T$.

After solving (8.15), the unknown coefficients a_n^* and b_n^* are obtained, and subsequently it becomes possible to obtain the reflection and transmission coefficients $|R_0|$ and $|T_0|$ due to flexural wave mode. Consequently, energy loss, the non-dimensional hydrodynamic force F_1 on the first porous barrier and the non-dimensional hydrodynamic force F_2 on the second porous barrier can be calculated by using Eqs. (7.38), (7.39) and (7.40), respectively.

8.4 Validation with experimental result

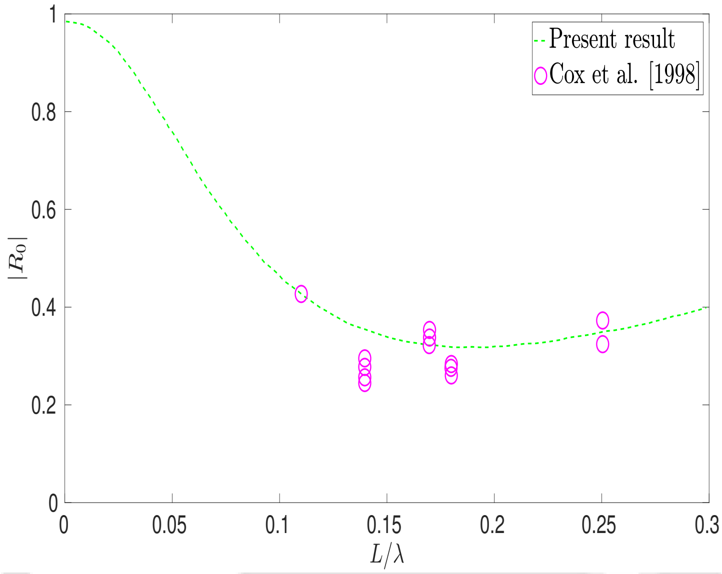

Figure 8.3: Validation between present result and experimental result of Cox et al. [19]

To validate the result against some experimental data, we consider the experimental data of Cox et al. [19]. We validate our present result with one of their experimental data set using the following parameter values $k_0h = 0.8\pi$, $\mathcal{G}_1 = 43.53 + 4.82\mathrm{i}$, $\mathcal{G}_2 = 0$, $d_2 = d_4 = 0$, $d_1 = d_3 = 0.5h$, $E = 0, \epsilon = 0$ and $Gh = 0$. Figure 8.3 shows the comparison between our result and the experimental result of Cox et al. [19] with Fig. 5. It may be mentioned that Liu and Li [58] had also earlier validated their result with the result of Cox et al. [19].

8.5 Results and discussion

For computational purpose, the values considered are the same as considered for Fig. 8.2 with an additional consideration of $\theta = 0^\circ$, $N = 13$.

Figure 8.4(a,b) presents the reflection and transmission coefficients against L/λ by considering $\mathcal{G}_1 = 0.5 + \mathrm{i}$, and $\mathcal{G}_2 = 0.5$. From Fig. 8.4, it can be noticed that the increase in the value of d_1/h, i.e., the submerged height of the first barrier, results in an increase in the reflection coefficient and a decrease in the transmission coefficient. One important observation is that higher reflection occurs for both barriers of greater height while lower

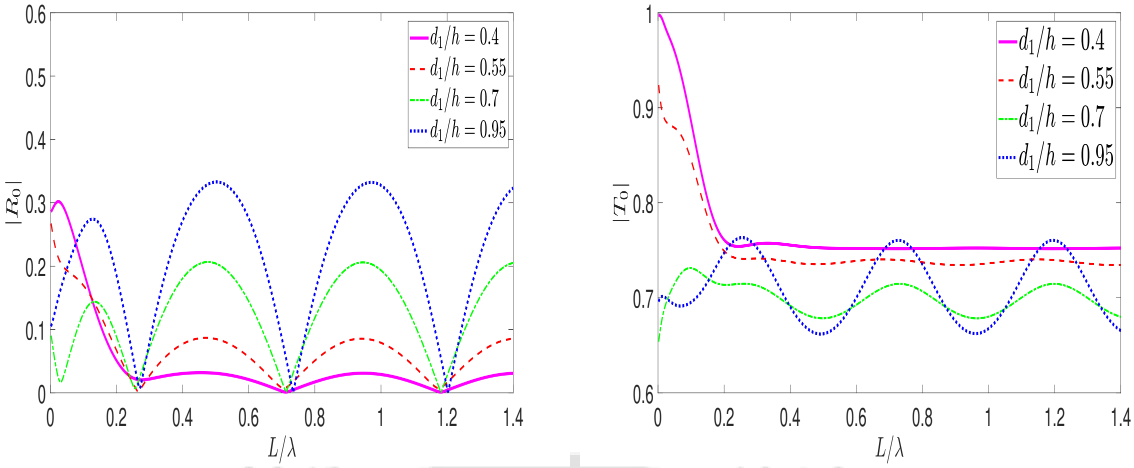

(a) (b)

Figure 8.4: Effect of (a) reflection coefficient $|R_0|$ and (b) transmission coefficient $|T_0|$ versus L/λ for different drafts of the lower tip of the first barrier with $\mathcal{G}_1 = 0.5+\mathrm{i}, \mathcal{G}_2 = 0.5$, $d_2 = 0.2h$, $d_3 = d_1$, $d_4 = d_2$, $Gh = 0.5$, $\theta = 0^0$ and $N = 13$

reflection occurs for lesser height. Both the maxima and minima for $|R_0|$ are obtained corresponding to some particular values of L/λ with respect to the values of d_1/h. The maximum/minimum values in wave reflection are due to the constructive/destructive interference of the incident and reflected waves in the presence of the porous barriers. Since the incident flexural gravity wave interacts with the porous barriers, occurrence of a specific phase change is observed for all of incident, reflected and transmitted waves. With regard to the mutual interaction amidst these waves, a certain oscillatory pattern is followed by both the reflection coefficient and transmission coefficient corresponding to various values of d_1/h. When the length of the barriers increases, a major portion of wave energy is reflected back by the barriers. It is noticed that higher oscillation for the coefficients occurs according to higher values of d_1/h. However, it is found that the reflection coefficient follows certain oscillatory patterns for all values of d_1/h. This happens because, when both submerged porous barriers are nearer to the porous sea-bed, a sufficient amount of the wave energy concentrated in the vicinity of the sea-bed gets reflected by the barriers while another portion of the wave energy gets dissipated when the waves pass through the porous barriers. Moreover, it can be inferred that, for complex values of the porous-effect parameter of the barriers, a significant attenuation of the reflected wave energy by the submerged porous barriers is observed. It establishes the occurrence of damping in the neighbourhood of the first porous barrier due to the presence of the imaginary part in $\mathcal{G}_1$ which can be attributed to the inertial effect.

Figure 8.5(a,b) presents the variations of energy loss with an adjustment of the position of the second porous barrier by making it touch the floating plate/ice-sheet while affecting

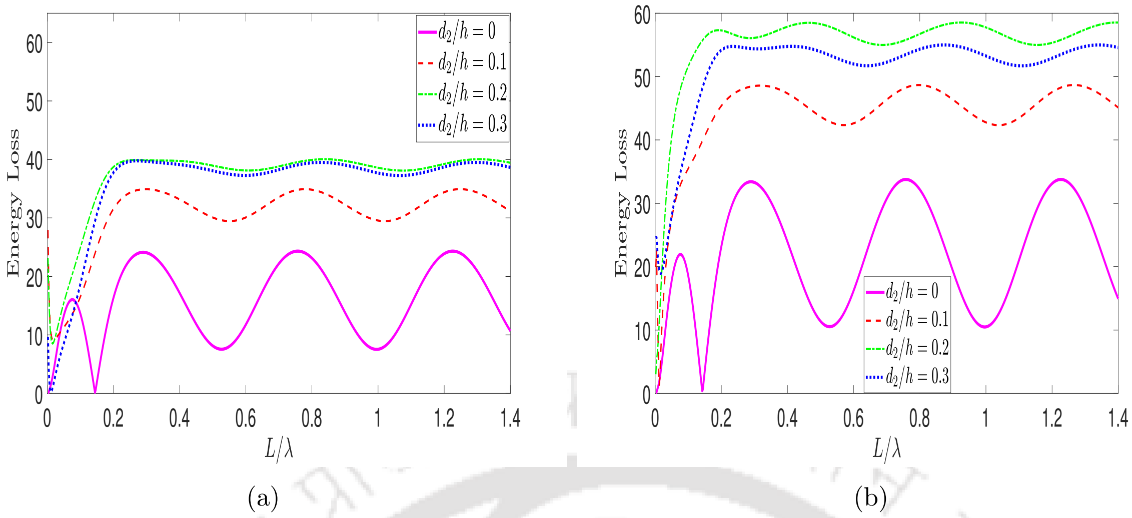

(a) (b)

Figure 8.5: Energy loss (in %) for different drafts of the upper tip of the first barrier with (a) $\mathcal{G}_1 = 0.5, \mathcal{G}_2 = 0.5 + \mathrm{i}$, and (b) $\mathcal{G}_1 = 0.5 + \mathrm{i}, \mathcal{G}_2 = 0.5$ with $d_1 = d_2 + 0.5h$, $d_3 = 0.5h$, $d_4 = 0$, $Gh = 0.5$, $\theta = 0^0$ and $N = 13$

a change of the position of the first porous barrier in the vertical direction under the water region. Here, the following structural parameters of the barriers for Fig. 8.5(a) are taken: $\mathcal{G}_1 = 0.5, \mathcal{G}_2 = 0.5 + \mathrm{i}$, $d_1 = d_2 + 0.5h$, $d_3 = 0.5h$, $d_4 = 0$. Figure 8.5(a) tells that, when $d_2/h = 0$ (when the first porous barrier touches the floating plate), energy loss is less than that for the other values of d_2/h. Further, it is also noticed that, when the first porous barrier is closer to the sea-bed, then energy loss is more. This is due to the fact that, when the first porous barrier is nearer to the porous sea-bed, a sufficient portion of the wave energy concentrated in the vicinity of the porous sea-bed gets reflected by the barrier while another portion gets dissipated while passing through the porous barriers. Therefore, it is concluded that porous structures have a very good ability of wave energy dissipation compared to the elastic structures. Then we plot Fig. 8.5(b) by changing the values of the porous-effect parameters from $\mathcal{G}_1 = 0.5, \mathcal{G}_2 = 0.5 + \mathrm{i}$ to $\mathcal{G}_1 = 0.5 + \mathrm{i}, \mathcal{G}_2 = 0.5$ for the same situation as considered for Figs. 8.5(a). From Fig. 8.5(b), it is noticed that, when the first porous barrier is closer to the floating ice-sheet, then energy loss is less than that for the case when the first porous barrier approaches the porous sea-bed. This is mainly due to the wave energy dissipation by the porous sea-bed. When Figs. 8.5(a) and 8.5(b) are compared, an appreciable increase in energy loss is found with an imaginary part incorporated to the otherwise real porous-effect parameter of the first porous barrier for the case when the second porous barrier touches the floating plate/ice-sheet. In other words, this happens when the porosity of the first barrier possesses inertial effect too.

In Fig. 8.6(a,b), another study is carried out by fixing the position of the first porous barrier by making it touch the floating ice-sheet while changing the position of the second

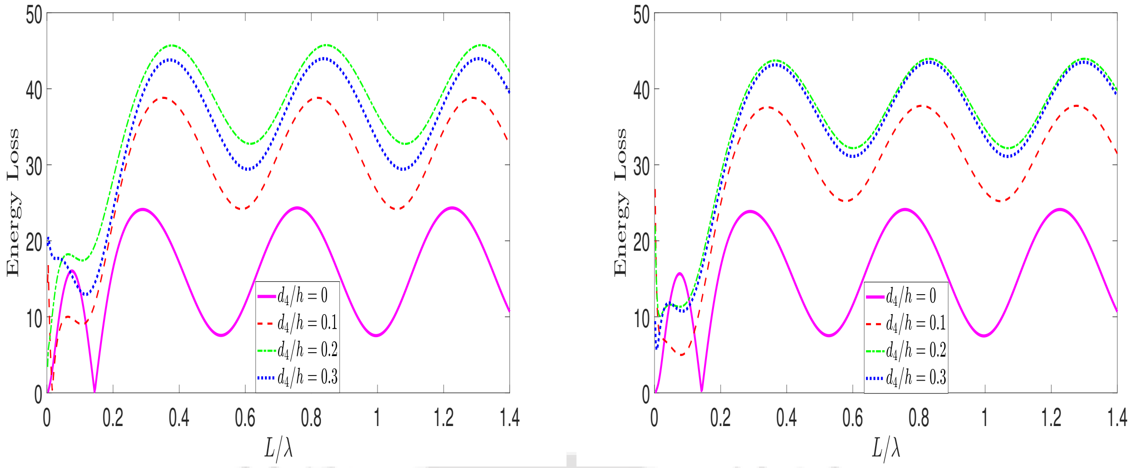

(a) (b)

Figure 8.6: Energy loss (in %) for different drafts of the upper tip of the second barrier with (a) $\mathcal{G}_1 = 0.5, \mathcal{G}_2 = 0.5 + \mathrm{i}$, and (b) $\mathcal{G}_1 = 0.5 + \mathrm{i}, \mathcal{G}_2 = 0.5$ with $d_3 = d_4 + 0.5h$, $d_1 = 0.5h$, $d_2 = 0$, $Gh = 0.5$, $\theta = 0^0$ and $N = 13$

porous barrier in the vertical direction under the water region. Here, the following structural parameters are considered for Figs. 8.6(a): $\mathcal{G}_1 = 0.5, \mathcal{G}_2 = 0.5 + \mathrm{i}$, $d_3 = d_4 + 0.5h$, $d_1 = 0.5h$, $d_2 = 0$. It is clearly noticeable from Fig. 8.6(a) that when $d_4/h = 0$ (i.e., for the case when the second porous barrier touches the floating plate), energy loss is less as compared to the case when the second porous barrier approaches the porous sea-bed. Here the same observation as for the first configuration is noticed when the second barrier is placed nearer to the floating sheet. Then we plot Fig. 8.6(b) by changing the values of the porous-effect parameters from $\mathcal{G}_1 = 0.5, \mathcal{G}_2 = 0.5 + \mathrm{i}$ to $\mathcal{G}_1 = 0.5 + \mathrm{i}, \mathcal{G}_2 = 0.5$ for the same situation as considered for Fig. 8.6(a). Comparison of Figs. 8.6(a) and 8.6(b) clearly points to the occurrence of a significant decrement in energy loss with the incorporation of an imaginary part to the porous effect parameter of the first porous barrier for the situation when the first porous barrier touches the floating ice-sheet. This is exactly the opposite of the observation from comparison of Fig. 8.5(a,b).

In Fig. 8.7(a,b), the effect of angle of incidence is investigated when both the barriers are submerged in the water region. In this case, the following values of structural parameters are taken: $\mathcal{G}_1 = 0.5 = \mathcal{G}_2$, $d_2 = d_4 = 0.2h$, $d_1 = d_3 = d_4 + 0.5h$. It is noticed that the optima in wave reflection take place in connection with the case of normal wave incidence. Certain periodic nature in wave reflection is found in all the graphs corresponding to higher values of angle of incidence θ resulting in lower frequency of oscillation. Further, it is observed from the figures that certain oscillatory patterns are followed by the reflection coefficient and transmission coefficient for different values of θ. It is important to note that, with the barriers placed closer to each other, the reflection coefficient shows

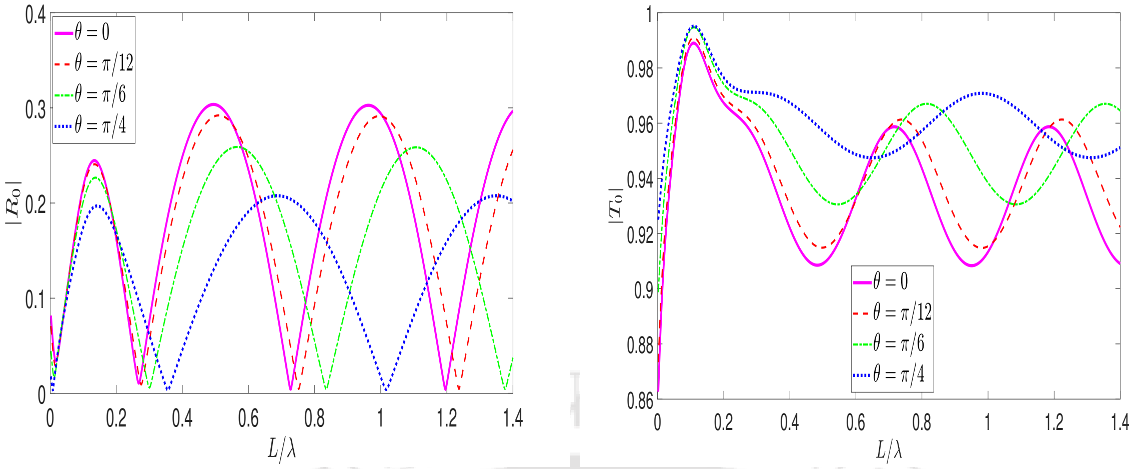

(a) (b)

Figure 8.7: Effect of (a) reflection coefficient $|R_0|$ and (b) transmission coefficient $|T_0|$ versus L/λ for different values of angle of incidence with $\mathcal{G}_1 = 0.5 = \mathcal{G}_2$, $d_2 = d_4 = 0.2h$, $d_1 = d_3 = d_4 + 0.5h$, $Gh = 0.5$ and $N = 13$

a small magnitude of oscillation, but the analogous transmission coefficient happens to be reasonably high – the occurrence of which can be attributed to the inefficiency of the second porous barrier for such a location of the barriers.

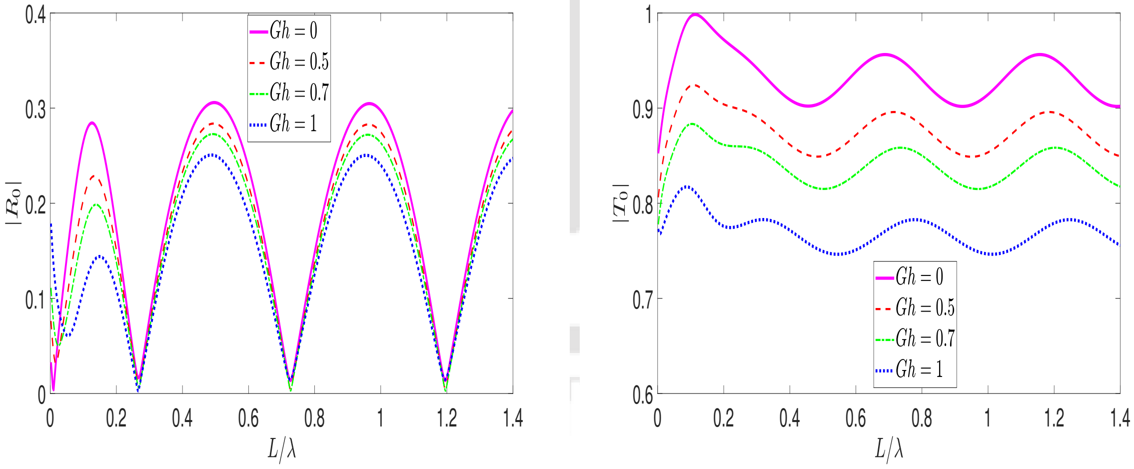

(a) (b)

Figure 8.8: Effect of (a) reflection coefficient $|R_0|$ and (b) transmission coefficient $|T_0|$ versus L/λ for different values of porosity Gh of the sea-bed with $\mathcal{G}_1 = 0.5, \mathcal{G}_2 = 0.5$, $d_3 = d_4 + 0.5h$, $d_1 = 0.5h$, $d_2 = 0$, $\theta = 0^0$ and $N = 13$

Figures 8.8(a,b) and 8.9, respectively, present plots of the reflection and transmission coefficients, and energy loss versus L/λ, for different sets of values of porosity Gh of the sea-bed. Here, the following parameter values are considered: $\mathcal{G}_1 = 0.5 = \mathcal{G}_2$, $d_2 = d_4 =$

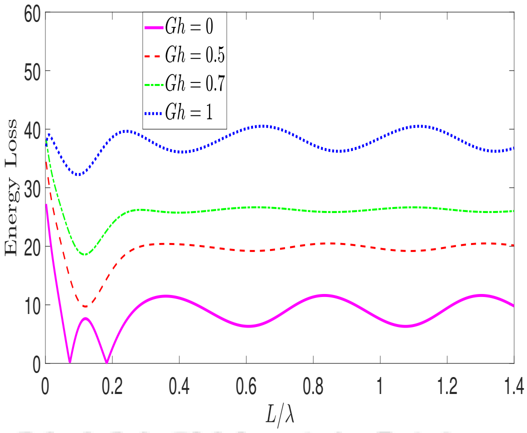

Figure 8.9: Energy loss (in %) for different values of porosity Gh of the sea-bed with $\mathcal{G}_1 = 0.5, \mathcal{G}_2 = 0.5$, $d_3 = d_4 + 0.5h$, $d_1 = 0.5h$, $d_2 = 0$, $\theta = 0^0$ and $N = 13$

$0.2h$, $d_1 = d_3 = d_4 + 0.5h$. Due to the real porosity of the sea-bed, nearly zero reflection and full transmission may occur. Figure 8.8 shows that the reflection coefficient and transmission coefficient take decreasing values corresponding to an increase in Gh. This happens because the wave energy also gets dissipated by the barriers and the sea-bed. The same feature was observed in Behera et al. [4] while considering water wave scattering by a floating plate over a porous sea-bed. However, Fig. 8.9 depicts that the energy loss is higher for higher values of porosity Gh of the porous sea-bed. This is due to the fact that when the wave passes through the porous barriers, a large amount of the wave energy gets dissipated by the sea-bed.

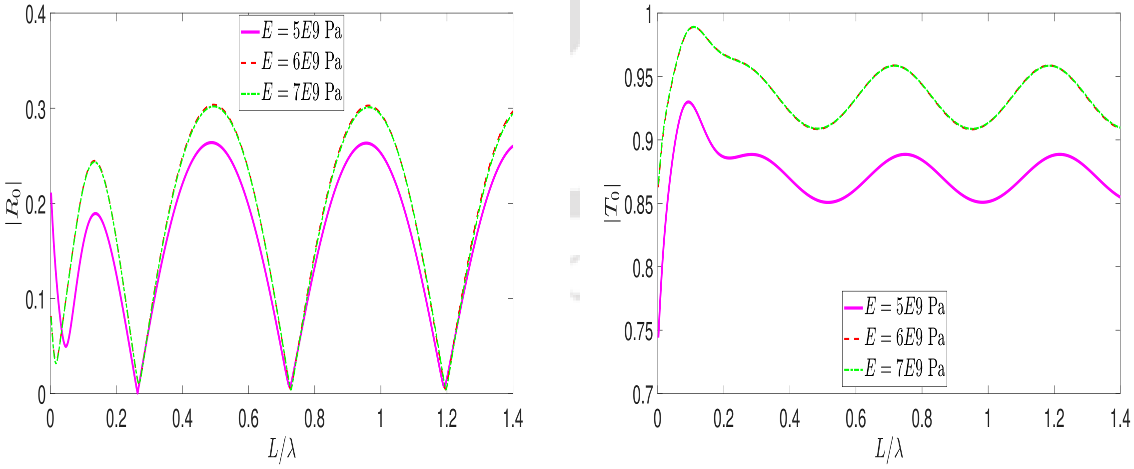

(a) (b)

Figure 8.10: Effect of (a) reflection coefficient $|R_0|$ and (b) transmission coefficient $|T_0|$ versus L/λ for different values of Young's modulus E of the ice-sheet with $\mathcal{G}_1 = 0.5 = \mathcal{G}_2$, $d_2 = d_4 = 0.2h$, $d_1 = d_3 = d_4 + 0.5h$, $Gh = 0.5$ and $N = 13$

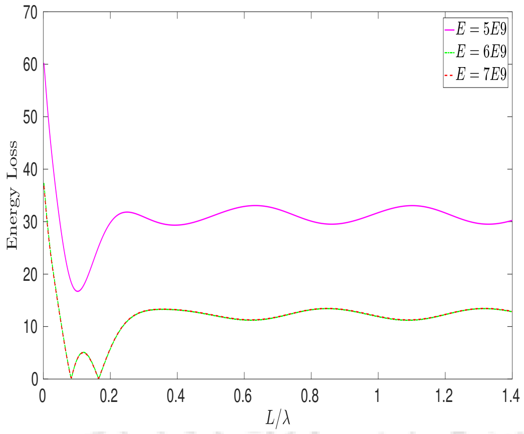

Figure 8.11: Energy loss (in %) for different values of Young's modulus E of the ice-sheet with $\mathcal{G}_1 = 0.5 = \mathcal{G}_2$, $d_2 = d_4 = 0.2h$, $d_1 = d_3 = d_4 + 0.5h$, $Gh = 0.5$ and $N = 13$

In Fig. 8.10(a,b) and 8.11, the reflection and transmission coefficients and energy loss are plotted against L/λ for various values of Young's modulus E of the floating ice-sheet. This time the values $\mathcal{G}_1 = 0.5 = \mathcal{G}_2$, $d_2 = d_4 = 0.2h$, $d_1 = d_3 = d_4 + 0.5h$ are considered. Figure 8.10(a) shows that the reflection coefficient takes increasing values corresponding to an increase in Young's modulus E of the floating ice-sheet. Furthermore, transmission coefficient also increases corresponding to an increase in E. From Fig. 8.11, it is observed that energy loss or energy dissipation decreases with an increment in E. According to the increment of E, the floating ice-sheet becomes more rigid and consequently, the wave cannot penetrate the floating ice-sheet and therefore, a very small amount of incident wave energy is transferred to the floating ice-sheet. This happens due to the presence of the porous sea-bed unlike the case of impermeable bed since wave energy dissipation by a porous medium is much more as compared to the energy dissipation by an elastic/flexible structure. Consequently, a moderate elasticity E of the floating ice-sheet is considered to be helpful for use in coastal engineering for wave attenuation.

Figure 8.12(a,b) shows the effect of hydrodynamic forces F_1 on the first porous barrier and F_2 on the second porous barrier plotted against L/λ for different values of porosity Gh of the sea-bed, where the parameter values are considered as $\mathcal{G}_1 = 0.5 = \mathcal{G}_2$, $d_2 = d_4 = 0.2h$, $d_1 = d_2 + 0.5h$, $d_3 = d_4 + 0.5h$. This figure demonstrates that the hydrodynamic wave force acting on the barriers takes decreasing values when the value of Gh increases. This is due to the reduction in reflection of waves with an increase in the value of Gh as observed in Fig. 8.8. But it is observed from Fig. 8.12 that the hydrodynamic forces are lower for moderate values of the porosity parameter of the sea-bed. Thus, it is concluded that a suitable sea-bed porosity is required to reduce the waveload on the barriers such that the barriers become more stable and attenuate the wave energy.

Figure 8.13(a) shows the effect of hydrodynamic force F_1 on the first porous barrier

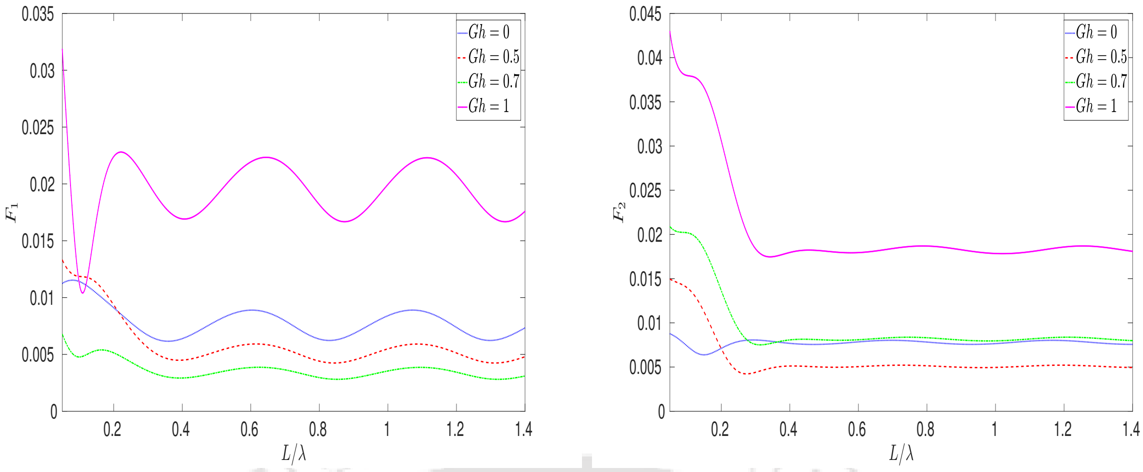

(a) (b)

Figure 8.12: Effect of (a) force F_1 on the first barrier and (b) force F_2 on the second barrier versus L/λ for different values of porosity parameter Gh of the sea-bed with $\mathcal{G}_1 = 0.5, \mathcal{G}_2 = 0.5$, $d_3 = d_4 + 0.5h$, $d_1 = d_2 = 0.2h$, $\theta = 0^0$ and $N = 13$

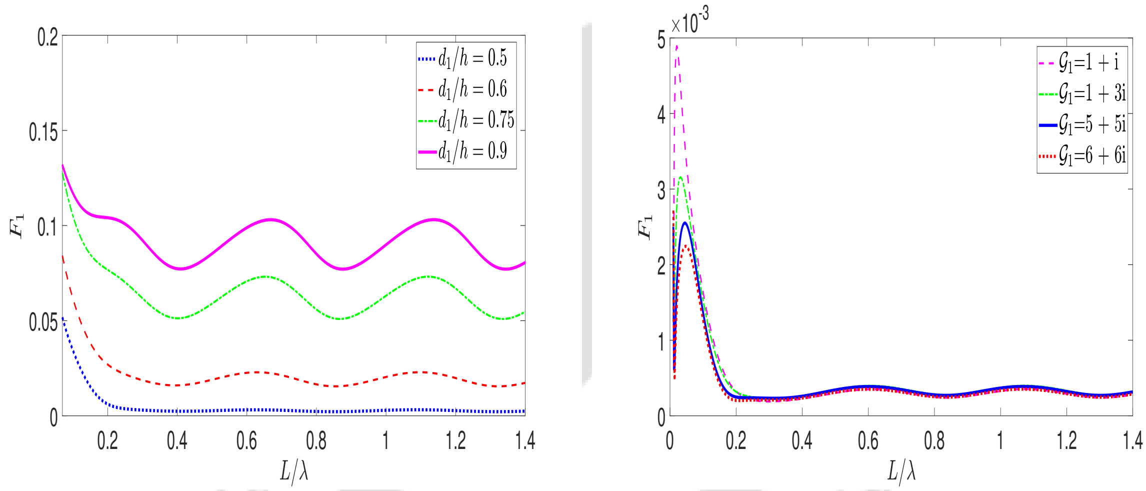

(a) (b)

Figure 8.13: Effect of force F_1 versus L/λ on the first barrier for (a) different values of d_1/h and (b) different values of $\mathcal{G}_1$

plotted against L/λ for different values of length of the first barrier, i.e., for d_1/h, where the parameter values are considered as $\mathcal{G}_1 = 0.5 = \mathcal{G}_2$, $d_2 = 0$, $d_4 = 0.2h$, $d_3 = d_4 + 0.5h$. This figure demonstrates that the hydrodynamic wave force acting on the barrier takes increasing values when the value of d_1/h increases. An oscillatory pattern in the wave force is observed corresponding to an increase in the length of the first barrier. However, by comparing it with Fig. 8.4(a), it is worthwhile to note that the optimum values in reflection coefficient are associated with the optimum values in the hydrodynamic wave forces acting on the barriers. In Fig. 8.13(b), the effect of the hydrodynamic force on the first porous barrier is plotted against L/λ for different values of porous-effect parameter $\mathcal{G}_1$ of the first barrier. Here, the following parameter values are taken: $\mathcal{G}_2 = 0.5$, $d_2 = 0$, $d_1 = 0.5h$, $d_4 = 0.2h$, $d_3 = d_4 + 0.5h$. It can be observed that, as we keep on increasing the values of $\mathcal{G}_1$, we observe a reduction in the values of the wave force. Here, the wave force follows an oscillatory nature corresponding to various values of $\mathcal{G}_1$. The wave force acting on the first barrier reduces because of the increment in wave energy dissipation and transmission by the porous barrier possessing greater porosity. Thus, it can be concluded that the positioning of the barriers in an appropriate manner is very essential in order to reduce the waveload and create a tranquility zone.

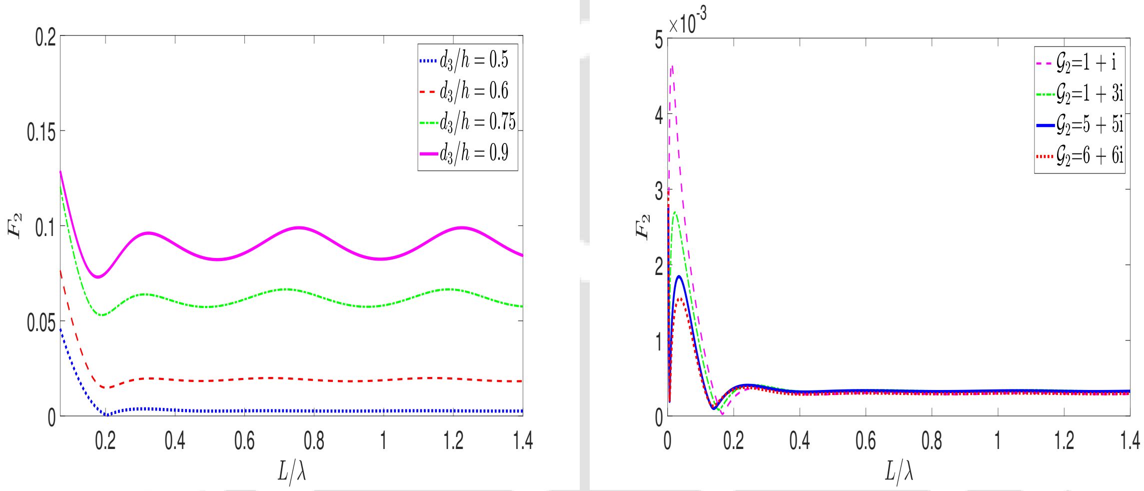

(a) (b)

Figure 8.14: Effect of force F_2 versus L/λ on the second barrier for (a) different values of d_3/h and (b) different values of $\mathcal{G}_2$

In Fig. 8.14(a), the effect of hydrodynamic force F_2 on the second porous barrier is plotted against L/λ for different values of the length of the second barrier, i.e., for d_3/h, where the parameter values are considered as $\mathcal{G}_1 = 0.5 = \mathcal{G}_2$, $d_2 = 0.2h$, $d_1 = d_2 + 0.5h$, $d_4 = 0$. Figure 8.14(a) shows that the wave force takes increasing values corresponding to an increase in the values of d_3/h. An oscillatory behaviour in the wave force is observed corresponding to an increase in the length of the second barrier. In Fig. 8.14(b), the effect of the hydrodynamic force on the second porous barrier is plotted against L/λ for different values of porous-effect parameter $\mathcal{G}_2$ of the second barrier. In this case, the following parameter values are taken: $\mathcal{G}_1 = 0.5$, $d_2 = 0.2h$, $d_1 = d_2 + 0.5h$, $d_3 = 0.5h$, $d_4 = 0$. A similar pattern as in Fig. 8.13(b) is also noticed in Fig. 8.14(b) which demonstrates the general pattern of wave force, i.e., the wave force reduces corresponding to an increase in the values of porous-effect parameter of the second barrier due to an increment in wave energy dissipation and transmission by the barrier. A similar phenomenon of wave trapping by dual porous barriers situated near a wall was also observed in the work of Kaligatla et al. [44] .

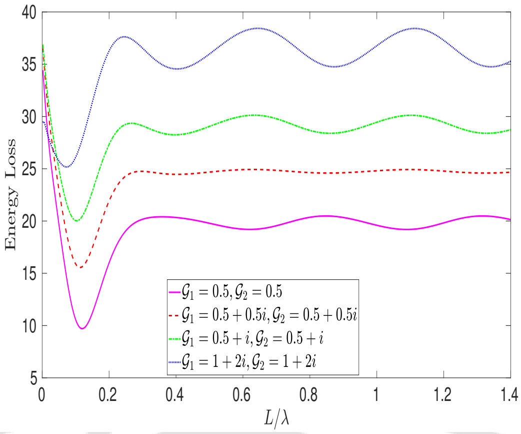

Figure 8.15: Energy loss (in %) versus L/λ for various porosities of the barriers with $d_2 = d_4 = 0.2h$, $d_1 = d_3 = d_4 + 0.5h$, $Gh = 0.5$, $\theta = 0^0$ and $N = 13$

Figure 8.15 shows the energy loss plotted against L/λ for various values of porous-effect parameters of both barriers. The values $d_2 = d_4 = 0.2h$, $d_1 = d_2 + 0.5h$, $d_3 = d_4 + 0.5h$, $Gh = 0.5$ are considered for computational purpose. Here, the energy loss follows a certain oscillatory pattern corresponding to increasing values of $\mathcal{G}_1$ and $\mathcal{G}_2$. It shows that energy loss increases corresponding to increasing values of $\mathcal{G}_1$ and $\mathcal{G}_2$. The rate of energy loss or dissipation of energy increases when the inertial effects of the barriers increase. It may be concluded that moderate values of the porous-effect parameter of the porous barriers are to be chosen in a suitable manner for wave energy dissipation. Overall, it can be inferred that if the porous barriers of reasonably greater height with moderate porosity are closer to the porous sea-bed, then energy dissipation is higher, and this model can be considered to be very efficient for various applications in coastal engineering.

Conclusion

In this chapter, using linearized water wave theory, we take up the problem of oblique flexural gravity wave scattering by two submerged porous barriers of different porosity located above a porous sea-bed. Results are computed and examined for the reflection and transmission coefficients, energy loss, hydrodynamic force to exhibit the effects of the wave and various structural parameters. From all the graphical results, the following important observations are noted:

- The porosity of the sea-bed is responsible for a reasonable amount of the wave energy getting dissipated.

- The study reveals that, for a fixed submergence depth of one of the porous barriers, lower reflection and higher transmission are acquired corresponding to an increment of the inertial effect of the porous barrier.
- In the presence of the floating ice-sheet, a small portion of energy loss takes place as a consequence of the interference of the incident and reflected waves while another portion of the wave energy is dissipated when it passes through the porous barriers. Therefore, a moderate plate elasticity can be considered to be helpful for use in coastal engineering for wave attenuation.
- The wave force acting on either of the porous barriers takes increasing values when the length of the barrier is increased.
- The wave force acting on the barriers decreases because of the increment in wave energy dissipation and transmission by the porous barrier of higher porosity.
- The occurrence of maximum energy loss or energy dissipation is observed for the case of submerged porous barriers with moderate porosity of greater height placed closer to the porous sea-bed.

CHAPTER 9

SUMMARY AND FUTURE DIRECTIONS

This chapter is devoted to a brief summary of the results highlighting the contributions made by this thesis. It also provides information for the scope of possible extensions of the present work and future investigations.

9.1 Summary

In this thesis, the scattering of a train of water waves by a small undulation of an elastic sea-bed in a two-layer fluid and also the interaction of water waves with dual submerged porous barriers in a homogeneous fluid are investigated by using linear water wave theory.

Chapter 2 is concerned with the investigation of the problem of propagation of oblique incident water waves over a small bottom undulation in a two-layer fluid over an elastic sea-bed of finite depth by assuming that the upper layer is free to the atmosphere. Following the Euler-Bernoulli beam equation, the elastic sea-bed is approximated as a thin elastic plate. Applying perturbation analysis, which involves a small parameter δ present in the representation of the small undulation of the elastic sea-bed, the boundary value problems are formulated which are satisfied by the velocity potential for the scattering of waves by a small undulating topography. The solutions are obtained by using Fourier transform technique. The corresponding reflection and transmission coefficients, which involve a shape function $b(x)$ for the sea-bed, are obtained by the application of residue theorem. It is observed that the reflected and transmitted energy corresponding to both free surface mode and interfacial mode increases when the elasticity of the sea-bed is increased. The transfer of incident wave energy of the smaller mode (interfacial mode) to the reflected and transmitted energy of the higher mode (free-surface mode) is feasible for all possible incident angles, but the energy transfer from the higher mode to the lower mode is possible only for the case when the angle of incidence is slightly less than the critical angle.

In **Chapter 3**, the previous work in Chapter 2 is extended to the problem in which the upper fluid is bounded above by a rigid lid, which replaces the free surface, and the lower fluid is bounded by an elastic bottom surface having a small undulation. The first-order corrections of reflection and transmission coefficients are evaluated by the use of Fourier transform technique. To evaluate these coefficients, different shape functions are considered in this chapter and the results are best presented graphically. We observe that a large amount of reflection of the incident wave energy is produced during the bed-interface interaction when the ratio of the ripple wavenumber of the bottom undulation and the interface wavenumber becomes very close to two, i.e., for the case of Bragg resonance. Also, it is noted that the elastic sea-bed does not show any significant effect on the reflected energy due to the bottom undulation described by two patches of two different wavenumbers instead of the one with one wavenumber.

Chapter 4 is concerned with the investigation of the problem of scattering of normal incident water waves by a small undulation located on an elastic sea-bed in a two-layer fluid in an ocean which is covered by a floating ice-sheet. Using the same mathematical procedure applied in Chapter 2, the the boundary value problems are solved which are satisfied by the velocity potentials for the scattering of waves by small undulating topography. The associated reflection and transmission coefficients are computed by carrying out appropriate integration for integrals containing a shape function depicting the sea-bed undulation. The complex resonant interactions are demonstrated concerning the wave propagation in an ice-covered two-layer fluid flowing over a rippled elastic sea-bed as a result of the action of the flexural and interfacial modes. It is observed that the conversion of incident wave energy to the reflected and transmitted energy takes place between the higher mode (interfacial mode) and the smaller mode (flexural mode) because of the non-zero values of the reflection and transmission coefficients arising out of the flexural wave movement and interfacial wave influence in the fluid region. For an interfacial wave mode, the reflection corresponding to the flexural wave influence and interfacial wave movement is not influenced by the variations in the elastic parameter of the floating ice-sheet.

Chapter 5 is concerned with the problem of oblique water wave scattering by two fully submerged thin vertical porous barriers of different heights located above a porous sea-bed in an infinite channel of constant depth. The porous barriers are assumed to follow the theory of thin plates and the wave propagation through the porous structure follows porous wave-maker theory. Time-harmonic propagating waves propagate with exactly one wavenumber along the free surface for any given frequency. The reflection and transmission coefficients as well as the energy loss are computed and those are examined corresponding to various values of the parameters such as the porous-effect parameter, the submergence depth of barriers from free surface, the angle of incidence, the porosity of the sea-bed. It is demonstrated that a periodic oscillation is evident in all the graphs. For fixed properties of the first porous barrier, the energy dissipation is less as compared to the energy dissipation due to fixed properties of the second porous barrier. Higher energy loss can be obtained by attenuating the inertial effect of the submerged porous barriers. It is observed that the reflection coefficient increases and transmission coefficient decreases corresponding to an increase in porosity of the sea-bed. Maximum energy loss is observed when the porous barriers of greater height just touch the porous sea-bed. Therefore, it can be inferred that a suitable positioning of the barriers is required in order to reduce the waveload and to create a tranquility zone.

In **Chapter 6**, the previous work in Chapter 5 is extended to a problem where the porous sea-bed is replaced by an elastic sea-bed. The complete analytical solution, under the assumption of linear water wave theory and structural response, is acquired by employing eigenfunction expansion and least square method for the problem of flexural gravity waves interacting with submerged porous barriers. The effect of various parameters such as the porous effect parameters, the height of the porous barriers, the distance from the free surface, the elasticity of the sea-bed on scattering phenomenon is studied graphically. Wave energy dissipation due to the fixed location of first porous barrier is less in comparison to that due to the fixed location of the second porous barrier. It is observed that, when both submerged porous barriers are nearer to the elastic sea-bed, a sufficient amount of the wave energy concentrated in the vicinity of the elastic sea-bed undergoes reflection by the barrier while some amount of the wave energy gets dissipated when the waves pass through the porous barriers. An important conclusion that can be drawn is that if the porous barriers of reasonably greater height with moderate porosity are closer to the elastic sea-bed, then energy dissipation is higher, and this model can be considered to be very efficient for various applications in coastal engineering.

Chapter 7 deals with the investigation of scattering of oblique flexural gravity waves by two totally submerged vertical porous barriers, placed at some distance from each other, in a homogenous fluid. Here a thin ice-sheet, replacing the usual free surface, is considered as the upper surface and the sea-bed is considered as an impermeable one. Computation for the reflection and transmission coefficients, energy loss and wave forces is carried out and discussed for different parameter values corresponding to the ice-sheet, porous barriers, angle of incidence. It is observed that, due to an increase in the inertial effect of the porous barrier, the minima in wave reflection occur. The vertical porous barriers are found to dissipate a significant portion of the wave energy when an increase in the inertial effect of the porous barriers is affected. The hydrodynamic forces on the barriers also follow an oscillatory pattern and it increases when the length of the barrier is increased. In the presence of the floating ice-sheet, a sufficient portion of energy loss occurs because of the interference of the incident and reflected waves, and another part of the wave energy gets dissipated while passing through the porous barrier.

In **Chapter 8**, the previous work in Chapter 7 is extended to a problem where the impermeable sea-bed is replaced by a porous sea-bed. The same mathematical procedure as applied in Chapter 7 is used here to get the analytical solution of the scattering problem. The reflection and transmission coefficients, energy loss and wave forces are plotted for different parameter values corresponding to the ice-sheet, the porous sea-bed and the porous barrier. When the length of the barriers increases, a major part of wave energy is reflected back by the barriers. One interesting observation is that the interchange of the positions of the barriers does not affect the transmission coefficient. Due to the real porosity of the sea-bed, nearly zero reflection and full transmission may occur. Energy loss is higher for the higher values of porosity of the sea-bed. Due to the presence of the porous sea-bed, a very small amount of incident wave energy is transferred to the floating ice-sheet. The wave force acting on either of the porous barriers takes increasing values when the length of the barrier is increased, and reducing values because of the increment in wave energy dissipation and transmission by the porous barrier of higher porosity.

9.2 Future work

We now present some informal observations pertaining to the possible extensions of our present results to different problems. We briefly outline some interesting problems which may be taken up in future.

In the first part of this thesis, we examine the problem of water wave scattering by a small bottom undulation on an elastic sea-bed in a two-layer fluid with layer-wise different densities where we restrict the uppermost layer to be covered by either a free surface or a rigid lid or an ice-sheet. Its extension to a three-layer fluid may also be considered.

It is observed that most of the sea-beds along the coast experience shear stress, strain and pressure when gravity waves propagate over them due to their permeable and elastic nature. The sea-bed may be considered as a viscoelastic or poroelastic one. The problems considered in Chapters 2, 3 and 4 with an elastic sea-bed may be revisited by considering a viscoelastic or a poroelastic sea-bed, which represents a formidable mathematical problem and a reasonable physical scenario.

In the later part of the thesis, we investigate water wave scattering by a dual submerged porous barrier in a homogeneous fluid subject to different kinds of upper and lower surface conditions. It is very likely that a physical situation involving a two-layer fluid will depict a more realistic scenario. The problems carried out here may be extended for the case of a two-layer fluid.

BIBLIOGRAPHY

[1] Internet site. https://perminc.com/resources/fundamentals-of-fluid-flow-in-porous-media/chapter-2-the-porous-medium/porosity/.

[2] M.-R. Alam. Broadband cloaking in stratified seas. *Physical Review Letters*, 108, 084502, 2012.

[3] H. F. Bauer. Hydroelastic vibrations in a rectangular container. *International Journal of Solids and Structures*, 17:639–652, 1981.

[4] H. Behera, C. O. Ng, and T. Sahoo. Oblique wave scattering by a floating elastic plate over a porous bed in single and two-layer fluid systems. *Ocean Engineering*, 159:280–294, 2018.

[5] H. Behera and T. Sahoo. Hydroelastic analysis of gravity wave interaction with submerged horizontal flexible porous plate. *Journal of Fluids and Structures*, 54:643–660, 2015.

[6] H. Behera, T. Sahoo, and C. O. Ng. Effect of a submerged porous plate on the hydroelastic response of a very large floating structure. *Journal of Marine Science and Application*, 17:564–577, 2018.

[7] K. A. Belibassakis. Water-wave induced groundwater pressure and flow in variable bathymetry regions and sandy beaches by an enhanced coupled-mode model. *Ocean Engineering*, 47:104–118, 2012.

[8] L. G. Bennetts. Wave Scattering by Ice Sheets of Varying Thickness. *PhD thesis, University of Reading, United Kingdom*, 2007.

[9] L. G. Bennetts, N. R. T. Biggs, and D. Porter. A multi-mode approximation to wave scattering by ice sheets of varying thickness. *Journal of Fluid Mechanics*, 579:413–443, 2007.

[10] J. Bhattacharjee, D. Karmakar, and T. Sahoo. Transformation of flexural gravity waves by heterogeneous boundaries. *Journal of Engineering Mathematics*, 62:173–188, 2007.

[11] L. Bjerrum. Geotechnical problems involved in foundations of structures in the North Sea. *Geotechnique*, 23:319–358, 1973.

[12] P. G. Chamberlain and D. Porter. Wave scattering in a two-layer fluid of varying depth. *Journal of Fluid Mechanics*, 524:207–228, 2005.

[13] H. Chen, R. P. Gilbert, and P. Guyenne. Dispersion and attenuation in a porous viscoelastic model for gravity waves on an ice-covered ocean. *European Journal of Mechanics / B Fluids*, 78:88–105, 2019.

[14] X. Chen, Y. Wu, W. Cui, and J. J. Jensen. Review of hydroelasticity theories for global response of marine structures. *Ocean Engineering*, 33:439–457, 2006.

[15] M. Chiba, H. Watanabe, and H. F. Bauer. Hydroelastic coupled vibrations in a cylindrical container with a membrane bottom containing liquid with surface tension. *Journal of Sound and Vibration*, 251(4):717–740, 2002.

[16] I. H. Cho and M. H. Kim. Interaction of a horizontal flexible membrane with oblique incident waves. *Journal of Fluid Mechanics*, 367:139–161, 1998.

[17] A. T. Chwang. A porous wavemaker theory. *Journal of Fluid Mechanics*, 132:395–406, 1983.

[18] S. Corvaro, A. Mancinelli, M. Brocchini, E. Seta, and C. Lorenzoni. On the wave damping due to a permeable seabed. *Coastal Engineering*, 57:1029–1041, 2010.

[19] R. Cox, P. Horton, and S. Bettington. Double walled, low reflection wave barriers. *In Proceedings of the 26th Coastal Engineering Conference, ASCE, Copenhagen, Denmark*, pages 2221–2234, 1998.

[20] W. Craig, P. Guyenne, and C. Sulem. Water waves over a random bottom. *Journal of Fluid Mechanics*, 640:79–107, 2009.

[21] W. Craig, P. Guyenne, and C. Sulem. Internal waves coupled to surface gravity waves in three dimensions. *Communications in Mathematical Sciences*, 13:893–910, 2015.

[22] A. D. D. Craik. The origins of water wave theory. *Annual Review of Fluid Mechanics*, 36:1–28, 2004.

[23] R. A. Dalrymple and P. A. Martin. Wave diffraction through offshore breakwater. *Journal of Waterway, Port, Coastal, and Ocean Engineering*, 116(10):727–741, 1990.

[24] D. Das, B. N. Mandal, and A. Chakrabarti. Energy identities in water wave theory for free-surface boundary condition with higher-order derivatives. *Fluid Dynamics Research*, 40:253–272, 2008.

[25] S. Das, H. Behera, and T. Sahoo. Flexural gravity wave motion over poroelastic bed. *Wave Motion*, 63:135–148, 2016.

[26] S. Das and S. N. Bora. Oblique water wave damping by two submerged thin vertical porous plates of different heights. *Computational and Applied Mathematics*, 37:3759–3779, 2018.

[27] A. G. Davies. The reflection of wave energy by undulations on the sea bed. *Dynamics of Atmospheres and Oceans*, 6:207–232, 1982.

[28] A. G. Davies and A. D. Heathershaw. Surface-wave propagation over sinusoidally varying topography. *Journal of Fluid Mechanics*, 144:419–443, 1984.

[29] T. H. Dawson. Wave propagation over a deformable sea floor. *Ocean Engineering*, 5(4):227–234, 1978.

[30] P. Devillard, F. Dunlop, and B. Souillard. Localization of gravity waves on a channel with a random bottom. *Journal of Fluid Mechanics*, 186:521–538, 1988.

[31] E. Eyov, A. Klar, U. Kadri, and M. Stiassnie. Progressive waves in a compressible-ocean with an elastic bottom. *Wave Motion*, 50:929–939, 2013.

[32] C. Fox and V. A. Squire. Reflection and transmission characteristics at the edge of shore fast sea ice. *Journal of Geophysical Research*, 95(C7):1629–1639, 1990.

[33] C. Fox and V. A. Squire. Coupling between an ocean and an ice shelf. *Annals of Glaciology*, 15:101–108, 1991.

[34] C. Fox and V. A. Squire. On the oblique reflexion and transmission of ocean waves at shore fast sea ice. *Philosophical Transactions of the Royal Society London A*, 347:185–218, 1994.

[35] Z. Gu and H. Wang. Gravity waves over porous bottoms. *Coastal Engineering*, 15:497–524, 1991.

[36] E. Guazzelli, E. Guyon, and B. Souillard. On the localization of shallow water waves by a random bottom. *Journal of Physics Letters*, 44:837–841, 1983.

[37] E. Guazzelli, V. Rey, and M. Belzons. Higher-order bragg reflection of gravity surface waves by periodic beds. *Journal of Fluid Mechanics*, 245:301–317, 1992.

[38] S. Gupta and R. Gayen. Scattering of oblique water waves by two thin unequal barriers with non-uniform permeability. *Journal of Engineering Mathematics*, 112:37–61, 2018.

[39] P. Guyenne and D. P. Nicholls. A high-order spectral method for nonlinear water waves over moving bottom topography. *SIAM Journal on Scientific Computing*, 30:81–101, 2007.

[40] U. L. M. Hassan, M. H. Meylan, and M. A. Peter. Water-wave scattering by submerged elastic plates. *The Quarterly Journal of Mechanics and Applied Mathematics*, 62(3):321–344, 2009.

[41] A. D. Heathershaw. Seabed-wave resonance and sand bar growth. *Nature*, 296:343–345, 1982.

[42] R. A. Ibrahim. Liquid Sloshing Dynamics: Theory and Applications. *Cambridge University Press, Cambridge, New York*, 2005.

[43] R. Kaligatla, S. Koley, and T. Sahoo. Trapping of surface gravity waves by a vertical flexible porous plate near a wall. *Zeitschrift für Angewandte Mathematik and Physik*, 66:2677–2702, 2015.

[44] R. Kaligatla, Manisha, and T. Sahoo. Wave trapping by dual porous barriers near a wall in the presence of bottom undulation. *Journal of Marine Science and Application*, 16:286–297, 2017.

[45] D. Karmakar, J. Bhattacharjee, and T. Sahoo. Oblique flexural gravity-wave scattering due to changes in bottom topography. *Journal of Engineering Mathematics*, 66:325–341, 2010.

[46] S. E. Kassem. Wave source potentials for two superposed fluids, each of finite depth. *Mathematical Proceedings of the Cambridge Philosophical Society*, 100:595–599, 1986.

[47] R. B. Kelman and A. K. Chester. Least square approximations for dual trigonometric series. *Glasgow Mathematical Journal*, 14:111–119, 1973.

[48] A. Kohout, M. Williams, S. Dean, and M. Meylan. Storm-induced sea ice breakup and the implications for ice extent. *Nature*, pages 604–607, 2014.

[49] S. Koley, R. B. Kaligatla, and T. Sahoo. Oblique wave scattering by a vertical flexible porous plate. *Studies in Applied Mathematics*, 135(1):1–34, 2015.

[50] S. Koley and T. Sahoo. Oblique wave trapping by vertical permeable membrane barriers located near a wall. *Journal of Marine Science and Application*, 16:490–501, 2017.

[51] S. Koley and T. Sahoo. Scattering of oblique waves by permeable vertical flexible membrane wave barriers. *Applied Ocean Research*, 62:156–168, 2017.

[52] M. Lamas-Pardoa, G. Iglesias, and L. Carral. A review of very large floating structures (VLFS) for coastal and offshore uses. *Ocean Engineering*, 109:677–690, 2015.

[53] H. Lamb. Hydrodynamics. ***6****th edn., Cambridge University Press, Cambridge*, 1932.

[54] A. Li, Y. Liu, and H. Li. Accurate solutions to water wave scattering by vertical thin porous barriers. *Mathematical Problems in Engineering*, Article ID 985731:11 pages, 2015.

[55] J. Li and D. S. Jeng. Response of a porous sea-bed around breakwater heads. *Ocean Engineering*, 35:864–886, 2008.

[56] C. M. Linton and J. R. Cadby. Scattering of oblique waves in a two-layer fluid. *Journal of Fluid Mechanics*, 461:343–364, 2002.

[57] C. M. Linton and M. McIver. The interaction of waves with horizontal cylinders in two-layer fluids. *Journal of Fluid Mechanics*, 304:213–229, 1995.

[58] Y. Liu and Y. Li. Wave interaction with a wave absorbing double curtain-wall breakwater. *Ocean Engineering*, 38(10):1237–1245, 2011.

[59] P. Maiti and B. N. Mandal. Scattering of oblique waves by bottom undulations in a two-layer fluid. *Journal of Applied Mathematics and Computing*, 22:21–39, 2006.

[60] P. Maiti and B. N. Mandal. Water wave scattering by bottom undulations in an ice-covered two-layer fluid. *Applied Ocean Research*, 30:264–272, 2008.

[61] P. Maiti and B. N. Mandal. Wave scattering by a thin vertical barrier submerged beneath an ice-cover in deep water. *Applied Ocean Research*, 32:367–373, 2010.

[62] P. Maiti and B. N. Mandal. Water wave scattering by an elastic plate floating in an ocean with a porous bed. *Applied Ocean Research*, 47:73–84, 2014.

[63] W. Mallard and R. Dalrymple. Water waves propagating over a deformeable bottom. *Offshore Technology Conference, Houston, Texas*, pages 141–146, 1977.

[64] S. R. Manam and R. B. Kaligatla. Effect of a submerged vertical barrier on flexural gravity waves. *International Journal of Engineering Science*, 49:755–767, 2011.

[65] S. R. Manam and M. Sivanesan. Scattering of water waves by vertical porous barriers: An analytical approach. *Wave Motion*, 67:89–101, 2016.

[66] S. C. Martha, S. N. Bora, and A. Chakrabarti. Oblique water wave scattering by small undulation on a porous sea-bed. *Applied Ocean Research*, 29:86–90, 2007.

[67] H. Mase and K. Takeba. Bragg scattering of waves over porous rippled bed. *In Proceedings of 24th ICCE. Kobe (Japan), ASCE*, pages 635–649, 1994.

[68] C. C. Mei. Resonant reflection of surface water waves by periodic sandbars. *Journal of Fluid Mechanics*, 152:315–335, 1985.

[69] J. W. Miles. Oblique surface wave diffraction by a cylindrical obstacle. *Dynamics of Atmospheres and Oceans*, 6:121–123, 1981.

[70] S. Mohapatra. Effects of elastic bed on hydrodynamic forces for a submerged sphere in an ocean of finite depth. *Zeitschrift für Angewandte Mathematik and Physik*, 68(91), 2017.

[71] S. Mohapatra and S. N. Bora. Oblique water wave scattering by bottom undulation in a two-layer fluid flowing through a channel. *Journal of Marine Science and Application*, 11:276–285, 2012.

[72] S. Mohapatra and S. N. Bora. Oblique wave scattering by an impermeable ocean-bed of variable depth in a two-layer fluid with ice cover. *Zeitschrift für Angewandte Mathematik and Physik*, 63:879–903, 2012.

[73] S. C. Mohapatra and T. Sahoo. Surface gravity wave interaction with elastic bottom. *Applied Ocean Research*, 33:31–40, 2011.

[74] S. Panda and S. C. Martha. Oblique wave scattering by undulating porous bottom in a two-layer fluid: Fourier transform approach. *Geophysical and Astrophysical Fluid Dynamics*, 108:587–614, 2014.

[75] R. Porter and D. V. Evans. Complementary approximations to wave scattering by vertical barriers. *Journal of Fluid Mechanics*, 294(10):155–180, 1995.

[76] R. Porter and D. Porter. Scattered and free waves over periodic beds. *Journal of Fluid Mechanics*, 483:129–163, 2003.

[77] M. Rahman. Water Waves: Relating Modern Theory to Advanced Engineering Applications. *Clarendon Press, Oxford, UK*, 1995.

[78] S. Rojanakamthorn, M. Isobe, and A. Watanabe. A mathematical model of wave transformation over a submerged breakwater. *Coastal Engineering in Japan*, 32(2):209–234, 1989.

[79] S. Rojanakamthorn, M. Isobe, and A. Watanabe. Modeling of wave transformation on submerged breakwater. *Proceedings 22nd ICCE. ASCE, New York*, pages 1060–1073, 1990.

[80] S. Saha and S. N. Bora. Flexural gravity waves trapped in a two-layer fluid of finite depth. *Applied Ocean Research*, 44:1–12, 2014.

[81] S. Saha and S. N. Bora. Elastic bottom effect on trapped waves in a two-layer fluid. *International Journal of Applied Mechanics*, 7(2):150028 (15 pages), 2015.

[82] T. Sahoo, A. T. Chan, and A. T. Chwang. Scattering of oblique surface waves by permeable barriers. *Journal of Waterway, Port, Coastal, and Ocean Engineering*, 126(4):196–205, 2000.

[83] M. R. Sarangi and S. Mohapatra. Investigation on the effects of versatile deformating bed on a water wave diffraction problem. *Ocean Engineering*, 164:377–387, 2018.

[84] M. R. Sarangi and S. Mohapatra. Hydro-elastic wave proliferation over an impermeable seabed with bottom deformation. *Geophysical and Astrophysical Fluid Dynamics*, 113:303–325, 2019.

[85] A. Sasmal, S. Paul, and S. De. Effect of porosity on oblique wave diffraction by two unequal vertical porous barriers. *Journal of Marine Science and Application*, 18:417–432, 2019.

[86] R. Silva, P. Salles, and A. Palacio. Linear waves propagating over a rapidly varying finite porous bed. *Coastal Engineering*, 44:239–260, 2002.

[87] S. Singla, S. C. Martha, and T. Sahoo. Mitigation of structural responses of a very large floating structure in the presence of vertical porous barrier. *Ocean Engineering*, 165:505–527, 2018.

[88] C. K. Sollitt and R. H. Cross. Wave transmissions through permeable breakwaters. *In: 13th International Conference on Coastal Engineering, Vancouver, Canada, ASCE*, pages 1827–1846, 1972.

[89] S. Som, G. Biswas, and S. Chakraborty. Introduction to Fluid Mechanics and Fluid Machines, Third Edition. *Mc Graw Hill Education*.

[90] V. A. Squire. Synergies between VLFS hydroelasticity and sea ice research. *International Journal of Offshore and Polar Engineering*, 18(3):1–13, 2008.

[91] G. G. Stokes. On the theory of oscillatory waves. *Transactions of the Cambridge Philosophical Society*, 8:441–455, 1847.

[92] I. V. Sturova. Planar problem of hydrodynamic shaking of a submerged body in the presence of motion in a two-layered fluid. *Journal of Applied Mechanics and Technical Physics*, 35:670–679, 1994.

[93] I. V. Sturova. Problems of radiation and diffraction for a circular cylinder in a stratified fluid. *Fluid Dynamics*, 34:521–533, 1999.

[94] P. Wadhams. The Seasonal Ice Zone. *The Geophysics of Sea Ice, Springer. US*, 88:825–991, 1986.

[95] C. M. Wang and Z. Tay. Very large floating structures: applications, research and development. *Procedia Engineering*, 14:62–72, 2011.

[96] E. Watanabe, T. Utsunomiya, and C. M. Wang. Hydroelastic analysis of pontoon-type VLFS: a literature survey. *Engineering Structures*, 26(2):245–256, 2004.

[97] T. D. Williams, L. G. Bennetts, V. A. Squire, D. Dumont, and L. Bertino. Wave-ice interactions in the marginal ice zone. part 1: Theoretical foundations. *Ocean Modelling*, 71:81–91, 2013.

[98] T. D. Williams, P. Rampal, and S. Bouillon. Wave-ice interactions in the neXtSIM sea-ice model. *The Cryosphere*, 11:2117–2135, 2017.

[99] Z. Xin, H. S. Hayley, and C. Sukun. Modeling ocean wave propagation under sea ice covers. *Acta Mechanica Sinica*, 31(1):1–15, 2015.

[100] X. Yu. Diffraction of water waves by porous breakwaters. *Journal of Waterway, Port, Coastal, and Ocean Engineering*, 121(6):275–282, 1995.

[101] X. Yu and A. T. Chwang. Wave induced oscillation in harbor with porous breakwaters. *Journal of Waterway, Port, Coastal, and Ocean Engineering*, 120 (2):125–144, 1994.

[102] A. Zhong and Y. Zhen. Band gaps and localization of water waves over one-dimensional topographical bottoms. *Applied Physics Letters*, 84:2952–2954, 2004.

[103] S. Zhu. Water waves within a porous medium on an undulating bed. *Coastal Engineering*, 42:87–101, 2001.

APPENDIX A

DISCUSSION OF THE ROOTS OF THE DISPERSION RELATION FOR A TWO-LAYER FLUID

We get different dispersion relations while studying the problems of oblique wave scattering over a small undulation located on an elastic sea-bed in a two-layer fluid (Chapters 2-4) under different upper surface boundary conditions. Theoretically it is acceptable that one mode arises due to the bottom elasticity. When we consider an elastic sea-bed in a homogeneous fluid as in Chapter 6, we get two positive real roots from the respective dispersion relations, i.e., two wave modes – one corresponding to the upper surface and another one corresponding to the bottom surface. But for the two-layer fluid case, when we solve the dispersion relation numerically for the problem in Chapter 2, we get one zero root (wavenumber) and two positive real roots (wavenumbers) corresponding to the free-surface and interfacial modes. Earlier, when Maiti and Mandal [59] considered the problem of oblique wave scattering over a small undulation located on a rigid (impermeable) sea-bed with a free-surface in a two-layer fluid, then the dispersion relation corresponding to this problem had exactly two positive real roots. When comparing the solutions of the dispersion relation corresponding to the rigid sea-bed and the elastic sea-bed, one extra root, i.e., the zero root, occurs for the case of the elastic sea-bed. This zero root corresponds to the bottom mode. If we approximate the upper-layer depth (uh_f) and the lower-layer depth (uh_b) by deep water and shallow water approximations, then we can put forward some conclusion about the zero root due to the bottom mode.

First we present the following table which includes nine cases corresponding to different kinds of upper and lower layer and the associated roots of the dispersion relation. Then we analyse the cases pertaining to the relevance of the zero root.

Case	Upper layer (free surface)	Lower layer	Number of +ve real roots	Number of −ve real roots	Number of roots at zero	Number of complex roots $(a+\mathrm{i}b)$
1	Finite	Finite	2	2	1	4
2	Finite	Shallow	2	2	1	4
3	Shallow	Shallow	2	2	1	4
4	Finite	Deep $(\mathrm{Re}(u)>0)$	3	3	0	2 $(\mathrm{Re}(u)>0)$
5	Deep $(\mathrm{Re}(u)>0)$	Deep $(\mathrm{Re}(u)>0)$	3	3	0	2 $(\mathrm{Re}(u)>0)$
6	Shallow	Deep	3	3	0	2
7	Shallow	Finite $(\mathrm{Re}(u)>0)$	2	2	1	4 $(\mathrm{Re}(u)>0)$
8	Deep $(\mathrm{Re}(u)>0)$	Finite	2	2	1	2 $(\mathrm{Re}(u)>0)$
9	Deep $(\mathrm{Re}(u)>0)$	Shallow	2	2	1	2 $(\mathrm{Re}(u)>0)$

Case 1: When the depth of both layers is finite, then the dispersion relation (Eq. (2.11)) has one zero root, which is already discussed in the Chapter 2.

Case 2: For shallow-water approximation of the lower layer fluid (when upper-layer depth is finite), assuming $uh_b \ll 1$, it can be seen that $\tanh(uh_b) \approx uh_b$. Using these assumptions, our dispersion relation can be obtained as

$$\begin{aligned}&K^3uh_b + K^2(Du^4+1-\epsilon K)u + \rho K^3 \tanh uh_f + \rho K^2u^2h_b(Du^4+1-\epsilon K)\tanh uh_f\\&-Ku^3h_b(Du^4+1-\epsilon K) - K^2u - Ku^2(Du^4+1-\epsilon K)\tanh uh_f - K^2u^2h_b\tanh uh_f\\&+u^4h_b(Du^4+1-\epsilon K)\tanh uh_f + Ku^2\tanh uh_f - \rho u^2K\tanh uh_f - \rho u^4h_b\\&\times(Du^4+1-\epsilon K)\tanh uh_f = 0.\end{aligned}$$

This dispersion relation has one zero root and one can see that this zero root occurs due to one of the terms $\tanh uh_f$. It also has four real roots and four complex roots.

Case 3: For shallow-water approximation of both layers of the fluid, assuming $uh_b \ll 1$ and $uh_f \ll 1$, it can be seen that $\tanh(uh_b) \approx uh_b$ and $\tanh(uh_f) \approx uh_f$. Using these assumptions, our dispersion relation can be obtained as

$$\begin{aligned}&K^3uh_b + K^2(Du^4+1-\epsilon K)u + \rho K^3uh_f + \rho K^2u^3h_bh_f(Du^4+1-\epsilon K) - Ku^3h_b\\&(Du^4+1-\epsilon K) - K^2u - Ku^3h_f(Du^4+1-\epsilon K) - K^2u^3h_bh_f + u^5h_bh_f\\&\times(Du^4+1-\epsilon K) + Ku^3h_f - \rho u^3Kh_f - \rho u^5h_bh_f(Du^4+1-\epsilon K) = 0.\end{aligned}$$

The left hand side of the above dispersion relation is a polynomial of order 9. This dispersion relation is a nine-order algebraic equation in wave number u. It is noticed that u is common in all the terms of the above expression from which one can conclude that $u = 0$ is one root of the dispersion relation for this case. Further, it has four positive real roots and four complex roots.

Case 4: For deep-water approximation of the lower layer fluid (when the upper-layer depth is finite), assuming $uh_b \gg 1$, it can be seen that $\tanh(uh_b) \approx 1$. Using these assumptions, our dispersion relation can be obtained as

$$\begin{aligned}&K^3 + K^2(Du^4 + 1 - \epsilon K)u + \rho K^3 \tanh uh_f + \rho K^2 u(Du^4 + 1 - \epsilon K)\tanh uh_f\\&-Ku^2(Du^4 + 1 - \epsilon K) - K^2u - Ku^2(Du^4 + 1 - \epsilon K)\tanh uh_f - K^2u\tanh uh_f\\&+u^3(Du^4 + 1 - \epsilon K)\tanh uh_f + Ku^2\tanh uh_f - \rho u^2 K\tanh uh_f - \rho u^3\\&\times(Du^4 + 1 - \epsilon K)\tanh uh_f = 0.\end{aligned}$$

This dispersion relation has no zero root and one can see that it has three positive real roots and four complex roots.

Case 5: For deep-water approximation of both layers of the fluid, assuming $uh_b \gg 1$ and $uh_f \gg 1$, it can be seen that $\tanh(uh_b) \approx 1$ and $\tanh(uh_f) \approx 1$. Using these assumptions, our dispersion relation can be obtained as

$$\begin{aligned}&K^3 + K^2(Du^4 + 1 - \epsilon K)u + \rho K^3 + \rho K^2 u(Du^4 + 1 - \epsilon K) - Ku^2(Du^4 + 1 - \epsilon K)\\&-K^2u - Ku^2(Du^4 + 1 - \epsilon K) - K^2u + u^3(Du^4 + 1 - \epsilon K) + Ku^2 - \rho u^2 K\\&-\rho u^3(Du^4 + 1 - \epsilon K) = 0.\end{aligned}$$

The left hand side of the above dispersion relation is a polynomial of order 7. This dispersion relation is a seven-order algebraic equation in wavenumber u. It is noticed that $u = 0$ is not a root of the dispersion relation for this case. This dispersion relation has three positive real roots and four complex roots.

Case 6: If we consider the shallow-water approximation of the upper layer fluid and deep-water approximation of the lower layer fluid, then our dispersion relation can be obtained as

$$\begin{aligned}&K^3 + K^2(Du^4 + 1 - \epsilon K)u + \rho K^3 uh_f + \rho K^2 u^2 h_f(Du^4 + 1 - \epsilon K)\\&-Ku^2(Du^4 + 1 - \epsilon K) - K^2u - Ku^3h_f(Du^4 + 1 - \epsilon K) - K^2u^2h_f\\&+u^4h_f(Du^4 + 1 - \epsilon K) + Ku^3h_f - \rho u^3 h_f K - \rho u^4 h_f(Du^4 + 1 - \epsilon K) = 0.\end{aligned}$$

This dispersion relation has no zero root and one can see that it has four real roots and four complex roots.

It is clear from the above cases that the root corresponding to $u = 0$ vanishes when the lower layer depth is very large. In other cases, no matter what the type of approximation is, a root always occurs at $u = 0$. To solidify that the root pertains to the elastic bottom, we compare our dispersion relation with the one due to the rigid ocean bottom. The dispersion relation with a rigid bottom is already available in the literature (see Maiti and Mandal [59]) and the study mentioned the occurrence of two positive real roots (non-zero). The comparison shows one extra root at $u = 0$ and four complex roots of the form $(a + \mathrm{i}b)$ for finite and shallow water approximations in either of the layers. These extra roots are definitely due to the elastic bottom. The contribution from the roots $a + \mathrm{i}b$ can be neglected as its effect can be incorporated in the evanescent part of the wave (Bennetts et al [9]). The other root corresponding to zero does not have any physical meaning to be incorporated in the study and hence deferred as Chapters 2-4 consider finite depth water for numerical computation. As far as the transformation of the root from zero to finite value, it is mainly due to the de-coupling of wave modes in deep water approximation for the lower layer. As the lower layer depth starts increasing, the de-coupling triggers the propagating wave mode in the ocean elastic bottom. Here the internal mode plays a significant role which cannot be explained completely while using linear theory. However, we will try to explain the process to the best of our knowledge for completeness. It is well established in the literature that wave energy can be transferred in the internal mode with the help of bottom undulation and can be proved mathematically using non-linear formulation of the problem. The experimental proof can be found in Alam [2] where the ocean bed is rigid but undulated. Although the said transfer takes place from the surface mode to the internal mode, it is our possible guess that a similar kind of energy transfer might be possible from the elastic bottom towards the internal mode as long as the modes are coupled. However, taking up such a non-linear problem is beyond the scope of this thesis as well as our current expertise.

Since we have considered the thesis problems in Chapters 2-4 for finite depth water only, that is why we get one zero root (wavenumber) corresponding to the bottom mode. We know that zero wavenumber does not give rise to any wave propagation and subsequently the bottom mode was not considered for our case.

In a similar manner, the explanation provided for the problem in Chapter 2 can be extended for the problems in Chapters 3 and 4 too.

APPENDIX B

EQUIVALENCE OF BOTTOM BOUNDARY CONDITIONS

Here we show how the bottom boundary condition (2.6) gets reduced to a condition equivalent to an impermeable condition under certain constraints. The velocity potential, in the lower layer fluid of density ρ_1, which is of time harmonic nature, may be expressed as $\Phi(x, y, z, t) = \mathrm{Re}\{\phi(x, y)e^{i\gamma z}e^{-i\omega t}\}$ for the case of oblique waves. The sea-bed is considered in the form $y = h_b + \eta(x, t)$ where $\eta(x, t)$ is the elevation of the bed. For the time being, we ignore the term $\delta b(x)$. The bottom boundary condition at the elastic sea-bed takes the following form:

$$K\Phi + \Big\{D\nabla^4_{x,z} + 1 - \epsilon K\Big\}\frac{\partial\Phi}{\partial n} = 0 \quad \text{on} \quad y = h_b + \eta(x, t), \tag{B.1}$$

where, $\nabla^4_{x,z} = \frac{\partial^4}{\partial x^4} + 2\Big(\frac{\partial^2}{\partial x^2}\Big)\Big(\frac{\partial^2}{\partial z^2}\Big) + \frac{\partial^4}{\partial z^4}$ is the two-dimensional biharmonic operator. Equation (B.1) is the combination of the following two conditions:

1. $\Big\{D\nabla^4_{x,z} - \epsilon K\Big\}\eta(x, t) = -\rho_1 g\Big[h_b + \eta(x, t)\Big] - \rho_1\frac{\partial\Phi}{\partial t}\Big|_{y=h_b}$,

2. $\dfrac{\partial\eta}{\partial t} = \dfrac{\partial\Phi}{\partial n}$.

Now we remove the elastic parameters from the system, i.e., take $D = 0$, $\epsilon = 0$. From the first of the above conditions, we get

$$\begin{aligned} & -\rho_1 g\Big[h_b + \eta(x, t)\Big] - \rho_1\frac{\partial\Phi}{\partial t}\Big|_{y=h_b} = 0 \\ \Rightarrow \quad & -\rho_1 g\eta(x, t) - \rho_1\frac{\partial\Phi}{\partial t}\Big|_{y=h_b} = \rho_1 g h_b. \end{aligned}$$

Since the elastic bed is now treated as a rigid bed, therefore there does not exist any wave at the bottom. Thus, $\eta(x,t) = 0$ identically and the above condition becomes

$$\rho_1 g h_b = -\rho_1 \frac{\partial \Phi}{\partial t}\Big|_{y=h_b}. \tag{B.2}$$

This is a direct consequence of Bernoulli's equation, where $\rho_1 g h_b$ is the total pressure exerted by the water column of height h_b due to its mass and this is the only pressure.

Let P be the pressure at a point in the lower layer fluid. From Bernoulli's equation, we get

$$\begin{aligned}
& P = -\rho_1 g y - \rho_1 \frac{\partial \Phi}{\partial t} \\
\Rightarrow \quad & \frac{\partial P}{\partial t} = -\rho_1 g \frac{\partial y}{\partial t} - \rho_1 \frac{\partial^2 \Phi}{\partial t^2} \\
\Rightarrow \quad & \frac{\partial P}{\partial t}\Big|_{y=h_b} = -\rho_1 g \frac{\partial}{\partial t}\Big[h_b + \eta(x,t)\Big] - \rho_1 \frac{\partial^2 \Phi}{\partial t^2}\Big|_{y=h_b} \\
\Rightarrow \quad & \frac{\partial P}{\partial t}\Big|_{y=h_b} = -\rho_1 \frac{\partial^2 \Phi}{\partial t^2}\Big|_{y=h_b}.
\end{aligned}$$

Also at $y = h_b$, the pressure remains the same for all time, i.e.,

$$\begin{aligned}
& \frac{\partial P}{\partial t}\Big|_{y=h_b} = 0 \\
\Rightarrow \quad & -\rho_1 \frac{\partial^2 \Phi}{\partial t^2}\Big|_{y=h_b} = 0 \\
\Rightarrow \quad & \phi = 0, \text{ on } y = h_b, \text{ since } \Phi \text{ is periodic in time.}
\end{aligned}$$

From Eq. (B.1), we get

$$\frac{\partial \phi}{\partial n} = 0 \quad \text{on} \quad y = h_b + \eta(x,t). \tag{B.3}$$

Equation (B.3) shows that Eq. (2.6) gets reduced to the bottom condition as was used in Mohapatra and Bora [71] in which the authors considered the problem of oblique wave scattering by a small undulating bed in a two-layer fluid with the upper layer covered by a rigid lid but they did not consider the bed to be an elastic one.

LIST OF PUBLISHED AND COMMUNICATED PAPERS

Based on the work in this thesis, the following published and communicated papers have resulted:

1. Ayan Chanda and Swaroop Nandan Bora, "Propagation of oblique waves over a small undulating elastic bottom topography in a two-layer fluid flowing through a channel", **International Journal of Applied Mechanics**, 12(2), 2050023, 2020 (30 pages).

2. Ayan Chanda and Swaroop Nandan Bora, "Scattering of linear oblique water waves propagating by an elastic bottom undulation in a two-layer fluid", **Zeitschrift für angewandte Mathematik und Physik (ZAMP)**, 71(4), 107, 2020 (32 pages).

3. Ayan Chanda and Swaroop Nandan Bora, "Effect of a porous sea-bed on water wave scattering by two thin vertical submerged porous plates", **European Journal of Mechanics - B / Fluids**, 84, 250-261, 2020.

4. Ayan Chanda and Swaroop Nandan Bora, "Investigation of water wave scattering by an elastic sea-bed of varying depth in two superposed fluids covered by an ice-sheet", **Ocean Engineering**, doi:10.1016/j.oceaneng.2020.108510, 221, 108510, online 21 January 2021 (18 pages).

5. Ayan Chanda and Swaroop Nandan Bora, "Scattering of flexural gravity waves by a pair of submerged vertical porous barriers located above a porous sea-bed", **ASME. Journal of Offshore Mechanics and Arctic Engineering**, February 2022; 144(1): 011201. https://doi.org/10.1115/1.4051475.

6. Ayan Chanda and Swaroop Nandan Bora, "Investigation of oblique flexural gravity wave scattering by a pair of submerged vertical porous barriers with different porosities", Revised version submitted to **Journal of Engineering Mechanics, ASCE**.

7. Ayan Chanda and Swaroop Nandan Bora, “Study of scattering of water waves by two submerged porous plates over an elastic sea-floor”, Revised version under preparation for submission to **Geophysical and Astrophysical Fluid Dynamics**.